Measurement of Tensor Analyzing Powers in Elastic Electron Deuteron Scattering with BLAST

by

Chi Zhang

Submitted to the Department of Physics
in partial fulfillment of the requirements for the degree of

Doctor of Philosophy

at the

MASSACHUSETTS INSTITUTE OF TECHNOLOGY

May 2006

Author . . . .
Department of Physics
May, 2006

Certified by . . . .
William Bertozzi
Professor
Thesis Supervisor

Accepted by . . . .
Thomas J. Greytak
Chairman, Department Committee on Graduate Students

Measurement of Tensor Analyzing Powers in Elastic Electron Deuteron Scattering with BLAST

by

Chi Zhang

Submitted to the Department of Physics
on May, 2006, in partial fulfillment of the
requirements for the degree of
Doctor of Philosophy

Abstract

This work reports a precision measurement of deuteron tensor analyzing powers T_{20} and T_{21} at the MIT-Bates Linear Accelerator Center. Data were collected simultaneously over a momentum transfer range of 2.15 to 4.5 fm^{-1} in the Bates Large Acceptance Spectrometer Toroid (BLAST) with a highly polarized internal gas target. Deuterium form factors G_C and G_Q were separated using the new data with better precision and the location of the first node of the deuteron monopole form factor was confirmed. The new data provide strong constraints on the nuclear models in a momentum transfer range covering the minima of T_{20} and the first node of G_C.

Thesis Supervisor: William Bertozzi
Title: Professor

Acknowledgments

I would like to express my deepest gratitude to my advisor, Prof. William Bertozzi, for the opportunity to work on this experiment. I truly admire the his deep insight in physics, respect to the students and the academic freedom he shares with the member of his group. I am greatly thankful to the members of my thesis committee, Dr. William Donnelly and Prof. Amihay Hanany. Even though many of his students have become leading experts in the field, Dr. Donnelly is personable and patient. He always managed to make the theoretical concepts easy to understand. I must also thank Dr. William Turchinetz who has truly been the spokesperson for the T_{20} experiment at Bates over the entire duration of the project. I also acknowledge Professors Ricardo Alarcon, John Calarco and Bob Redwine, especially for the useful suggestions by John on the ed-elastic analysis.

I would like to than Dr. Zilu Zhou, Simon Sirca, Shalev Gilad, and Tancredi Botto for the guidance on my research over the years. Zilu is one of the best scientists I have had the privilege to work with. His knowledge, devotion and integrity make him truly special. He continued to offer his expert opinions even after leaving the collaboration. Simon is my mentor who helped me made my first baby steps into my research. He helped me write my first program in C++ and understand the physics of deuteron structure. It was a great loss to me and the collaboration that he had to leave the project early. Tancredi played an extremely important role in the commissioning of BLAST. I learned a great deal of data analysis from him. Thanks also go to Akihisha Shinosaki for his work on the UGBS and for giving me the script to make T_{20} figures, which evolved to produce all the figures in the results chapter.

I would like to thank Dr. Doug Hassel and Karen Dow for their tremendous contributions to the BLAST project. They have always been patient, friendly and understanding. They also helped proofreading several chapters of this thesis. I also owe a great deal to Prof. Tim Smith and Dr. Tong Lee, who guided me into the BLAST software projects. I would also like to thank Dr. Taylan Akdogan who, times again, patiently answered my questions on programming and the Compton polarimeter. Taylan also helped proofreading the relevant sections of this thesis. Thanks to Dr. Renee Fatemi who took over Aaron's analysis and provided the information for Tab. 4.15. Thanks also go to the research staff at Bates, Dr. Wilbur Franklin, Michael Kolhm and Townsend Zwart.

I am deeply indebt to my fellow students. It is hard to imagine how to overcome the long road without their hard work and friendship. Chris Crawford is always such a source of inspiration. Every discussion with him, on physics, math or anything else have been an enlightening experience. I would like to offer my special thanks to Nikolas Meitanis, who I can always talk to when the going get tough. Thanks to Yuan Xiao, who is such a faithful friend and devoted tremendous effort to the ion polarimeter. Thanks go to the friendship from Aaron Maschinot, who deserves the respect from all of us for single handed implemented the six dozen rotations in GEANT. Thanks Adam Degrush for the auto-control system without which everyone would be insane after three years of shifts. Thanks to Jason Seely, Ben Clasie for the many friendly conversations. Thanks to Vitaliy Ziskin for reading and working on DGen and many other things. Thanks to my friends Tavi Filoti, Peter Karpius, Adrian Sindile and Eugine Geis.

This thesis would not have been possible if not for the hard work of the Bates staff: the engineers Ernie Ihloff and Jim Kelsey; and the technicians and RPO.

I must thank the faculty members at the Experimental Nuclear Physics group, University of Maryland. George Chang, Jim Kelly, Nick Chant and Elizabeth Beise, who introduced me to the field of electron scattering.

No words can express my gratitude to my parents who have devoted their unconditional love to me. Last but certainly not least, I owe a great deal to my wife who, through good times and bad, has always supported me.

Dedicated to my family.

Contents

List of Figures

List of Tables

Chapter 1

Introduction

One of the principal goals of nuclear physics is to understand the nucleon-nucleon (NN) interaction. The NN interaction is a particular manifestation of the strong interaction described by Quantum Chromodynamics (QCD), in which the building blocks of the world are quarks and gluons. The current understanding is that the nuclear degrees of freedom are only the effective ones after the "freeze-out" of the fundamental quark degrees of freedom. For instance, in the simplest form of the bag models [1], hadrons serve as "bags" that confine the quarks and gluons. The quarks move freely inside the bag, known as the asymptotic freedom of the strong interaction. However, the freeze-out is not complete. For example in the Chiral bag model, pions arise as Goldstone bosons to conserve the chiral symmetry at the boundary of the bag [2]. At large inter-nucleon distances of the order of 2 fm $\sim 1/m_\pi$, the NN interaction is well understood in terms of model-independent one-pion exchange first proposed by Yukawa 70 years ago [3]. At shorter ranges, the nucleons themselves have substantial overlap, and therefore the underlying quark and gluon degrees of freedom play an important role in the inter-nucleon interaction. Due to the nonperturbative nature of strong interaction at this range, it is not yet possible to describe the NN interaction as solutions to the QCD Lagrangian.

Many realistic NN interaction models have been constructed by fitting NN scattering data. Some of the well-known NN potentials are: Paris [4], Reid [5, 6], Argonne $v18$ [7], Nijmegen [6], and CD Bonn [8]. The modern NN potentials try to include all possible operator structures permitted by symmetry, continuity and differentiability considerations, and are fit to low-energy NN scattering data. In this light, these potential models are analogous to the effective field theory (EFT) approach where one starts by defining the most general Lagrangian consistent with the symmetries of the underlying theory [9]. Since the potentials are fit to *np* or *pp* scattering data, the deuteron, as the only stable two-nucleon bound state, plays a special role in the understanding of the NN interaction.

Since the electromagnetic probe is well understood in terms of Quantum Electrodynamics (QED), and the electromagnetic interaction is much weaker than the NN interaction between nucleons, electron scattering experiments provide an excellent tool to study nuclear structure [10]. Experimental study of electron-deuteron scattering started in the 60s, and extensive data were collected on the cross section of unpolarized ed-elastic scattering (Sec. 2.1.2) [11, 12, 13, 14, 15, 16, 17, 18, 19, 20, 21, 22, 23, 24, 25, 26, 27, 28]. These cross section data, combined with the Rosenbluth separation [29] technique, provide two structure functions of the deuteron, $A(Q)$ and $B(Q)$. However, the elastic scattering of electrons off a spin-1 particle, such as the deuteron, is described by three form factors, the charge monopole, magnetic dipole and charge quadrupole form factors. At least one additional measurement is required to completely separate the form factors. It was only in the last two decades that innovative accelerator and target technologies provided new experimental techniques to measure polarized observables.

Among the polarized observables, T_{20} is the most extensively measured one [30, 31, 32, 33, 34, 35, 36, 37, 38, 39] (Sec. 2.1.3), thanks to its large size and the fact that it can be measured with unpolarized electron beams. The first measurement of T_{20} was carried out at MIT Bates laboratory in 1984. Two decades after, unfortunately, the data on T_{20} are stillunsatisfactory. Only 26 data points are available (41 with T_{21} data included) compared to the few hundred cross section data points, statistical precisions are poor, and inconsistencies between data sets exist.

Calculations based on nonrelativistic impulse approximation (NRIA) and phenomenological NN potentials are able to fit $A(Q)$ and $B(Q)$ data reasonably well up to a momentum transfer of about 2 fm^{-1} [40] (Sec. 2.2). However the deviation between these calculations and data at higher momentum transfers is significant, demonstrating the important contributions from two-pion exchanges, meson exchange currents, and relativistic corrections. Discrepancy between NRIA and T_{20} data is significant too at $Q \gtrsim 4$ fm^{-1}, while at lower Q the poor precision and accuracy in existing data could not establish the contribution from those corrections unambiguously.

The limitations of NRIA motivated more sophisticated theoretical models which include meson exchange currents and other relativistic effects. These models can be divided into a few categories:

- Addition of MEC and relativistic corrections to a nonrelativistic impulse approximation [41, 42, 43, 44, 45, 46];
- Quasipotential equations with relativistic impulse approximation [47, 48, 49].
- Chiral Perturbation Theory (χPT) [50].

These approaches are nicely reviewed in Ref. [51]. All models are able to explain part of data reasonably. However, none of them is able to be consistent with all the deuteron form factor and static moment data, and there is no concensus on which is the best approach. The lack of precision polarized measurements and the poor consistency within the data make it hard to test the various theories.

This thesis reports a measurement of the tensor analyzing powers T_{20} and T_{21} carried out at the MIT Bates Linear Accelerator Laboratory with the Bates Large Acceptance Spectrometer Toroid (Chap. 3). The experiment utilized a few innovative accelerator, target and detector technologies offering unique advantage in the study of deuteron structure:

- An electron storage ring capable of storing over 200 mA of highly polarized electron beam (Sec. 3.1).
- An Atomic Beam Source and an internal target providing a pure deuterium target with strong vector and tensor polarizations; and a target holding mechanism capable of directing the quantization axis of the target spin to arbitrary direction in the horizontal plane (Sec. 3.2). Coupled with the polarized electron

beam, it allowed the experimental study of electron-deuteron spin asymmetries across many different beam-target spin states. The low target density compared to liquid targets used in extracted beam experiments are compensated by the high beam current.

- A large acceptance magnetic spectrometer with left-right symmetric geometry (Sec. 3.3), allowing data collection across a large acceptance over many reaction channels simultaneously.

The experiment was carried out between June 2002 to May 2005, and many reaction channels from a deuterium target were studied, including, besides the tensor asymmetries in $\overleftrightarrow{D}(e, e'd)$ detailed in this work, vector analyzing powers in $\vec{D}(\vec{e}, e'd)$ [52], vector and tensor asymmetries in $\overleftrightarrow{\vec{D}}(\vec{e}, e'p)$ [53], G_E^n measurement via $\vec{D}(\vec{e}, e'n)$ [54], G_M^n measurement via inclusive quasi-elastic $\vec{D}(\vec{e}, e')$ scattering [55].

Chapter 2

Theoretical Motivation

This chapter discusses the formalism of elastic electron deuteron (ed-elastic) scattering. In Sec. 2.1, the kinematics are defined, and observables are presented for both unpolarized and polarized scattering. A detailed discussion is devoted to the Non-relativistic Impulse Approximation (NRIA) in Sec. 2.2. The purpose is to illustrate some of the main properties of the deuteron and to motivate the more sophisticated theoretical models that include meson exchange currents (MEC) and additional relativistic effects. A brief review of these models is given with an emphasize on the contribution of MEC to both unpolarized and polarized observables. The chapter concludes with an brief review of the world data for ed-elastic scattering and the comparison with the theoretical models (Sec. 2.3).

2.1 Elastic Electron-Deuteron Scattering

2.1.1 Kinematics

Under the one-photon exchange (OPE) approximation [10], the incident electron exchanges one virtual photon with the target particle. The kinematics with a polarized target are illustrated in Fig. 2-1. The incident electron with energy E_0 is scattered in the direction $\Omega_e = (\theta_e, \phi_e)$ with energy E'. The 4-momentum transfer from the electron to the target deuteron is $q \equiv k_1 - k_2 = (\omega, \mathbf{q})$. Let M_d be the deuteron mass;

then

$$E' = E_0/f, \quad \text{and} \quad Q^2 \equiv -q^2 = 4E_0E' \sin^2 \frac{\theta_e}{2} \tag{2.1}$$

where $f = 1 + \frac{2E_0}{M_d} \sin^2 \frac{\theta_e}{2}$ is usually called the recoil factor.

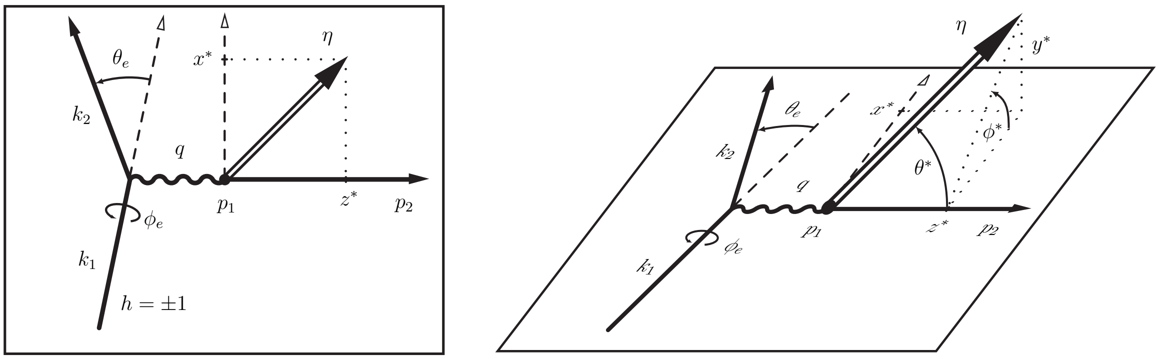

Figure 2-1: Kinematics for the polarized elastic scattering OPE amplitude in the scattering plane (left), and in three dimensions (right). The polar angles (θ^*, ϕ^*) and components (x^*, y^*, z^*) of the target polarization vector η are also shown.

2.1.2 Unpolarized Cross Section

Assuming parity and time-reversal invariance, elastic electron-deuteron (ed-elastic) scattering under OPE is completely described by three form factors: the charge monopole G_C, the quadrupole G_Q and the magnetic dipole G_M. The unpolarized elastic electron-deuteron cross section can be written as [10, 56, 51, 40, 57]:

$$\frac{d\sigma_0}{d\Omega} = \frac{\sigma_{\text{Mott}}}{f} S, \quad \text{with} \quad \sigma_{\text{Mott}} = \frac{\alpha^2 \cos^2(\theta_e/2)}{4E_0^2 \sin^4(\theta_e/2)}, \tag{2.2}$$

the Mott cross section which describes the scattering off a point target, and

$$S = A(Q^2) + B(Q^2) \tan^2 \frac{\theta_e}{2}, \tag{2.3}$$

originates from the electromagnetic structure of the deuteron. The structure functions A and B are given by the electromagnetic form factors

$$
\begin{aligned}
A(Q^2) &= G_C^2(Q^2) + \frac{8}{9}\eta^2 G_Q^2(Q^2) + \frac{2}{3}\eta G_M^2(Q^2), \qquad (2.4)\\
B(Q^2) &= \frac{4}{3}\eta(1+\eta) G_M^2(Q^2), \qquad (2.5)
\end{aligned}
$$

where $\eta = \dfrac{Q^2}{4M_d^2}$.

$A(Q^2)$ and $B(Q^2)$ can be determined through Rosenbluth separation [29] of the unpolarized ed-elastic cross section. Since there are three form factors and the Rosenbluth separation only gives two observables, additional measurements are needed to completely separate the form factors. These measurements can be made using electron scattering from a polarized target.

2.1.3 Polarized Observables

As a spin-1 particle, the deuteron can have vector and tensor polarizations. Let M denote the projection of deuteron spin along its quantization axis. The vector polarization is given by $P_z = n_+ - n_-$ where $n_\pm$ is the relative population of the deuteron in the $M = \pm 1$ states. The tensor polarization is defined as $P_{zz} = n_+ + n_- - 2n_0 = 1 - 3n_0$ where n_0 is the relative population of the $M = 0$ state. P_z can be between -1 and 1, P_{zz} can be between -2 and 1, and the vector and tensor polarization are related by the constraint $n_+ + n_- + n_0 = 1$. For example, vector polarization P_z must be 0 when $P_{zz} = -2$.

The cross section of elastic electron scattering off a polarized deuterium target can be written as [10, 40, 51, 56, 57]:

$$
\frac{d\sigma}{d\Omega}(h, P_z, P_{zz}) = \frac{d\sigma_0}{d\Omega}\left(1 + P_{zz}\Gamma + hP_z\Delta\right), \qquad (2.6)
$$

where $\dfrac{d\sigma_0}{d\Omega}$ is the unpolarized cross section, and

$$\Gamma = \frac{1}{\sqrt{2}}\left[\left(\frac{3}{2}\cos^2\theta^* - \frac{1}{2}\right)T_{20} - \sqrt{\frac{3}{2}}\sin 2\theta^*\cos\phi^* T_{21} + \sqrt{\frac{3}{2}}\sin^2\theta^*\cos 2\phi^* T_{22}\right], \tag{2.7}$$

$$\Delta = \sqrt{3}\left[\frac{1}{\sqrt{2}}\cos\theta^* T^e_{10} - \sin\theta^*\cos\phi^* T^e_{11}\right], \tag{2.8}$$

where (θ^*, ϕ^*) is the direction of the target spin orientation defined in the LAB frame with respect to the momentum transfer, as shown in Fig. 2-1. The analyzing powers T_{ij} can in turn be expressed in terms of the three form factors [1],

$$T_{20}(Q^2,\theta_e) = -\frac{1}{\sqrt{2}S}\left[\frac{8}{3}\eta G_C G_Q + \frac{8}{9}\eta^2 G_Q^2 + \frac{1}{3}\eta\left[1 + 2(1+\eta)\tan^2\frac{\theta_e}{2}\right]G_M^2\right], \tag{2.9}$$

$$T_{21}(Q^2,\theta_e) = -\frac{2}{\sqrt{3}S}\eta\sqrt{\eta + \eta^2\sin^2\frac{\theta_e}{2}}G_M G_Q, \tag{2.10}$$

$$T_{22}(Q^2,\theta_e) = -\frac{1}{2\sqrt{3}S}\eta G_M^2, \tag{2.11}$$

$$T^e_{10}(Q^2,\theta_e) = -\frac{1}{S}\eta\sqrt{\frac{2}{3}(1+\eta)\left(1+\eta\sin^2\frac{\theta_e}{2}\right)}G_M^2\sec\frac{\theta_e}{2}\tan\frac{\theta_e}{2}, \tag{2.12}$$

$$T^e_{11}(Q^2,\theta_e) = \frac{2}{\sqrt{3}S}\sqrt{\eta(1+\eta)}G_M\left(G_C + \frac{1}{3}\eta G_Q\right)\tan\frac{\theta_e}{2}. \tag{2.13}$$

The superscript ^{e} in T^e_{10} and T^e_{11} indicates that a polarized electron beam is needed to measure them.

This work is devoted to the experimental determination of the tensor analyzing powers T_{20} and T_{21}. The 3rd tensor analyzing power T_{22} is proportional to G_M^2, which is redundant with $B(Q^2)$ and is very small in size. The vector analyzing powers, T^e_{10} and T^e_{11}, are the subject of the dissertation of Dr. P. J. Karpius [52] whose data were taken simultaneously with this work.

T_{20} can be expressed in terms of the ratio between the electric monpole and quadrupole form factors. Let $Y = \dfrac{2\eta}{3}\dfrac{G_Q}{G_C}$ and $X = \sqrt{\dfrac{\eta\left[1+2(1+\eta)\tan^2\frac{\theta_e}{2}\right]}{3}}\dfrac{G_M}{G_C}$;

[1] Following the convention in Ref. [10].

then

$$T_{20} = -\sqrt{2}\frac{Y(2+Y) + \frac{1}{2}X^2}{1 + 2Y^2 + 2X^2}. \tag{2.14}$$

X is typically very small in size compared to Y. It is customary to introduce $\tilde{T}_{20}$ where the X contributions are eliminated:

$$\tilde{T}_{20}(Q^2) = \frac{T_{20}(Q^2,\theta_e) + \frac{\delta}{2\sqrt{2}}}{1-\delta} = -\sqrt{2}\frac{Y(2+Y)}{1+2Y^2}, \quad \text{with} \quad \delta = \frac{2X^2}{1+2Y^2+2X^2}. \tag{2.15}$$

$\tilde{T}_{20}$ reaches its minimum of $-\sqrt{2}$ when $Y = 1$, and at the node of the charge form factor where $G_C = 0$, $\tilde{T}_{20} = -1/\sqrt{2}$. Therefore T_{20} sheds light on the location of the node of $G_C(Q^2)$ which is intimately related to the repulsive core in the NN potential (Sec. 2.2.1).

2.2 Nonrelativistic Impulse Approximation

In this section, we discuss the simplest picture of the deuteron structure, namely the nonrelativistic impulse approximation (NRIA). Under this approximation, the deuteron is viewed as a nonrelativistic two-body system bounded by the NN potential. The deuteron is then described with wave functions obtained by solving the Schrödinger equation with the NN potential.

2.2.1 Nonrelativistic Deuteron Wave Function

The tensor component of the NN interaction dictates that the deuteron wave function be a mixture of $^3S_1$ and $^3D_1$ states [44]:

$$\Psi_d^M(\mathbf{r}) = \frac{u(r)}{r}\mathcal{Y}_{101}^M(\theta,\phi) + \frac{w(r)}{r}\mathcal{Y}_{121}^M(\theta,\phi), \tag{2.16}$$

where $u(r)$ and $w(r)$ are the reduced radial wave functions for S- and D-state respectively.

$$\mathcal{Y}_{JLS}^M(\Omega_r) = \sum_{m_L,m_S} \langle J,M|L,m_L;S,m_S\rangle\, Y_{LM}|S,m_S\rangle$$

are the spin-spherical harmonics for a state with respective total, orbital and intrinsic angular momenta J, L, S, and M denotes the projection of the total angular momentum along its polarization axis. Fig. 2-2 shows the reduced S- and D- radial wave functions with the Argonne v_{18} potential [7]. Both $u(r)$ and $w(r)$ drop steeply at small r as a consequence of the repulsive core of the NN potential.

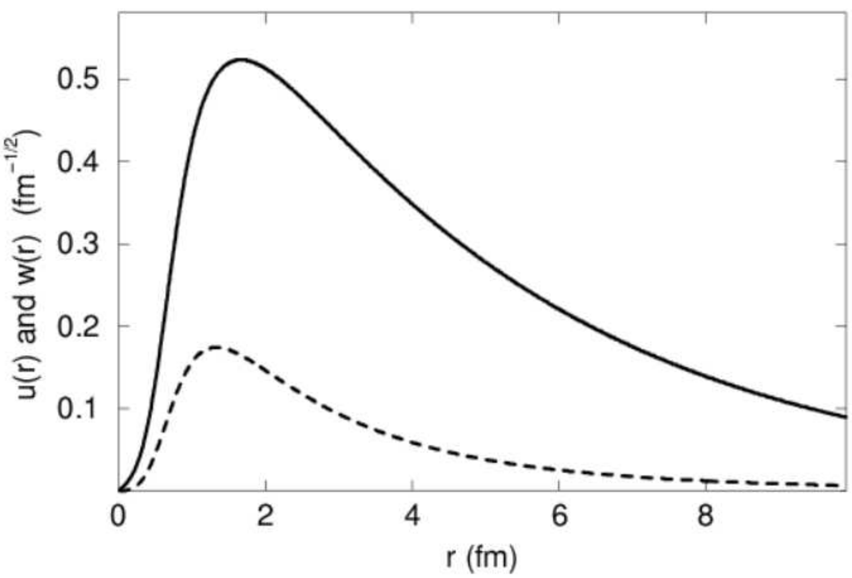

Figure 2-2: The S- and D-state radial wave functions, $u(r)$ (solid line) and $w(r)$ (dashed line) , for the Argonne v_{18} potential. Both reduced radial wave function drop steeply at small r due to the repulsive core.

Since the nuclear force has short range, for r outside of roughly 1 fm, the wave functions decrease exponentially just like the free-wave solutions of corresponding angular momentum. The rate of the decrease is determined by the binding energy E_B of the deuteron:

$$u(r) \to A_S e^{-\gamma r} \quad \text{and} \quad w(r) \to A_D e^{-\gamma r} \left\{ 1 + \frac{3}{\gamma r} + \frac{3}{\gamma^2 r^2} \right\} \quad \text{as} \quad r \to \infty, \qquad (2.17)$$

with $\gamma = \sqrt{\frac{1}{2} E_B (M_n + M_p)} = 0.23161$ fm^{-1}. The asymptotic D/S ratio $\eta_d = \dfrac{A_D}{A_S}$ is measured to be 0.0256 [58].

In this simple picture, the S- and D- state probabilities are

$$P_S = \int_0^\infty u^2(r)dr \quad \text{and} \quad P_D = \int_0^\infty w^2(r)dr. \tag{2.18}$$

In general the D-wave admixture predicted by various NN potential is about 4-8%. The static properties of the deuteron can be computed from the wave function. The magnetic moment is entirely determined, in the non-relativistic wave function approximation, by the D-state probability,

$$\mu_d = \mu_p + \mu_n - \frac{3}{2}\left(\mu_p + \mu_n - \frac{1}{2}\right) P_D, \tag{2.19}$$

where $\mu_p = 2.79285\ \mu_N$ and $\mu_n = -1.91304\ \mu_N$ are the proton and neutron magnetic moments respectively. The deuteron magnetic moment is experimentally found to be $\mu_d = 0.85744\ \mu_N = 1.714\ \frac{M_p}{M_d}\mu_N$ [2], which is close to $\mu_p + \mu_n$. However, μ_d can not be used to determine the D-wave probability due to the presence of meson exchange currents (MEC), isobar components and relativistic effects in addition to the simple model presented here.

The electric quadrupole moment arises purely due to the D-wave admixture,

$$Q_d = \frac{1}{50}\int_0^\infty w(r)\left[u(r) - \frac{1}{\sqrt{8}}w(r)\right] r^2 dr. \tag{2.20}$$

The quadrupole moment is dominated by the interference between the S- and D-state wave functions, and the integrand is weighted by r^2, which means that the static quadrupole moment is dominated by the long-range asymptotic behavior of the wave functions. Therefore, the quadrupole function and the asymptotic D/S ratio contain similar information. The deuteron electric quadrupole moment is measured to be $0.2859\ \mathrm{fm}^2 = 25.83\ \mathrm{M_d^{-2}}$.

[2] M_p and M_d are the is the proton and deuteron mass respectively.

From Eqs. 2.16, the wave function for each M state can be obtained:

$$\begin{aligned}
\Psi_d^0(\mathbf{r}) &= \sqrt{\frac{4}{\pi}}\left[\frac{u(r)}{r} - \sqrt{2}\frac{w(r)}{r}\left(\frac{3}{2}\cos^2\theta - \frac{1}{2}\right)\right]|1,0\rangle \\
&\quad + \sqrt{\frac{9}{\pi}}\frac{w(r)}{r}\sin\theta\cos\theta\left[e^{-i\phi}|1,+\rangle - e^{i\phi}|1,-\rangle\right], \qquad (2.21) \\
\Psi_d^{\pm1}(\mathbf{r}) &= \sqrt{\frac{4}{\pi}}\left[\frac{r(r)}{r} + \sqrt{\frac{1}{2}}\frac{w(r)}{r}\left(\frac{3}{2}\cos^2\theta - \frac{1}{2}\right)\right]|1,\pm\rangle \\
&\quad \pm\sqrt{\frac{9}{\pi}}\frac{w(r)}{r}e^{\pm i\phi}\sin\theta\cos\theta\,|1,0\rangle + \sqrt{\frac{9}{2\pi}}\frac{w(r)}{r}e^{\pm 2i\phi}\sin^2\theta\,|1,\pm\rangle. \qquad (2.22)
\end{aligned}$$

The probability density is, $\rho_d^M(\mathbf{r}) \equiv \Psi_d^{M*}(\mathbf{r})\Psi_d^M(\mathbf{r})$, or explicitly

$$\left\{\begin{aligned}
\rho_d^0(\mathbf{r}) &= \frac{4}{\pi}\left[C_0(r) - 2C_2(r)P_2(\cos\theta)\right] \\
\rho_d^{\pm1}(\mathbf{r}) &= \frac{4}{\pi}\left[C_0(r) + C_2(r)P_2(\cos\theta)\right]
\end{aligned}\right. , \qquad (2.23)$$

where

$$\left\{\begin{aligned}
C_0(r) &\equiv \left(\frac{u(r)}{r}\right)^2 + \left(\frac{w(r)}{r}\right)^2 \\
C_2(r) &\equiv \frac{w(r)}{r}\left(\sqrt{2}\frac{u(r)}{r} - \frac{1}{2}\frac{w(r)}{r}\right)
\end{aligned}\right. , \qquad (2.24)$$

and $P_2(\cos\theta) \equiv \frac{3}{2}\cos^2\theta - \frac{1}{2}$ is the Legendre polynomial of order 2. Fig. 2-3 shows the deuteron densities in the $M = 0$ and $M = \pm1$ states.

2.2.2 Wave Function in Momentum Space

It is convenient to discuss the dynamic properties of deuteron in the momentum space. Taking Fourier transformations of the wave functions in position space yields

$$\tilde{\Psi}_d^M(\mathbf{p}) \equiv \frac{1}{(2\pi)^{3/2}}\int e^{-i\mathbf{p}\cdot\mathbf{r}}\Psi_d^M(\mathbf{r}). \qquad (2.25)$$

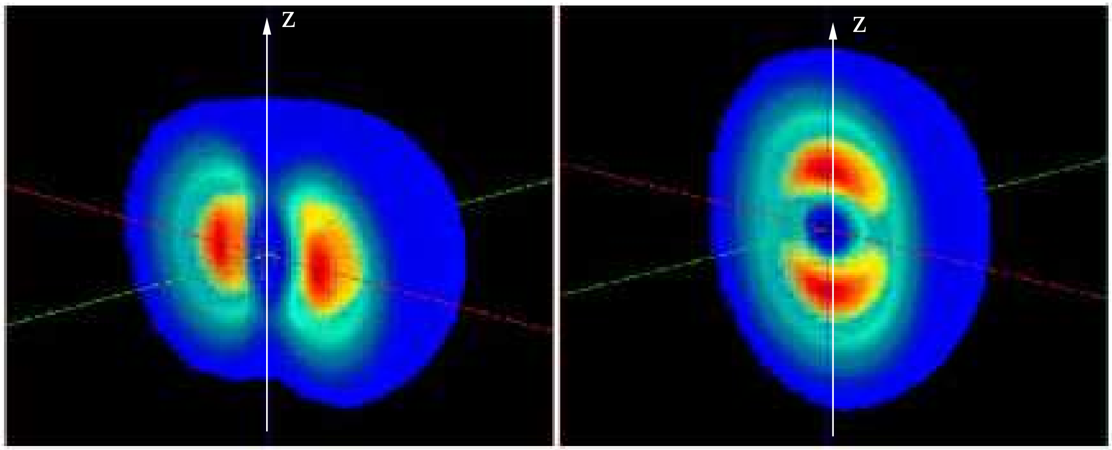

Figure 2-3: Deuteron densities in $M = 0$ (left) and $M = 1$ (right). Red represents the maximal nucleonic density, while dark volumes correspond to lower densities [51].

The corresponding momentum-space density functions, $\tilde{\rho}_d^M(\mathbf{p}) \equiv \tilde{\Psi}_d^{M*}(\mathbf{p})\tilde{\Psi}_d^M(\mathbf{p})$, take on a form similar to that of the position-space densities (Eq.2.23):

$$\left\{ \begin{array}{lcl} \tilde{\rho}_d^0(\mathbf{p}) & = & \frac{1}{4\pi}\left[\tilde{C}_0(p) - 2\tilde{C}_2(p)P_2(\cos\theta_p)\right] \\ & & \\ \tilde{\rho}_d^{\pm 1}(\mathbf{p}) & = & \frac{1}{4\pi}\left[\tilde{C}_0(p) + \tilde{C}_2(p)P_2(\cos\theta_p)\right] \end{array} \right. . \tag{2.26}$$

The $\tilde{C}_\ell(p)$ terms are defined in a similar manner as the $C_\ell(r)$, (Eqs. 2.24):

$$\left\{ \begin{array}{lcl} \tilde{C}_0(p) & \equiv & \tilde{R}_0(p)^2 + \tilde{R}_2(p)^2 \\ & & \\ \tilde{C}_2(p) & \equiv & \tilde{R}_2(p)\left(\sqrt{2}\tilde{R}_0(p) - \frac{1}{2}\tilde{R}_2(p)\right) \end{array} \right. . \tag{2.27}$$

In these equations, $\tilde{R}_\ell(p)$ is the Fourier-transformed radial wave function:

$$\tilde{R}_\ell(p) \equiv i^\ell \sqrt{\frac{2}{\pi}} \int_0^\infty r j_\ell(pr) u_\ell(r) \tag{2.28}$$

where $j_\ell(x)$ is the spherical Bessel function of order L.

Momentum space wave functions, $\left|\tilde{R}_\ell(p)\right|$, are shown in Fig. 2-4. There are a couple distinct features: 1) $\tilde{R}_0(p)$ displays a node at $p \gtrsim 0.4$ GeV (2 fm^{-1}); 2) The dominance of D-wave components at high momenta. The node arises from the sharp drop of $u(r)$ at small distance, which is a consequence of the repulsive core of the NN potential. $\tilde{\rho}_d^M(\mathbf{p})$ is observable in the electro-disintegration of deuteron [53].

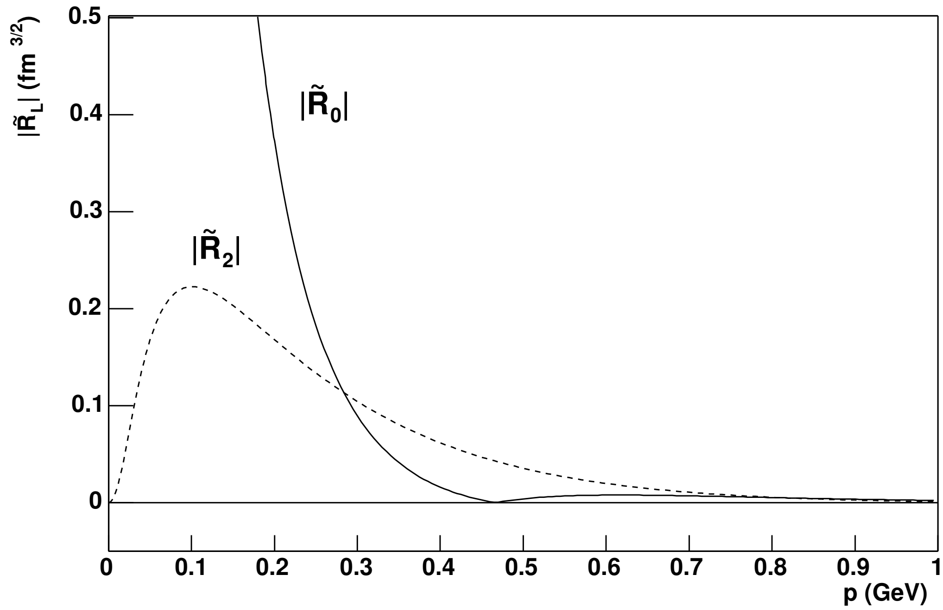

Figure 2-4: The magnitudes of the Fourier-transformed S- and D-state radial wave functions, $\left|\tilde{R}_0(p)\right|$ and $\left|\tilde{R}_2(p)\right|$. Note the node of $\tilde{R}_0(p)$ at $p \gtrsim 0.4$ GeV which is a consequence of the repulsive core of the NN potential.

2.2.3 Nonrelativistic Impulse Approximation

The nonrelativistic impulse approximation (NRIA) is based on the nonrelativistic deuteron wave function. In addition to the wave function, the impulse approximation assumes that the electron interacts with only one of the constituent nucleons while the other acts as a spectator. Therefore in NRIA, the deuteron electromagnetic form factors can be written as the product of nucleon form factors and the body form factor which depends on the deuteron wave function [59],

$$G_C(Q^2) = (G_E^p + G_E^n) \int \left[u^2(r) + w^2(r)\right] j_0\left(\frac{Qr}{2}\right) dr \tag{2.29}$$

$$G_Q(Q^2) = \frac{3}{\eta\sqrt{2}}(G_E^p + G_E^n) \int w(r) \left[u(r) - \frac{w(r)}{\sqrt{8}}\right] j_2\left(\frac{Qr}{2}\right) dr \tag{2.30}$$

$$\begin{aligned} G_M(Q^2) = {} & 2(G_M^p + G_M^n) \int \left\{ \left[u^2(r) - \frac{w^2(r)}{2}\right] j_0\left(\frac{Qr}{2}\right) \right. \\ & \left. + \left[\frac{u(r)w(r)}{\sqrt{2}} + \frac{w^2(r)}{2}\right] j_2\left(\frac{Qr}{2}\right) \right\} dr \\ & + \frac{3}{2}(G_E^p + G_E^n) \int w^2(r) \left[j_0\left(\frac{Qr}{2}\right) + j_2\left(\frac{Qr}{2}\right)\right] dr \end{aligned} \tag{2.31}$$

where $j_\ell(Qr/2)$ are spherical Bessel functions. Since both G_C and G_Q are proportional to $G_E^p + G_E^n$ in the NRIA, one immediate observation is that G_Q/G_C and thus $\tilde{T}_{20}$ is independent of nucleon form factors in this approximation [51].

The observables $A(Q)$, $B(Q)$ and T_{20} can be calculated from the various NN potentials in NRIA and the results are shown in Fig. 2-5 and 2-6. It is apparent that the NRIA approach agrees with the data only up to 2-3 fm^{-1}, and the deviation in $A(Q)$ between the data and the NRIA calculation is significant. All the NRIA approximations predict an $A(Q)$ that is 40-60% lower than the data at $Q \sim 6$ fm^{-1}. NRIA also underpredicts $B(Q)$; as a result, the first node of $B(Q)$ predicted by NRIA is lower in Q than indicated by data. The NRIA calculations using different NN potentials have similar behaviors, indicating the inherent limitation of the approximation itself. Comparison with T_{20} shows that NRIA clearly cannot explain the data at high momentum transfer ($Q \gtrsim 4$ fm^{-1}). In addition, at lower Q, the NRIA is only consistent with the Bates-84 data, while the NIKHEF T_{20} data are consistently lower (more negative) than any NRIA calculations by about one standard deviation.

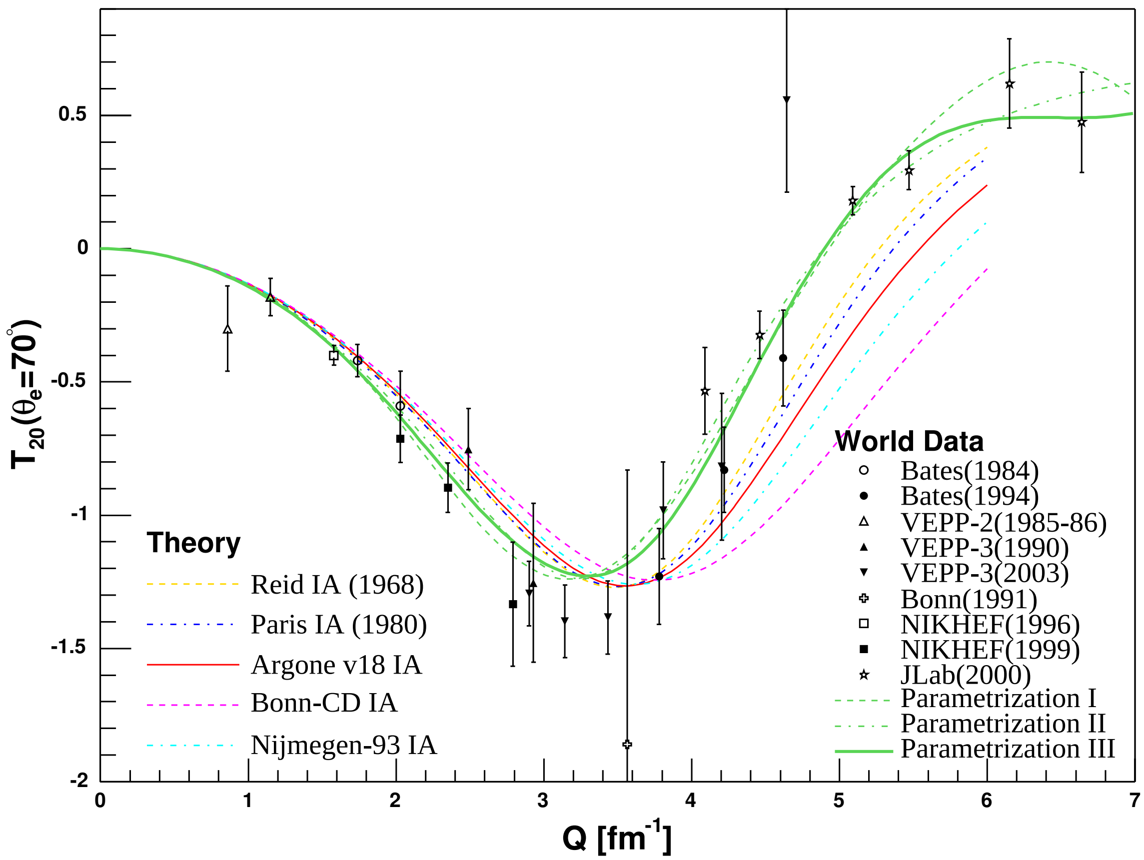

Figure 2-5: T_{20} in NRIA with different NN potentials. The potentials shown are the same as Fig. 2-6. World data and the three parameterizations are shown too (Sec. 2.3). The NRIA calculation deviate from the data at high momentum transfer. At lower Q, NRIA are consistent with Bates-84 data while the NIKHEF data are consistently lower by about 1-σ.

2.2.4 Relativistic Corrections

The limitation of NRIA motivated more sophisticated theoretical models. At above 2 fm^{-1}, the momentum transfer starts to become comparable to the nucleon mass, therefore relativistic effects must be taken into consideration. Theoretical models have been developed to include the meson exchange current (MEC), isobar components and other relativistic corrections to the nonrelativistic potential models [41, 42, 43, 44, 45]. Efforts are also devoted to construct intrinsically covariant theories, for example, the relativistic impulse approximation (RIA) with the addition of MEC contributions [47, 48, 49]. Recently, the development in Chiral perturbation theory provided new theoretical tools to understand the deuteron structure [50]. Ref. [40,

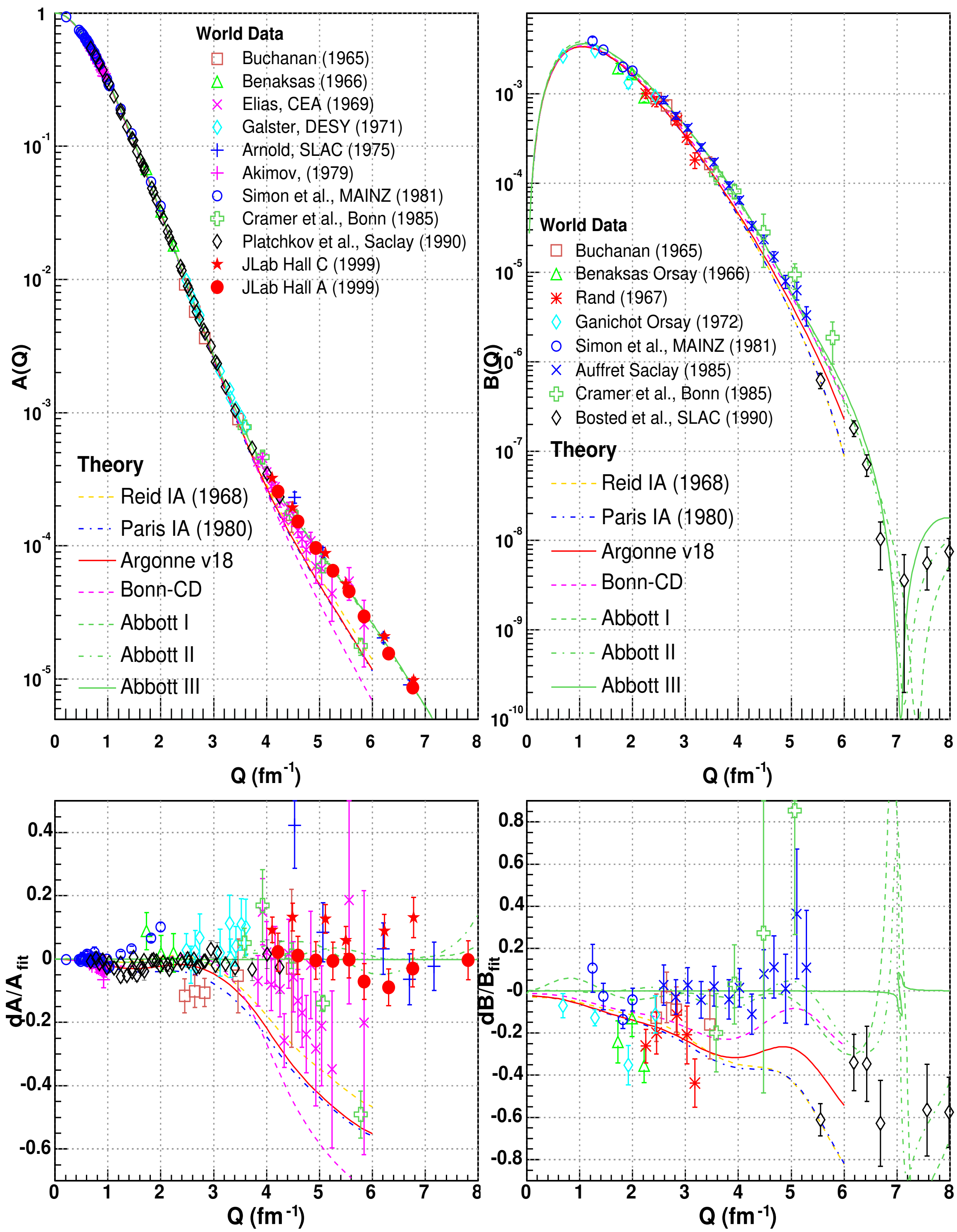

Figure 2-6: $A(Q)$ and $B(Q)$ in NRIA with different NN potentials (Reid [5], Paris [4], Argonne $v18$ [7], CD-Bonn [8] and Nijmegen [6]). World data and the three parameterizations are shown too (Sec. 2.3). The lower panels show the relative deviation from Parameterization III $(A(Q)-A_0(Q))/A_0(Q)$, where $A_0(Q)$ is the predicted value by Parameterization III (Sec. 2.3.3). It is apparent that the NRIA approach agrees with the data only up to 2-3 fm^{-1}, and NRIA predictions are significantly lower than data at higher Q.

51, 56, 57] provide very detailed review on different approaches, models and their comparison with data. We illustrate below the MEC contribution.

The long-range part of the NN interaction is well understood in terms of one-pion exchange. At medium and short range, two-pion exchange, as well as the exchange of heavier mesons such as ρ and ω, become important. MEC give rise to currents in the nuclear medium and the simple two body wave function description is no long valid. The virtual photon emitted by the electron can also couple to the exchanged meson itself. The diagrams for MEC effects are shown in Fig. 2-7. Since the deuteron has isospin zero, isovector contributions are forbidden in the ed-elastic scattering.

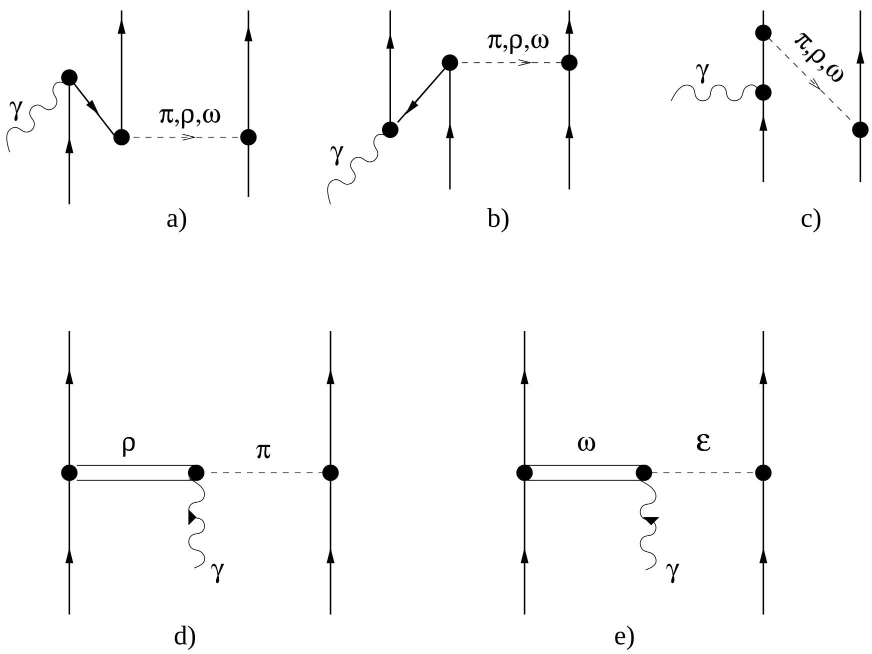

Figure 2-7: Meson-exchange current diagrams: a), b) pair terms, c) retardation, d) $\rho\pi\gamma$ term, e) $\omega\epsilon\gamma$ term

The effect of relativistic effects are shown in Figs. 2-8 and 2-9. It is seen that for T_{20}, MEC corrections play an important role in brings the NRIA into agreement with data at high momentum transfer. At low Q, the $\pi\rho\gamma$ contribution is small, yet the MEC effect is still significant. Pure NRIA lies above the Bates-84 data at $Q \leq 2$ fm^{-1}, while the addition of MEC increases the size (absolute value) of T_{20} such that the NRIA+MEC lies closer to the NIKHEF data. The inclusion of MEC into

NRIA is significant in $A(Q)$ and $B(Q)$ too, especially beyond $Q = 4$ fm^{-1}. It brings the NRIA model into better agreement to the $A(Q)$ data. On the other hand, the RIA includes some of the MEC contribution and the addition of the $\pi\rho\gamma$ diagram has relatively smaller effect, especially on $A(Q)$. The momentum transfer predicted by NRIA where G_M reaches its first node is higher than experimental value, while the node position derived from RIA is lower than experimental value. The agreements with experimental data, in the position of the node, by both NRIA and RIA are improved after the inclusion of the MEC and the $\pi\rho\gamma$ respectively.

It is interesting to observe that the contributions of MEC to the NRIA and $\pi\rho\gamma$ to the RIA have a different sign. In fact it is generally true that the contributions from individual MEC diagrams are comparable in size and have different signs, therefore, all MEC diagrams must be included consistently.

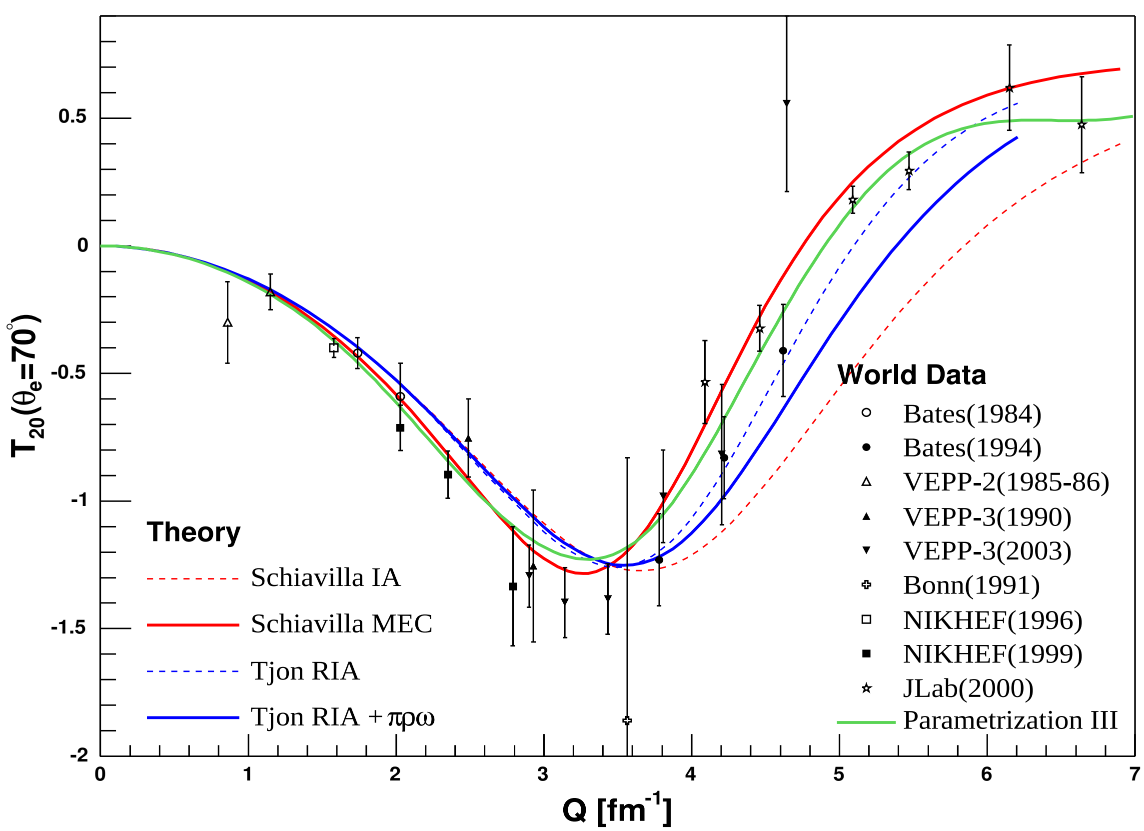

Figure 2-8: Relativistic corrections to impulse approximations in T_{20}. Two calculations, Schiavilla [45, 46] and Tjon [47]. The former is a nonrelativistic (NRIA) approach with MEC corrections, while that later is a relativistic approach (RIA) with the $\pi\rho\gamma$ correction.

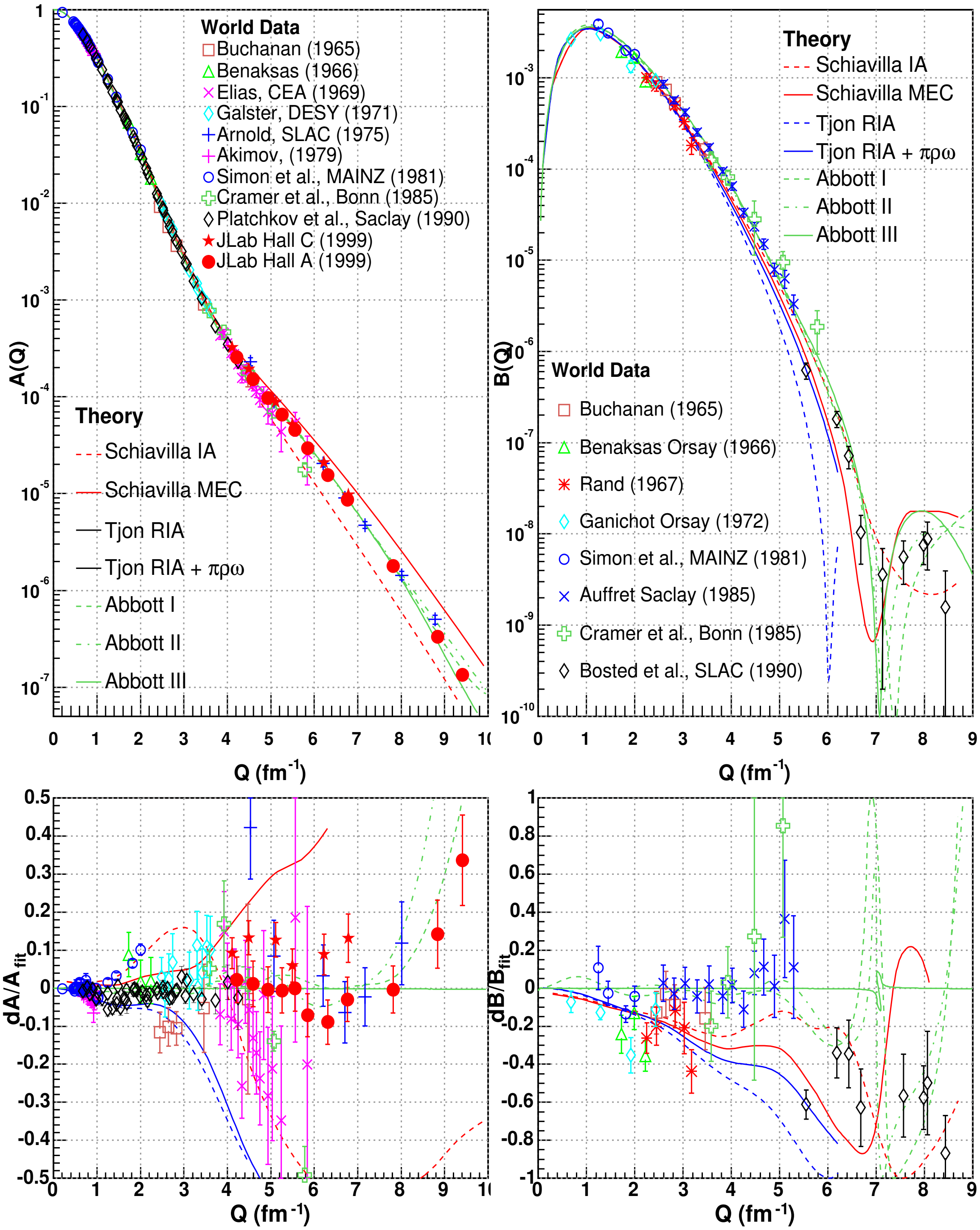

Figure 2-9: Relativistic corrections to impulse approximations in $A(Q)$ and $B(Q)$. Two calculations, Schiavilla [45] and Tjon [47]. The former is an NRIA with MEC corrections, while that later is an IRA with the $\pi\rho\gamma$ correction. From the left panels, NRIA prediction is significantly lower than the data at $Q > 4$ fm^{-1}. The addition of MEC (red solid) to NRIA (red dash) brings the model to better agreement with the data. On the right, The inclusion of MEC brings the model predicted node closer to the experimental value around 7 fm^{-1}. The lower panels show the relative deviation from Parameterization III, see the caption of Fig. 2-6.

2.3 The World Data

2.3.1 Cross Section Data

Extensive effort has been devoted to the measurement of the elastic electron-deuteron cross section [11, 12, 13, 14, 15, 16, 17, 18, 19, 20, 21, 22, 23, 24, 25, 26, 27, 28]. Some of these experiments measured the back scattering cross section [15, 16, 19, 25] to extract $B(Q)$. Some measured the cross section at forward angles [17, 18, 20, 21] for $A(Q)$. The rest made measurements at different Q^2 and θ_e and performed Rosenbluth separations on $A(Q)$ and $B(Q)$. World data for A and B are shown in Fig. 2-10.

It is worth noticing that at $Q \approx 2$ fm^{-1}, the $A(Q)$ measured by Simon *et al.* at Mainz [22], and by Platchkov *et al.* at Saclay [26] differ by about 10%, which is greater than 5-σ [60]. Mainz data at this momentum transfer lie consistently above the Saclay data, which are consistent with the earlier Benaksas measurements [15] except at the lowest Q^2 covered by Benaksas. This discrepancy has a profound implication on the work here and will be discussed in Sec. 4.6.1.

2.3.2 Polarized Data

The most extensively measured tensor analyzing power is T_{20} [30, 31, 32, 33, 34, 35, 36, 37, 38, 39] because of its large size and the fact it can be measured with an unpolarized electron beam. The previous world data are shown in Fig. 2-11. The knowledge of the target polarization is of great importance in these measurements. Most of these experiments used one of the three types of techniques in terms of the polarization determination: 1) unpolarized target with recoil-polarimetry measurements [30, 35, 38]; 2) polarized target with absolute target polarimetry [31, 32, 36, 37] [3]; 3) polarized target with target polarization measured by normalizing the data to models at low momentum transfer [33, 39]. The calibration of the target or recoil polarimeter is one major source of systematic error in the first two approach, while the 3^{rd} technique

[3] The VEPP-2(85/86) [31, 32] experiments did not have an internal target storage cell. The target was a polarized atomic jet. The polarization of the target gas jet was measured by standalone polarimeters, as documented in the publications.

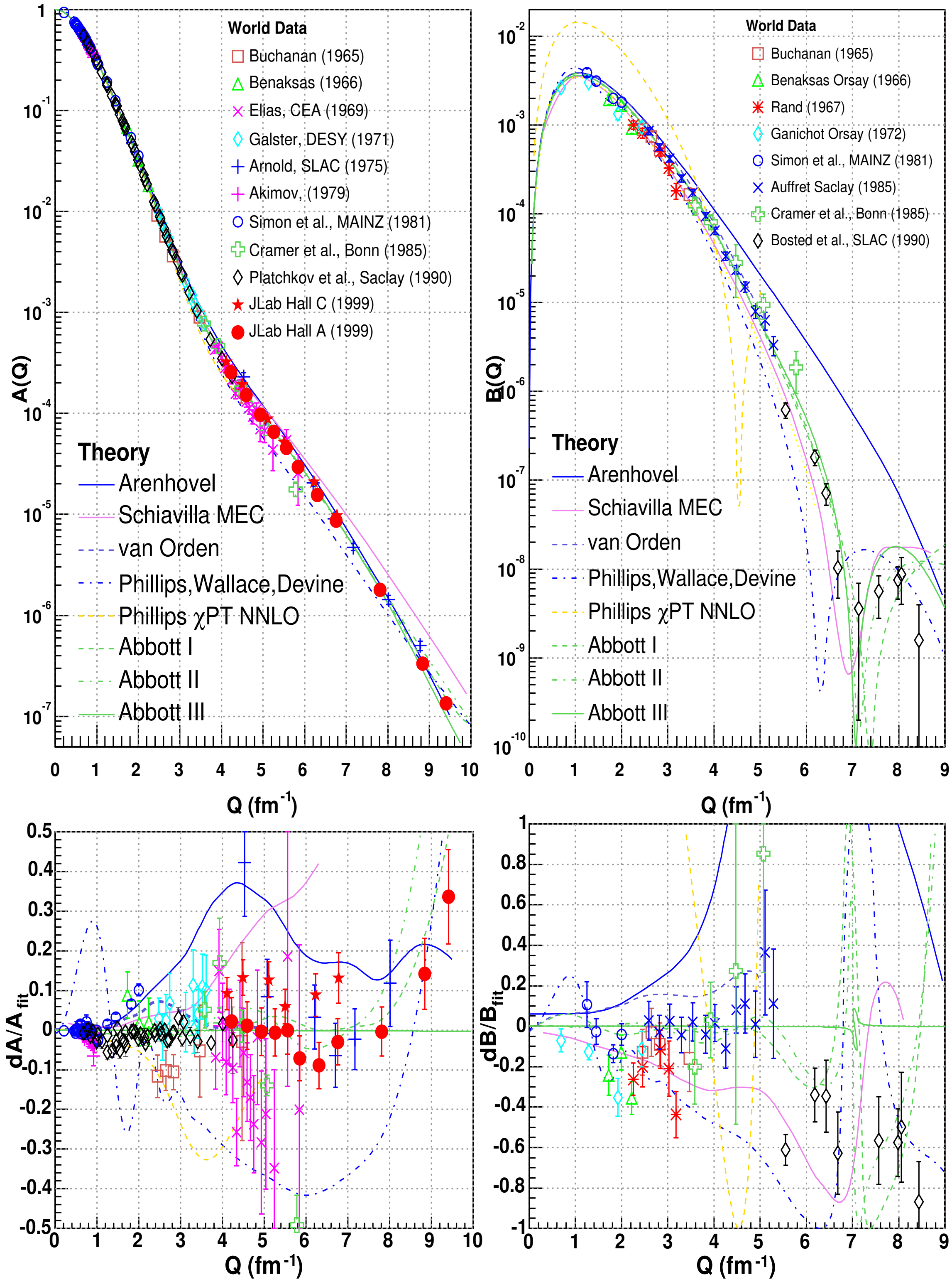

Figure 2-10: World data for $A(Q)$ and $B(Q)$ and comparison to theoretical models. The large discrepancy between Simon (MAINZ 1981, blue circle) and Platchkov (Saclay 1990, black diamond) at 2 fm^{-1} can be seen in the lower left panel. The lower panels show the relative deviation from Parameterization III, see the caption of Fig. 2-6

suffers from the drawback that the polarization measurement is not independent of the observables to be measured; therefore the results depend on the particular model used for the normalization.

The existing data on T_{20} are hardly satisfactory. The statistical precisions are poor, and insufficient to distinguish between the state-of-art deuteron structure models. The Q^2 coverage is fragmented, leading to difficulties in determining the shape of the T_{20} curve.

At 2 fm^{-1}, the Bates-1984 data and the NIKHEF-1999 data are only marginally consistent with each other. The difference is 1-σ or $\sim 15\%$. In addition, all NIKHEF measurements are consistently lower (more negative) than the Bates-1984 data in their overlap region. Again, this difference has profound implications for the work presented in this thesis and will be discussed again in Sec. 4.6.1. At higher momentum transfer, the agreement between Bates-1994 and JLab-2000 data are not satisfactory either. At about 4.1 fm^{-1}, the Bates-1994 data point is about 1-σ lower (more negative) than the JLab-2000, and this trend is repeated in the data at higher Q of 4.5 fm^{-1}.

T_{21} was measured as a by-product in some of the recent experiments [35, 38, 39]. The results are shown in Fig. 2-11. However, all these measurements were at relatively high Q^2 and suffer from significant statistical and systematic uncertainty.

2.3.3 Parameterization of World Data

The JLab t_{20} collaboration performed parameterizations of the world data [61] using three phenomenological models of the form factors. The three models are,

Parameterization I:

$$G_X(Q^2) = G_X(0) \cdot \left[1 - \left(\frac{Q}{Q_X^0}\right)^2\right] \cdot \left[1 + \sum_{i=1}^{5} a_{X_i} Q^{2i}\right]^{-1} \tag{2.32}$$

where $X = C,\ Q$, or M and Q_X^0 is the location of the first node of each form factor. Q_X^0 and a_{X_i} are fit to data and this parameterization produces explicitly the location

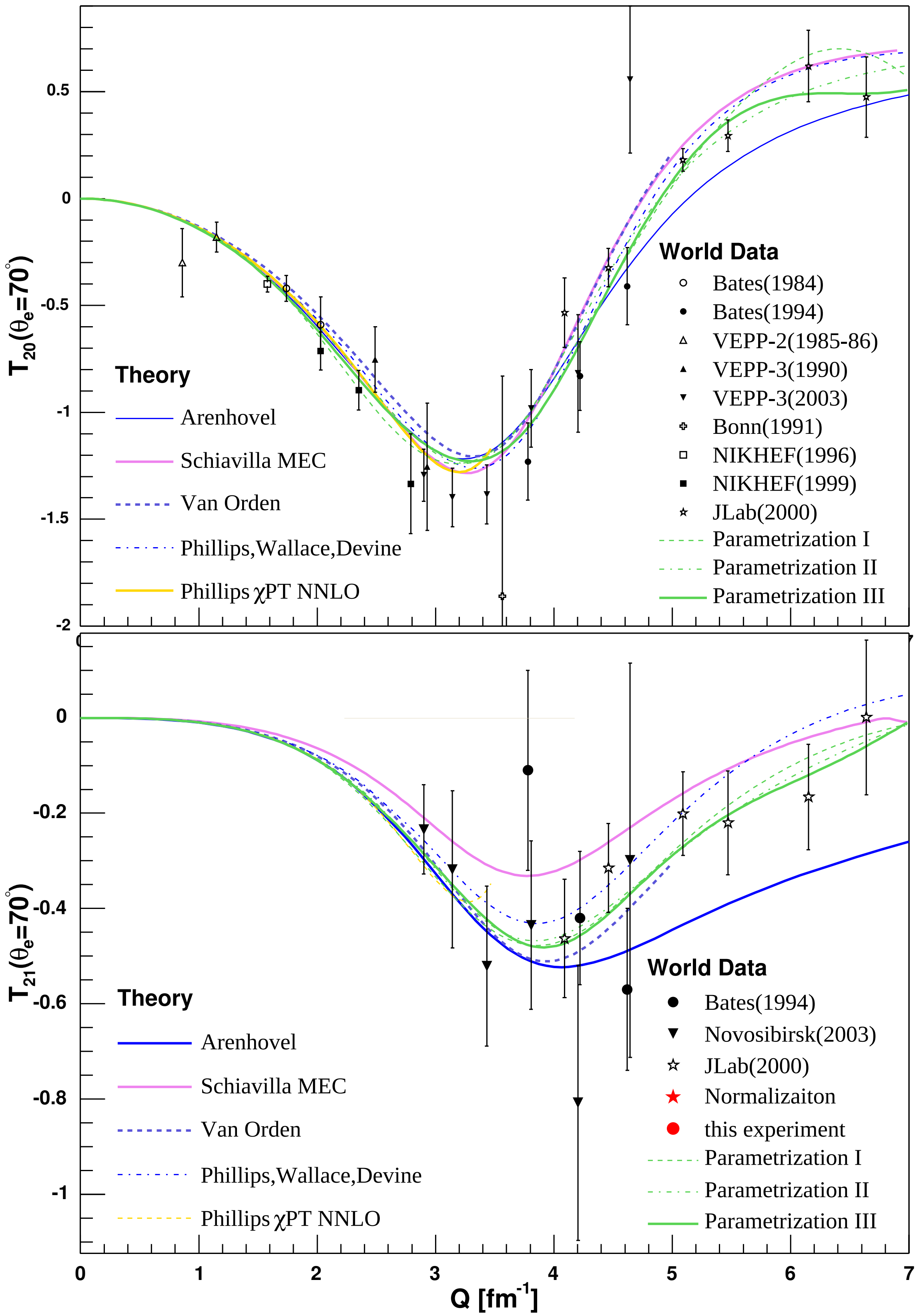

Figure 2-11: World data for T_{20} and T_{21}. All except for the VEPP-3 data are with absolute normalization in the sense that either the target or the recoil deuteron tensor polarization were measured.

of the first nodes of the form factors.

Parameterization II:

$$\begin{pmatrix} G_C \\ G_Q \\ G_M \end{pmatrix} = G_D^2 \left(\frac{Q^2}{4}\right) \cdot \mathcal{M}(\eta) \begin{pmatrix} g_0 \\ g_1 \\ g_2 \end{pmatrix} \tag{2.33}$$

where G_D^2 is the square of a dipole nucleon form factor and g_k are reduced helicity transition amplitudes defined in terms of four Lorentzian factors which themselves depend on two parameters, $g_k = Q^k \sum_{i=1}^{4} \frac{a_{ki}}{\alpha_{ki}^2 + Q^2}$.

Parameterization III:

$$G_X(Q^2) = G_X(0) \cdot e^{-\frac{1}{4}Q^2\gamma^2} \sum_{i=1}^{25} \frac{A_i}{1 + 2R_i^2/\gamma^2} \cdot \left(\cos(QR_i) + \frac{2R_i^2}{\gamma^2 \frac{\sin(QR_i)}{QR_i}}\right) \tag{2.34}$$

This parameterization is called a Sum-of-Gaussian (SOG), where the form factors are decomposed into sum of Gaussian wavelets. A_i, R_i and γ are the amplitudes, center and widths of the Gaussian respectively, and are obtained by fitting to world data.

All three parameterizations are fit to world cross section and polarized data. The reduced χ^2 are 1.5 for parameterization I and II, and 1.8 for parameterization III. It must be pointed out that Simon *et al.* (Mainz) cross section data at about $Q \sim 2$ fm^{-1} could not be fit consistently with the rest of the world data, therefore, were excluded from the fit [4].

2.3.4 Comparison Between Data and Theory

Figs. 2-10 and 2-11 include some of the "state-of-art" models. The addition of MEC to NRIA improves the agreement with $A(Q)$ and $B(Q)$ data. The models by Schiavilla *et al.* [45, 46] and Van Orden *et al.* [49] seem to fit the data reasonably, while Arenhövel *et al.* [43] seem to overshoot both A and especially B. The Chiral perturbation

[4]These data points remains over 5-σ outliers when Parameterization I was refit with the entire Platchkov data set excluded. This shows that these data points are not even consistent with the cross section data taken in the other experiments at neighboring Q^2.

theory [50], though promising for the very first time to understand the detueron structure from first principles, still has a long way to go. In particular, the fit between the $B(Q)$ calculation by the χPT theory and the data is still much worse than the rest of the models.

On the other hand, the comparison between theory and T_{20} data remains inconclusive. Although at momentum transfer of ~ 2 fm^{-1}, Bates-84 data are in good agreement with NRIA calculation (Sec. 2.2.3), NIKHEF-96 and -99 data lie consistently lower (more negative) by about 1-σ and seem to indicate the presence of MEC effects. At higher Q, the inclusion of relativistic effects improves the agreement between T_{20} data and models; however the Bates-94 data are consistently lower (more negative) than JLab-2000 by about 1-σ in their overlapping region. This slight discrepancy and the large statistical uncertainties presented in both data sets do not differentiate among the various state-of-art models. It is also interesting that the prediction by Arenhövel [43] is in very good agreement with the data up to about 4.5 fm^{-1}, while those models that better fit A and B do not fit as well.

The striking fact is that none of the $G_Q(Q)$ predicted by the theoretical models reproduces the static quadrupole moment Q_d of the deuteron when extrapolated to $Q = 0$. Precise measurement of T_{20} at low Q combined with high-quality low-Q cross section data could provide additional constraints on the asymptotic behavior of G_Q when $Q \to 0$. This discrepancy is very vividly captured by graphing a quantity $\tilde{T}_{20R}$ proposed by Garçon and Van Orden [51]:

$$\tilde{T}_{20R}(Q^2) = -\frac{3}{\sqrt{2}Q_d Q^2}\tilde{T}_{20}(Q^2), \tag{2.35}$$

where Q_d is the static deuteron quadrupole moment and $\tilde{T}_{20}(Q^2)$ is defined in Eq. 2.15. At $Q^2 = 0$, one has,

$$\tilde{T}_{20R}(0) = \frac{G_Q(0)}{Q_d M_d^2}. \tag{2.36}$$

Since experimentally $G_Q(0) = Q_d$ with Q_d expressed in units of $1/M_d^2$, the experimental value of $\tilde{T}_{20R}(0)$ is 1. $\tilde{T}_{20R}$ calculated by a few models are shown in Fig. 2-12 along with the world data. $\tilde{T}_{20R}$ helps highlighting features at low Q^2 which are not as obvious in figures of T_{20} itself. It is obvious that the $G_Q(0) < Q_d$ for most models. The figure also highlights the difference between various models and the discrepancy between theory and data at low Q.

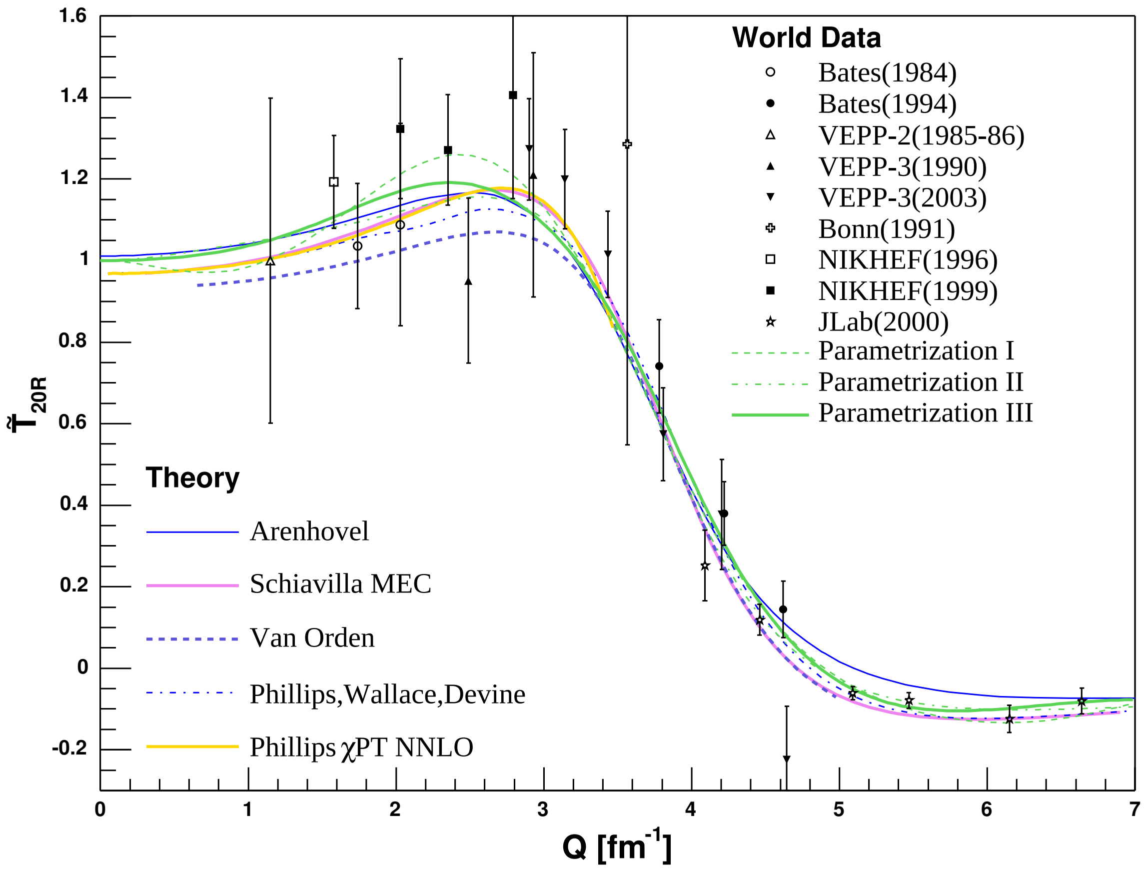

Figure 2-12: $\tilde{T}_{20R}$ world data and model predictions. Since experimentally $G_Q(0) = Q_d$ with Q_d expressed in units of $1/M_d^2$, the experimental value of $\tilde{T}_{20R}(0)$ is 1. It is shown in this figure that when $G_Q(Q^2)$ calculated by the various models is extrapolated to $Q^2 = 0$, none of them reproduces the static deuteron quadrupole moment.

It was therefore proposed to measure T_{20} with BLAST for momentum transfers in the range $2 < Q < 4.5$ fm^{-1} [62]. The measurements provide additional constraints on T_{20} in this Q range, crosscheck the systematic errors in data previously taken at different facilities at different times, and provide unique information on the evolution of T_{20} with Q over a large range. The measurements were carried out during the period from July 2004 to May 2005 at the MIT Bates Linear Accelerator Center. The experimental setup, data analysis and results are presented in this work.

Chapter 3

Experimental Setup

The experiment described in this thesis was performed at the Bates Linear Accelerator Center in Middleton, MA. The three key components of the apparatus: the South Hall Ring (SHR), the Atomic Beam Source (ABS) and the Bates Large Acceptance Spectrometer Toroid (BLAST) detector complex, are described in this chapter.

3.1 Stored Polarized Electron Beam

A longitudinally polarized electron beam with an energy of 850 MeV was injected and stored in the Bates South Hall Ring. Over 1 Million Coulomb of integrated charge was delivered to BLAST for production data taking.

3.1.1 Polarized Source

Longitudinally polarized electrons were produced by photoemission from a strained GaAs crystal photo-cathode illuminated with a circularly-polarized laser [63]. A Cesium coating was applied to reduce the work function of the crystal. The coating had to be restored about once a week. The actual polarization of the emitted electrons was between 75% to 80%. The beam polarization at the source was periodically measured with a transmission polarimeter [64].

The laser beam was generated by a commercially available 150 Watts fiber-coupled diode array laser system with fixed wavelength of 808 nm. A $\lambda/2$ wave-plate was mechanically moved in or out of the path of the laser beam, reversing the polarization of the laser and in turn the beam helicity which was monitored in real time by a Compton polarimeter (Sec. 3.1.3).

After an initial 360 keV acceleration from the crystal, the electrons entered into the linear accelerator (LINAC). The LINAC consists of 190 meters of RF cavities capable of energies up to 540 MeV. A recirculator transported the beam back to the beginning of the LINAC for a second pass through the RF cavities to nearly double the energy.

3.1.2 South Hall Storage Ring

The electron beam from the LINAC was injected into the South Hall Ring (SHR). The SHR may be operated either as a storage ring for internal targets or in pulse stretcher mode to produce nearly continuous beam for external target experiments. Beam pulses of a few mA were stacked at an injection rate of 2-20 Hz to achieve currents in excess of 200 mA. Fig. 3-1 shows a floor plan of the MIT-Bates Linear Accelerator Facility including the polarized electron source, linear accelerator, recirculator and SHR. Key ring specifications during this experiment are listed in Tab. 3.1.

Beam energy	E	850.0 ± 0.8 MeV ($\gamma = 1663.$)
Beam spread	ΔE	0.20 MeV
Sync. Loss/Turn	U_0	5.1 keV
Max. Current	I	230 mA
Lifetime	τ	25 min
Beam Polarization	P_b	$0.6558 \pm 0.0007 \pm 0.04$
Ring length	L	190.205 m
Harmonic number	h	1812
Rev. Frequency	$\beta c/L$	1.577 MHz
RF frequency	$\approx h\beta c/L$	2856 MHz
RF Wavelength	$\approx L/h$	10.5 cm
Bending radius	ρ	9.144 m
Magnetic rigidity	$B\rho$	2.8353 T m

Table 3.1: South Hall Ring (SHR) specifications.

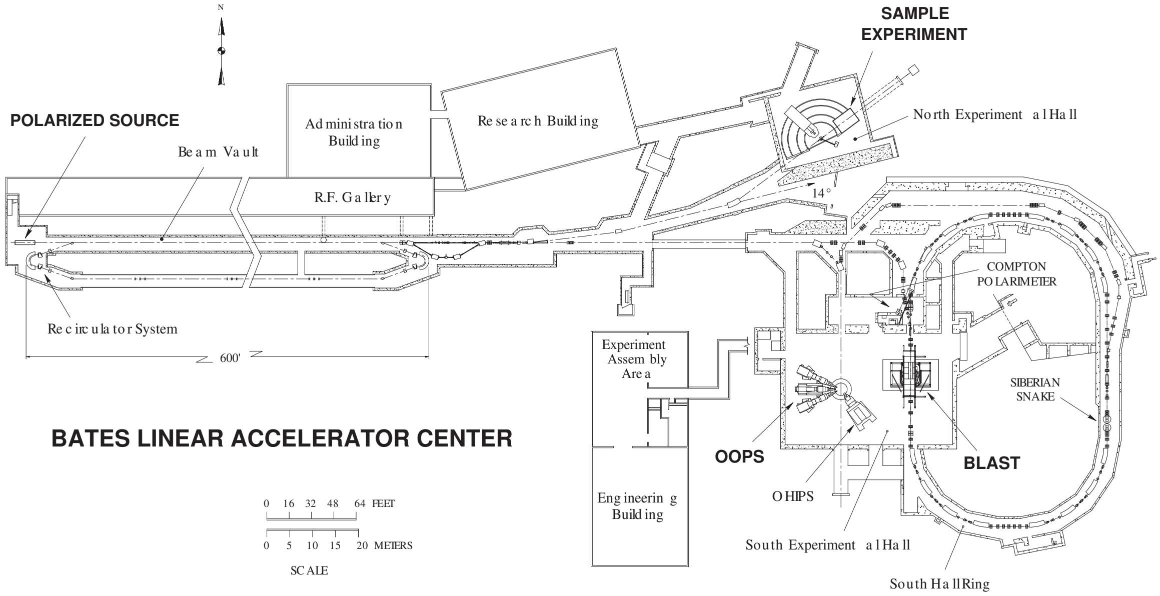

Figure 3-1: Plan of the BATES Linear Accelerator Center.

The SHR has 16 dipole magnets each bending the beam by 22.5°. An RF cavity compensates for energy loss due to synchrotron radiation. The beam energy $E = 850.0 \pm 0.8$ MeV is calibrated by a precise field-map of the integrated magnetic field along the dipoles in the ring [65].

The longitudinal polarization of the electron beam in the storage ring is preserved by a full Siberian snake on the opposite side of the ring to the internal target [64]. The snake, designed by the Budker Institute of Nuclear Physics in Novosibirsk, consists of two superconducting solenoids and 5 quadrupoles. The solenoids rotate the electron spin by 180° about the momentum vector such that the precession of the electron spins in the north arc of the ring compensates that in the south arc.

The beam current in the ring is measured non-destructively with a zero-flux Lattice DC Current Transformer (LDCCT) [66]. LDCCT uses a saturatable core primary winding around the beam with a nonlinear magnetic response to the current. A secondary winding driven by a fixed signal is coupled to the primary. The second harmonic generated by the nonlinear response is proportional to the absolute beam current passing through the coil with absolute accuracy of 0.05%. The output voltage goes to a 16 bit ADC and then a voltage-to-frequency converter (VFC). The number of oscillations in the VFC is proportional to the instantaneous beam current passing through the LDCCT. The digitized voltage is broadcast to the Experimental Physics and Industrial Control System (EPICS) (Sec. 3.4.2) slow-control system and the number of oscillations of the VFC are counted in two scaler channels, DCCT and BDCCT. The trigger supervisor inhibited the counting in BDCCT whenever data acquisition was inhibited due to electronic dead time, target transition between well-defined states or high voltage trips. Therefore integration of BDCCT over time measures the actual charge delivered through the target while the experiment is taking data.

The LDCCT was regularly calibrated with current injected into a calibration loop and measured by an ammeter with 1 pA resolution. Due to the nonlinearity of the VFC, the scaler read outs are not exactly proportional to the beam current. The scalers were calibrated during fake runs when beam was turned off and currents from 0 to 200 mA in 5 mA steps were injected into the calibration loop. The beam current I, good to 0.5% for currents between 20 and 250 mA, is

$$I = \left(2.90027 + 3.01409\times10^{-4}\,S + 6.18094\times10^{-10}\,S^2\right)\ \text{mA}, \tag{3.1}$$

where S is the DCCT or BDCCT scaler value minus a pedestal of 2400 counts.

During the injection of beam pulses from the LINAC into the SHR, the detector high voltage power supply systems were ramped down to preset "standby" voltages to protect the detectors from the injection flash. Once the ring was filled, the detectors were ramped up, and data acquisition started. The downtime for each fill was about one to two minutes. The beam intensity in the ring dissipated due to the scattering of the beam electrons with target gas, residual gas in the ring vacuum and beam halo scratching beam line components. The maximum current and lifetime achievable depended on the quality of the stored beam. Fig. 3-2 shows the typical current and lifetime monitored by LDCCT.

Assuming an exponential decay of the beam current,

$$I(t) = I_{max}e^{-t/\tau}, \tag{3.2}$$

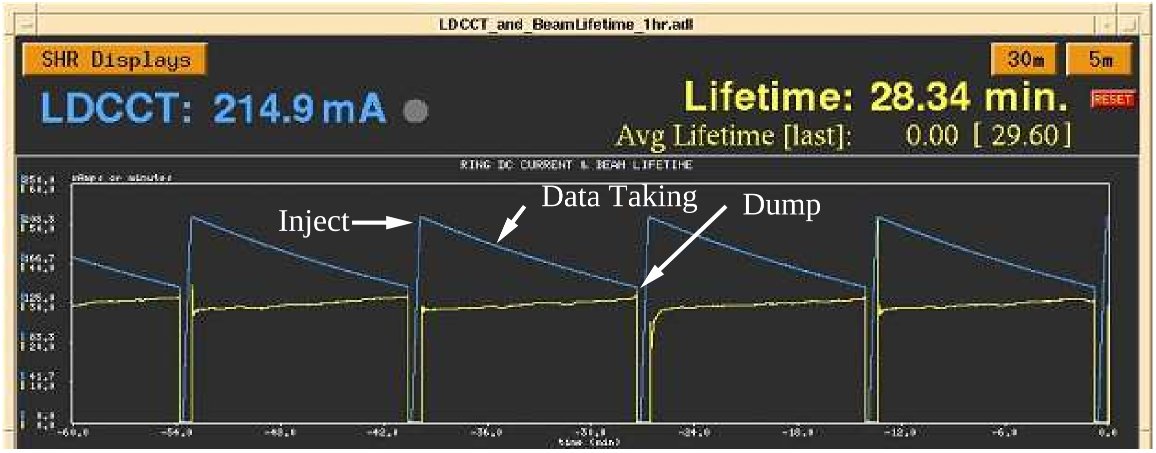

Figure 3-2: Inject, data taking and dump cycles in the South Hall Ring. The blue curve is the beam current stored in the ring. The yellow curve is the measured beam lifetime. For these series of fills, the ring was filled to 215 mA and dumped at 180mA. The beam life time was about 30 minutes.

and defining the down time, t_{down}, as the time during which data acquisition was inhibited for the detector high voltages to be ramped down, beam in the ring to be dumped and refilled, and detectors ramped back up to operating conditions, one can determine the optimal data acquisition time, t_{DAQ}, to maximize the average current,

$$t_{DAQ} \approx \sqrt{2 \cdot \tau \cdot t_{down}}. \tag{3.3}$$

In operation, Eq. 3.3 was used as a guide to choose the length of the data taking cycles.

There are 32 beam position monitors (BPM) throughout the ring. There are synchrotron light monitors which measure the beam position in horizontal and vertical directions. Four plastic scintillator beam quality monitors (BQM) were placed approximately 1 m downstream of the target to monitor the forward angle scattering rate. The detector background tended to be minimal when BQM rates were minimized; hence, they helped the operators to tune the ring for optimal detector performance. Four beam scrapers (top, bottom, left and right) in the ring, upstream to the target area, reduced the beam halo. The beam scrapers were retracted during injection to avoid injection splash and inserted once the beam was stably stored in the ring.

3.1.3 Compton Polarimeter

The beam polarization in the ring was monitored in real time by a Compton polarimeter [67, 68]. The polarimeter used a 5W 532nm circularly polarized laser. A Pockels cell was used for fast helicity reversal. The interaction point was upstream of the injection point and the crossing angle between the laser and the electron beam was below 2°. Backscattered photons were detected by a CsI crystal used as a calorimeter and the laser beam was chopped with a mechanical wheel to allow simultaneous background measurement. The helicity asymmetry as a function of photon energy was formed and fit to theoretical asymmetry simulated by Monte Carlo simulation to extract the beam polarization. The analysis was performed in real time by a dedicated Compton control-analysis software package for immediate feedback, then the complete data set was analyzed for secondary corrections. The typical energy-dependent yield and helicity asymmetry from one fill is shown in Fig. 3-3.

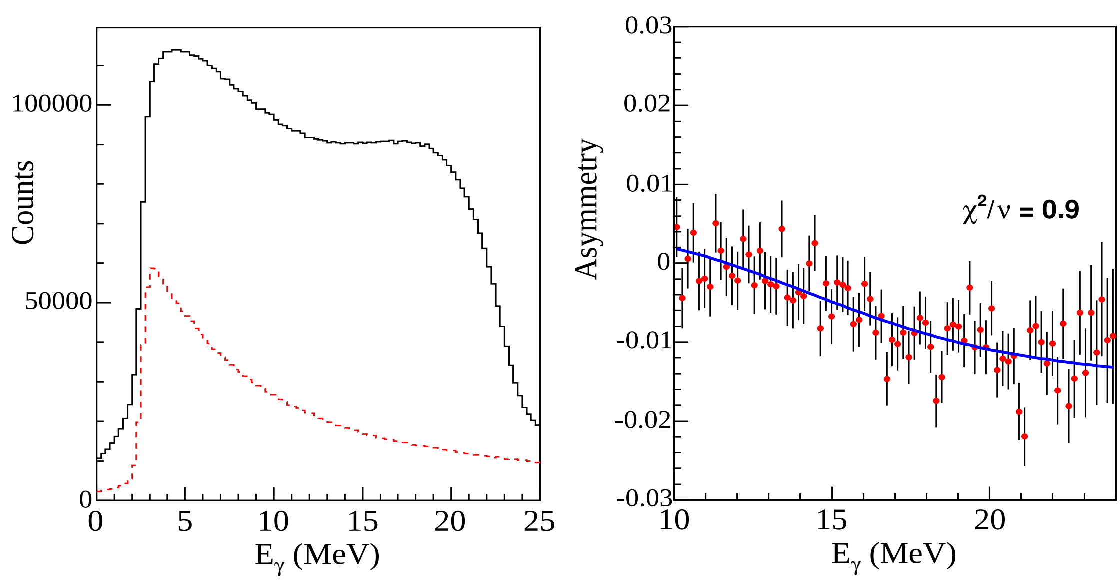

Figure 3-3: The yield (left) and asymmetry (right) of the Compton scattering during one fill of the storage ring. The total yield (solid black curve) is shown with the the background (dashed red curve). The laser helicity asymmetry is fit to the theoretical asymmetry to extract the beam polarization.

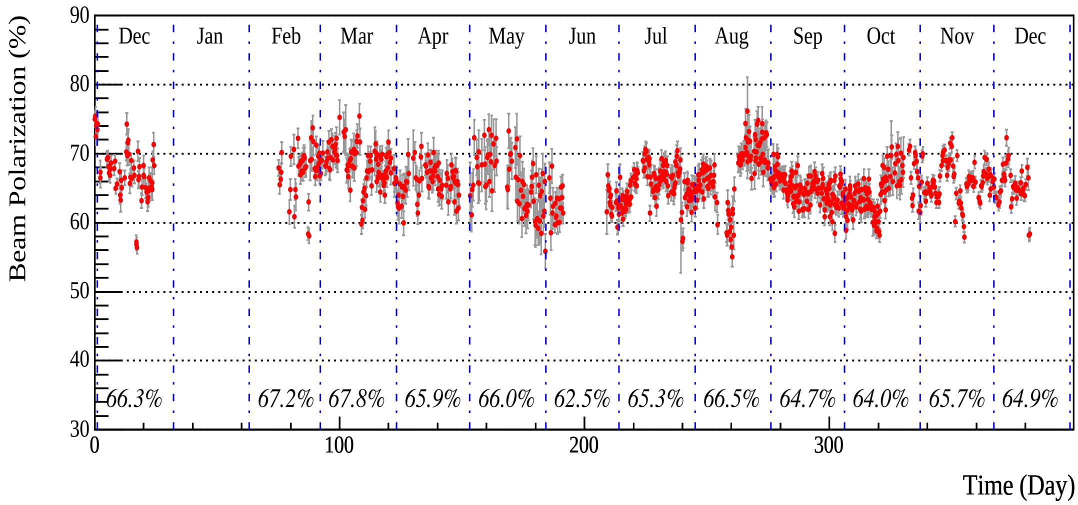

Figure 3-4: Time-dependence of the beam polarization.

The beam polarization was measured with a statistical accuracy of 5% for each single fill. Main causes of the systematic errors were [69]: 1) Energy calibration of the CsI crystal calorimeter (± 0.03); 2) Laser polarization (± 0.02); 3) misalignment between the electron and laser beam (± 0.01). The beam polarization measured by the Compton polarimeter during 2004 running is shown in Fig. 3-4. The average polarization for the deuterium production run period from July to October of 2004 was $65.58 \pm 0.07_{stat} \pm 0.04_{sys}$. The uncertainty is dominated by the aforementioned systematic errors in the polarimeter. Beam polarizations in other running periods are similar.

A spin flipper [70] was instrumented to reverse the helicity of the electron beam while it was stored in the ring. It was employed to study the false asymmetry in the Compton Polarimeter [69]. 16 sets of data were taken, each lasting 5 hours. The helicity was flipped once during a fill such that the instrumental false asymmetries in the Compton Polarimeter were canceled. The flipper efficiency, defined as the polarization maintained after the flip, $\dfrac{(h^+ + h^-)_{after}}{(h^+ + h^-)_{before}}$, was measured to be 96%. It was concluded that the electron beam was equally polarized in the two helicity states, $\Delta h = (h^+ + h^-)/2 = 0.0008 \pm 0.0068$.

3.2 Polarized Deuterium Target

BLAST utilized an Atomic Beam Source (ABS) for polarized atomic deuterium gas. Polarized atoms were injected into an open-ended cylindrical storage cell embedded in the SHR vacuum.

3.2.1 Atomic Beam Source

The BLAST ABS was originally built and used at NIKHEF [36, 71, 72] and moved to Bates after the accelerator and AmPS storage ring [73] at NIKHEF were closed. Most of the components were replaced and many redesigned to adapt to the geometric constraints and the strong toroidal magnetic field at BLAST [54]. The physical layout of the ABS is illustrated in Fig. 3-5.

The ABS consists of 4 differential vacuum chambers. The nozzle and skimmer chambers are pumped by 4 turbo pumps with a total capacity of 5240 l/sec, located on the mezzanine above the detector complex outside of the BLAST toroidal field. The pumps are connected to the ABS via 1.5 m long, 30 cm diameter pipes. The 6pole-top and 6pole-bottom chambers are each pumped by a 3000 l/sec cryopump. Heavy magnetic shielding was installed for the cryopumps to operate in the strong magnetic field.

Molecular deuterium is dissociated into atoms by an intense radio frequency (RF) field of 27.1 MHz in the dissociator. At the center of the dissociator is a 2 mm thick Pyrex glass tube with 9 mm inner diameter surrounded by an RF coil. An aluminum nozzle with 2.1 mm diameter is attached to the end of the dissociator. The nozzle is cryogenically cooled to 70K to prevent the recombination of atoms into molecules. A small amount (0.05-0.1SCCM) of oxygen is injected through the dissociator, combining with the deuterium to form an ice coating on the nozzle. Experience shows the ice coating further reduces recombination of atoms. In operation, the ice layer becomes so thick that it blocks the nozzle opening after about a week of operation and the nozzle must be warmed to room temperature and refrozen again. The procedure takes about 5-7 hours. The discharge in deuterium sputters the glass and a whitish residual

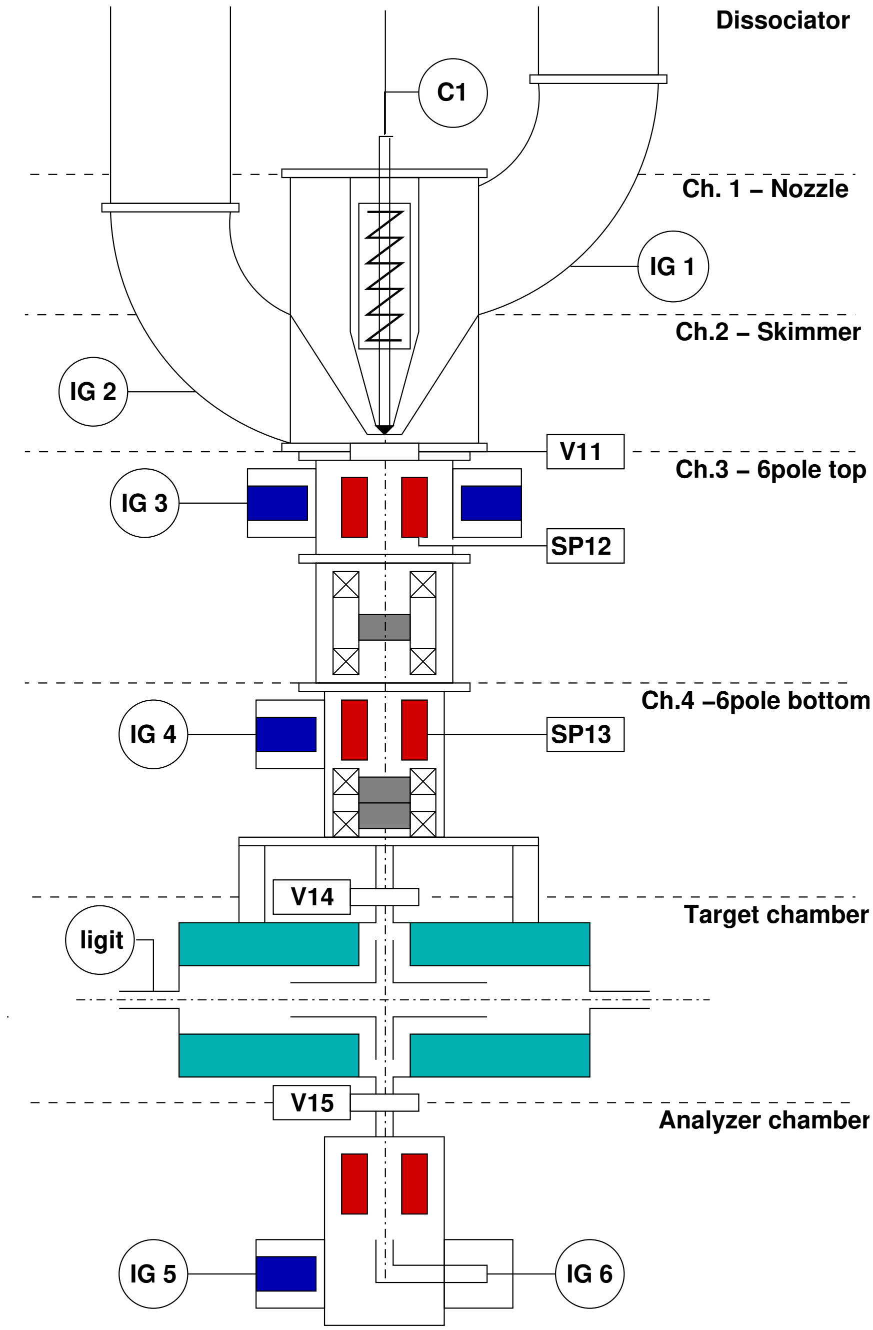

Figure 3-5: Schematic of the Bates Atomic Beam Source (ABS). IG stands for ion gauges, SP stands for Sextupoles and V11, V14 and V15 are vacuum valves.

accumulates on the internal surface of the nozzle. The nozzle must be replaced every 3 weeks during deuterium runs. Prior to the integration into the ABS assembly, the dissociator efficiency was studied by mounting a Quadrupole Mass Analyzer (QMA) underneath the nozzle [54]. The dissociator efficiency was measured to be $\sim 90\%$.

The atomic beam ejected from the dissociator is polarized by a series of Stern-Gerlach type spin filters and RF transitions. The polarization scheme exploits the degeneracy breaking of hyperfine multiplets in the presence of static magnetic field. In a single electron atom, the spin of the electron ($\boldsymbol{S}$) and nucleus ($\boldsymbol{I}$) couple through the hyperfine interaction. Under a static external magnetic field, the hyperfine interaction Hamiltonian can be written as:

$$\mathcal{H}_{HF} = \frac{2}{3}h\nu_0 \mathbf{I}\cdot\mathbf{S} + \mu_B(g_I\mathbf{I} + g_S\mathbf{S})\cdot\mathbf{B}, \tag{3.4}$$

where $g_I = -0.00047$ and $g_S = 2.0023$ are the gyromagnetic factors for deuterium nuclei and electrons respectively, and μ_B is the Bohr magneton. Fig. 3-6 shows the energy levels of deuterium under a static external magnetic field. At zero field, the two possible total spin states, $F = 1 \pm \frac{1}{2}$, of deuterium atoms are in $(2F+1)$-fold degeneracy. The energy gap between the two states is $\nu_0 = 327.4$ MHz.

The critical magnetic field B_c characterizes the strength with which the two spins couple:

$$h\nu_0 = \mu_B(g_S - g_I)B_c = 117.4G. \tag{3.5}$$

When a static external magnetic field is applied, the degeneracy is fully broken and each of the two multiples splits into energy substates. At large B ($B >> B_c$) the electron and nuclear spins decouple and the spin projections m_S and m_I become "good" quantum numbers. The hyperfine interaction can be treated as perturbations upon the interaction between individual spins and the external field; therefore, the energy split increases linearly with respect to the external field. In the target chamber, a strong target holding magnetic field defines the quantization directions. The field strength is 400 to 600 G depending on the required target spin orientation. Therefore the nuclear polarization of the ensemble of deuterium atoms is entirely determined

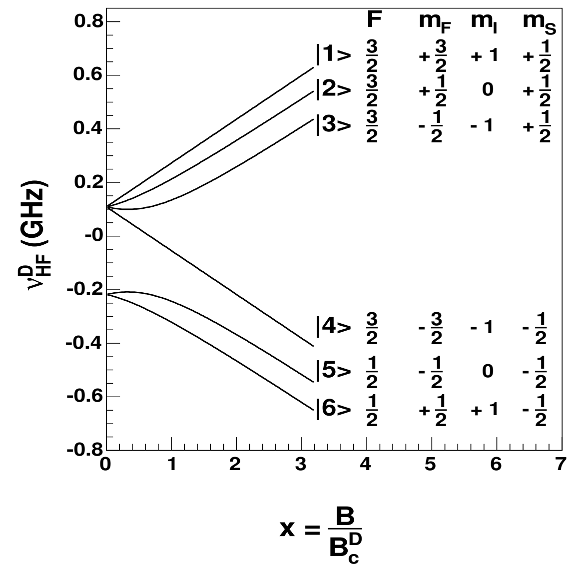

Figure 3-6: Breit-Rabi diagram of the energy levels of deuterium in the presence of a static external magnetic field.

by the relative populations $n_k (k = 1, ..., 6)$ of the hyperfine states.

The atomic states are filtered by two sets of sextupole magnets. The top sextupole includes 4 magnets with tapered inner diameter, the bottom sextupole is composed of 3 magnets with constant inner diameter. The magnets are mounted on retractable frames and can be moved out of the jet path via pneumatically activated linear feedthroughs. Each of the sextupole magnets consists of 24 permanent magnet plates with direction of magnetization rotated by 30° from plate to plate.

The magnetic field inside an ideal sextupole magnet is

$$B_x = B_0 \frac{x^2 - y^2}{r_0^2}, \quad B_y = -B_0 \frac{2xy}{r_0^2}, \tag{3.6}$$

where $B_0 \sim 12$ kG is the pole-tip field and $r_0 \sim 1cm$ is the pole-tip radius. The magnetic moment of the atoms is dominated by the electron spin since $\mu_B >> \mu_N$ and in the strong sextupole field, the nuclei and electron spin projection m_I and m_S are individually conserved. Therefore when the atomic beam passes through the sextupole, the electron magnetic moment is adiabatically aligned to the magnetic field $\mu = \mu \boldsymbol{B}$ or $\mu = \mu_B g_S m_S$ where $m_S = \pm\frac{1}{2}$ is the spin projection of the electron spin along the direction of the field. The force exerted on the atoms by the sextupole magnetic field is therefore,

$$\boldsymbol{F} = \boldsymbol{\nabla}(\boldsymbol{\mu} \cdot \boldsymbol{B}) = \mu B_0 \boldsymbol{\nabla} \left(\frac{r^2}{r_0^2} \right) = 2\mu B_0 \frac{\boldsymbol{r}}{r_0^2} \tag{3.7}$$

The force is radial which means the atoms are focused or defocused depending on whether the electron spin is parallel or anti-parallel to the field. Effectively this separates the states 1-3 from 4-6 in Fig. 3-6.

The ABS is embedded in the BLAST toroidal magnetic field (Sec. 3.3.1) which is over 2 kG in the vicinity of the sextupoles. Although the approximately constant external field does not change the magnitude of the force, it does affect its direction, hence reducing the focusing efficiency. The sextupoles are therefore encased in magnetic shields. A ray-tracing program is also employed to study the sextupole performance and optimize the location and shape of the magnets. A simulation of the atomic beam passing through the sextupole optics of the ABS is shown in Fig. 3-7. The simulation was used to optimize the design of the sextupole magnets.

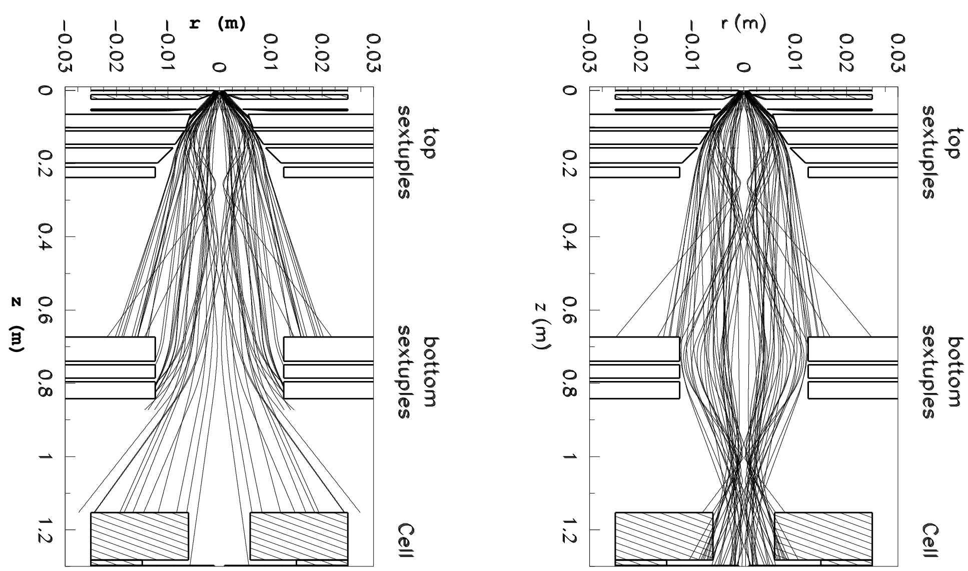

Figure 3-7: Simulations of the atomic beam passing through the ABS optics [54]. The first sextupole system focuses atoms in hyperfine states with $m_S = \frac{1}{2}$ $(B >> B_c)$. In the left figure the electron spins transition from $m_S = +\frac{1}{2}$ to $m_S = -\frac{1}{2}$ between the two sets of sextupoles and get defocused in the second. In the right figure the atoms keep their electron spin and get focused in the second sextupole set.

When a time-varying RF field of frequency $h\nu = \Delta E$ is applied in addition to the static magnetic field, transitions are induced between two hyperfine states separated by energy ΔE. There are two types of RF transitions. The σ-transition is induced by an RF field parallel to the static field, while the π-transition is induced by a perpendicular RF field. σ-transitions obey the $\Delta m_F = 0$ selection rule and the selection rule for π-transitions is $\Delta m_F = \pm 1$.

There are three types of RF transition units. The Weak Field Transition (WFT) is a π-transition unit operating around $B/B_c = 0.1$ and a frequency of 5-15 MHz. Within this regime of static external field, the WFT induces transitions across the very small energy gaps within the same F multiplet. Transitions between all substates occur at the same time. For example, the cascade transitions 1-2,2-3 and 3-4 result in the so-called 1-4 WFT transition where m_F is reversed. The Medium Field Transition (MFT) for BLAST deuterium target uses a static field around $B/B_c = 0.2 \sim 0.3$ and $\nu \sim 35$ MHz. It is a π-transition unit between sub-states within the same F multiplet. The resonances between sub-states in this field regime are separated from each other, thus one can selectively induce certain transitions. The Strong Field Transition (SFT) operates at $B/B_c \sim 1$ and a frequency around 400 MHz. σ-transitions between states belonging to different multiplets ($\Delta F = \pm 1$) are induced.

By selecting the proper sequence of transitions, a polarized deuterium beam in various spin states can be achieved. As an example, the transition scheme for deuterium with $P_z = +1$ and $P_{zz} = +1$ is shown in Tab. 3.2. During the deuterium data taking, the target switched among three spin states: $(P_z = +1, P_{zz} = +1)$, $(P_z = -1, P_{zz} = +1)$ and $(P_z = 0, P_{zz} = -2)$, or hyperfine states $(1, 6)$, $(3, 4)$ and $(2, 5)$ respectively. The duration between consecutive target state flips was about 5 minutes and the sequence of spin states was randomized. The correlation between target spin and electron beam helicity is therefore minimal as the beam helicity was reversed every fill, which typically lasted 10 to 15 minutes.

A Breit-Rabi Polarimeter (BRP) with a dipole magnet was used to monitor the ABS performance. The dipole magnet has a very strong (2.5 kG/cm) and uniform gradient and is placed after a 2 mm diaphragm below a small sampling outlet of the

$$
\begin{pmatrix} n_1 \\ n_2 \\ n_3 \\ n_4 \\ n_5 \\ n_6 \end{pmatrix}
\underset{\longrightarrow}{6-pole}
\begin{pmatrix} n_1 \\ n_2 \\ n_3 \\ 0 \\ 0 \\ 0 \end{pmatrix}
\underset{\longrightarrow}{MFT}
\begin{pmatrix} n_1 \\ n_2 \\ 0 \\ n_3 \\ 0 \\ 0 \end{pmatrix}
\underset{\longrightarrow}{6-pole}
\begin{pmatrix} n_1 \\ n_2 \\ 0 \\ 0 \\ 0 \\ 0 \end{pmatrix}
\underset{\longrightarrow}{SFT}
\begin{pmatrix} n_1 \\ 0 \\ 0 \\ 0 \\ 0 \\ n_2 \end{pmatrix}
$$

Table 3.2: The ABS transitions and sextupole magnet process for producing deuterium with positive vector and tensor polarization. The six n_i entries in the leftmost column correspond to the populations in the six hyperfine states in Fig. 3-6 as they enter the ABS transition region. As the atomic beam progresses through the ABS, various states are switched and/or removed.

storage cell. Three compression tubes (CT) are placed 1.5 m below the magnet [1]. When the dipole magnet is off, the central CT collects both atoms and molecules. With magnet on, atoms are deflected into the left or right CT depending on their polarizations. Therefore the atomic fraction and their polarization in the ABS efflux can be measured; thus providing an in-situ diagnostic of ABS performance. However, it only samples the center portion of the ABS flow, and therefore could not provide reliable measurement of the overall dissociator efficiency and ABS polarization.

3.2.2 Internal Target

The atomic beam from the ABS is injected into a T-shaped storage cell which confines the target gas to the region around the electron beam, resulting in an increase in the target thickness by orders of magnitude in comparison to a pure jet target. The cell is a 15 mm diameter and 60 cm long cylindrical tube manufactured from 50 μm thick aluminum foil. The atoms are injected through an inlet tube of 11.9 mm diameter and 15 cm length at the middle of the cylinder. The dimension of the inlet is so chosen to approximately match the conductance of a half-cell. The gas atoms disperse through the length of the cell and are pumped out once they exit at either end. Both the inlet and the cell are coated with Dri-film to minimize depolarization [74] and cooled

[1] Compression tubes are small vacuum cavities with an ion gauge installed inside. When gas flow is injected into the cavity, the pressure built up in the cavity is proportional to the inflow.

to around 100 K to increase the target density and reduce depolarization as well. The cell temperature is monitored with sensors on the target mounting frame and is recorded at 1 sec interval into the EPICS data stream. A small sampling tube was attached at the middle of the cell directly facing the injection inlet. It allows direct sampling of the atomic beam from the ABS into the BRP as mentioned in Sec. 3.2.1. A schematic drawing is included in Fig. 3-8.

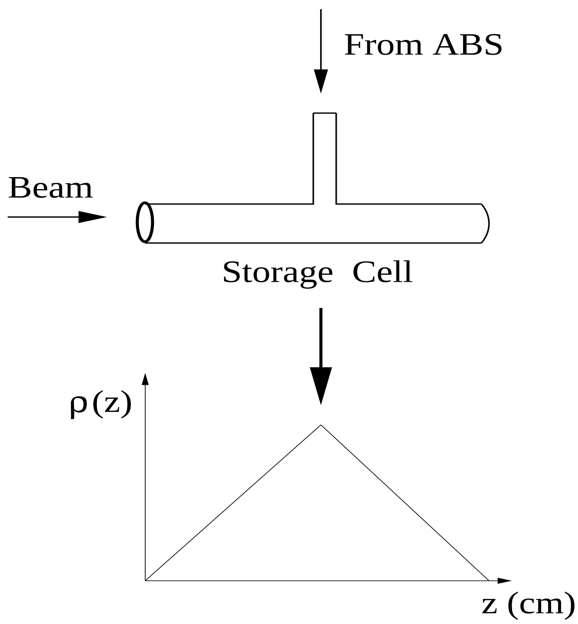

Figure 3-8: Schematic of the storage cell. The gas density profile along the cell is approximately triangular.

The conductance of the target cell is the sum of conductances of the storage cell and the inlet tube,

$$C = C_{cell} + C_{inlet}. \tag{3.8}$$

The conductance of a cylindrical tube of length l and diameter d can be expressed as [75]

$$C = \frac{v_0}{4}\frac{d^2}{4\pi}w, \tag{3.9}$$

where

$$v_0 = \sqrt{\frac{8k_BT}{\pi M}}, \quad w = \frac{8}{3a} - \frac{36\ln a + 91}{18a^2} + \frac{32\ln a + 8}{3a^3} - \frac{8\ln^2 a}{a^4}, \quad \text{and} \quad a = \frac{2l}{d}.$$

T is the temperature of the cell and inlet and M is the mass of the target particles. To the lowest order of a, Eq. 3.9 reduces to [2]

$$C_{cell} = 2C_0 \frac{d_{cell}^3}{l_{cell}/2} \sqrt{\frac{T}{M}}, \quad \text{and} \quad C_{inlet} = C_0 \frac{d_{inlet}^3}{l_{inlet}} \sqrt{\frac{T}{M}}, \tag{3.10}$$

where $C_0 = 3.81 \times 10^3$ cm/s is the conductance constant and M is measured in atomic mass units (a.u.). The factor of 2 in C_{cell} is due to the two open ends of the cell. When a gas flux of Φ is injected from the inlet, the density in the cell forms a triangular profile [75, 72],'

$$\rho(z) = \frac{2\Phi}{Cl_{cell}} \left(\frac{l_{cell}}{2} - |z| \right). \tag{3.11}$$

The integrated density between $-l/2$ and $l/2$ is then,

$$\rho = \frac{\Phi l}{C} \left(1 - \frac{l/2}{l_{cell}} \right). \tag{3.12}$$

A strong magnetic holding field for the target is provided by transverse and longitudinal coils wound around iron yokes above and below the scattering chamber [3]. The function of the holding field is two-fold. First, the field defines the orientation of the quantization axis of the target nuclear polarization. Secondly, the magnetic coils generate a strong field a few times the critical field B_c between -20 to 20 cm along the target cell which suppresses the depolarization processes due to the hyperfine interaction (Sec. 3.2.1). Beyond the central 40 cm, the magnetic holding field decreases dramatically, therefore only the events originating from the central 40 cm of the target are used for physics analysis. By adjusting the current in the coils, the target spin can be set to arbitrary directions in the horizontal plane. Small openings in the coils and iron plates have been left to allow the passage of the inlet to the sampling tube from the target cell. These discontinuities create a slight non-uniformality in the holding fields.

The longitudinal and transverse target holding field were measured prior to the in-

[2] Akihisa Shinozaki pointed out that the lowest order approximation overestimates the conductance by as much as 14.87%. [76]

[3] The magnets were shipped from NIKHEF and only small adjustments were applied.

stallation of the cell into the target chamber. In-situ surveys were performed in April 2004 and January 2005 during down time between production runs. Components of magnetic fields were measured at positions along the target and the holding field direction was calculated. Upon the completion of the production runs, the holding field direction and intensity were measured every 2 cm along the target in June of 2005. All measurements were made using a 3-D Hall Probe. During the deuterium production runs, tensor asymmetries in elastic electron deuteron scattering were used to monitor the average holding field angle in a semi-realtime fashion (Sec. 4.3.3). Tensor asymmetries in the $D(e, e'd)$ reaction originating at different locations along the cell were used to check the spin angle profile obtained from the surveys. These measurements are compared to simulations by the electromagnetic calculation package TOSCA [77].

The various spin angle profiles are show in Fig. 3-9. There are discrepancies between the Hall-Probe surveys at different times. The discrepancy is clearly systematic, for example the June 2005 surveyed spin angle profile is every-where below the January 2005 one by 0.5-1°. There are also discrepancies between the survey and the tensor $D(e, e'd)$ results. These discrepancies, those seemingly small, have large impact on the analysis presented in this work. Sec. 4.5.3 discusses these discrepancies in detail.

Over the duration of time the atoms spend in the cell, physical processes happen that could lead to a decrease of the nuclear polarization. The residual interaction between the electron and nuclei spins could induce transitions between states with different m_I. The beam RF did not induce any depolarizing resonances in the holding field strength [78]. When an atom collides with the cell wall, the electron spin interacts with the magnetic dipoles found in the molecules in the cell surface through spin exchanges and Pauli exclusion interactions [79]. Depolarization then occurs through hyperfine interactions. The deuterium target works in a magnetic holding field which is a few times as strong as the critical field B_c, therefore the polarization relaxation due to residual hyperfine interaction and cell wall collision is weak. The dri-film molecules are chemically saturated, therefore they have no free electron orbits or electric dipoles to bond with the target gas atoms, thus reducing the spin spin exchange interaction

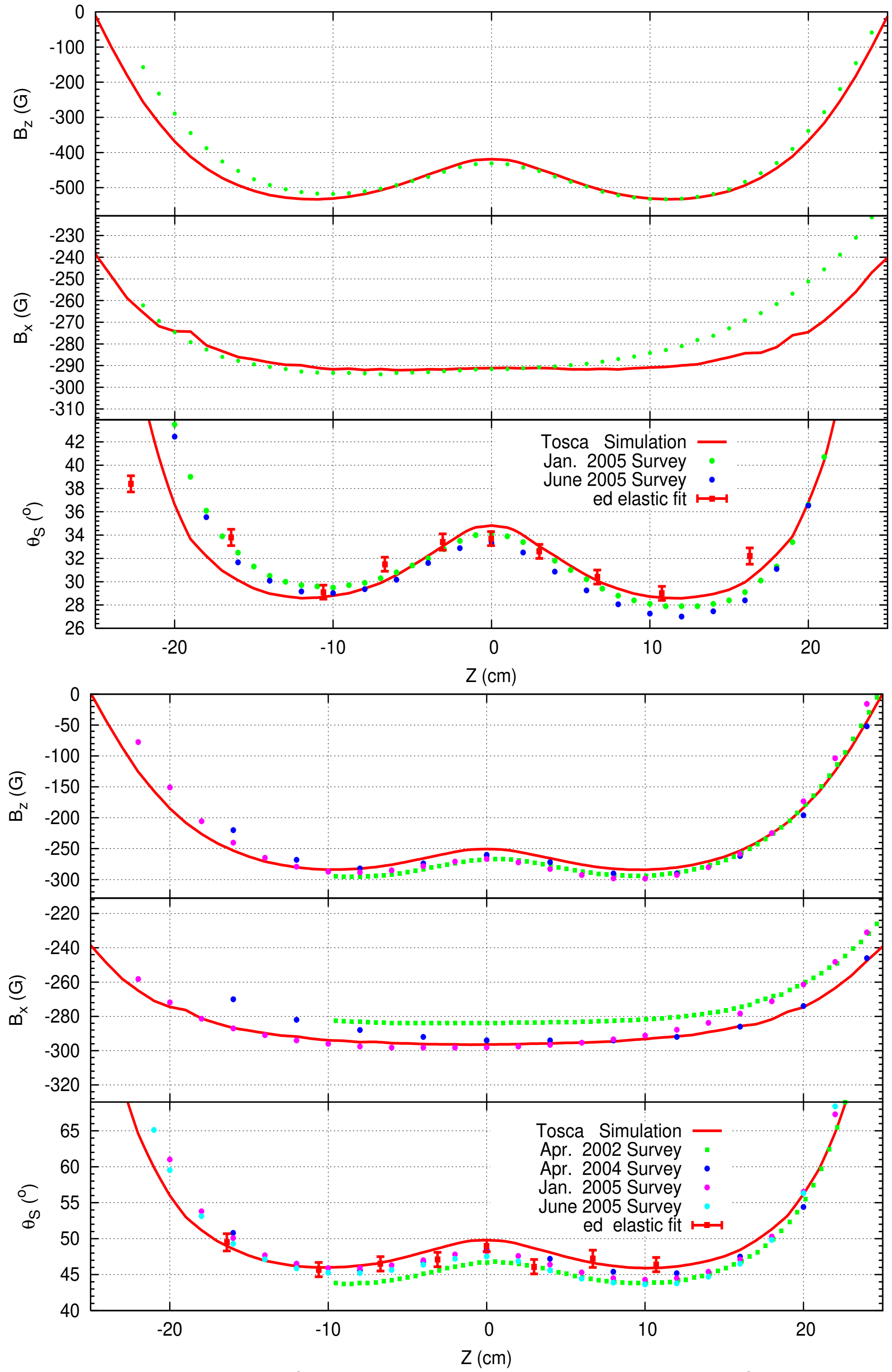

Figure 3-9: Target holding field components and the holding field direction along the cell. On the top is the field for nominal spin angle of 32° and on the bottom the nominal spin angle of 47°. Transversal (B_x) and longitudinal (B_z) from survey measurements, the TOSCA simulation are displayed. The spin angle calculated from the fields (Apr. 2002, Apr. 2004, Jan. 2005 and June 2005), elastic electron deuteron tensor asymmetries and TOSCA simulations are shown. The 2002 survey was made before all the magnetic materials were installed, therefore is less reliable than the later holding field surveys (2004 and 2005 ones).

between the atoms and the surface.

The atoms could recombine into molecules when they collide. It is not clear if the atoms maintain their nuclear polarization and how much polarization they maintain if any. There have been inconclusive evidences that the recombined molecules do preserve some of the nuclear polarization [4]. Nevertheless, high nuclear polarizations, $P_z = 0.86$ and $P_{zz} = 0.68$, were observed through nuclear reactions in the experimental data [5]. This leads to the belief that either there is no strong recombination in the target cell or the molecules remain highly polarized. Tensor asymmetries in $D(e, e'd)$ reaction originated at different locations along the cell were used to measure the overall depolarization in the cell (Fig. 3-10). The reduction in tensor polarization from the cell center to the ± 20 cm ends is less than 8%.

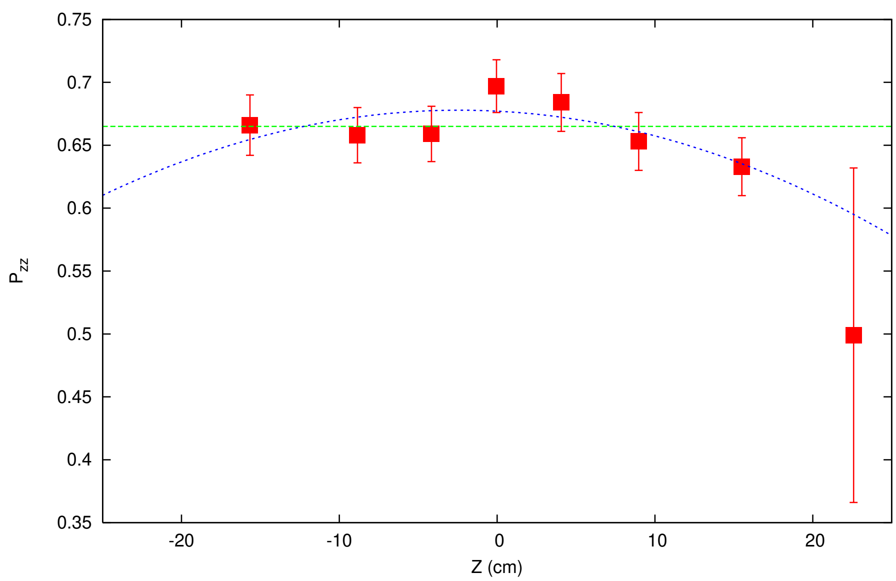

Figure 3-10: Reduction in P_{zz} from center of the cell to the ends measured by tensor ed-elastic asymmetries.

During early 2003, the dri-film coating sustained severe damage and showed visible

---

[4]NIKHEF reported measurements in which the molecules are observed to preserve as high as 81% of the nuclear polarization.

[5]The tensor asymmetries in electron deuteron elastic scattering was used to measure the target tensor polarization, and the vector asymmetries in the deuteron electro-disintegration was used to measure the product of electron beam and target vector polarization. Given the electron beam polarization measured by the Compton polarimeter (Sec. 3.1.3), the target vector polarization was derived.

burn marks after being exposed to the beam halo. A 10.2 mm aperture tungsten collimator was installed immediately upstream of the cell to protect it. The collimator generated significant positron showers into the drift chamber and underwent several redesigns to reduce the impact on drift chamber performance. The final design was installed on March 9$^{\text{th}}$, 2004 [6].

The nuclear polarization of the target gas in the storage cell was measured by electron scattering reactions. This method measured the combined polarization of atoms and molecules in the target cell, as opposed to the polarization of the atomic component alone with the ion-extraction polarimeter employed by NIKHEF [80]. Therefore, precise knowledge of the molecular fraction in the cell and molecular polarization is not required. The drawbacks of the approach are: 1) the momentum transfer region used for polarimetry can not be presented as new measurements; 2) reliance on theoretical predictions cause the results to depend on the particular models used, therefore reducing the discrimination power of the data. Sec. 4.6 is devoted to the uncertainty introduced by the various models.

The product of beam and target vector polarization was obtained by comparing the observed asymmetries in the exclusive electro-disintegration channel to theoretical calculations at low Q^2 and low missing momentum. The target tensor polarization was determined by comparing low Q^2 tensor asymmetries in electron-deuteron elastic scattering to the prediction of theoretical models. Knowing the beam polarization from the Compton Polarimeter (Sec. 3.1.3), the target vector polarization was then deduced to be $P_z = 0.858 \pm 0.014_{stat} \pm 0.056_{sys}$ for 2004 running period and $P_z = 0.678 \pm 0.005_{stat} \pm 0.045_{sys}$ for 2005 [53]. Tensor polarizations were determined to be

[6] The first collimator was installed on September 23$^{\text{rd}}$, 2003 after a long period of down time. $H(e, e'p)$ data taken from a 40 cm long target cell immediately afterward measured a polarization of $P_t = 0.39 \pm 0.03$, compared to the optimal polarization of $P_t = 0.80 \pm 0.003$ obtained in late 2004. Intense effort was devoted to ABS and target performance during the Spring of 2004, including addition of pumping capacity, cooling contact on the inlet tube, and a new target cell. Due to constrained in time and resources, the impact on target polarization by each individual improvement was not separately studied. The data immediately before and after the installation of the new collimator did not show immediate improvement in target polarization. Experience did show that the quality of the target cell is critical. All the production data with high polarization were taken with the same target cell, while other cells failed to perform as well.

$P_{zz} = 0.678 \pm 0.020_{stat} \pm 0.034_{sys}$ in 2004 and $P_{zz} = 0.558 \pm 0.020_{stat} \pm 0.028_{sys}$ in 2005 [7]. The determination of tensor polarization and the various uncertainties involved will be discussed in detail as a part of data analysis (Sec. 4.3.3). Both polarizations were monitored daily during the experiment. Weekly P_z results for 2004 and daily P_{zz} results are shown in Fig. 3-11.

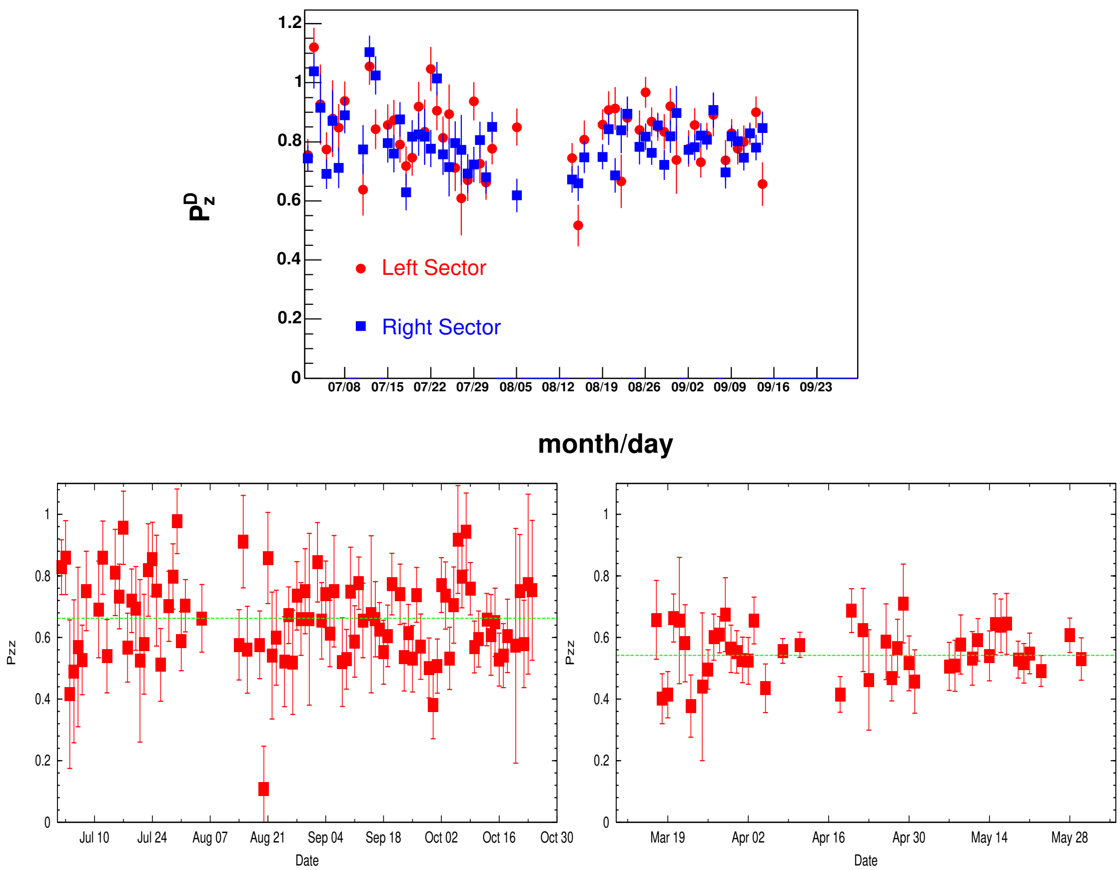

Figure 3-11: Weekly target vector polarization P_z for 2004 running period [53] and daily tensor P_{zz} polarization over the course of the experiment in both 2004 (left) and 2005 (right)

[7]The cause is not understood for the reduced polarizations observed in 2005. One plausible conjecture is that the inner surface of the target cell was damaged from the prolonged exposure to the beam resulting in stronger depolarization effect. Beam current in 2005 is almost twice as high as in 2004 which may deliver more power to the cell, causing more damage and temperature fluctuation. Though the holding field in 2005 was weaker to orient the target spin in a different direction from 2004 (See beginning of Chap. 4), it was concluded that the weaker holding field was not the cause after the same reduced polarization was observed at the same holding field configuration as in 2004.

The difference between vector and tensor polarizations is not well understood. One suggestion is that transitions only occur between adjacent states in the Breit-Rabi diagram where energy gaps are narrow (Fig. 3-6), i.e., $1 \leftrightarrow 2$, $2 \leftrightarrow 3$, $4 \leftrightarrow 5$ and $5 \leftrightarrow 6$. While each of these transition changes the vector nuclear polarization by 1 (e.g., $P_z = 1 \rightarrow P_z = 0$), the tensor polarization is changed by 3 (e.g., $P_{zz} = 1 \rightarrow P_{zz} = -2$). Therefore the depolarization processes have a larger impact on the tensor polarization. For example, suppose initially the target is in a equal mixture of state 1 and 6, hence having $P_z = 1$ and $P_{zz} = 1$. If an equal fraction ξ of the 1 and 6 states undergoes transition to 2 and 5 respectively, the final polarizations will be

$$P_z = 1 - \xi, \quad P_{zz} = 1 - \xi + (-2) \times \xi = 1 - 3\xi. \tag{3.13}$$

Assuming the initial polarizations are 0.95 for both vector and tensor states, the transition probability ξ can be solved to be 9.5%.

3.2.3 Unpolarized Gas Buffer System, ABS intensity

For calibration purposes, an Unpolarized Gas Buffer System (UGBS)[8] was developed to deliver unpolarized H_2 or D_2 gas directly into the target cell. The system was used to determine the intensity of the ABS efflux and study the over efficiency of the detector system. It was based on the simple idea that when gas is allowed to discharge from an unknown volume, the intensity of the gas flow from the volume is proportional to the rate at which the pressure decreases.

Fig. 3-12 is a schematic of the UGBS. The system consisted of two gas tanks with well known volumes. One of the tanks served as a differential reservoir to fill the buffer tank. The pressure P in the buffer was monitored by Baratrons with absolute error 0.012 torr and was recorded in the EPICS data stream at 1 sec intervals. The buffer tank has a volume of $V = 3.068 \pm 0.018$ l, calibrated by flowing well known flux of nitrogen into the tank and measuring the differential pressure increase. The

[8]The UGBS was proposed in writing in 2002 by Z.-L. Zhou, *etc.* and implemented in late 2003 to replace the unpolarized gas feed system based on Mass Flow Controller (MFC) technology, which was not able to deliver precisely controlled gas flow at the low intensity comparable to the ABS.

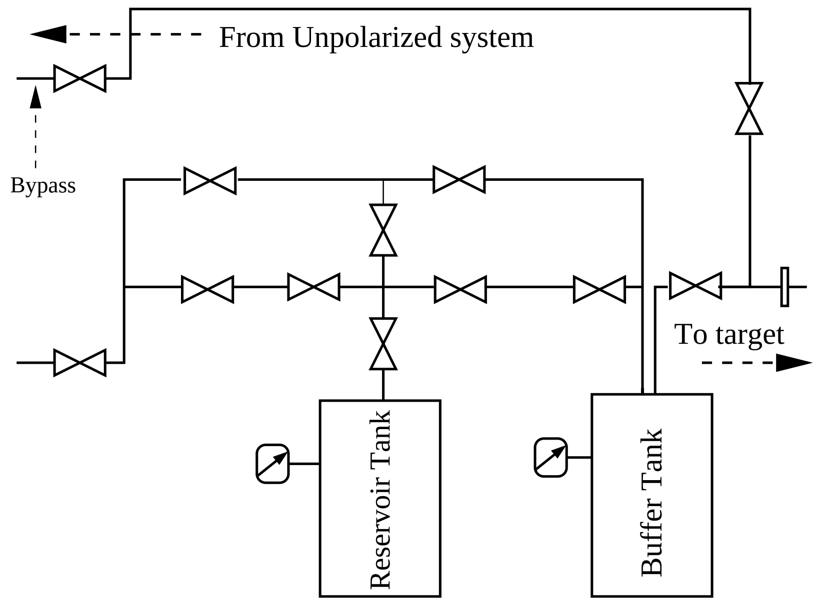

Figure 3-12: Schematic drawing of the UGBS.

calibrating 1 SCCM nitrogen flow was controlled by a Mass Flow Controller with 0.5% accuracy.

The buffer was filled with gas at preset pressure P_{high} and was allow to discharge passively to into the target cell. The buffer pressure drops exponentially and was refilled to P_{high} from the reservoir when a preset minimum pressure P_{low} was reached. A discharge cycle typically lasted 20-30 minutes. The UGBS flow rate Φ_{UGBS} can be determined from the ideal gas law

$$\Phi_{UGBS} = -2\frac{V}{k_B T}\frac{dP}{dt}, \tag{3.14}$$

where k_B is the Boltzmann constant, T is taken as the ambient temperature in the South Hall measured by thermostats in the Hall and the factor of 2 represents the fact that each molecule contains 2 atoms. $\frac{dP}{dt}$ is determined by fitting the buffer pressure P as an exponential decay in time. Fig. 3-13 shows the buffer pressure measured as a function of time during runs 10935 and 10937 taken on September 7$^{\text{th}}$ of 2004. The fit is also displayed in the figure. Twelve hours of UGBS runs were taken on that day. The cell temperature for that period of time was 94.04 ± 0.65 K, the mean

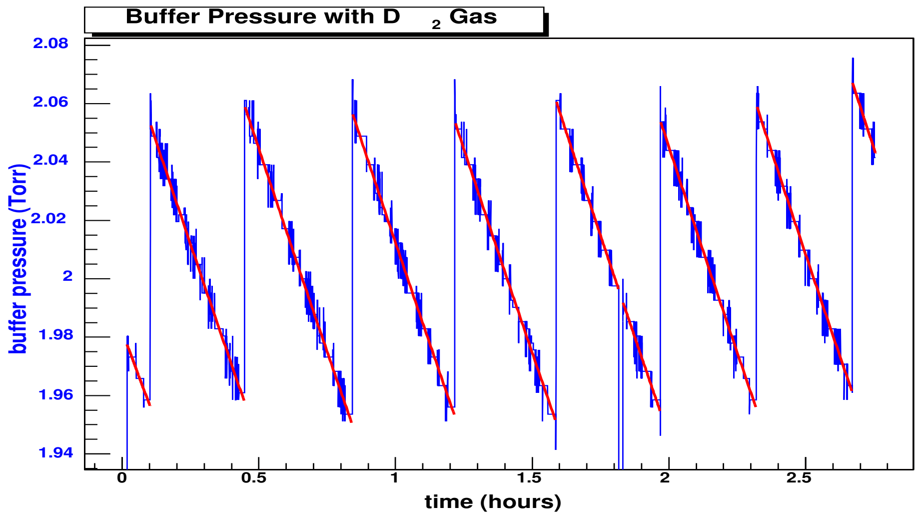

Figure 3-13: Pressure in the UGBS as a function of time. The blue curve is the pressure in the buffer bottle measured by the Baratron, the red curve is the fit of the data to an exponential decay.

temperature in the South Hall was 302.1 ± 3.9 K and the average buffer pressure was 2.01 torr. The cell conductance for D_2 molecules at this temperature is calculated from Eq. 3.9 to be $5.452{\times}10^3$ cm^3/s. The average UGBS flux extracted from the fit is 1.504 ± 0.039^{16} atoms/sec, giving a target thickness of $7.36 \pm 0.19{\times}10^{13}$ nuclei/cm^2 over the central 40 cm of the target cell [9].

Calibration runs using the UGBS as the target source were taken in between polarized deuterium runs during ABS maintenance on September 7$^{\text{th}}$ and October 5$^{\text{th}}$ in 2004 and on April 15$^{\text{th}}$, 23$^{\text{rd}}$ and May 13$^{\text{th}}$ of 2005 with buffer pressure set to about 2 torr, which produces comparable event rates to the ABS. The ABS flux intensity Φ_{ABS} is determined by

$$\frac{\Phi_{ABS}}{\Phi_{UGBS}} = \sqrt{\frac{M_{D_2}}{M_D}}\frac{\rho_{ABS}}{\rho_{UGBS}} = \sqrt{\frac{M_{D_2}}{M_D}}\frac{R_{ABS}}{R_{UGBS}}, \tag{3.15}$$

where ρ_{ABS} and ρ_{UGBS} are the target thickness, R_{ABS} and R_{UGBS} are the number events observed under the same event selection rules per Coulomb of integrated beam current during ABS and UGBS runs respectively. Comparing the yields in elastic

[9]The uncertainty is dominated by the $\frac{dP}{dt}$ term. Each discharge has a pressure drop of about 0.1 torr and the Baratron has an absolute accuracy of 0.012 torr, therefore the accuracy in the fitted pressure decay rate is roughly $\sim \frac{10\%}{\sqrt{n}}$ with n being the number of discharges.

electron deuteron scattering, the long term average ABS flux intensity as determined from Eq. 3.15 is $\sim 2.3\times10^{16}$ atoms/sec for both the 2004 and 2005 run period. Actual flow intensities fluctuate around this average value. The corresponding target thickness is $\sim 6\times10^{13}$ nuclei/cm^2, leading to a typical luminosity of $\sim 4\times10^{31}$ /cm^2/sec with a beam current of 100 mA.

This method does not require precise knowledge of detector efficiencies. The uncertainties in the ABS target thickness are introduced by the error in the UGBS target thickness (2-3%), uncertainty in the cell conductance (which could be significant and is not known conclusively), and possible shifts in detector efficiency between ABS runs and UGBS runs, which were taken close to each other in time. The errors in cell conductance cancel out in the ABS intensity extraction; however, the assumption that the target gas is purely atomic introduces an additional error. As the dissociator efficiency is believed to be at the 90% level and the molecules do not focus in the sextupoles, the atomic fraction produced by ABS is believed to be very high. However, the amount of recombination in the storage cell is not known.

3.3 The BLAST Detector Package

The BLAST detector complex is instrumented around eight coils of toroid magnet which divide the space around the beam line into eight sectors. The top and bottom sectors between the coils contain the ABS and target diagnostics. The two horizontal sectors host the detector packages featuring a left-right symmetrical design. Scattered particles originated from the target cell pass through, in an radially outward sequence, Drift Chambers (WC), Čerenkov detectors (CC), time-of-flight (TOF) scintillator and neutron counters (NC). Neutron detection capability in the right sector is augmented by two extra sets of scintillator (LADS). The neutron detectors thus are the only asymmetric components of BLAST. A coordinate system is defined for the BLAST detector with Z along the beam line, pointing down stream, Y axis pointing vertically upward and X pointing into the left sector of the detector as viewed along Z direction. The BLAST detector package and the magnet coils are shown in Fig. 3-14. The elastic electron-deuteron scattering experiment made use of the wire chambers and time-of-flight detectors, which will be detailed in this section. The Čerenkov detectors are not used in this work.

3.3.1 BLAST Toroid

The BLAST toroidal magnetic field is generated by eight copper conductor coils symmetrically arranged around the beam line, as shown in Fig. 3-15. The toroidal design minimized the field gradient in the target chamber, and the field at PMTs used in the Čerenkov and TOF scintillators. Also, the Lorentz force on charged particles is in the plane spanned by the beam line and the momentum of the particle, hence the particles stay "in-plane", making the reconstruction of trajectories more accurate and less demanding computationally. Each coil consists of two adjacent layers of thirteen windings of 1.5×1.5 in^2 hollow copper conductor, with water coolant circulating through the core. The coils are shaped to provide maximum dispersion for the forward electrons and have a 1-meter-wide opening in the back to accommodate the ABS and internal target. The coils operated, during all production runs, at their maximum current of 6731 A to provide maximal momentum resolution. The maximum magnetic field at this current is 3800 Gauss, which occurs ~ 1 m from the beam line in the vicinity of the drift chambers. Strong aluminum frames support the coils in place, and the maximum deflection of the frame is 7-8 mm when the field is energized at full strength.

The geometric position of the coils were surveyed and the field carefully mapped before the detectors were installed [81, 82]. The mapping was done with an automated x-y-z table with spatial resolution 0.05 mm and two three-dimensional Hall probes with 0.1% precision. The probe positions (in BLAST coordinate system) were surveyed at 10 to 20 points and related to the x-y-z table coordinates. The uncertainties in the probe positions was ~ 1 mm. The table coordinates and fields were recorded at each of the $\sim 43,000$ points, measured in a grid of 5 cm spacing in each direction. The mapped field was interpolated into a rectangular grid of 5 cm step in each direction in the BLAST coordinate system and is analytically extended beyond the measured

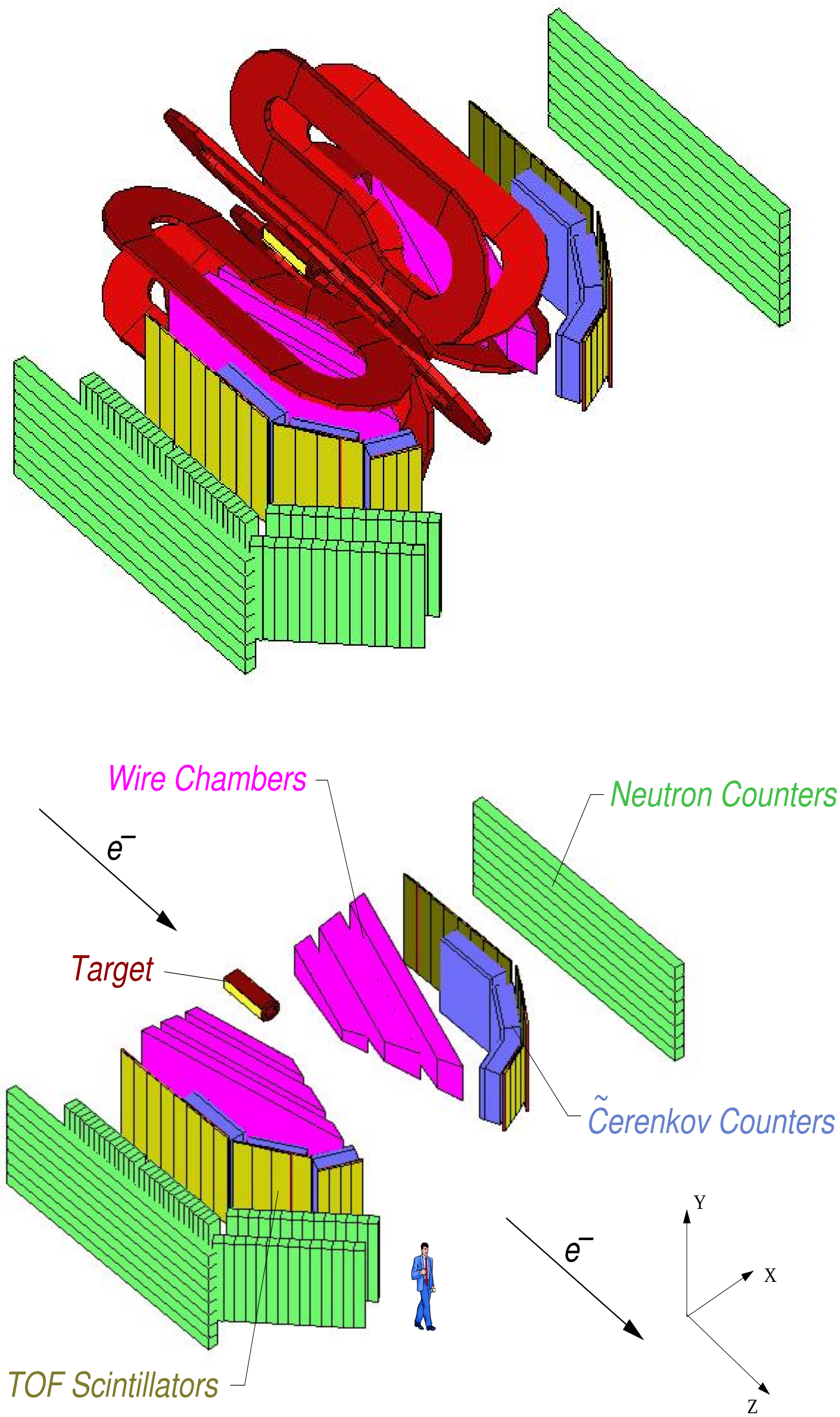

Figure 3-14: The BLAST detector package shown with and without the magnetic coils of the toroid. The BLAST coordinate system is shown in the bottom figure.

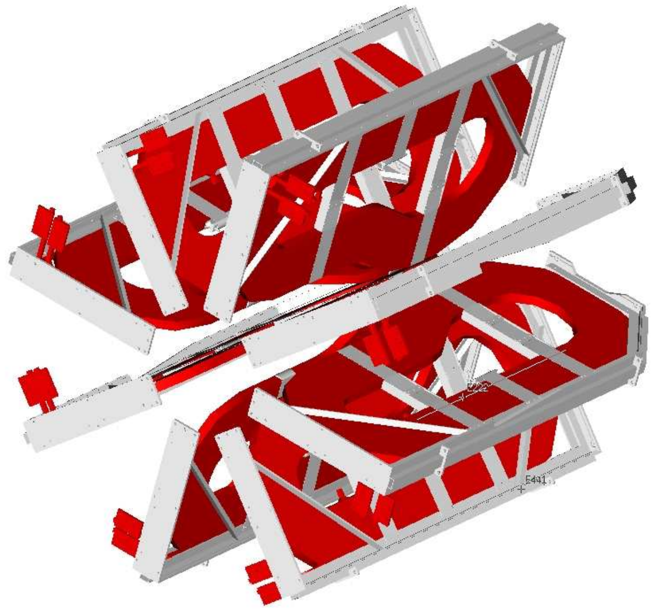

Figure 3-15: Magnetic coils with the supporting subframes in BLAST.

region for a more robust trajectory fitting. The field is also modeled in TOSCA and an analytical Biot-Savart calculation and the field map agrees with both models to within 1%. The 7-8 mm displacement observed in geometric survey of coil positions is also confirmed by the Bio-Savart calculations where coil positions are moved to fit the observed field values. The interpolated and extended grid covers a rectangular volume of $-200\text{cm} \leq X \leq 200\text{cm}$, $-70\text{cm} \leq Y \leq 70\text{cm}$ and $-10\text{cm} \leq Z \leq 290\text{cm}$ (See Fig. 3-14 for the definition of the coordinate system). There are about 150 points in the $143,289$-point grid where the mapped values differ from the Bio-Savart calculation by more than 200 G. This is attributed to occasional x-y-z table jamming during the mapping, which caused missing field values for these points. The measured field value is replaced with the Bio-Savart calculation for these points. The field-map of B_y in the central horizontal plane is shown in Fig. 3-16.

3.3.2 TOF Scintillators

Sixteen time-of-flight (TOF) scintillators in each sector provided the trigger and timing-based particle identification [52]. The TOFs covered the entire geometric

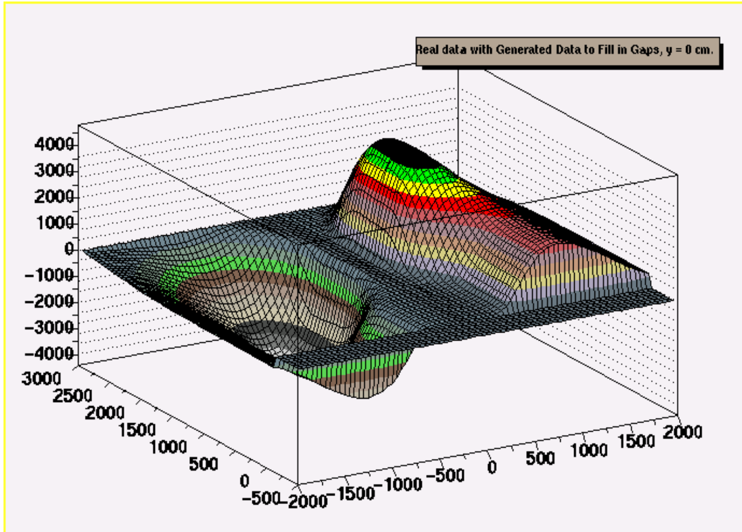

Figure 3-16: Magnetic field map of B_y in the central horizontal plane of BLAST.

acceptance of the drift chambers. All the TOFs were made of 2.5 cm thick Bicron BC-408 scintillator. The most downstream four paddles were each 120 cm tall while the remaining twelve were 180 cm tall. The forward four TOFs were shorter because they were mounted closer to the beam line, needed to cover a smaller azimuthal acceptance of wire chamber at forward angle and had a higher background rate caused by their positioning. All but the last four had 10 mil (0.254 mm) of lead shielding in front of the scintillator material [10]. A photomultiplier tube (PMT) was mounted on each end of each TOF paddle through Lucite light guides. The light guides bent the path of light such that the PMTs could be mounted with their cylindrical axis perpendicular to the residual BLAST field. The TOFs were mounted on retractable aluminum supporting subframes which could be pulled open to provide space for drift chamber and target work. Fig. 3-17 is a photograph of the right sector before the drift chambers were installed. The TOFs with their PMTs mounted can be seen. The subframe was open.

The PMT signals were split into two branches. One was delayed and passed into a Lecroy 1881M FASTBUS ADC module, which measured the energy deposited by the

[10] The lead shielding was removed from the last four TOFs in winter of 2003 because they stopped recoil deuterons in elastic electron deuterium scattering before they could reach the scintillation material.

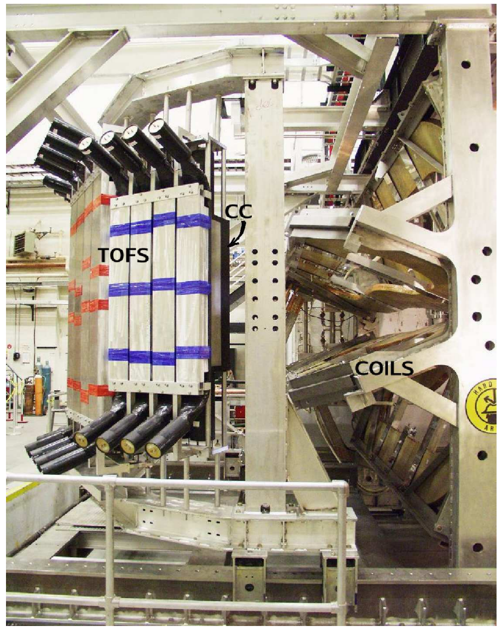

Figure 3-17: Upstream View of BLAST, Right Sector TOFs and Coils; the first CC box mounted behind the first four TOFs can also been seen. The electron beam comes out of the paper towards the reader off the right edge of the picture.

particle inside the scintillator. The delay allowed a trigger decision to be made prior to the ADC digitization. The other branch went to a constant fraction discriminator (LeCroy 3412 CFD), removing the dependence of the timing on signal strength(walk effect). A coincidence between the two PMTs was always required to reduce random backgrounds. The timing signal from the two PMTs gives both the mean time t and the position p of the hits along the length of the scintillator,

$$\begin{cases} t &= (t^d_{ch} t_d + t^u_{ch} t_u)/2 - L/v_{sc} \\ y &= (t^d_{ch} t_d - t^u_{ch} t_u) v_{sc}/2 \end{cases}, \tag{3.16}$$

where $t^{u,d}_{ch} \approx 50$ ps/channel is the resolution of the TDC modules, $v_{sc} \approx 14.7$ cm/ns is the effective speed of light in the scintillator, and t_u and t_d are the TDC values from the top and bottom PMT respectively, discriminated with the CFD. t_{ch} was calibrated for each PMT by adding predetermined delays to the signals from each PMT and measuring the corresponding shift in the TDC channels. v_{sc} is calibrated for each scintillator by matching the range of y to the length of the TOF paddle. The mean time t is independent of the position y. The timing resolution of the TOFs was measured to be 320 ps (FWHM) or $\sim$ 150 ps (σ) on a cosmic ray test rig prior to installation in the South Hall, so the position resolution is therefore $\pm$3 cm [52]. At a kinetic energy of 0.4 GeV or lower, the typical time difference between a pion and a proton, or between a proton and a deuteron, traveling from the target to a TOF is $\sim$ 10 ns. Therefore the timing resolution well satisfies the demand for particle identification [11].

BLAST timing is relative to the earliest TOF to be hit rather than using a start counter. The mean-timed signal from the first TOF detector to be hit generates the start strobe which triggers all TOF TDC modules, and a delayed signal from each TOF stops the corresponding TDC. Therefore the TDC of the triggering TOF measures the electronics delay of that particular detector (the self-timing peak). The time difference of other TOFs relative to the self-timed scintillator can be extracted, where the common start cancels as illustrated in Fig. 3-18 and Eqs. 3.17. t_{trig} is the TDC value from the triggering scintillator, t_i represents the TDC in a later TOF hit in the i^{th} paddle, δ_{trig} and δ_i are the electronics delay for the corresponding TOFs and Δt_i is the actual time elapsed between the start strobe and the hit in the i^{th} TOF.

$$\begin{cases} t_{trig} & = & \delta_{trig} \\ t_i & = & (\Delta t_i + \delta_i) \\ t_i - t_{trig} & = & \Delta t_i + (\delta_i - \delta_{trig}) \end{cases} \tag{3.17}$$

Although the term $\delta_i - \delta_{trig}$ in Eqs. 3.17 can be corrected in software, the BLAST drift chambers require a constant common stop strobe. The drift chamber TDC modules are started by the signal from the sense wires and stopped by a strobe generated by the delayed mean-timed signal from the triggering TOF. This requires that the delays in different TOFs be the same, such that the stop strobe is constant regardless of which TOF generated the stop strobe so long as the particle traveled at close to the speed of light. During the commissioning of the BLAST detector, a thin

[11] The e^+ observed in BLAST detector are mostly showers from upstream. They typically have low momentum ($p < 0.1 GeV$) and are easily identified. Additional electron-pion discrimination is provided by the CC.

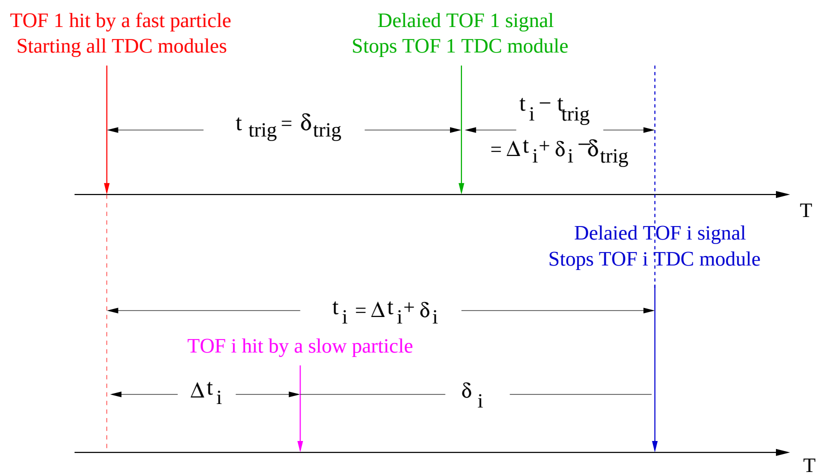

Figure 3-18: BLAST TOF timing. The start strobe was generated by the first TOF to be hit. After a period of Δt_i, the i^{th} TOF was hit. The TDC module of each TOF was stopped by the delayed signal from the corresponding TOF. Therefore the TDC for the trigger TOF measures the electronics delay δ_{trig} for that channel, while the TDC of the other TOF i measures $t_i = \Delta t_i + \delta_i$. The Difference between the TDCs is therefore $t_i - t_{trig} = \Delta t_i + (\delta_i - \delta_{trig})$. The term $\delta_i - \delta_{trig}$ is corrected in software leading to measurement of the true time difference Δt_i between the two TOF hits.

scintillator similar to the TOF paddles were installed adjacent to the target chamber in a horizontal orientation. Particles from the target cell had to pass through the start counter before they reached the TOF scintillators. The BLAST toroidal magnetic field was turned off during this measurement; therefore, the particles traveled along straight tracks. Due to the extended target and the width of the TOF paddles, the pathlength of the tracks hitting any one TOF is known to within ± 20 cm; thus the absolute time of flight from the start counter to the TOF is know to within ± 1 ns. The mean-timed signals from the start counter was used to generate the start strobe leading to absolute timing measurements. The programmable delay for each TOF was adjusted to within ± 1 ns in each sector. Fig. 3-19 illustrates the setup. The start counter was removed once the delays were properly adjusted. During production runs, horizontal cosmic rays passing through one TOF in each sector were used to cross check the relative timing of the left and right sectors [83].

A flasher system was used to monitor changes in the TOF timing. A single laser pulse from an LSI model VSL-337ND-S ultraviolet nitrogen laser unit was split into multiple fiber optic cables, each of which was attenuated and coupled to the

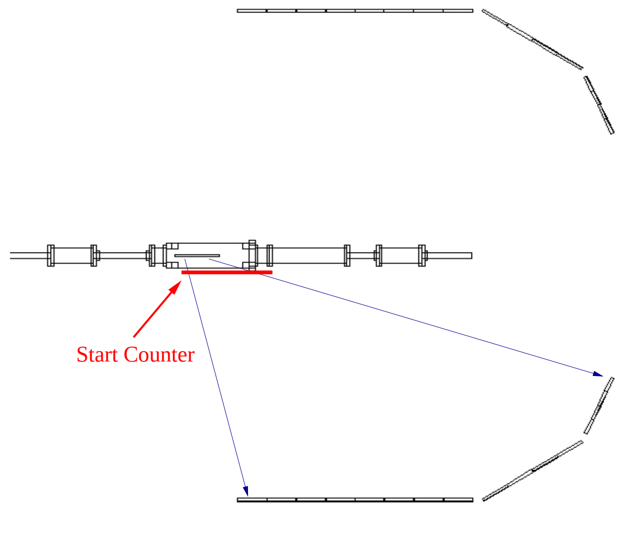

Figure 3-19: Calibration of absolute timing using a start counter during the commissioning before the wire chambers were installed. The start counter was removed after the calibration was completed to make room for the chambers. With the start strobe generated by the start counter, the absolute time of flight was measured by the TDC difference between the start counter and the TOF paddle. With the BLAST toroidal field turned off, the path lengths were known to within ±20 cm. The electronic delays for each TOF paddle were adjusted to within ±1 ns.

center of a TOF, Čerenkov or neutron detector scintillator. The laser was pulsed at 1 Hz. Flasher events were recorded in the data stream along with events triggered by scattered particles from the target and were used to monitor time shifts. Flasher events define sharp peaks in the TOF TDC spectra and any shift in the timing, for example after replacement of a broken PMT, was identified in the shift of the peaks.

The TOF efficiency was studied with ep-elastic events from hydrogen target runs by Dr. Chris Crawford as a part of his dissertation [83]. The efficiency of all the TOFs were shown to be close to 100% (Fig. 3-20). Unfortunately, the selection of deuterons require strong TOF timing cuts, and the under-constrained production channel kinematics exclude similar studies of TOF efficiency for deuterons and pions. However, there is no strong evidence that TOF efficiencies depend on particle species strongly.

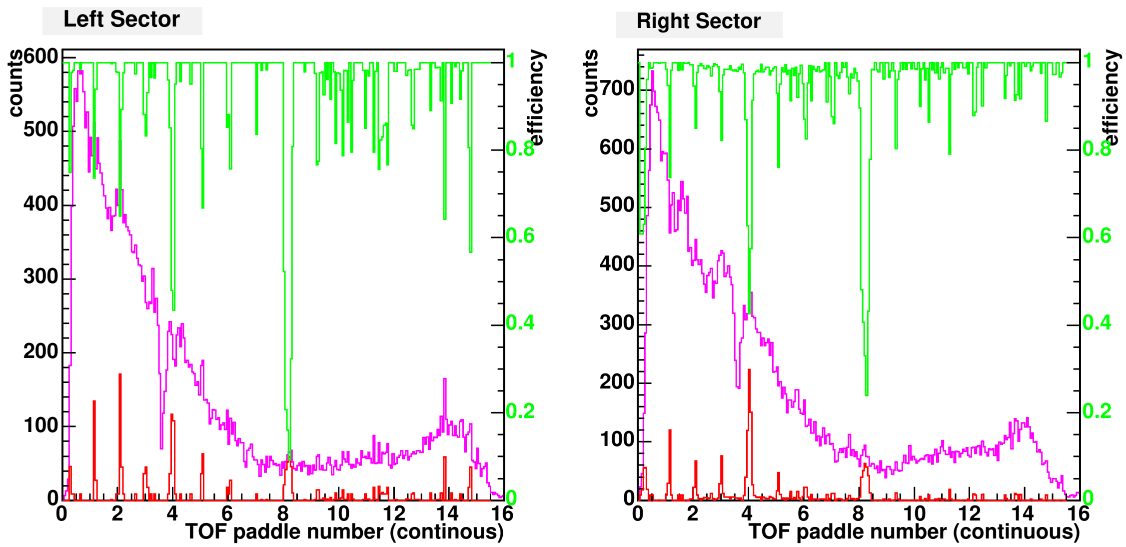

Figure 3-20: Efficiency of each TOF along the width of the scintillator. Figure taken from Ref. [83]. The horizontal axis is the horizontal position where the tracks impact the TOF paddles as determined from the reconstructed trajectories. The purple curve shows the distribution of events where a TOF hit is expected, the red curve corresponds to events where the TOF failed to trigger and the green curve is the TOF efficiency. The gap between each TOF is clear.

3.3.3 TOF Based Particle Identification Algorithm

Because the BLAST TOF detectors did not have a start counter during production data taking, the absolute time of flight could only be obtained by making assumptions about the particle identification that triggers the common start strobe. The algorithm is illustrated in Fig. 3-21. The track reconstruction algorithm returns the momentum as well as the path length of the track from the vertex to the front plane of the hit TOF detector. The absolute time of flight of the triggering particle is then easy to calculate if one assumes it is an electron. The time t_v when the reaction happened at the vertex is found by tracing the electron back in time. The absolute time of flight of the other particle in the opposite sector is then $T = t_1 - t_v$. Knowing the track length L and momentum p of the other particle, two particle identification (PID) parameters, speed of flight (β) and particle mass (m) can be extracted.

Fig. 3-22 shows the relation between reconstructed speed of flight and the particle

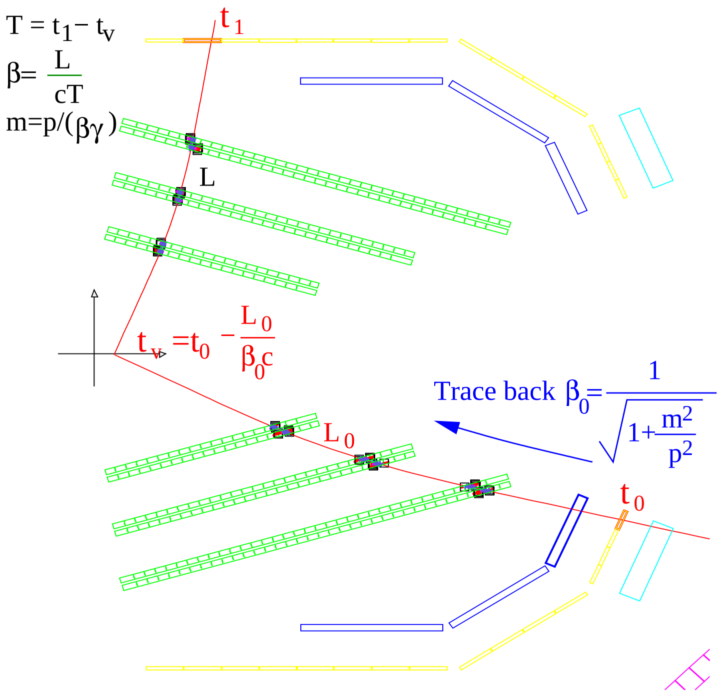

Figure 3-21: Particle identification algorithm. The time when the reaction occurred at the vertex is determined by tracing back the triggering particle. The absolute time of flight T, the speed of flight β and the mass m of the other particle in the event can be reconstructed from its momentum p and length of trajectory L.

momentum for positively charged particles detected in the left sector during a series of deuterium target runs. The separations between e^+, π^+, proton and deuteron are clearly visible. The calculated mass spectrum is also shown in Fig. 3-22 where π^+, proton and deuteron mass peaks are identified and the standard deviations (σ) obtained by fit to Normal distributions. Several factors contribute to the width of the peaks. The path lengths are known to $\delta L \sim 20$ cm, which, combined with the TOF timing resolutions, leads to $\delta T \sim 1.5$ ns resolution in absolute time of flight T. For 400 MeV protons, the time of flight is typically ~ 20 ns over a typical path length $\gtrsim 250$ cm, hence the uncertainty on speed of flight is $\delta\beta \sim 0.05$. The resolution in the reconstructed mass is therefore ~ 100 MeV/c [12].

[12] A more detailed error analysis is included as follows. With ultra-relativistic particles generating the trigger, $\delta\beta_0$ is very small. Therefore the error in track length dominates the error in $\frac{L_0}{\beta_0 c}$. Even though the intrinsic timing resolution of each TOF is on the order of 0.15 ns, the calibration off electronics delay between any pair of TOF Δt is only good to about 1 ns. For $T = t_1 - t_0 + \frac{L_0}{\beta_0 c}$, $\delta T = \sqrt{\delta t_1^2 + \delta t_0^2 + \Delta t^2 + \left(\frac{\delta L_0^2}{\beta_0 c}\right)^2} \approx 1.5$ ns, when $\delta L \sim 20$ cm, $T \sim 20$ ns and

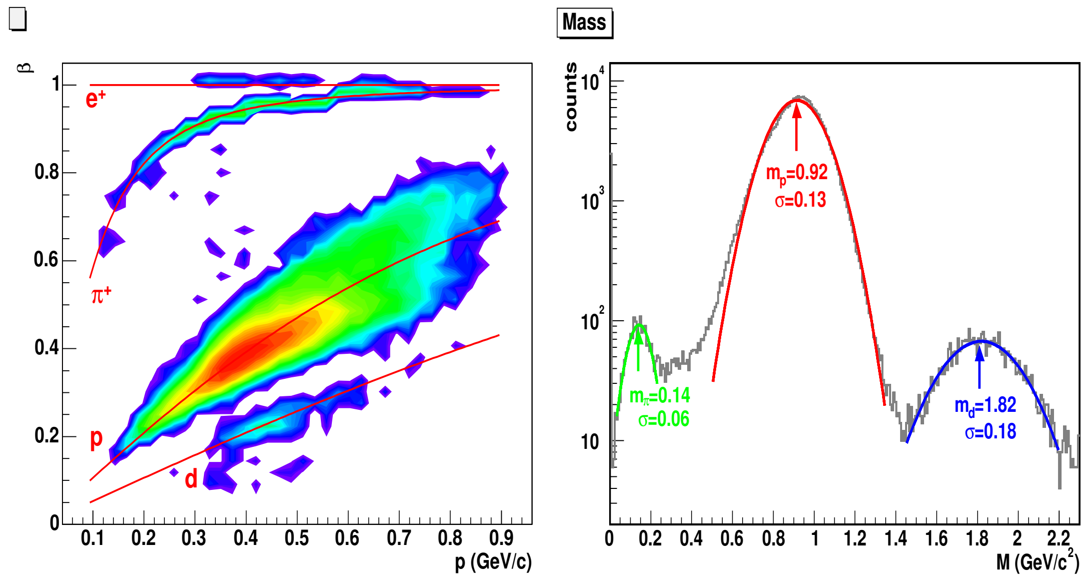

Figure 3-22: The timing based particle identification parameters. The β-p relation for the positively charged particles observed in the left sector is shown on the left. Ideal β - p relationships for typical particle species are marked by red curves. The reconstructed mass spectrum for positive particles is shown on the right. Three peaks are visible in the spectrum. They are fit to Gaussian distributions and identified as π^+ (Green curve), proton (red curve) and deuteron (blue curve). The position (m) and standard deviation (σ) of each Gaussian fit is shown.

There is no guarantee that the common start strobe was triggered by electron. The WC reconstruction does determine the charge of the particle, therefore the triggering particle could be electron or π^- for negatively charged particles, and positron, π^+, proton or deuteron for positively charged particles. To resolve this ambiguity, a hypothesis testing algorithm was developed. For example, when the common strobe is triggered by a negatively charged particle, it is first assumed to be an electron. The mass of the rest of the particles detected are reconstructed. Each is compared to the

$L \sim 300$ cm. It follows that the speed of flight β of the slower particle has an uncertainty of $displaystyle\delta\beta = \sqrt{\left(\frac{\delta L}{cT}\right)^2 + \left(\frac{L\delta T}{cT^2}\right)^2} \approx \sqrt{0.035^2 + 0.035^2} \approx 0.05$. With $\beta \sim 0.5$ and $p \sim 0.4$ GeV/c, $\delta m = \sqrt{\left(\frac{\gamma p \delta\beta}{\beta^2}\right)^2 + \left(\frac{\delta p}{\beta\gamma}\right)^2} \approx \sqrt{0.09^2 + 0.04^2} \approx 0.1$ GeV/c. $\delta\beta$ is a dominating source in δm, and δL and Δt contribute to $\delta\beta$ with comparable significance.

mass of known particles, and a χ_M^2 is computed,

$$\chi_M^2 = \sum_i \left(\frac{M_i - \tilde{M}_i}{\tilde{M}_i} \right)^2 , \tag{3.18}$$

where $\tilde{M}_i$ is the mass of known particles that is closest to the reconstructed mass M_i. For instance, when M_i is 1.1 GeV/c^2 for a positively charge track, $\tilde{M}_i$ will be the proton mass which is the closest to M_i among the mass of positron, π^+, proton and deuteron. The hypothesis is tried next that the triggering particle was π^-, χ_M^2 is computed for this hypothesis too. The hypothesis that resulted in the least χ_M^2 is adopted.

Monte Carlo simulations revealed that about 50% of the times in the production channel $H(e, e'\pi^+)$, π^+ reaches the time of flight earlier than the electron. When the reconstruction and above hypothesis testing algorithm was applied to these simulations, the program correctly identified that the start strobe was generated by a π^+ over 60% of the time. The algorithm correctly identified about 50% of these events that the other particle is an electron. 30% of the π^+ were misidentified as protons, while most of the electrons not correctly identified were recognized as π^-. Overall, 30-40% of the $e'\pi^+$ events were properly identified, even though the start strobe was generated by the π^+. Because $H(e, \pi^-\pi^+)X$ events are highly unlikely, it is easy to over ride the event identification in the analysis which will identify over 50% of the $e'\pi^+$ events. The performance with actual data is likely to be worse. However, the particle identification algorithm described here is only meant for generic use. In the physics analysis, kinematics, TOF ADC, Čerenkov signals could be used to obtain more accurate and efficient event identifications.

The TOF ADC provides additional discrimination between heavy and minimum ionizing particles. A generic π^+ ID independent of reaction kinematics is shown in Fig. 3-23.

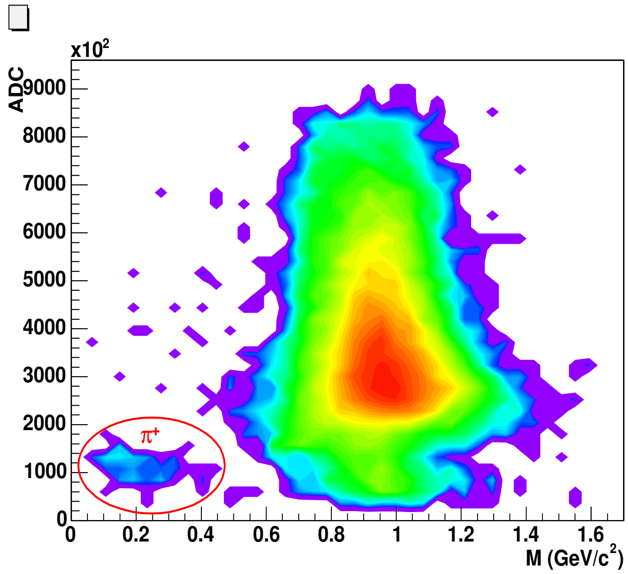

Figure 3-23: Generic π^+ ID from detector responses. No reaction mechanism or kinematic cuts were applied.

3.3.4 Čerenkov Detectors

The Čerenkov counters (CC) were thin layers of transparent Aerogel packaged in a light-tight box with reflective inner surface. The boxes were mounted on the inner side of the TOF detectors (see Figs. 3-14 and 3-17). Three boxes in each sector covered the acceptance except for the most upstream four TOFs [13]. Relativistic particles emitted Čerenkov radiation when traveling faster than the speed of light in the medium. The emitted photons were collected by PMTs mounted on the top and bottom of the Čerenkov boxes. The CC boxes were used for the identification of relativistic particles, primarily to allow discrimination between electrons and pions. The index of refraction of the Aerogel for the most downstream CC box was 1.02 while the others was 1.03. The Aerogel was 7 cm thick in the most downstream box and 5 cm in the remaining boxes. The index of refraction was chosen to distinguish between electrons and pions with momenta up to 700 MeV. Due to the ~ 100 Gauss BLAST fringe field, the PMTs were heavily shielded magnetically. A detailed description of

[13] A 4$^{\text{th}}$ box was installed in front of the four upstream TOFs. Simulations in 2002, and actual data in early 2003, demonstrated that it stopped recoil deuterons before they reached the TOF, resulting in a large loss of $D(e, e'd)$ statistics. The two boxes, one in each sector, were removed in July 2003.

the BLAST Čerenkov detectors can be found in Ref. [84].

Since $H(e, e'p)$ events can be selected from drift chamber and TOF information with a high confidence level, the electrons in these events are used to measure the efficiencies of the CC detectors. The efficiencies are found to be $\sim 85\%$. The efficiency was not ideal and some of the CC's displayed noisy behavior.

The main challenge in the $D(e, e'd)$ event selection was the separation of deuterons from protons while π^--d or π^--p background was very low. This can be successfully achieved through a set of timing and kinematics cuts (Sec. 4.2). Therefore CC detectors are not used in the analysis of elastic electron deuteron scattering, because of the loss of statistical precisions caused by their low efficiencies, and the less ideal reliability of the CC.

3.3.5 Drift Chambers

The drift chambers provided position information on the trajectory of charged particles. Combined with knowledge of the magnetic field, the charge, momentum and geometric trajectory can be reconstructed. A detailed discussion of the design and construction of the drift chambers can be found in Ref. [53]

The BLAST drift chambers (WC) were embedded in the horizontal openings between the magnet coils and were designed to maximize the acceptance within the geometric constraints. Each sector contained three chambers constructed of one-piece aluminum frames joined together with spacers into one single air-tight chamber. The frames were pre-stressed to compensate for the deformation from the wire tension. Compared to the layered-frame design, the single-chamber design reduced the amount of material the particles have to penetrate by eliminating the windows between chambers, thus reducing the energy loss and multiple scattering. The chambers were in a planar design with each of the 6 faces a trapezoidal shape. Fig. 3-24 is a photograph of one of the two chamber assemblies before installation into the supporting frame.

A mixture of 82.3% helium and 17.7% isobutane flowed through the chambers at just above the atmospheric pressure. Charged particles traversing the gas stochastically ionized the noble gas, leaving a trail of free electrons, which subsequently

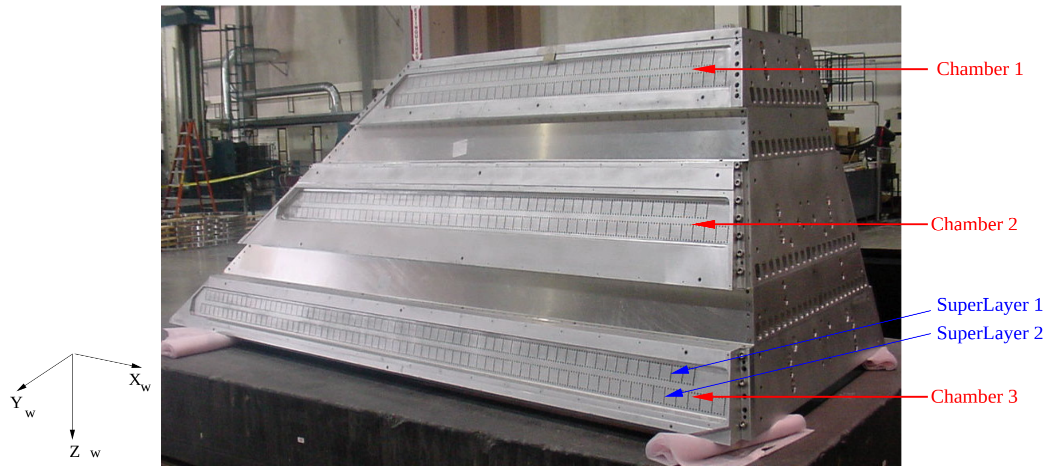

Figure 3-24: Photograph of one chamber assembly prior to integration into BLAST. Each of the two assembly contains three chambers. Each chamber contains two superlayers as explained in the text. When installed into the BLAST subframe, Chamber 1 is the closest to the beam line, facing the target chamber. Particles emerging from the target traverse chamber 1, 2 and 3 in that order.

"drifted" from their originating sites toward the designated readout wires under the influence of an electric field produced by an arrangement of field wires. The electrons accelerate for an average distance dictated by the mean free path ($\sim 1\mu$m) and decelerated by collisions with gas molecules. The net effect is thus an approximately constant drift velocity of ~ 20 μm/ns. By measuring the drifting time, the position of the initial ionization could be determined. The position resolution was worse at longer drift distance due to the diffusion of ionized electrons in the gas. The readout wire was 25 μm thick. The electric field near the wire behaves as $\sim 1/r$. The field close to the wires was strong enough to cause avalanche ionization, which served as an amplification mechanism. The strong field, however, does increase the drift velocity which causes a non-linearity in the drift time to drift distance relationship. As a result, the position resolution was reduced in the region close to the wires. The isobutane in the mixture served as the quenching gas, absorbing the energetic photons caused by recombinations in the avalanche region. These photons, left unchecked, would cause secondary ionizations resulting in constant space electric discharges.

A coordinate system is defined for each of the six chambers where x_w is in the horizontal plane pointing toward the upstream direction at an angle of $\alpha = 163.5°$ with respect to the beam direction, y_w points vertically up in the left sector and down in the right sector and z_w forms a right-hand system with y_w and x_w. For all the chambers, z_w points away from the target.

Each chamber contained two "superlayers", each of which contained three "layers" of sense wires. Each layer is a plane, perpendicular to z_w and parallel to the x_w-y_w plane, within which were the wires strung in an up-down orientation. The wires in the inner superlayers were rotated about the z_w direction by a stereo angle of $+5°$ and those in the outer superlayers by $-5°$. Fig. 3-25 is a view of the outer most chamber from the beam line along the z_w direction, the sense wires and the $\pm 5°$ stereo angles are shown. The layers were shifted by ± 0.5 mm in x_w to resolve the Left/Right ambiguities. The distance between layers in each superlayer was 1 cm, and the middle layer of the two superlayers in each chamber were separated by 6 cm. Each superlayer was further divided into "cells". The numbers of cells in the layers were, from inner most outward, 18, 19, 26, 27, 34, 35.

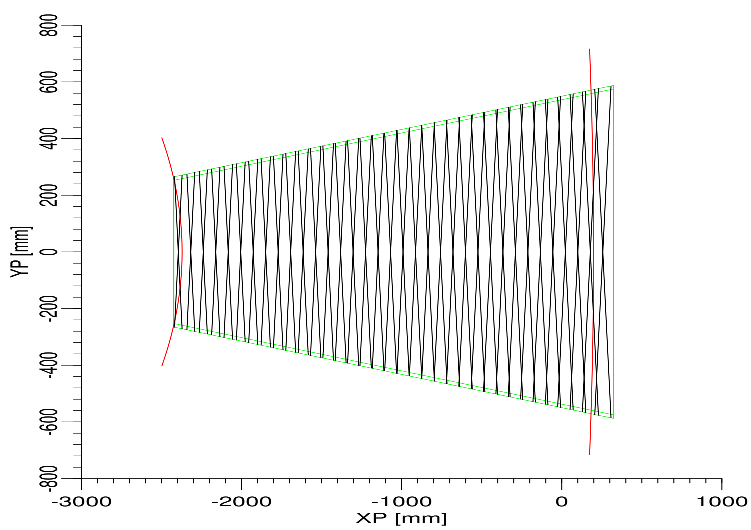

Figure 3-25: A view of the 3rd chamber along z_w direction. The wires and the stereo angles are illustrated.

A cell is a rectangular array of thirty-nine wires with foot-print of 4.0cm $\times$7.8cm in the x_w-z_w plan e as shown in Fig. 3-26. The wires in a cell fall into one of three functional categories: sense, field and guard. High voltages (HV) were applied to the field wires creating an electric gradient toward the sense wires. The HV on the guard wires are optimized to shape the field between the sense wires. The sense wires were set at 3850 V. This arrangement produces a electric field, as shown in Fig. 3-27, that resembles two oppositely directed "jets" for each sense wire. In the absence of magnetic field, the ionized electrons drift along the electric field line. With the presence of BLAST toroidal magnetic field, the drift lines are distorted. The effect of BLAST magnetic field was studied with a GARFIELD simulation and is included in Fig. 3-27.

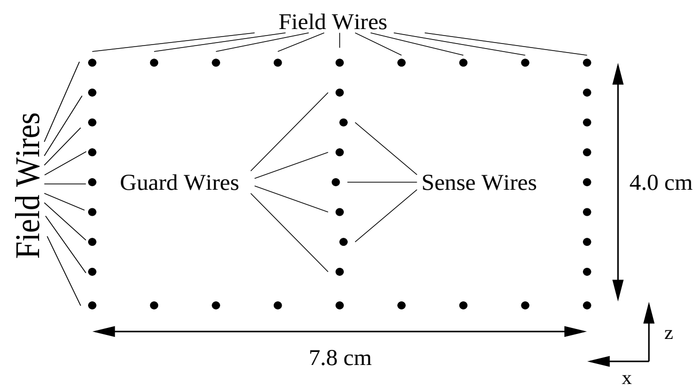

Figure 3-26: Overhead view of a drift cell in BLAST. The sense wire stagger is evident.

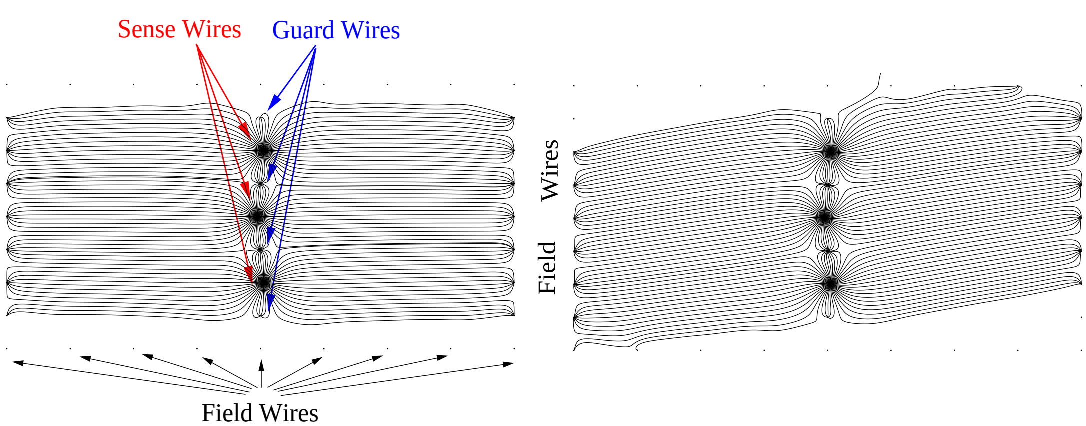

Figure 3-27: Drift lines in a drift cell without (left) and with (right) BLAST magnetic field.

An isochrone connects points of equal drift time along the drift lines. When a particle passes through the vicinity of a wire, the drift time measured is the drift time of the isochrone that is tangential to the trajectory. There are no isochrones in the jet-style cell tangential to tracks with an impact angle greater than $60°$, leading to ambiguity in the determination of drift time. This affects the resolution of forward electron track reconstruction [14].

The sense wire signals were preamplified and discriminated in custom made readout cards mounted on the outside of chamber frame, and were digitized by LeCroy 1877 FASTBUS TDC modules. The TDC modules were started by the leading edge of the wire signal and stopped by the common stop strobe generated by the delayed triggering TOF signal. Fig. 3-28 illustrates the sequence of timing events leading to a TDC value from a sense wire.

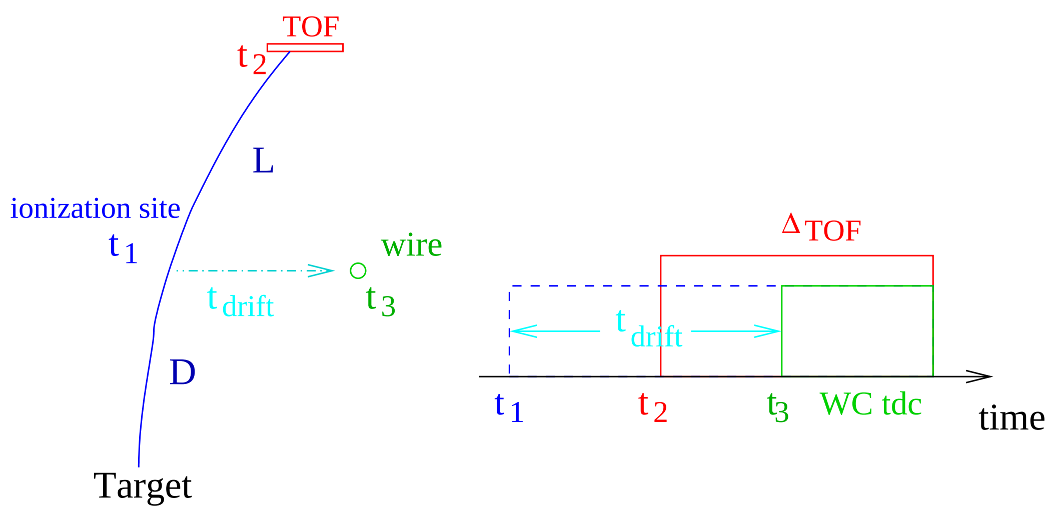

Figure 3-28: Schematic illustrating the meaning of drift chamber TDC.

A charged particle ionizes the chamber gas at time t_1. The ionization electron drifts toward a wire close by and produces a signal at t_3. The charged particle travels on at velocity v across a path length of L from the ionization site, and hit a TOF at $t_2 = t_1 + L/v$. The stop strobe is generated by the TOF hit and arrives at time $t_2 + \Delta_{TOF}$ where Δ_{TOF} is the electronics delay for the common step. It is easy to see from the figure that the drift chamber TDC measures $t_{wc} = t_2 + \Delta_{TOF} - t_3$. The

[14] In comparison, the hexagon cells featured in CLAS drift chambers in Hall B of JLab do not have this limitation [85].

drift time t_{drift} can then be calculated as,

$$t_{drift} = t_3 - t_1 = \Delta_{TOF} + L/v - t_{wc} = t_0 - t_{wc}, \tag{3.19}$$

where the drift chamber time offset t_0 is defined as $\Delta_{TOF} + L/v$. The TOF delays Δ_{TOF} are adjusted prior to the installation of the drift chamber with a reference start counter so that $t_0 = \Delta_{TOF} + L/v$ is constant regardless of the TOF paddle that generated the common stop strobe (Sec. 3.3.2), as long as the particle travels at close to speed of light, $\beta = \frac{v}{c} = 1$. Since the track length L_0 from the target to a given TOF is approximately constant, t_0 can be written as $t_0 = \Delta_{TOF} + L_0/v - D/v$ where D is the distance from target to the cell. This relationship is used in reconstruction software to correct for the drift times for slow particles (Eq. 3.22).

A typical TDC spectrum is shown in Fig. 3-29. The right edge of the plateau is TDC signals generated from ionization sites close to the wire, where the drift times are short, $t_{drift} \approx 0$ and $t_{wc} \approx t_0$. The sharp spike is due to the strong nonlinearity in the field close to the wires. The left edge corresponds to the cell boundary and is not as well defined due to the diffusion of the ionized electrons.

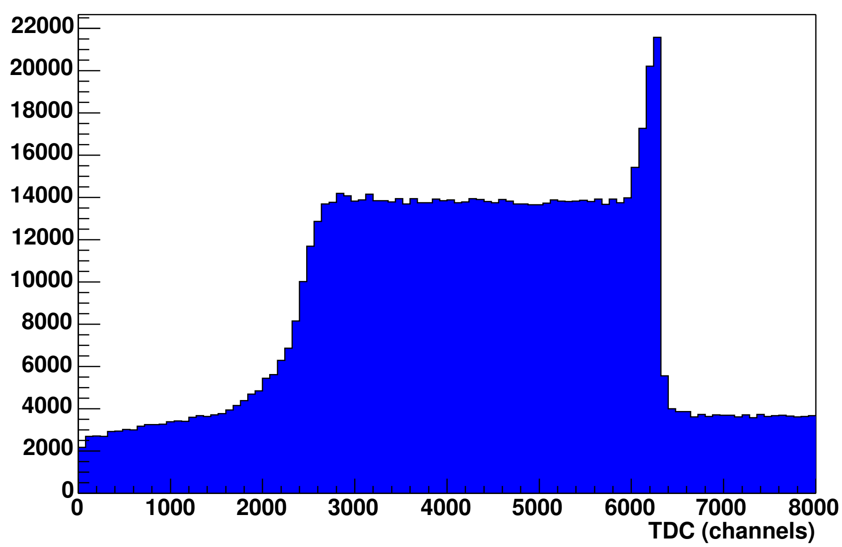

Figure 3-29: Drift chamber TDC spectrum.

In practice the distance d along the x_w direction between the track and the wire is calculated from the "time-to-distance" (T2D) conversion functions. The conversion function depends on the wires, denoted by the cell number c and the layer number $l = 0, 1, 2$, and the side of the wire, $s = left,\ right$, to which the track traversed,

$$x - x_{l,c} = d_{l,c,s}\left(t_{drift}\right) = d_{l,c,s}(t_0 - t_{wc}), \tag{3.20}$$

where t_{drift} is the drift time and t_{wc} is the time measured by drift chamber TDC. Fig. 3-30 illustrate the conversion where a track and the Garfield simulated drift lines are projected onto the horizontal plane at $y_w = 0$. The track passes the cell at an impact angle $\theta_{impact} = 90° - \theta_{trk}$ and is tangent to the $t = 100$ ns isochrone. The distance from the wire to the tangent point d_0 is projected along the track to the wire plane to obtain the distance d which is returned by the time-to-distance function. Due to the distribution of the BLAST toroidal field and the asymmetry in drift lines it caused in the two halves of the cell, the time-to-distance relationships for each wire and on the two sides of a wire are generally different. The distance d depends on two other variables besides the drift chamber TDC. The BLAST magnetic field has a different direction and strength within the same cell at different heights in the y_w direction, therefore d is a function of the y_w coordinate at which the tracks pass the cell. Also, the projection from the tangent point to the wire plane is dependent on the impact angle of the track. In Fig. 3-30, the drift of ionized electrons inside the chamber gas was modeled independent of data using a Garfield simulation. The electric field inside the cell was calculated from the voltages on the wires, the BLAST toroidal field was then superimposed, and the ion velocity at each point in the cell was calculated using the fields and the gas mixture property. Isochrone contours were calculated by numerical integration of the ion velocity. The distance d can then be calculated geometrically for tracks with a given impact angle and tangent to each isochrone.

Across the distance of 2 cm between the first and last layer in a cell, the particle trajectories are essentially straight lines. The three sense wires in a cell determine the projection of the straight line onto the $Y = 0$ (beam height) horizontal plane by

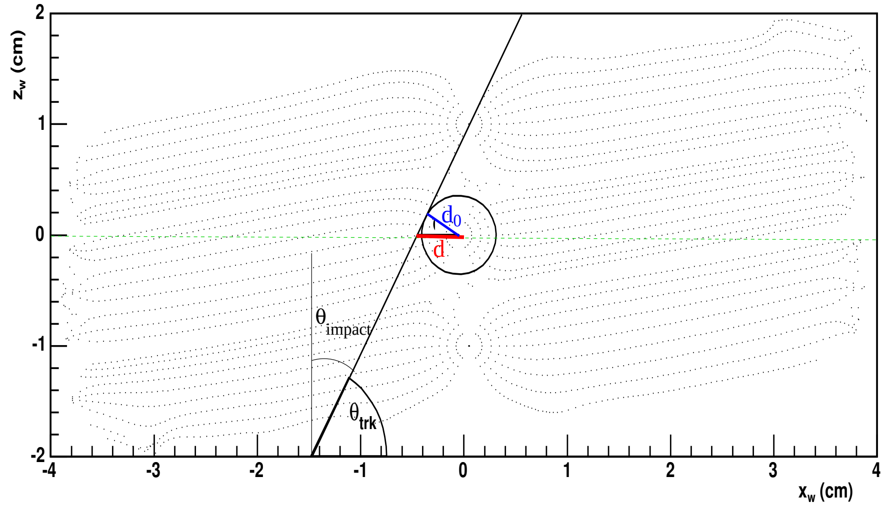

Figure 3-30: Illustration of the Garfield simulation of the time-to-distance function. A track with incident angle $\theta_{trk} = 90° - \theta_{impact}$ is shown tangent to the $t = 100$ ns isochrone along with the distance d returned by the T2D function.

sampling three points along the track. The middle sense wire is staggered by 1 mm upstream with respect to the other two, thereby eliminating the left-right ambiguity which occurs due to the lack of directional information recovered from the TDC. The left-right ambiguity and the stagger are illustrated in Fig. 3-31.

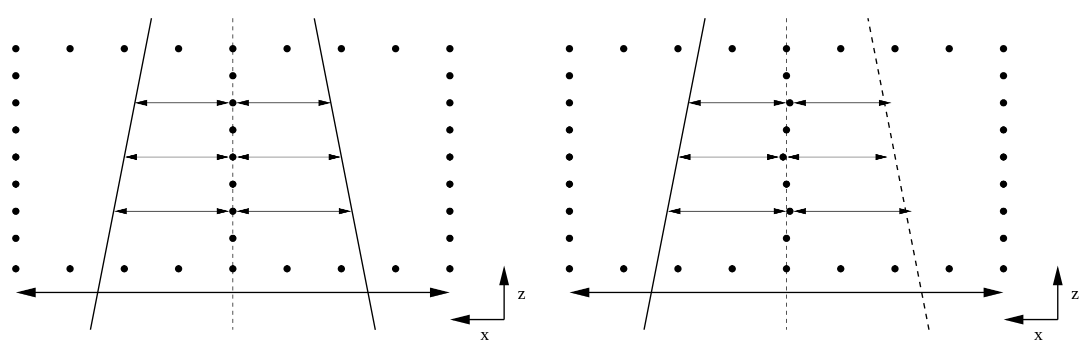

Figure 3-31: Track reconstruction without any sense wire stagger (left) and with ± 0.5 mm sense wire stagger (right). Without a stagger, the side of the traversing particle cannot be determined. With a stagger, the three hit distances form a straight line only if the correct side is chosen.

3.3.6 Drift Chamber Reconstruction

The reconstruction of particle trajectory is performed in two stages: track linking and track fitting. Track linking contains four steps: hits, stubs, segments and tracks. Track fitting is also done in stages. The algorithms are outlined in this section. An overview of the reconstruction software package is give in Ref. [83].

The linking stages are illustrated in Fig. 3-32. First the "hits" are reconstructed from TDCs with the time-to-distance conversion functions. The plane parallel to the wires with the minimal sum of square distances to the hits is called a "stub". The two stub planes in the two superlayers within a chamber intersect and determine a line "segment". The $\pm 5°$ stereo angles in the two superlayers guarantee the existence of segments. The mid-points of the three segments provide 6 independent coordinate positions $x_{1,2,3}$ and $y_{1,2,3}$, while $z_{1,2,3}$ are constraint by the planar drift chamber geometry. $\frac{y_i}{x_i}$, $i = 1, 2, 3$ are used to determine the azimuthal angle ϕ of the trajectory. The toroidal nature of the BLAST magnetic field guarantees that the geometric track of the particle lies in the plane expanded by the beam line and its initial momentum, and if the magnetic field is approximately constant, the trajectory of a charged particle is a circle which can be determined by three degrees of freedom x_1, x_2 and x_3. The circle, known as a "track", is parameterized by five variables $(p, \theta, \phi, z; q)$, where p is the momentum obtained from the curvature of the circle and the average magnetic field along the circle, z is the vertex, θ and ϕ are the polar and azimuthal direction of the momentum at the vertex and $q = \pm 1$ is the charge of the track deduced from the direction in which the center of the circle lies relative to the track.

The tracks found in the link stage are fed, as initial points, through an iterative Newton-Rhapson fitting program [83]. The Newton-Rhapson method searches, in the parameter space (p, θ, ϕ, z), for the root of the equation,

$$\boldsymbol{x}(t) - \boldsymbol{x}_h(p, \theta, \phi, z; q) = 0, \tag{3.21}$$

where $\boldsymbol{x}(t) = (x^1(t_1), x^2(t_2), ...)$ is up to an 18-dimension vector whose components are the positions of all the wire hits measured from the the drift chamber TDC,

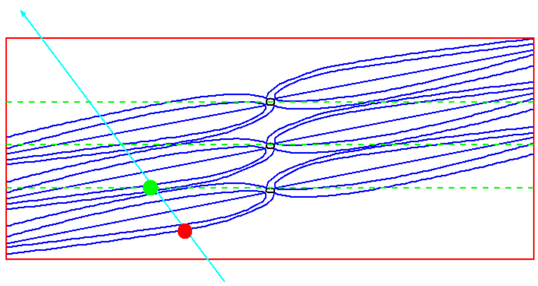

(a) Time-to-distance function calculates the perpendicular distance of the track from the wire

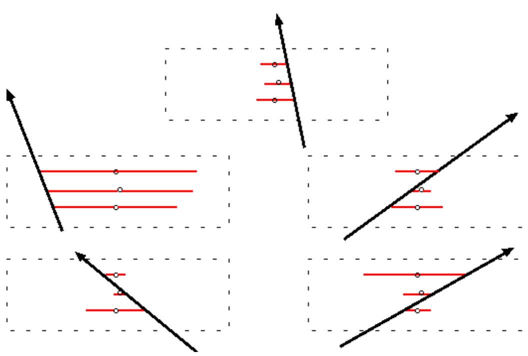

(b) Stub-finder determines to which side of each wire the track passed. 5 different cases of the 8 possibilities are shown

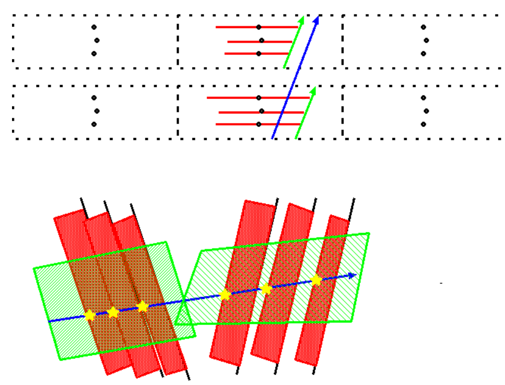

(c) In each chamber, the intersection of two stub planes forms a line segment

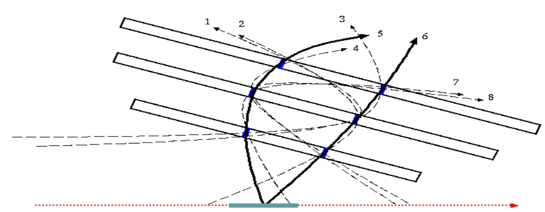

(d) The line segments are linked to form the most likely tracks

Figure 3-32: Steps of track reconstruction from hits in the drift chambers.

and $\boldsymbol{x}_h(p, \theta, \phi, z; q)$ is the vector whose components are the positions where a track with charge q, initial momentum $\boldsymbol{p} = (p, \theta, \phi)$ originating from vertex $\boldsymbol{x} = (0, 0, z)$ would intersect the wire planes. $\boldsymbol{x}_h(p, \theta, \phi, z; q)$ is found by numerically integrating the equation of motion of a charged particle in the magnetic field from the vertex outward and locating the intersection with each of the 18 wire planes. The x and y coordinates of the vertex ars fixed at 0, as the beam location is known much better than the tracking resolution. Compared to conventional χ^2 minimization methods, the root finding algorithm is more robust against local minima by preserving the directional information.

Track fitting is performed in two stages. First, all particles are treated as ultra-relativistic due to lack of timing information. Once a solution is found, the trajectory is extended according to the equation of motion to outer detectors. Hits in TOF, CC, NC are linked to drift chamber tracks according to geometric intersections of the tracks and the detectors. The absolute time of flight and the velocity of the particle can then be resolved (Sec. 3.3.2). The L/v term in Eq. 3.19 is corrected and the assumption that the particle travels at speed of light is removed by correcting the drift chamber TDC offset t_0,

$$t_0 \rightarrow t_0 - \frac{D}{c}(1 - \frac{1}{\beta}). \tag{3.22}$$

The $3(chambers) \times 2(superlayers) \times 3(layers)$ configuration provides minimally sufficient information for the unambiguous identification of a track. However, multiple hits and background noise produce unresolved multiplicities in terms of the number of stubs in a cell. Poor calibrations lead to realized intrinsic position resolutions that fall short of the 120-200 μm design specification. While the 1 mm stagger is 5 times the nominal resolution, it reduces to only a 2σ distance when the realized resolution is 500 μm. Therefore poor resolution gives rise to increased multiplicity also. In order to reduce the combinatorics, only the best candidates are kept at each stage in the track linking. In the track fitting stage, candidates with bad χ^2 or slow convergence are discarded every few iterations.

Hits may be missing due to inefficiencies. When only two wires respond to a track, there is a 4-fold multiplicity in the cell, which usually leads to two segments combined with the stub in the neighboring superlayer. When only one wire was hit, a continuum of stubs are possible due to the lack of constraint in the orientation. A segment can be constructed by assuming that the stub is perpendicular to the wire plane. When all three wires in a cell failed to trigger, the segment is constructed by the intersection of the stub in the other superlayer and the reaction plane determined by segments in other chambers. The 1-hit and 0-hit situations lead to reduced accuracy in the segments, however, the errors are corrected in the track fitting stage, where the Newton-Rhapson fitter directly utilizes hit information.

3.3.7 Drift Chamber Calibration and Performance

The calibration of the drift chamber has several parts: the calibration of the time offset t_0 in Eq. 3.19; the precise determination of the position of each wire $x_{l,c}$ in Eq. 3.20; and the calibration of the time-to-distance conversion function $d_{l,c,s}$ in Eq. 3.20.

The timing offset t_0 is calibrated for each wire using its TDC spectrum. Noise is removed by selecting only hits linked to tracks and t_0 is taken as the location where the right edge falls to zero (see Fig. 3-33). The calibration is good to within ± 2 ns, corresponding to $\sim$ 40 μm in position resolution which is much smaller than the resolution arising from the time to distance conversion. Any change in t_0 over time is monitored for each sense wire.

The center position of each wire feedthrough is measured by the manufacturer to within 10 μm, but the feedthroughs have an inner diameter of 250 μm, constraining the wire position, in the worst case, to within ± 125 μm. The sense wires are strung with 50 g tension to resist deformation under electro-magnetic fields. The positions of the wires are further calibrated with data and are believed to be known to within ± 50 μm [86].

An empirical method of iterative relaxation was developed to calibrate the drift chamber time-to-distance conversion functions. The iterative relaxation method draws from the successful experience with the CLAS drift chambers in Hall B of JLab [85].

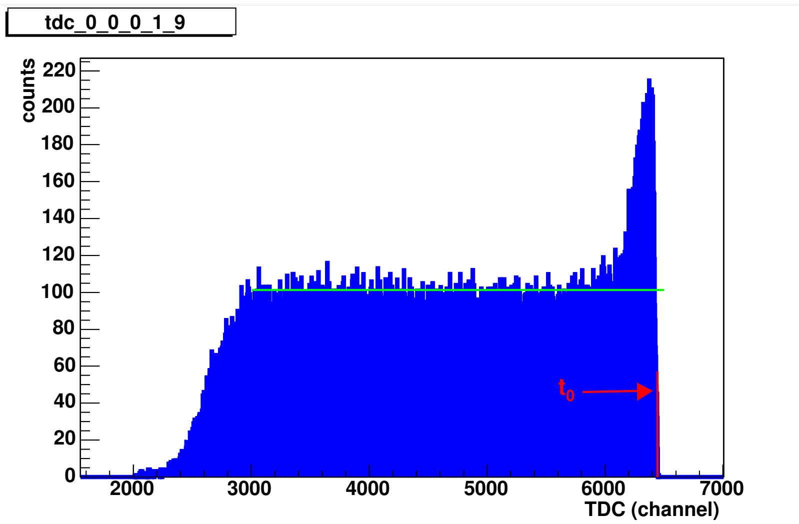

Figure 3-33: Calibration of drift chamber TDC offsets t_0 for left sector, chamber #0, superlayer #0, layer #1 and cell #9. The green line is a fit to the plateau, and the red line marks the t_0 obtained.

The Garfield simulation was used as a starting point. Tracks are reconstructed, and those that converged with χ^2 values and traced back to the target are used. The distances d_{trk} from the tracks to the wires are fit to 9^{th} order polynomials of the drift chamber TDC. The polynomials are connected continuously in both the 0^{th} and 1^{st} derivatives to linear functions fit to distance over the TDC in the range $2500 < t_0 - t < 4000$ to avoid numerical instability in the polynomial at large TDC values. Reconstruction is reperformed with the updated T2D functions, and the procedure was iteratively repeated until the T2D functions converge. 270 deuterium target runs taken during the summer of 2004 were used to calibrate the 1908 T2D polynomials [15]. Electro-disintegration of the deuteron offers wider coverage of the drift chamber than the very narrowly defined elastic kinematics.

Fig. 3-34 shows the distribution of distances d_{trk} as a function of TDC channel on both sides of one of the wires. The calibrated time to distance (T2D) functions are superimposed. The right panel of the figure shows, as a function of the TDC, the

[15] The very first few cells of each layer failed to converge due to poor signal to noise ratio. These cells are dominated by tracks with large impact angle which are not tangential to any of the isochrones. Therefore the Garfield simulated T2D function does not present a valid starting point for the iterative method. The original Garfield simulated T2D relations were used for these cells.

distance with a linear function subtracted: $d(t_0 - t_{wc}) - k \times (t_0 - t_{wc})$. This figure highlights the nonlinearity of the T2D conversion function even at medium to large drift time ($t_0 - t_{wc} > 500$ ch). This nonlinearity could be due to variations of drift velocity along the drift lines due to uneven distribution of the fields, a nonlinearity in the TDC module, *etc*. The empirical polynomial fit is capable of accommodating these nonlinearities as well as small errors in t_0 and wire position $x_{l,c}$.

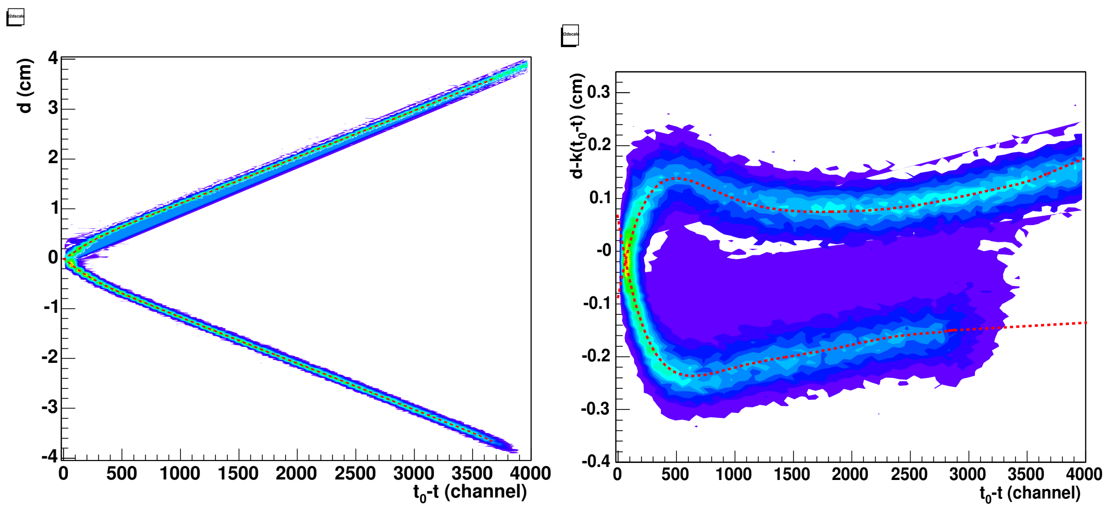

Figure 3-34: Calibration of drift chamber time to distance (T2D) conversion function. The red dashed curves are the calibrated T2D functions. In the right figure, the distance minus a linear function, $d(t_0 - t_{wc}) - k \times (t_0 - t_{wc})$, is shown as a function of $t_0 - t_{wc}$. The nonlinearity at medium and large drift time is clearly shown on the right.

Fig. 3-35 is a histogram of the typical residual of $\delta_d = d_{trk} - d_{l,c,s}(t)$ in the range (1500 ch $< t_0 - t_{wc} <$ 2000 ch) which excludes the highly nonlinear regions. The intrinsic position resolution measured by the standard deviation of the residual is typically ~ 600 μm [16]. The resolution close to and far from the wire is lower due to nonlinearities in the field and the diffusion of the ionized electrons [17].

[16]This falls short of the 200 μm drift chamber design specification. The lack of redundancy in the BLAST drift chamber presents special difficulties in obtaining precise calibrations. The three chambers are more than 40 cm away from each other while each chamber is only 8 cm in depth. The chambers therefore exerts little constraint on each other. The 3-layer cell has no redundancy so that individual wires can not be calibrated independently. The hexagonal cell design in CLAS drift chambers has more redundancy and more close neighboring cells.

[17]The wires in BLAST drift chambers have 4 cm pitch compare to the 2 cm wire pitch in CLAS drift chambers.

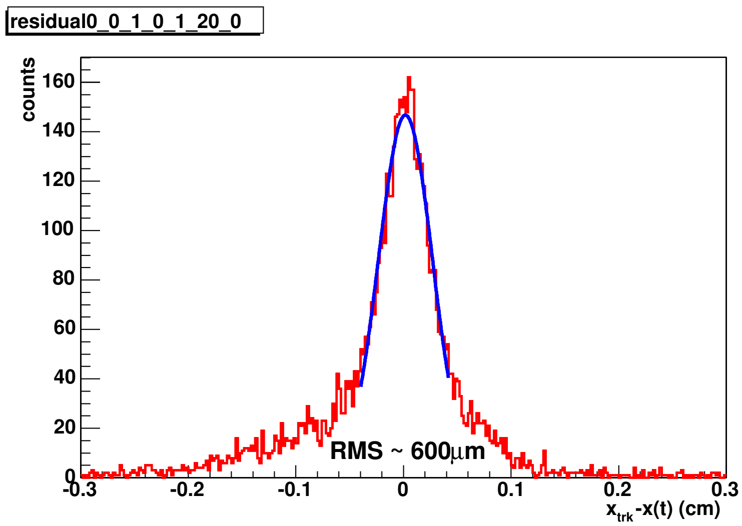

Figure 3-35: Drift chamber resolution with T2D function. The residual for left sector, chamber #1, superlayer #0, layer #1, cell #20, left side is shown. The center portion fits to a normal distribution with $\sigma = 250\mu$m, however, there are clearly higher tails than a normal distribution, which give rise to a standard deviation of $\sigma \sim 600\mu$m.

Tracking resolution is measured by the over-determined kinematics in elastic $H(e, e'p)$ and $D(e, e'd)$ reactions. For example, the reconstructed electron momentum p_e is compared to the momentum value calculated from the reconstructed θ_e, and the standard deviation is used to measure the tracking resolution. Using the elastic electron-proton scattering events, the following resolution measures are extracted:

$$
\begin{aligned}
\delta_{p_e} &= p_e - p_e(\theta_e), \\
\delta_{\theta_p} &= \theta_p - \theta_p(\theta_e), \\
\delta_{p_p} &= p_p - p_p(\theta_e), \\
\delta_{\phi} &= \phi_{right} - \phi_{left} - 180^\circ, \\
\delta_z &= z_e - z_p.
\end{aligned}
\tag{3.23}
$$

Fig. 3-36 shows the comparison of reconstructed θ_p and $\theta_p(\theta_e)$ and the angular resolution measured. On the right panel, the distribution of δ_{θ_p} is fit to a Gaussian and the width of which is use to measure the resolution. This estimation is dominated by low Q^2 ep-elastic events while the actual tracking resolutions depend on the momentum of the scattered particles; therefore this procedure provides only a rough estimate of the resolutions. For typical electrons ($p_e \approx 0.8$ GeV/c) and protons ($p_p \approx 0.3$ GeV/c), the resolutions are determined to be,

$$\sigma_{p_e} \sim 25 \text{ MeV}, \quad \sigma_{\theta_p} \sim 0.5\ ^\circ, \quad \sigma_{p_p} \sim 20 \text{ MeV}, \quad \sigma_\phi \sim 0.6\ ^\circ, \quad \sigma_z \sim 0.9 \text{ cm}. \tag{3.24}$$

The resolution in invariant mass is typically $\sigma_W \sim 30$ MeV and the beam energy is re-

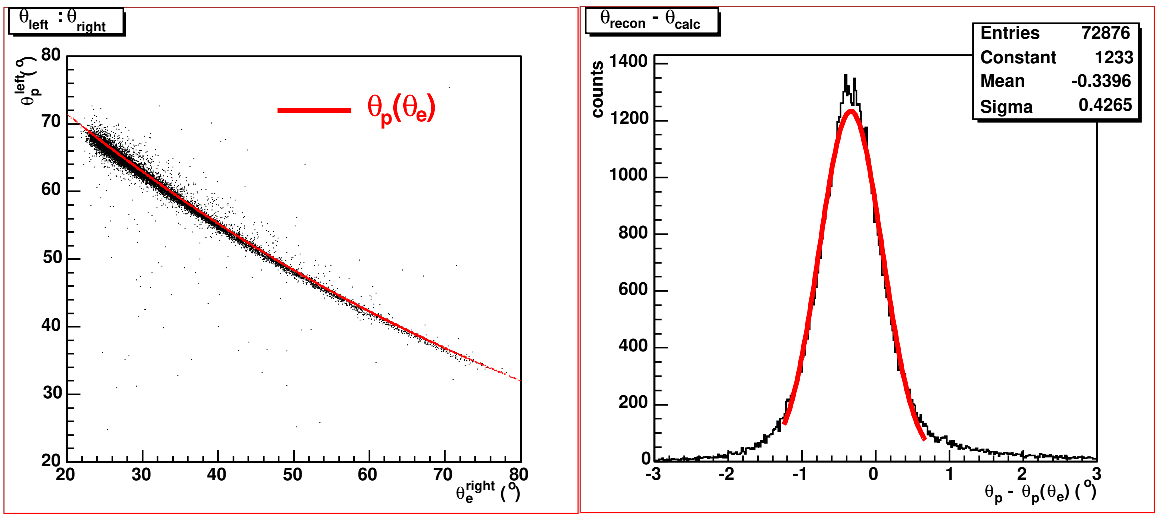

Figure 3-36: Angular tracking resolution for electrons and protons in the left and right sectors from elastic scattering from a hydrogen target. The red curve on the left panel is the proton scattering angle, $\theta_p(\theta_e)$ calculated from the electron scattering angle according to ideal ep-elastic kinematics. The residual $\theta_p - \theta_p(\theta_e)$ is shown in the right panel and fit to a Gaussian (the red curve).

constructed typically with $\sigma_{E_0} \sim 26$ MeV. The resolutions extracted with this method are in fact functions of Q^2. In general, tracking resolutions depend on the particle species, the sector, and the region where the tracks passed. The same method can be applied to the $D(e, e'd)$ reaction, which was used to monitor tracking performance during deuterium target runs.

The reduced χ^2 of each fitted track is defined as

$$\chi^2 = \frac{\sum_1^N (x_{trk}^i - x_{hit}^i)^2}{(N-4)\delta_d}, \tag{3.25}$$

where N is the number of hits the track was reconstructed from, δ_d is wire resolution,

x^i_{trk} is the position where the track crosses the $i^{\rm th}$ wire plane and x^i_{hit} is the position determined from the wire TDC. The degrees of freedom are $N-4$ because of the four tracking parameters. The average χ^2 is 1 with $\delta_d \approx 600\mu$m, consistent with the findings from the T2D calibration (Fig. 3-35).

Besides the position resolution in drift chambers, multiple scattering by the particle from the atoms in the media it traversed can also affect the tracking resolution. The energy loss by the particle causes the curvature to increase along the path, which is not corrected for in the tracking algorithm. The BLAST GEANT simulation package "blastmc" is used to study the impact of various factors. Resolutions and physical processes along the particle trajectory are simulated with GEANT, and the simulated drift chamber hits are reconstructed with the same software package as used for real data. The same resolution measures are extracted. The results are listed in Tab. 3.3. Energy loss does not have a significant effect on resolutions while multiple scattering alone limits the angular resolutions to about 0.5°, vertex resolution to ~ 1 cm and momentum resolutions to not better than 10 MeV. The realized angular and vertex resolutions are close to the limit imposed by multiple scattering. The large impact angle on drift chamber cells for the forward angle electrons significantly limits their reconstruction resolution.

The efficiencies of the wires were determined in a study in which a track was deemed to have traversed the cell whenever two of the three wires in a cell were hit [18]. The efficiency of the third wire was then determined as the fraction of time that a hit was in fact produced. The efficiency of most wires is found to be greater than 95%. The reconstructed tracks have an average hit number of 17, consistent with the 95% figure.

The drift chamber tracking efficiency was studied, in the dissertation of Dr. Chris Crawford, by selecting a elastic *ep* event sample from the TOF scintillator cuts [83]. The efficiency measured in this manner is a convolution of wire efficiencies, efficiencies of track linking and fitting algorithms, and the robustness of tracking algorithms

[18] When the impact angle is large, the $3^{\rm rd}$ wire could in fact be in the neighboring cell. Such cases are excluded from the total sample in the study.

LOSS	MULS	$\delta_x(t)$ ($\times 200$ μm)	$\delta_x(\theta_{impact})$	δ_{p_e} (MeV)	δ_{p_p} (MeV)	δ_{θ_p} ($^\circ$)	δ_ϕ ($^\circ$)	δ_z (cm)
off	off	0	off	5	5	0.1	0.2	0.5
off	off	1	off	6	6	0.2	0.3	0.6
on	off	1	off	6	6	0.2	0.3	0.6
off	on	0	off	15	10	0.4	0.5	0.9
on	on	1	off	15	10	0.5	0.5	1.0
on	on	2.5	off	15	15	0.5	0.5	1.0
on	on	2.5	on	20	15	0.5	0.5	1.1

Table 3.3: Monte Carlo study on contributions to tracking resolution. LOSS stands for energy loss and MULS stands for multiple scattering simulation, $\delta_x(t)$ is the standard chamber position resolution simulated for each wire, $\delta_x(\theta_{impact})$ simulates worsening of resolution caused by large impact angles. The resolution measures are same as defined in Eqs. 3.23, but applied on reconstructed Monte Carlo data. The difference between the 3$^{\text{rd}}$ and 2$^{\text{nd}}$ rows shows that energy loss does not affect tracking resolution significantly. The difference between the 4$^{\text{th}}$ and the 1$^{\text{st}}$ demonstrates the big impact of multiple scattering. Realized angular and vertex resolutions are close to the limit imposed by multiple scattering (the 4$^{\text{th}}$ row).

under event selection rules. The non-biased event base is constructed with timing and coplanarity cuts in the TOF along with single arm drift chamber tracks which conform to $H(e, e'p)$ kinematics. The percentage of missed tracks was tabulated as a function of Q^2. Progressive cuts on resolutions were applied to study the robustness. The four track parameters (p, θ, ϕ, z) are used along with invariant mass W. The tracking efficiency, which includes both detector efficiency and reconstruction robustness, is shown in Fig. 3-37. Track linking is highly efficient, as a result of the highly efficient wire response. The Newton-Rhapson method converges for most of the tracks found in the linking stage. However, the subsequent event selection cuts lead to significantly reduced efficiency, which points to poor resolutions and mis-reconstructions. The overall efficiency after event selection is determined by comparing the yields observed to the yields predicted by Monte Carlo simulations for a given target density. For reactions requiring double coincidence of drift chamber tracks, the Monte Carlo study indicates an efficiency of 50-60%, consistent with, for example, the convolution of "Left Proton" and "Right Electron" efficiencies in Fig. 3-37.

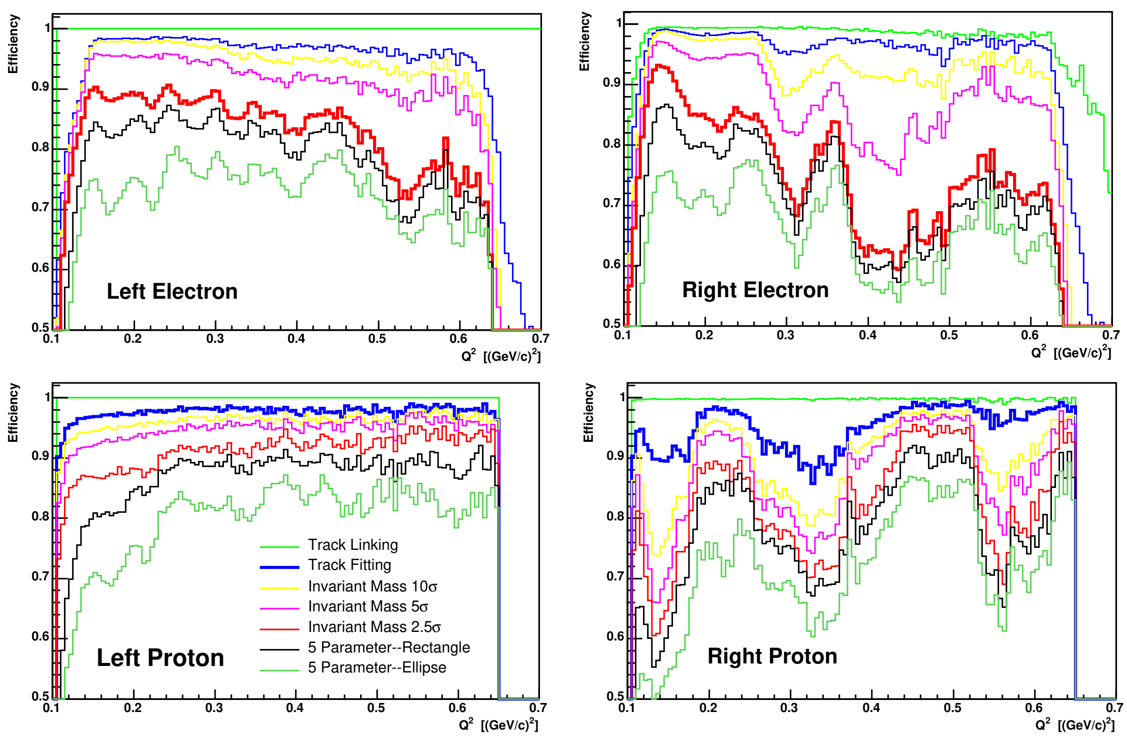

Figure 3-37: Drift chamber tracking efficiency for electrons and protons in the left and right sectors. Figure taken from Ref. [83]. The curves, listed in the same order in the legend as they appear in the plot, correspond to different cuts on tracking qualities (10-σ, 5-σ in invariant mass W, *etc.* as indicated in the lower left panel). Ellipse cuts further eliminate the corners of the rectangular cuts. The five parameters are p, θ, ϕ, z and invariant mass W.

3.4 Electronics

3.4.1 Trigger

The trigger system was developed in conjunction with JLab Hall A. Signals from the TOF, NC and CC detectors were sent through a passive analog splitter. One branch, called the prompt, was sent to discriminators, while the other, delayed by 500 ns was sent to the ADCs. After discrimination, the prompt signals were sent to TDCs after a delay, and a sector LeCroy Memory Lookup Unit (MLU). The MLU was programmed to demand coincidence between the two PMTs in each TOF, *etc.* The outputs of the two sector MLUs were combined in a cross MLU (XMLU), where the coincidence among multiple detectors and across the two sectors was demanded. Fig. 3-38 is a schematic of the electronic components. The physics trigger settings used during the experiment are tabulated in Ref. [83].

Analysis of earlier detector performance revealed that over 90% of the triggers failed to reconstruct into drift chamber tracks. The source of such events was presumed to be upstream electron-positron showers and gamma rays which left sporadic trails in the chambers. The addition of a collimator into the beam line to protect the target cell walls aggravated the noise problem and increased the detector dead time to a level of $\sim 40\%$. In order to reduce the number of trackless events, a second-level trigger was instrumented, in December of 2003, to demand at least one hit in each of the three drift chamber in one sector. The second level trigger reduced the detector dead time to below 5% and reduced the trackless events to less than 10% of the total number of triggers.

The trigger supervisor (TS) provided trigger distributions, gates and starts to ADC and TDC modules, the common stop to the drift chamber TDC, event synchronizations, *etc.* The TS was developed by JLab and is controlled by the CODA software.

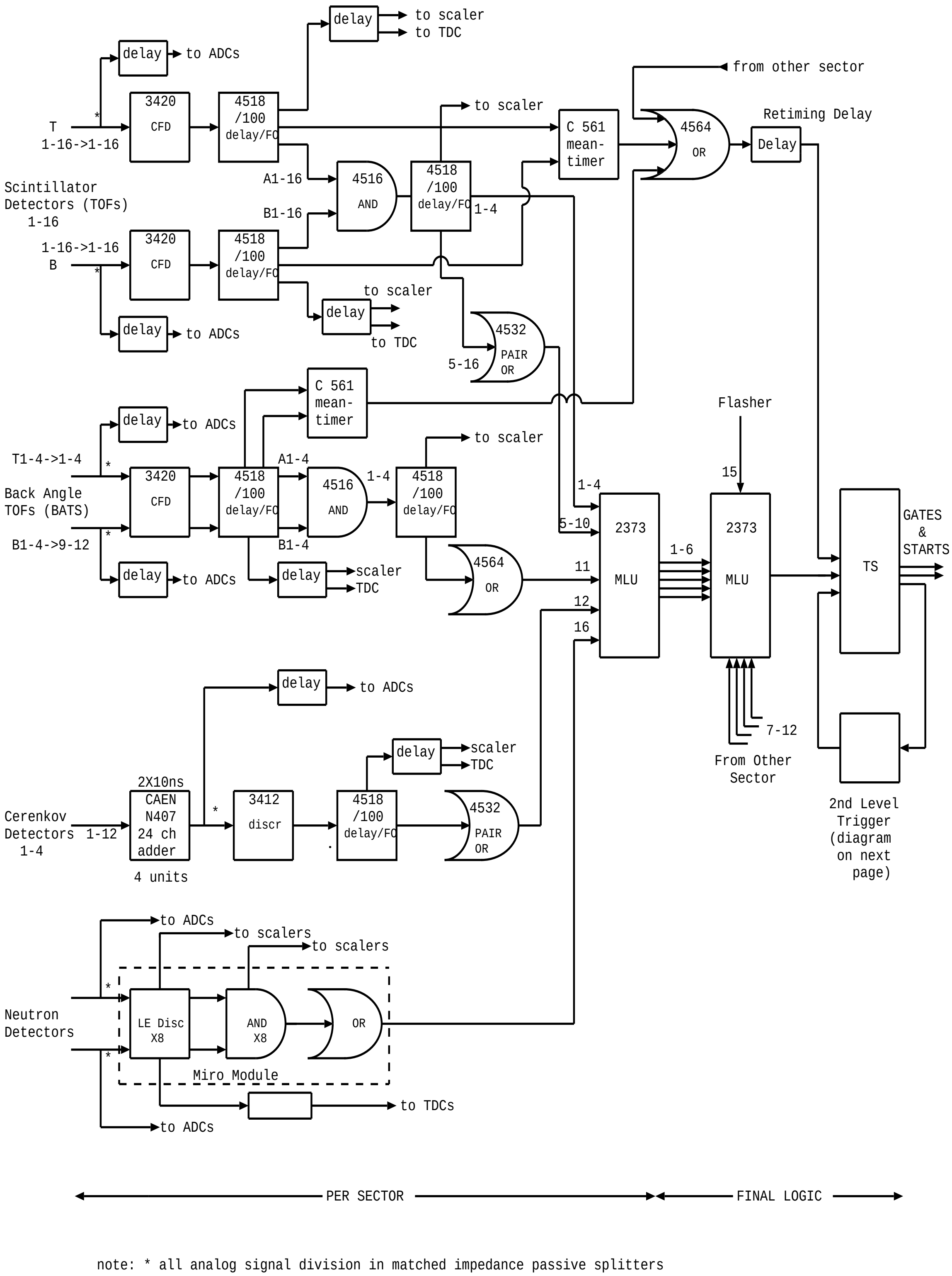

Figure 3-38: A schematic of the trigger logic. Only one circuit is shown for each detector, and only the left sector is shown. The logic from the left sector MLU and right sector MLU are combined in the cross MLU to form the final trigger processed by the trigger supervisor.

3.4.2 Data Acquisition

BLAST used the CEBAF Online Data Acquisition (CODA) system from JLab. Two FASTBUS crates, one for each sector, digitized the data. Readout controllers (ROC) read the data through the Struck FASTBUS Interface (FSI) and communicated data fragments to a Linux host computer via local DAQ Ethernet. The Linux host ran the CODA graphical interface RunControl and the main CODA processes. The Event Builder (EB) assembled fragments into a raw CODA event. Event Transport (ET) buffered the event, merged events from input pipes, such as EPICS, scalers and the Compton controller, and responded to queries from output pipes such as online monitors. The Event Recorder (ER) wrote data to disk.

The Experimental Physics and Industrial Control System (EPICS) is used to control and monitor slowly varying settings and parameters such as high voltages, beam current, vacuum gauges, and temperatures. EPICS variables were recorded at a frequency of 1 Hz into the CODA data stream. Scaler readouts were also recorded into the CODA stream every second. All events were time-stamped by the ROCs and the synchronization was better than 10 ms. Physics event must be bracketed by EPICS and scaler events in order to be valid, as important run parameters such as beam current, and target and beam helicity states, are carried by scalers. Alarm systems were implemented to prompt operators when the EPICS or scaler stream was disrupted.

3.5 Monte Carlo Package

A `C++` software package, DGen, was developed for BLAST physics simulations. DGen incorporates theoretical calculations for the electron scattering reactions studied with BLAST. Cross sections and spin dependent observables are computed, events are generated accordingly and fed into the BLAST GEANT package, known as blastmc. The GEANT package propagates the particles in the BLAST magnetic field and simulates the detector responses and physical processes such as energy loss and multiple scattering. Several physics channels are implemented in DGen, including $D(e, e'd)$, deuteron electro-disintegration [19], $H(e, e'p)$ [20], and pion production from the nucleons [21]. Polarized observables in ep-elastic and ed-elastic reactions with radiative corrections are implemented through a translated version of MASCARAD [87] from FORTRAN [22]. Multiple channels can be mixed in one simulation, which proved useful in the study of contamination caused by elastic reactions in the inclusive deuteron electro-disintegration channel.

DGen is a quasi-Monte Carlo event generator. It uses the Sobol low-discrepancy sequence [88], which is a deterministic sequence sampling the unit interval in N-dimensional space more "uniformly" than standard computer generated pseudo-random numbers [89]. It is proven that for Monte Carlo sampling in a s-dimensional space, the mean value converges to the true mean at a rate of $B = \dfrac{\zeta \times log^{s-1} N}{N}$, where ζ is a constant related to the quality of the sequence, i.e., the degree of "discrepancy". This error bound is deterministic, which means the difference between any quasi-Monte Carlo and the true value is smaller than this bound while the error bound in standard Monte Carlo methods is the standard deviation which is statistical.

Several operating modes are implemented in DGen. In a stochastic simulation, events are distributed according to the cross section. DGen automatically distributes events across spin states and reaction channels with weights determined by the total cross sections of the various channels. Analysis programs developed to treat actual data can be applied almost as is. It can be shown that the error in asymmetries is bounded by the error bound B of the low-discrepancy sequence [89].

DGen can also be used as a quasi-Monte Carlo integrator where the generated events are taken as the weighting in the integration,

$$\int_\Omega f(x)w(x)dx = \sum_i^N f(x_i), \tag{3.26}$$

with x_i, $i = 1, 2, ..., N$ distributed as $w(x)$. The error bound of the integral is $\sigma_f \times B$,

[19] Courtesy of Dr. Hartmorth Arenhövel [43]

[20] Courtesy of Ben Clasie, Chris Crawford and Jason Seely for the underlying software

[21] Courtesy of MAINZ collaboration for the MAID source codes.

[22] Courtesy of Dr. Afanasev from JLAB for MASCARAD source code and Vitaliy Ziskin for the adaptation into C++.

where σ_f is the standard deviation of the function f and B is the error bound of the sequence. Spin asymmetry observables are bounded by ± 1, hence σ_f within a typical bin in the analysis is much smaller than 1. The Monte Carlo integrator mode takes advantage of the accelerated convergence, albeit special analysis code must be prepared for the generated data.

The importance sampling technique [88] was also used with DGen. When the region of phase space under consideration has a very small cross section, very few events would fall into that region, leading to poor accuracy in Monte Carlo results. The importance sampling method samples the phase space uniformly and restores the physical distribution by assigning, after generation, an appropriate weight proportionally for each event. Analogous to Eq. 3.26, the importance sampling method can be expressed as,

$$\int_{\Omega} f(x)w(x)dx = \sum_{i}^{N} f(x_i)w(x_i), \tag{3.27}$$

where x_i, $i = 1, 2, ..., N$ are uniformly distributed.

Chapter 4

Data Analysis

The BLAST detector complex and the ABS target were commissioned from June 2002 to June 2004 when optimal detector and target performances were achieved. Data for this experiment were taken during two periods using the same 60 cm target cell. Key parameters of the two periods are listed in Tab. 4.1 [1].

		Run 1	Run 2
start date		2004/07/02	2005/03/17
end data		2004/10/18	2005/05/31
beam charge	q	370 kC	560 kC
ave. beam current	I	100 mA	180 mA
target thickness	ρ	$6{\times}10^{13}$ cm^{-2}	$6{\times}10^{13}$ cm^{-2}
luminosity	$\mathcal{L}$	$4{\times}10^{31}$ cm^{-2} sec^{-1}	$7{\times}10^{31}$ cm^{-2} sec^{-1}
int. luminosity	$\int dt\mathcal{L}$	139 pb^{-1}	236 pb^{-1}
tensor pol.	P_{zz}	0.683	0.563
pol. angle	θ_S	31.7°	47.7°

Table 4.1: Beam, target, and spectrometer conditions for the two data-taking periods of BLAST with the ABS D_2 target.

The main differences between the two periods are: 1) The 2005 runs had higher average beam current as the performance of the ring and the detectors were better understood; 2) The 2005 runs had lower polarization (Sec. 3.2.2); 3) The 2004 runs

[1] There are another 8 series of runs under various conditions. The total charge in those runs is 230 kC and the average tensor polarization was about 0.4. The cumulative Figure of Merit (FOM), measured by the product of cumulated charge and polarization $Q \times P_{zz}^2$, in these runs is about 10% that of the data used in this work. As a result, these runs are not used in this work

had the target spin angle held at 32° to the left of the beam, which is optimal for the high Q^2 T_{20} and the G_E^N measurement from $D(e, e'n)p$ channel [54], while the 2005 runs had the spin angle set at 47° on the left side of the beam, which is optimal for low Q^2 T_{20} measurement. Production data with the hydrogen target were taken in between. With the target polarization pointing to the left of the beam, the 3-momentum transfer is approximately parallel (perpendicular) to the deuteron spin when the electrons scatter into the right (left) sector. Therefore the kinematic configurations are referred to as parallel and perpendicular kinematics respectively.

4.1 ed-elastic Monte Carlo

Monte Carlo simulations are performed to help understanding the apparatus and the data. Events distributed according to the ed-elastic cross section were generated and passed to the dedicated GEANT package [53] which simulates the physical processes, such as energy loss and multiple scattering in the BLAST detector system and detector signals. The GEANT simulated detector signals were then processed by the same reconstruction package (Sec. 3.3.6) [83] used for actual data. The reconstructed events, therefore, have the BLAST simulated acceptance and detector resolutions included.

The target polarizations are assumed to be 100%, i.e., $P_{zz}^+ = 1$ and $P_{zz}^- = -2$ for the simulations. The reconstructed Monte Carlo data were analyzed to obtain the "Monte Carlo asymmetry":

$$A_{MC} = \sqrt{2}\frac{N_{MC}^+ - N_{MC}^-}{P_{zz}^+ N_{MC}^- - P_{zz}^- N_{MC}^+},$$

where, $N_{MC}^{+,-}$ is the number of events generated and reconstructed in the tensor $+$, $-$ states respectively. Polarizations less than 100% lead to a multiplicative scaling factor on the asymmetry, $A(P_{zz} < 100\%) = P_{zz} \times A_{MC}$; therefore the actual target polarization can be measured by comparing the experimental asymmetry to the Monte Carlo, $P_{zz} = \dfrac{A_{raw}}{A_{MC}}$, with A_{raw} representing the measured asymmetry (Secs. 4.3.2 and 4.3.3). To facilitate the comparison to experimental data, the Monte Carlo asymmetries at $Q^2 < 0.35$ (GeV/c)^2 are fit to polynomials of the form, $A_{MC}(Q^2) = a_1 Q^2 + a_2 Q^4 + a_3 Q^6$, which conforms to the constraint that $A(Q^2 = 0) = 0$. Fig. 4-1 shows the Monte Carlo asymmetries in the parallel and perpendicular kinematics, and the fit to the polynomials. Simulations assuming spin angles between 28° and 50° with 1° separation were performed. The results are compared to data to measure the actual spin angle (Sec. 4.3.3).

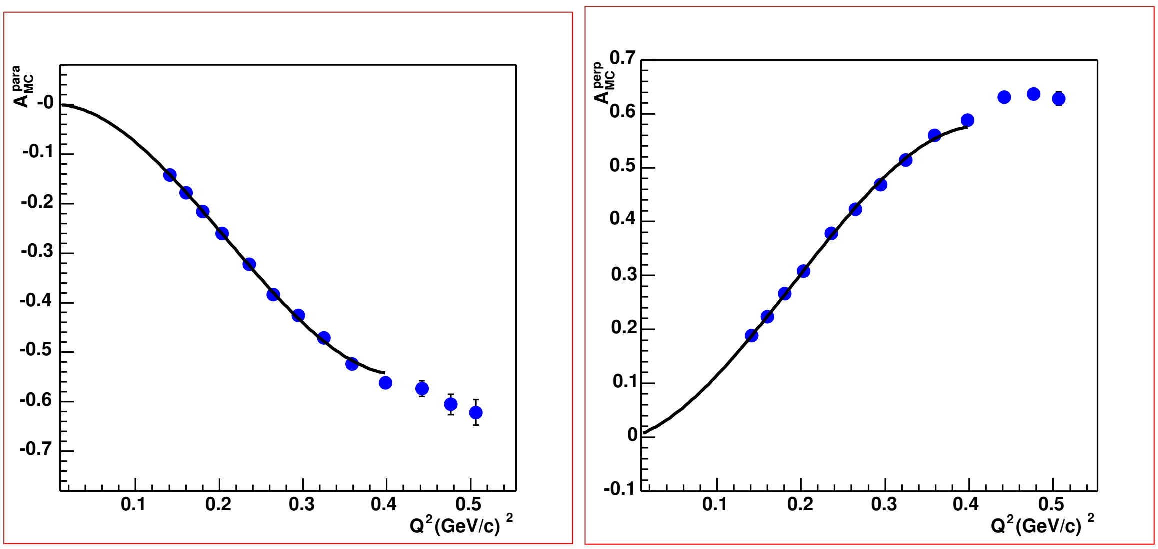

Figure 4-1: The Monte Carlo asymmetries A_{MC} with spin angle 32°. The polynomial fit $A_{MC}(Q^2) = a_1 Q^2 + a_2 Q^4 + a_3 Q^6$ is also shown.

Special simulations were performed where different degree of polarization were assigned to different target states. These simulations were used to study the systematic errors described in Sec. 4.5.2.

Many deuteron models are implemented and simulated. For the determination of tensor polarization P_{zz} and spin angle θ_S, Abbott's parameterization III [61] (Sec. 2.3.3) is used, while the other models are simulated for the purpose of comparison and study of model dependence and theoretical error. The choice of parameterization III is discussed in detail in Sec. 4.6.2.

4.2 Event Selection

Robust yet efficient event selection rules are important to establish a clean e-d elastic event sample. The elastic electron-deuteron cross section is very small compared to the electro-disintegration of the deuteron. The observed $D(e, e'p)n$ rate was almost 40 times the elastic rate. Some preliminary requirements were established to ensure the quality of the reconstruction: 1) One wire chamber track in each sector, one with positive charge and the other negative; 2) Each track must be reconstructed from no less than 12 wire chamber hits, and converge to a reduced χ^2 less than 100; 3) Each track must link to a TOF hit to ensure timing-based particle identification (PID); 4) The mean z vertex of the two tracks must be within -20 cm to 20 cm where the target holding field is strong, and the target spin angle $\theta_S(z)$ is within $\pm 10°$ from the average spin angle. A set of cuts based on information provided by the time-of-flight (TOF) scintillators and drift chambers (WC) are applied in addition to these preliminary requirements.

4.2.1 Elastic TOF Cuts

The TOF cuts are based on the timing, coplanarity and energy deposit of particles in the scintillators. An ed-elastic event triggers one TOF in each sector. The timing cuts are created for 142 out of the 256 (16 on the left $\times$ 16 on the right) paddle combinations which are shown in Fig. 4-2. A Monte Carlo study showed that the remaining 114 left-right combinations have absolutely no elastic events in them. A typical timing spectrum has two peaks. Deuterons, being twice as heavy as protons, are associated with the later peak. The later timing peak survives kinematic cuts demanding the reconstructed drift chamber tracks lie close to the ed-elastic kinematic ridge. This is deemed a strong confirmation of the identity of the deuteron timing peak. For paddles with sufficient elastic statistics, the deuteron timing peaks were fit to Gaussian distributions and 5-σ cuts were used. For paddles whose statistics were too low to fit for Gaussians, the cuts were positioned to exclude the proton timing peaks. The cuts are marked by green vertical lines in Fig. 4-2. The typical width of

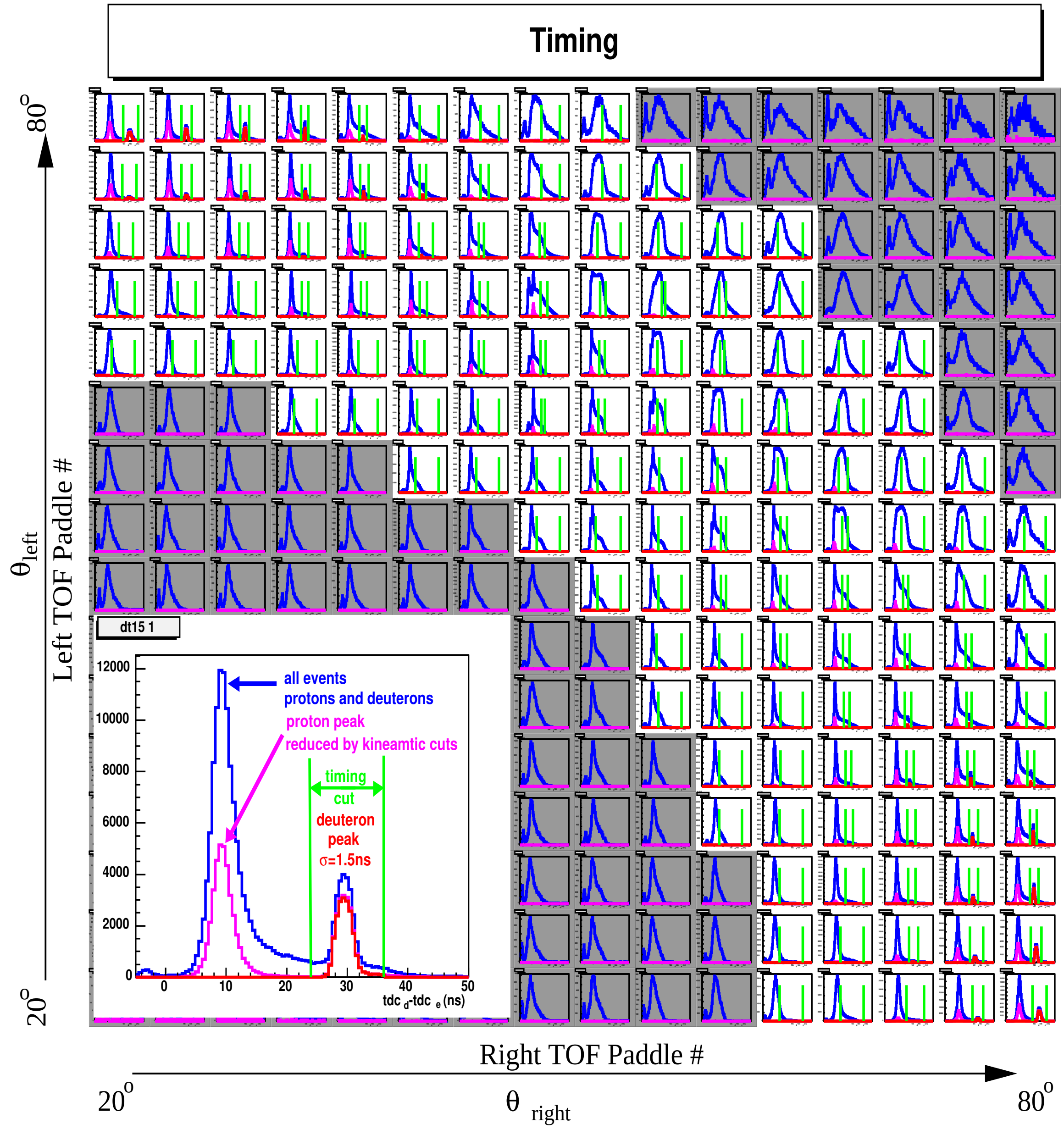

Figure 4-2: An illustration of the TOF timing cuts. Timing delays between a positively charged particle in coincidence with an electron are shown for each combination of the 16 TOFs in the left sector (vertical) and the 16 TOFs in the right sector (horizontal). The shaded combinations are forbidden by elastic kinematics. The combination of left #15 and right #1 is shown in the inset. The blue curve shows all the events, protons (peak at 10 ns and deuterons (peak at 30 ns). The purple curve shows the events after WC kinematics cuts which are discussed in Sec. 4.2.2. The proton peak at 10 ns is reduced by a factor of 2.5 in its peak value, while the deuteron peak at 30 ns is almost intact. The red curve is the events after the timing cuts marked by the green lines. The red curve overlaps with the purple in the second timing peak.

a deuteron timing peak is $\sim$ 1.5 ns, attributed to the dispersion in momentum and path length due to the extensions of the target and TOF paddles, and the intrinsic timing resolution of the two TOFs involved (0.15 ns each).

The azimuthal angular resolution reconstructed from TOFs only is $\delta\phi_{TOF} \sim$ 1-2°, where $\phi_{TOF} = \tan^{-1}\left(\frac{y}{X}\right)$ is calculated from the vertical position y where the particle hit the TOF paddle, based on the timing difference between the top and bottom PMTs (Eq. 3.16), and X is the distance from the beam line to the paddle, which is about 150 cm for the forward angle paddles and 250 cm from the backward ones. X is known to within a few mm from the geometric survey of the detector frame. The azimuthal angular resolution is dominated by the $\pm$3 cm intrinsic position resolution of the TOFs (Sec. 3.3.2) [2]. ϕ_{TOF} was used to construct a set of TOF coplanarity cuts as shown in Fig. 4-3. 5-σ cuts determined from a fit to Gaussian are used. Both the fit and the cuts are shown in Fig. 4-3.

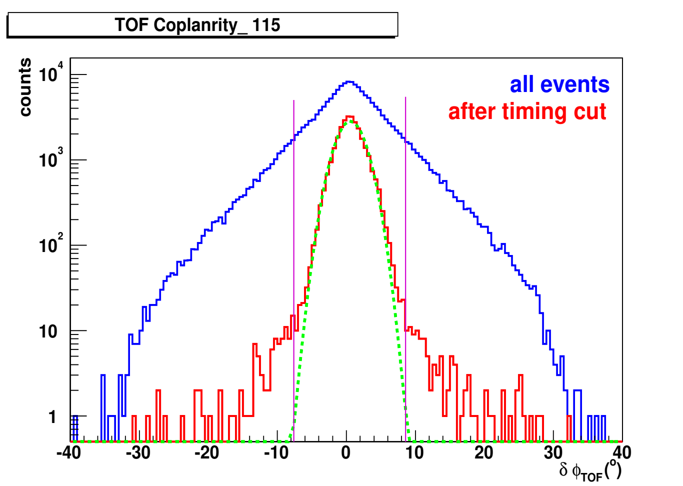

Figure 4-3: TOF coplanarity cuts in combination left #1 and right #15. $\delta\phi_{TOF} = \phi_{TOF}^{right} - \phi_{TOF}^{left} - 180°$. The distribution of all events is shown in blue, the event distribution after the timing cut is shown in red, and is fit to a normal distribution (green dashed curve). The standard deviation is $\sigma = 1.5°$. 5-σ cuts are marked by the purple lines.

The energy deposit of the deuterons in the scintillators is also used for PID. In the three paddles at the most backward angles, deuterons impact with very low

[2]Close to $\phi_{TOF} \sim 0$, $\delta\phi_{TOF} \sim \frac{\delta y}{X} \approx 0.03$ rad, which is about 1°, at larger ϕ_{TOF} the error is larger.

energy and are stopped in the plastic scintillator. Therefore the energy deposits are not separated from those by protons. Both protons and deuterons penetrate the paddles covering higher Q^2. The energy deposits are then proportional to $1/\beta$ and well separated. Fig. 4-4 illustrates both situations and the ADC cut used is shown with the purple curve.

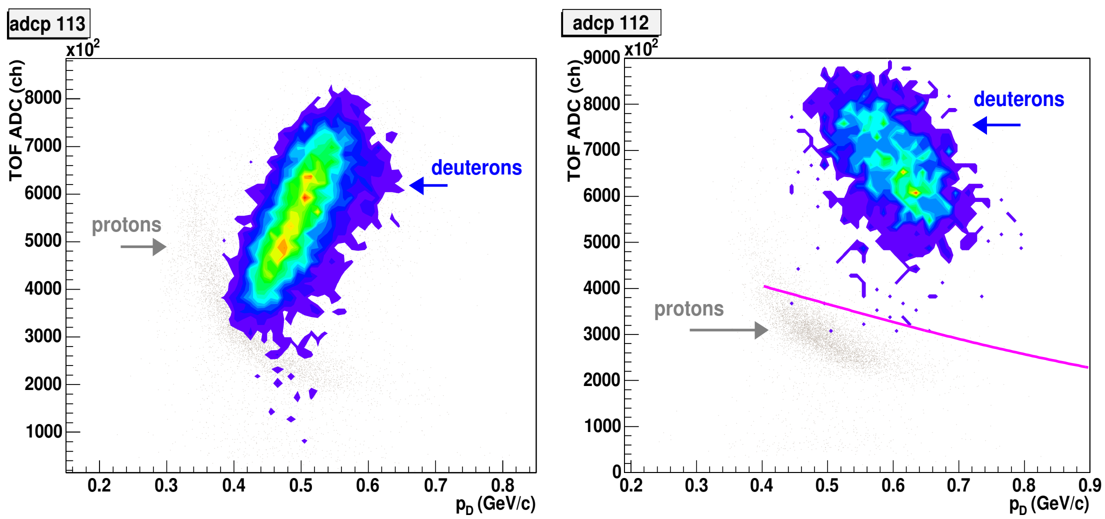

Figure 4-4: TOF ADC cuts for proton deuteron differentiation. The vertical axis in the product of the ADC values from both the top and bottom PMTs. On the left, the ADC in left TOF #13 is plotted against reconstructed particle momentum. Deuterons are stopped in this TOF resulting in low ADC values which are not separable from proton ADCs, which makes ADC based PID between protons and deuterons impossible. On the right, ADC vs. momentum in left TOF #12 is shown. Both deuterons and protons penetrate the TOF. Deuterons experience greater energy loss due to their lower speed. The purple curve shows the cut used. Particles with ADC values below the purple curve are determined to be protons, not deuterons.

4.2.2 Elastic WC Cuts

A set of fiducial cuts were developed to delimit the geometric "trust region" in the drift chambers. The regions close to the edges of wire chambers have large possibilities for reconstruction errors. Such regions include, for instance at large azimuthal angles ($|\phi| \gtrsim 15°$ in the left and $|\phi - 180°| \gtrsim 15°$ in the right), and at very forward or backward polar angles. The polar scattering angles are required to be within the interval $24° < \theta < 76°$. The events are then binned into slices in θ and the ϕ

distribution within each bin is fit to a trapezoidal shape. The full width at half the plateau height is taken as the trusted region in ϕ for the corresponding θ. The ϕ boundaries of the trusted regions are fit to 2^{nd} order polynomials in θ to facilitate the application of these cuts. Fig. 4-5 illustrates the acceptance cuts.

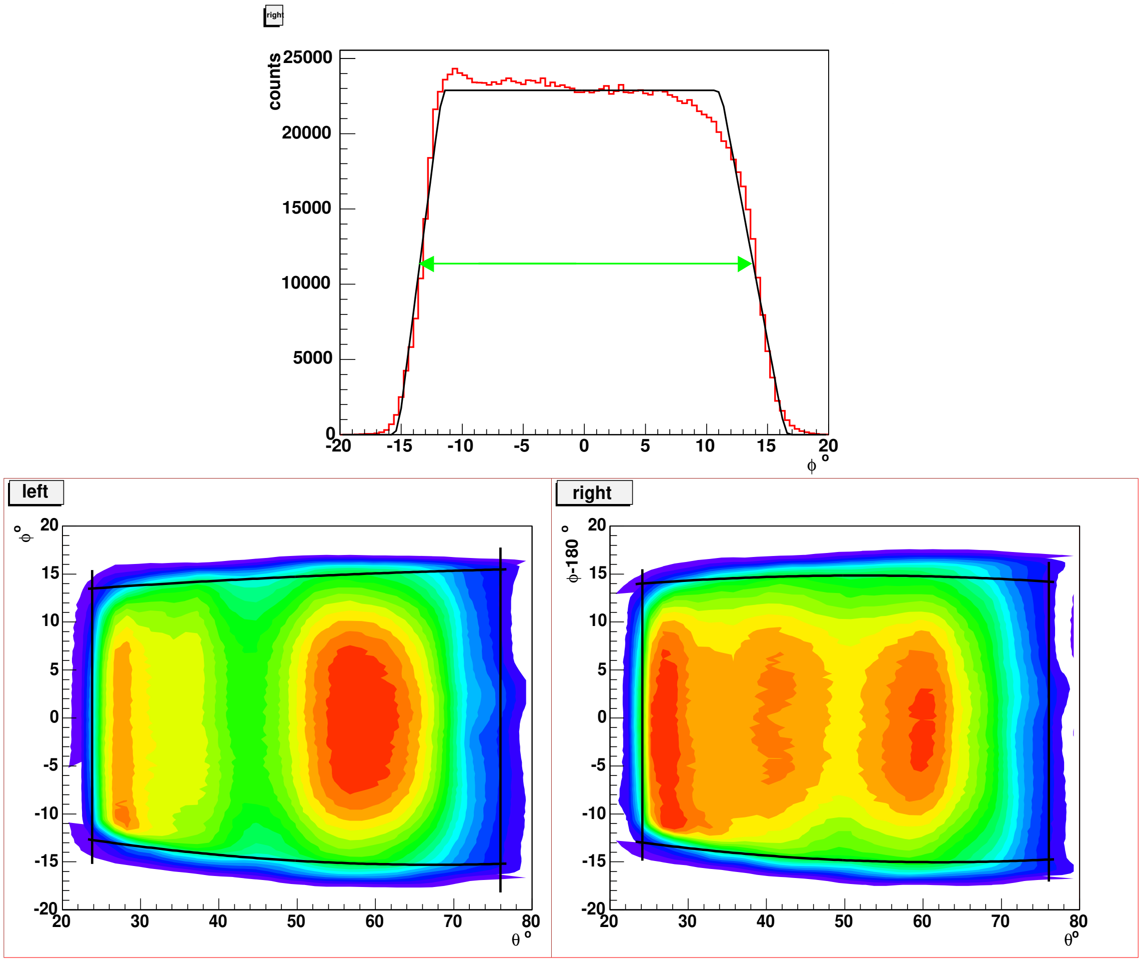

Figure 4-5: The geometric acceptance of BLAST detectors. On the top, the ϕ distribution in a θ slice is fit to a trapezoid shape, the full width at half the plateau height is taken as the trust region. On the bottom, the boundaries of ϕ trust regions are fit to quadratic polynomials in θ for left and right sectors, and are shown by the dark curves.

For the coincident elastic channel, the BLAST drift chambers provide 4 tracking parameters (p,θ,ϕ,z) for both the electron and deuteron. Elastic kinematics can be determined from only three coordinates, for example (θ_e, ϕ_e, z_e), while the others (p_e, p_d, θ_d, ϕ_d and z_d) are redundant. In particular, with ideal reconstruction, $z_d = z_e$, $\phi_d = \phi_e \pm 180°$ and p_e, p_d and θ_d are functions of θ_e. The electro-disintegration channel, on the other hand, does not have such over determined kinematics due to the Fermi motion of the nucleons inside the deuteron. The drift chamber tracking parameters thus form a very powerful set of kinematic cuts that separate the ed-elastic events and the $D(e, e'p)$ events from the electro-disintegration of the deuteron.

The tracking resolution is observed to have a strong dependence on polar scattering angle, and the resolution is considerably worse at very forward angles where tracks impact the drift chamber cells at large angles (Sec. 3.3.5). The kinematic cuts are therefore calibrated as functions of electron scattering angle θ_e. For example, the θ_e acceptance is binned into slices of 1° in width. The difference $\delta p_e(\theta_e) = p_e - p_e(\theta_e)$, where p_e is the measured electron cementum and $p_e(\theta_e)$ is the electron momentum calculated from the measured electron scattering angle, is histogramed for each bin and fit to a normal distribution with mean μ_{p_e} and standard deviation σ_{p_e}, both of which are in turn fit to 2^{nd} order polynomials in θ_e. The reconstructed p_e values are corrected with $\mu_{p_e}(\theta_e)$ to remove the slight systematic deviations and symmetric 3-$\sigma_{p_e}(\theta_e)$ cuts are then applied around zero. At high Q^2 where statistics are insufficient for reliable estimation of σ, cuts with constant width are used.

The reconstruction algorithm does not correct for any energy loss by the particles in the detector media. In contrast to electrons and protons, the energy loss of deuterons causes significant systematic errors in tracking [3]. Energy loss of deuterons was simulated in GEANT, the difference between the reconstructed deuteron momentum and the true value was parameterized into a 2^{nd} order polynomial of θ_e which was used to up-shift the measured deuteron momentum before any further corrections and cuts were applied. At high Q^2, all the quadratic polynomials are connected continuously to a constant function to avoid numerical instabilities. Fig. 4-6 shows the resolutions in θ_d, p_e, p_d, ϕ and z. The centroid of the distributions and the kinematics cuts are also shown. The green curves depict the 3-σ boundary of the histograms, the

[3] GEANT simulation showed that maximum systematic error in proton momentum due to uncorrected energy loss is 3-4 MeV, while this error could be as large as 20 MeV for deuterons. Deuteron momentum reconstruction is also more suseptible to multiple scattering with the atoms in the detector media, therefore has lower resolution as well. However, reconstructed deuteron momentum is only used in event selection, therefore the larger systematic error and poorer resolution are not critical.

black curves are quadratic fits to those boundaries and the means. The low statistics at large θ_e preclude reliable fits of the mean μ and standard deviation σ. The purple curves in the p_d figures are the parameterized energy loss curves obtained from GEANT simulation. It must be stressed that the kinematics corrections were only used to simplify the event selection process and had no effect on the Q^2 determination, which depends solely on the electron scattering angle.

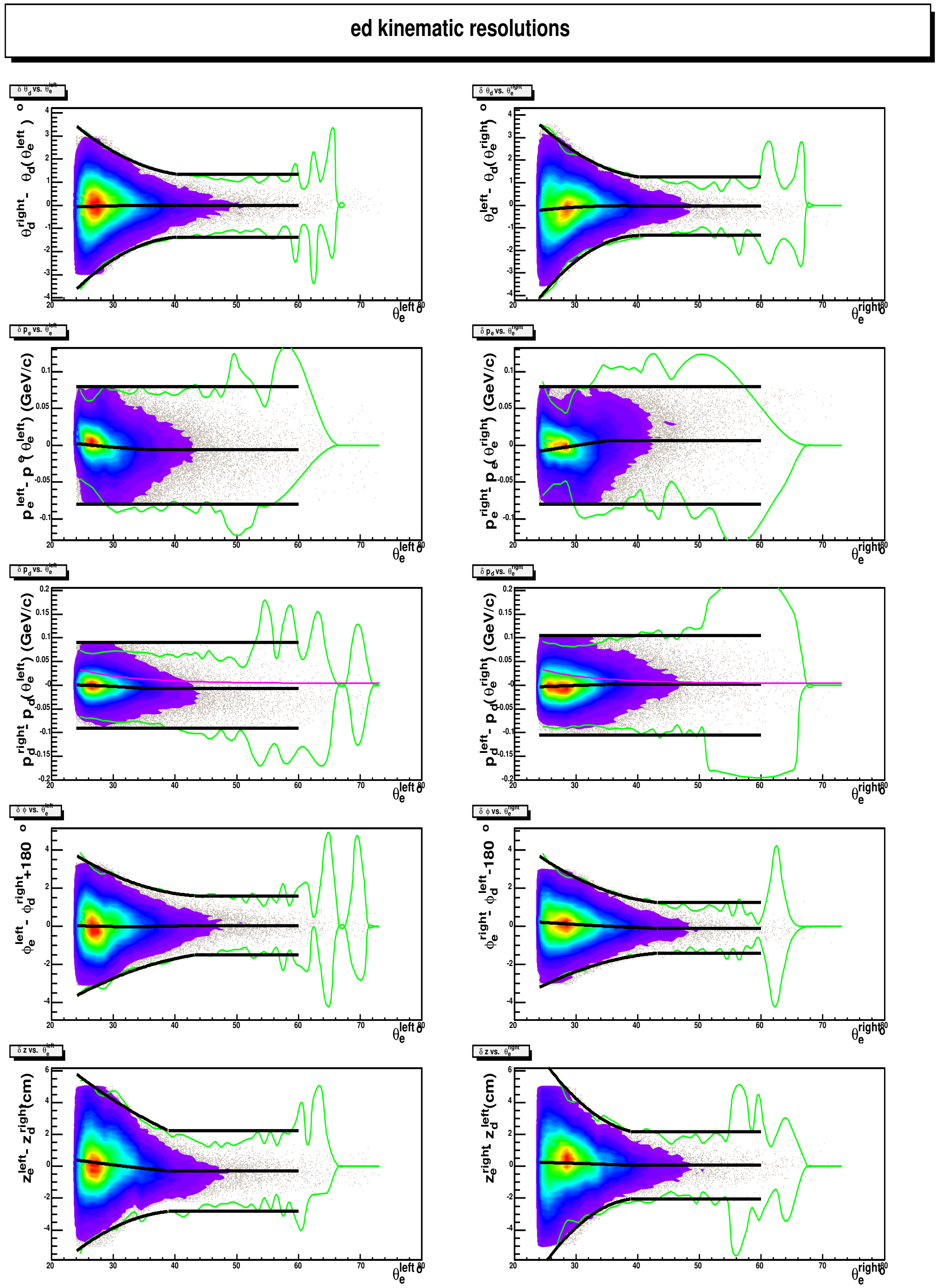

Figure 4-6: Distribution of kinematic variables compared to the calculated values from θ_e. The left (right) panels correspond to events with the electron scattering into the left (right) sector. From top to bottom, $\theta_d - \theta_d(\theta_e)$, $p_e - p_e(\theta_e)$, $p_d - p_d(\theta_e)$, $\phi_e - \phi_d \pm 180$ and $z_e - z_d$ are drawn. See text for the meaning of the curves.

4.2.3 Backgrounds and Yields

The background in the elastic ($D(e, e'd)$) sample comes from two major sources: proton or deuteron knockout from the target cell wall ($X(e, e'p)$ and $X(e, e'd)$), and $D(e, e'p)$ events, from the electro-disintegration of deuteron, not rejected by the cuts.

Empty target runs are taken during ABS down times to study cell wall backgrounds. 144 kC of empty target data were analyzed and the mis-identified ed-elastic rate is 0.00024 /C. This background includes $X(e, e'p)$ as well as $X(e, e'd)$ from the cell wall. Under the presence of the target gas, the collision of beam electrons with the target gas particles causes the electron beam to broaden slightly, thus increase the possibility of the beam halo striking the target cell wall. 342 kC of hydrogen target data were also analyzed [4]. The mis-identified ed-elastic rate is 0.00039 /C. The background rate with gas in target was indeed higher than with an empty target cell. This background estimation includes $X(e, e'p)$ and $X(e, e'd)$ from the cell wall, elastic $H(e, e'p)$ from the hydrogen target gas not rejected by the cuts, as well as the actual elastic scattering from the deuterium contamination in the hydrogen target gas [5]. Both background rates are lower than 0.1% of the ed-elastic rate obtained with the deuterium target. As a result, no background subtraction was necessary.

The electro-disintegration of deuterium produces large numbers of protons. With the most probable Fermi momentum of the proton inside the deuteron about 50 MeV, the knocked-out protons are smeared into the ed-elastic kinematic cuts. The signal to noise ratio in timing and kinematics are low when used separately, especially at high Q^2. However, the reconstructed mass spectra, combining both kinematic and timing information, serve as a good particle identification. Fig. 4-7 shows the typical mass spectra in the bin 0.465 $(\text{GeV/c})^2 < Q^2 <$ 0.532 $(\text{GeV/c})^2$. Two histograms are shown, one with 6-σ WC kinematic cuts and the other with 3-σ cuts. The 6-σ cuts include many protons from the electro-disintegration channel, which manifest

[4] Almost all the hydrogen runs were taken in between the two deuterium run periods (Oct.-Dec. 2004) with the ABS target.

[5] The abundance of D_2 in natural hydrogen gas is 1.4×10^{-4}. The ABS transition units and sextupole magnets do not focus deuterons when operating for polarized hydrogen target. Therefore the deuterium contamination in the polarized hydrogen target is extremely low.

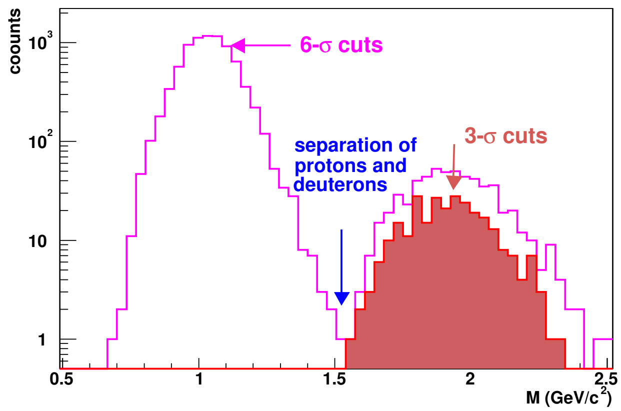

Figure 4-7: The reconstructed mass of the positively charge particles in the bin $0.465(\mathrm{GeV/c})^2 < Q^2 < 0.532(\mathrm{GeV/c})^2$ in coincidence with an electron in the right sector. Events after 6-σ kinematics are shown for reference where the proton mass peak is clearly visible. The tighter 3-σ kinematic cuts properly excludes all the events under the proton peak. The separation between the proton and deuteron mass peak is 5-σ_M.

themselves in the peak about the proton mass of 1 GeV/c^2. On the other hand, the 3-σ cuts cleanly select the deuterons, which concentrate in the peak around deuteron mass of 1.8 GeV/c^2. The mass resolution σ_M is about 100 MeV/c^2 (Sec. 3.3.3 and Fig. 3-22). The proton and deuteron mass peaks are clearly separated at 1.5 GeV/c^2, which is 5-σ_M higher than the proton mass. This gives strong confidence that the misidentified $D(e,e'p)$ contamination is only $\sim 0.1\%$ of the ed-elastic sample [6]. The reconstructed mass spectrum is used as a supplementary PID, where the mass of the positively charged particle is required to be greater than 1.5 GeV/c^2.

The elastic yield was monitored on a daily basis as shown in Fig. 4-8 [7]. The ABS flow intensity was estimated with the UGBS system (Sec. 3.2.3). The yields are

[6] A rough estimate of proton contamination can be given as follows. The observed ratio between $D(e,e'p)$ and elastic ($D(e,e'd)$ yields is 40 for all the Q^2 bins. Since the mass peaks are separated by at least 4-σ, the contamination is thus estimated as: $\frac{n_p}{n_d} = 40 \times N(4,\infty) \sim 0.126\%$ where $N(\zeta,\infty)$ is the probability for a standard normal distribution to lie beyond ζ. The kinematic cuts help to further reduce this contamination

[7] Before April 14th in the 2005 running period, a miscalibration in LDCCT 3.1.2 caused beam current to be overestimated leading to underestimated yields by about 10%. The mistake is yet to be corrected at the time of this writing. Nevertheless, there is no evidence that the the effect on integrated charge was correlated to beam helicity of target polarizations; therefore, the measured asymmetries should not be affected.

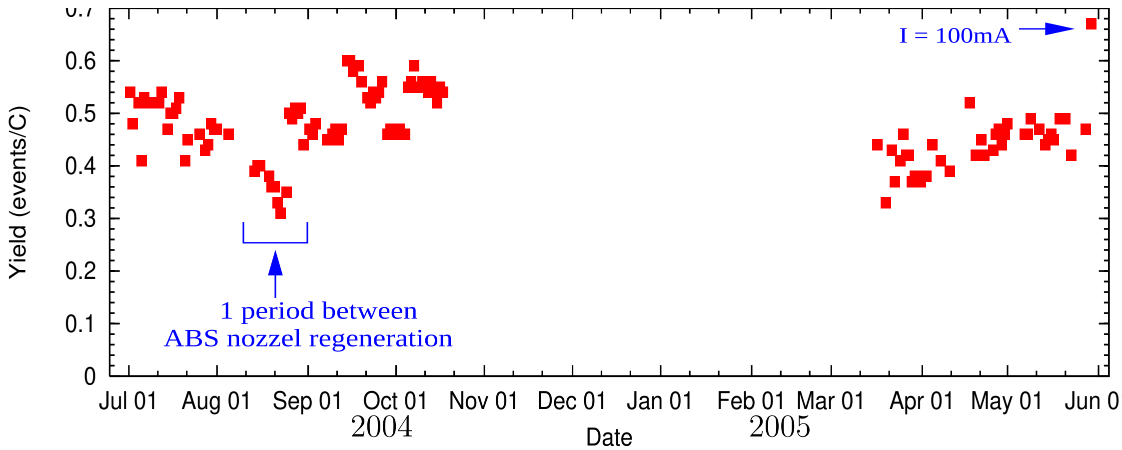

Figure 4-8: Elastic yields observed on a daily basis. Yield in the 2005 run period was 20% lower than in 2004. Some of the periods between ABS nozzle regenerations are visible, where the rate was high immediately after the service and decreases with time. The beam current was 100 mA on the last three days which established a dependence of rate on beam current.

compared to the estimations from Monte Carlo (MC), thereby obtaining the ed-elastic detection efficiency. For the 2004 run period, the efficiency was 58% and in 2005, 50%. The Q^2 dependence of the yield is compared to simulations in Fig. 4-9. The MC is normalized by a factor corresponding to the efficiency. Cell wall backgrounds are also shown in the figure for comparison. The background is properly normalized according to the charge accumulated in the deuterium and empty/hydrogen runs. The background is concentrated at low Q^2 and is lower than 0.1% of the elastic yield.

There is a large inefficiency at low Q^2 when electrons are detected in the right sector, which is clearly visible in the difference between the blue and red curves at $0.1 < Q^2 < 0.2$ (GeV/c)^2 in Fig. 4-9. Albeit inconclusive, it is traced to the drift chambers at large backward angle in the left sector. 2-σ TOF timing and coplanarity cuts are used to establish a reasonably clean ed-elastic trigger sample without resorting to the drift chambers. The drift chamber efficiency is then determined by the fraction of events with tracks reconstructed. Fig. 4-10 illustrates the findings. The left plot shows that the region close to the backward edge of the left chambers has considerably lower efficiency, where only $\sim$ 82% of the triggers selected by the

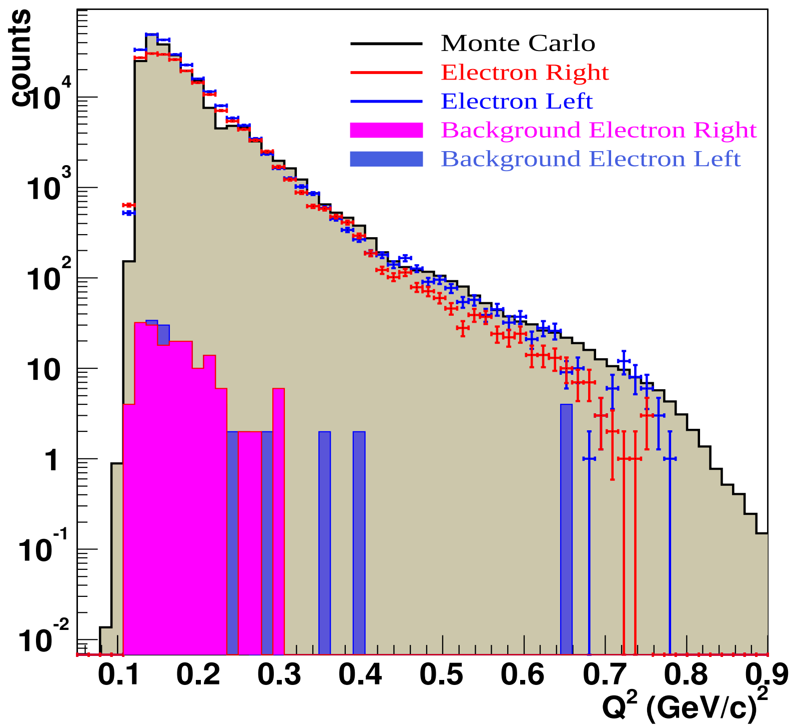

Figure 4-9: Elastic yield as a function of Q^2 compared to Monte Carlo simulation. The cell wall backgrounds extracted from empty and hydrogen target runs are also shown. The Monte Carlo is normalized to match the total counts in data and the scaling factor is used to estimate the overall detection efficiency.

TOF cuts have a deuteron trajectory reconstructed. Convoluted with the tracking efficiency at the right forward angle ($\sim 92\%$), the coincidence efficiency of the left-15 and right-0 combination is only 75% as shown in Fig. 4-10 [8]. The study also established that the poor robustness in tracking under kinematic cuts is the main cause of the low elastic detection efficiency. Almost 90% of the triggers selected by the TOF cuts reconstruct to coincidence events in the drift chambers. Yet many of the events did not survive the kinematic restrictions, leading to the low final ed-elastic event detection efficiency (58% for 2004 and 50% for 2005). This finding is consistent with elastic electron proton scattering [83] (Sec. 3.3.7). This inefficiency results in loss of statistics but has no other adverse impact on the asymmetry measurements.

[8] The drift chamber efficiency study using elastic events from hydrogen target (Sec. 3.3.7) failed to reveal the inefficiency in this very backward region in the chamber since very few protons recoil elastically into that region.

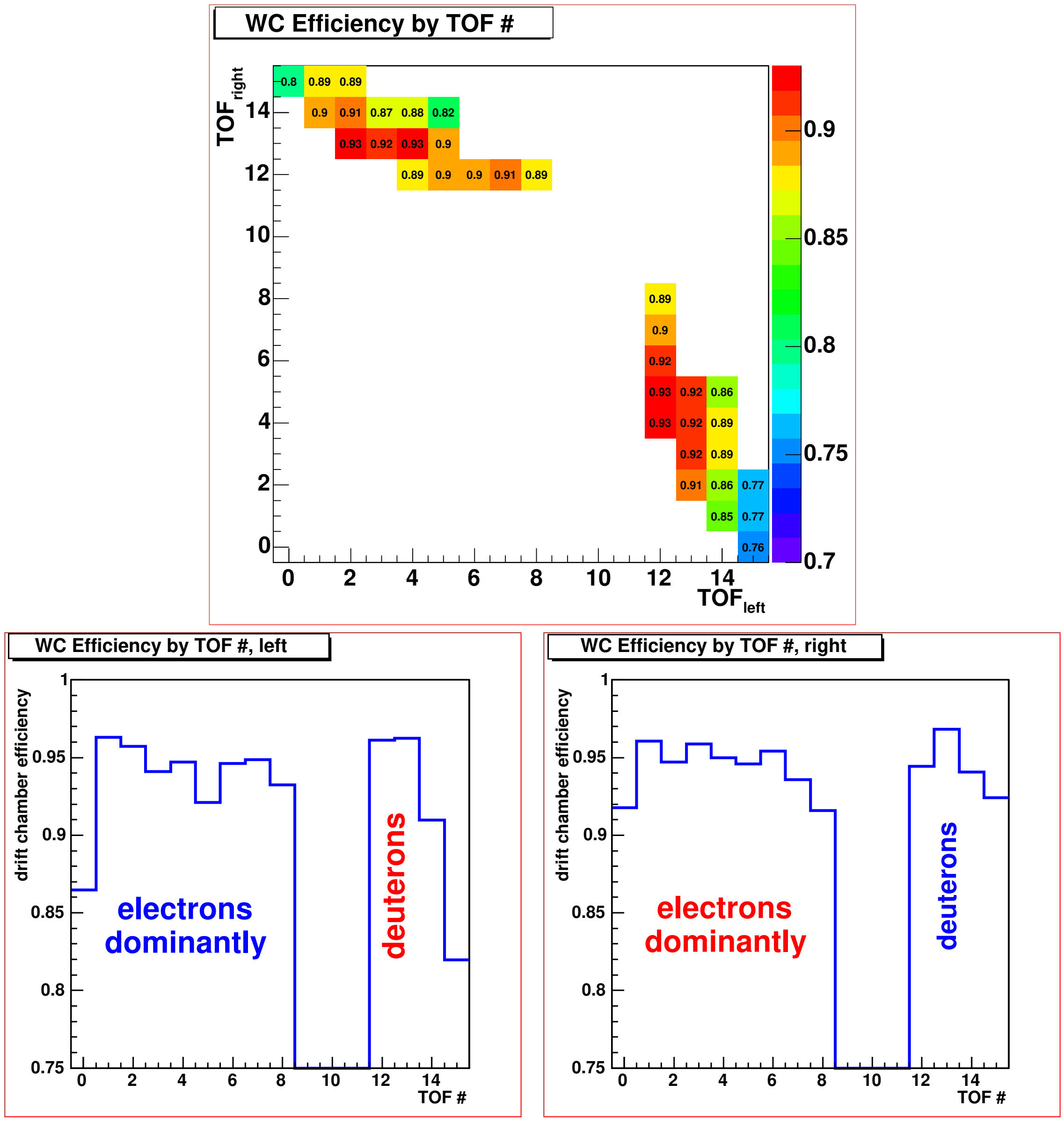

Figure 4-10: The cause of missing statistics at low Q^2 when electrons scatter into the right sector is suspected to be the low drift chamber efficiency in the left sector backward region. Define N_{TOF} to be the number of events selected by the 2-σ TOF timing and coplanarity cuts, $N_{coinc\pm}$ represents the number of events with one track reconstructed in each sector with opposite charges and N_{trk} is the number of events with at least one track found in either sector. On the top the ratio $\frac{N_{coinc\pm}}{N_{TOF}}$ is shown. The acceptance covered by left TOF 15 shows considerably lower efficiency. This results in the low deuteron detection efficiency. On the bottom the ratio $\frac{N_{trk}}{N_{TOF}}$ is shown. Without requiring a coincidence in left and right drift chambers, the inefficiencies in the bottom figures are further separated, while the top figure illustrates the convolution across the two sectors. Again, the edge efficiency of the left drift chambers is considerably lower.

4.3 Asymmetry

4.3.1 Q^2 Determination

Q^2 is determined from the electron scattering angle θ_e alone. In principle, in the coincident elastic channel, it can also be determined from three other independent kinematic variables reconstructed from drift chamber hits: p_e, p_d and θ_d. Deuteron reconstruction suffered systematic errors due to edge effects in the drift chambers, strong multiple scattering and energy loss. Moreover, θ_e appears to have better accuracy and resolution than p_e. The advantage in resolution and accuracy in θ_e against p_e is also observed in the elastic hydrogen reaction [83] and other channels from the deuterium target. The entire Q^2 acceptance is divided into 11 bins. The average Q^2 value in each bin is associated with the measured asymmetries $A(Q^2)$ [9].

4.3.2 Experimental Asymmetry

The deuterium experiment had six combinations of beam and target polarizations. The beam helicity $h = \pm$ was flipped every fill which typically lasted 10-15 minutes. The target polarization switched randomly among three possible vector-tensor (P_z-P_{zz}) states: $(+,+)$, $(-,+)$ and $(0,-2)$, with 5 minutes residence time between switches. Hence the six beam-target spin states can be denoted, with (h, P_z, P_{zz}) triplets, as: $(+,+,+)$, $(+,-,+)$, $(+,0,-2)$, $(-,+,+)$, $(-,-,+)$, and $(-,0,-2)$. The following definition is used to extract the experimental asymmetries [10],

$$A_{exp} = \sqrt{2}\frac{Y^+ - Y^-}{P_{zz}^+ Y^- - P_{zz}^- Y^+}, \tag{4.1}$$

where $Y^\pm$ are the counts in tensor $\pm$ states respectively normalized by the corresponding accumulated charges, and $P_{zz}^\pm$ is the polarization in the tensor $\pm$ states. As

[9] It is well known that: $\langle Y(X)\rangle = Y(\langle X\rangle) + \frac{1}{2}Y''(\langle X\rangle)\Delta X^2$, where $\langle . \rangle$ stands for the mean value operation, Y'' is the 2^{nd} derivative of Y with respect to X, and $\Delta X^2 = \left\langle (X - \langle X\rangle)^2 \right\rangle = \left\langle X^2 \right\rangle - \left\langle X \right\rangle^2$ is the Mean Square Error of X. Therefore, the error resulting from associating it with the average Q^2 value is given by $\frac{1}{2}Y''(\langle X\rangle)\Delta X^2$ which is less than 0.5%.

[10] Although the tensor + states are simultaneously vector polarized, it is a simple algebraic exercise to show that the beam-vector asymmetries cancel out when charge is evenly distributed among the

discussed in Sec. 4.2.3, background contributions from both the cell wall ($X(e,e'p)$ and $X(e,e'd)$) and electro-disintegration channel are less than 0.1% of the elastic yield; hence, no background correction was deemed necessary. Since the target tensor polarization is measured from the elastic reaction, the raw asymmetry is first measured based on the assumption that all states are equally polarized: $P_{zz}^{-} = -2P_{zz}^{+} = -2\overline{P}_{zz}$,

$$A_{raw} = \sqrt{2}\frac{Y^{+} - Y^{-}}{Y^{-} + 2Y^{+}} = \overline{P}_{zz} \times A_{exp}. \tag{4.2}$$

The raw asymmetries are tabulated in Tab. 4.2 and shown in Fig. 4-11 [11].

4.3.3 Target Polarization and Spin Angle

The target tensor polarization P_{zz} is measured by normalizing A_{raw} at $Q^2 < 0.18$ (GeV/c)^2 (the first two of 11 bins) to model predictions. The extracted P_{zz} value therefore depends on the choice of the theoretical model. Abbott's parameterization III [61] of

---

four possible beam-vector states. The proof goes as follows:

$$Y^{+} = \frac{\sigma_{(+,+,+)}q_{(+,+,+)} + \sigma_{(+,-,+)}q_{(+,-,+)} + \sigma_{(-,+,+)}q_{(-,+,+)} + \sigma_{(-,-,+)}q_{(-,-,+)}}{q_{(+,+,+)} + q_{(+,-,+)} + q_{(-,+,+)} + q_{(-,-,+)}},$$

with $$q = \frac{q_{(+,+,+)} + q_{(+,-,+)} + q_{(-,+,+)} + q_{(-,-,+)}}{4}, \quad \text{and} \delta q(h, P_z, P_{zz}) = q(h, P_z, P_{zz}) - q,$$

$$\begin{aligned} Y^{+} = \frac{\sigma_0}{4q} \big[& (1 + A_{(+,+,+)})(q + \delta q_{(+,+,+)}) + (1 + A_{(+,1,+)})(q + \delta q_{(+,-,+)}) \\ & + (1 + A_{(-,+,+)})(q + \delta q_{(-,+,+)}) + (1 + A_{(-,-,+)})(q + \delta q_{(-,-,+)}) \big], \end{aligned}$$

where
$$A_{(+,+,+)} = +hP_zA_{ed}^{V} + P_{zz}^{+}A_d^{T} \qquad A_{(+,-,+)} = -hP_zA_{ed}^{V} + P_{zz}^{+}A_d^{T}$$
$$A_{(-,+,+)} = -hP_zA_{ed}^{V} + P_{zz}^{+}A_d^{T} \qquad A_{(-,-,+)} = +hP_zA_{ed}^{V} + P_{zz}^{+}A_d^{T}$$

$$Y^{+} = \sigma_0 \left(1 + P_{zz}^{+}A_d^{T} + hP_zA_{ed}^{V}\frac{q_{(+,+,+)} - q_{(+,-,+)} - q_{(-,+,+)} + q_{(-,-,+)}}{4q} \right)$$

$$Y^{-} = \frac{\sigma_{(+,0,-2)}q_{(+,0,-2)} + \sigma_{(-,0,-2)}q_{(-,0,-2)}}{q_{(+,0,-2)} + q_{(-,0,-2)}} = \sigma_0 \left(1 + P_{zz}^{-}A^{T}\right)$$

therefore

$$A_{exp} = A^{T}\left[1 + \frac{hP_zA_{ed}^{V}}{A_d^{T}}\frac{1 + P_{zz}^{-}A_d^{T}}{P_{zz}^{+} - P_{zz}^{-}}\frac{q_{(+,+,+)} - q_{(+,-,+)} - q_{(-,+,+)} + q_{(-,-,+)}}{4q}\right].$$

Typically $\frac{hP_zA_{ed}^{V}}{A_d^{T}} \sim 0.1$, $\frac{1 + P_{zz}^{-}A_d^{T}}{P_{zz}^{+} - P_{zz}^{-}} \sim 0.1$, and $\frac{q_{(+,+,+)} - q_{(+,-,+)} - q_{(-,+,+)} + q_{(-,-,+)}}{4q} \sim 0.01$, so the error introduced is on the order of 0.01% of A_{exp} itself. The definition used avoids low-count statistics by combining counts in different states.

[11] The last bin in the perpendicular kinematics in 2004 data set had less than 10 counts. The statistical uncertainty for this low yield bin is adjusted according to the Neyman construction of 31.7% confidence interval for Poisson counting processes [90].

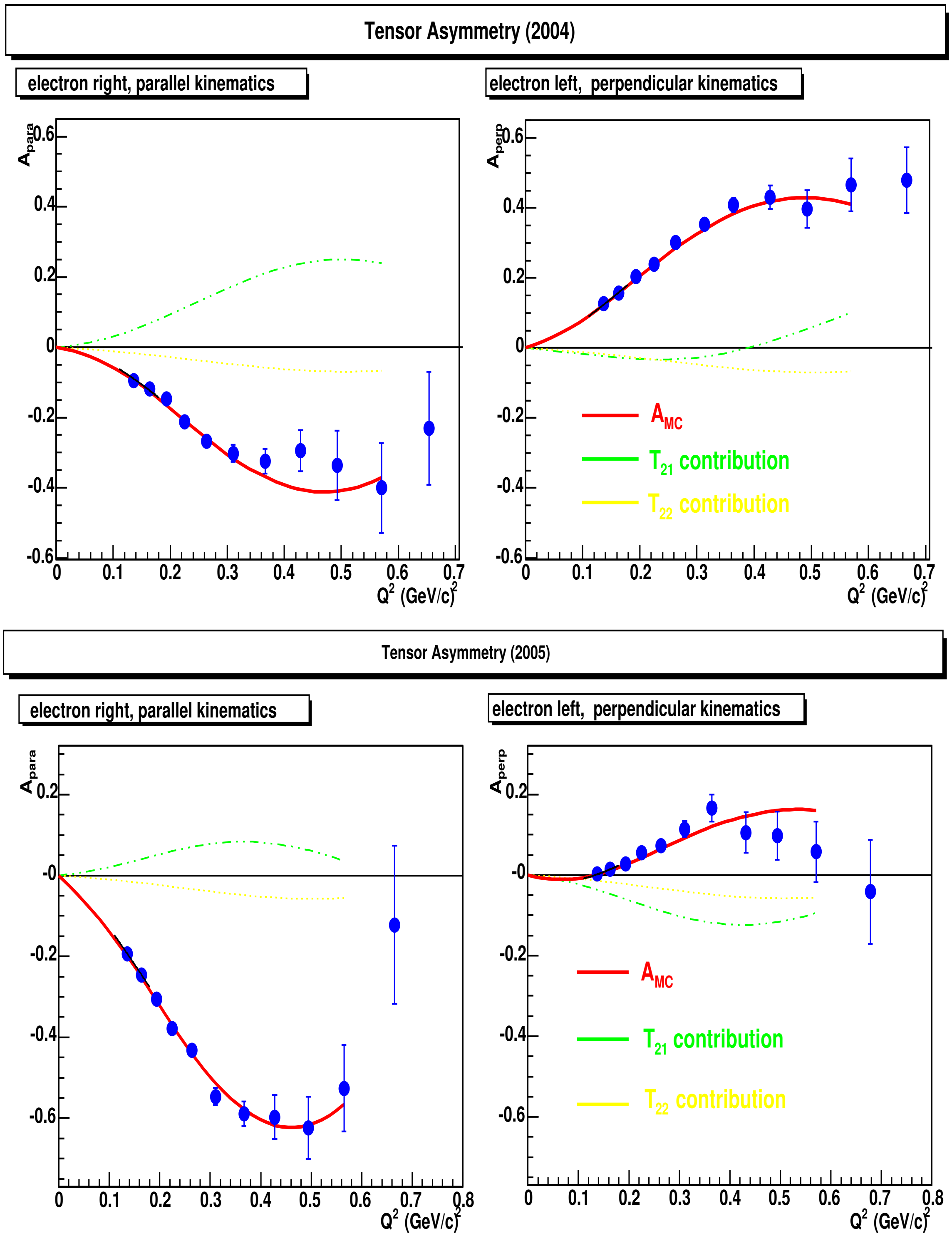

Figure 4-11: Asymmetries A_{raw} observed for 2004 and 2005 data sets. The nominal spin orientations are 32° and 47° respectively. The Monte Carlo fits to data at $Q^2 < 0.18$ (GeV/c)^2 are shown. The T_{21} and T_{22} contributions to the asymmetries are also show to illustrate the sensitivities.

Year	Charge	$q_{++ +}$ (kC)	q_{+-+} (kC)	q_{+0-2} (kC)	q_{-++} (kC)	q_{--+} (kC)	q_{-0-2} (kC)
2004	$\int I_{live} dt$	60.93	60.87	60.78	61.99	61.23	61.49
2005	$\int I_{live} dt$	94.62	93.43	93.34	91.77	93.41	94.77

2004 Nominal Spin Angle $\theta_d = 32°$ beam left

Perpendicular Kinematics (e' left)						Parallel Kinematics (e' right)					
Q^2 (GeV/c)^2	δQ^2 (GeV/c)^2	N$^+$	N$^-$	$A^{\perp}_{raw}$	$\delta A^{\perp}_{raw}$	Q^2 (GeV/c)^2	δQ^2 (GeV/c)^2	N$^+$	N$^-$	$A^{\parallel}_{raw}$	$\delta A^{\parallel}_{raw}$
0.1371	3.9×10^{-5}	28926	10874	0.1267	0.0047	0.1358	4.9×10^{-5}	17030	10348	-0.0957	0.0062
0.1632	4.6×10^{-5}	25543	8935	0.1566	0.0050	0.1642	5.2×10^{-5}	16298	10387	-0.1196	0.0063
0.1934	6.4×10^{-5}	13746	4259	0.2046	0.0067	0.1933	6.8×10^{-5}	9514	6399	-0.1469	0.0082
0.2252	1.0×10^{-4}	7600	2151	0.2384	0.0089	0.2250	1.1×10^{-4}	4866	3718	-0.213	0.011
0.2631	1.7×10^{-4}	4475	1055	0.302	0.011	0.2641	1.8×10^{-4}	2767	2348	-0.268	0.015
0.3131	3.1×10^{-4}	1830	366	0.353	0.017	0.3104	3.3×10^{-4}	1010	915	-0.302	0.024
0.3640	4.6×10^{-4}	1120	183	0.409	0.020	0.3664	5.6×10^{-4}	466	442	-0.327	0.035
0.4281	8.9×10^{-4}	407	63	0.422	0.033	0.4285	0.0011	168	150	-0.295	0.059
0.4926	0.0014	166	28	0.400	0.054	0.4926	0.0016	59	57	-0.34	0.10
0.5693	0.0029	78	10	0.466	0.072	0.5705	0.0031	33	36	-0.40	0.13
0.6668	0.0061	50	6	0.479	0.088	0.6538	0.0047	24	19	-0.23	0.16

2005 Nominal Spin Angle $\theta_d = 47°$ beam left

Perpendicular Kinematics (e' left)						Parallel Kinematics (e' right)					
Q^2 (GeV/c)^2	δQ^2 (GeV/c)^2	N$^+$	N$^-$	$A^{\perp}_{raw}$	$\delta A^{\perp}_{raw}$	Q^2 (GeV/c)^2	δQ^2 (GeV/c)^2	N$^+$	N$^-$	$A^{\parallel}_{raw}$	$\delta A^{\parallel}_{raw}$
0.1374	3.6×10^{-5}	31296	15709	0.0019	0.0046	0.1361	4.5×10^{-5}	18564	13806	-0.1935	0.0058
0.1632	4.1×10^{-5}	29288	14320	0.0142	0.0048	0.1643	4.7×10^{-5}	17924	14752	-0.2464	0.0058
0.1932	5.8×10^{-5}	14917	7079	0.0281	0.0067	0.1935	6.2×10^{-5}	10090	9299	-0.3061	0.0076
0.2248	9.3×10^{-5}	7781	3484	0.0546	0.0092	0.2249	9.8×10^{-5}	5154	5444	-0.378	0.010
0.2638	1.6×10^{-4}	4529	1949	0.072	0.012	0.2642	1.6×10^{-4}	3008	3523	-0.433	0.013
0.3107	2.9×10^{-4}	1677	656	0.114	0.020	0.3103	2.8×10^{-4}	989	1440	-0.546	0.021
0.3644	6.2×10^{-4}	560	193	0.167	0.034	0.3667	4.8×10^{-4}	450	713	-0.589	0.030
0.4319	9.5×10^{-4}	258	103	0.105	0.050	0.4276	0.0010	136	219	-0.598	0.055
0.4939	0.0011	182	74	0.097	0.060	0.4942	0.0014	66	112	-0.624	0.077
0.5705	0.0018	117	53	0.058	0.075	0.5647	0.0023	40	56	-0.53	0.11
0.6782	0.0060	40	22	-0.042	0.13	0.6649	0.0066	17	11	-0.12	0.20

Table 4.2: Integrated beam current $q_{(h,P_z,P_{zz})}$ (for beam helicity h and target polarization (P_z, P_{zz})), average Q^2 ((GeV/c)^2), counts $N^{P_{zz}}$, and asymmetries A_{raw} for each Q^2 bin. The error δA_{raw} is statistical only. Q^2 is in units of (GeV/c)^2.

the form factors was used as it is based on world data and lies approximately at the middle of the range covered by various models. A indepth discussion of the systematic caused by this normalization procedure is provided in Sec. 4.6.

Since two asymmetries, $A^{\parallel}_{raw}$ and $A^{\perp}_{raw}$, were observed simultaneously in parallel and perpendicular kinematics respectively, one additional parameter can be determined besides P_{zz}. The elastic asymmetries were therefore used to monitor an important experimental parameter, namely the target spin angle, θ_S, defined as the angle between the target spin quantization axis and the beam line [12].

P_{zz} is extracted as the overall scaling factor that fits the asymmetries in the first two bins to the polynomials representing Monte Carlo asymmetries A_{MC} (Sec. 4.1), or simply put [13],

$$P^{\parallel}_{zz}(\theta_S) = \frac{A^{\parallel}_{raw}}{A^{\parallel}_{MC}(\theta_S)}, \quad \text{and} \quad P^{\perp}_{zz}(\theta_S) = \frac{A^{\perp}_{raw}}{A^{\perp}_{MC}(\theta_S)}. \tag{4.3}$$

The measured average spin angle is the $\overline{\theta}_S$ where $P^{\parallel}_{zz}(\overline{\theta}_S) = P^{\perp}_{zz}(\overline{\theta}_S)$. The uncertainty of $\overline{\theta}_S$ is estimated by the confidence interval whose end points are defined by,

$$\chi = \frac{P^{\parallel}_{zz}(\theta_S) - P^{\perp}_{zz}(\theta_S)}{\sqrt{[\delta P^{\parallel}_{zz}(\theta_S)]^2 + [\delta P^{\perp}_{zz}(\theta_S)]^2}} = \pm 1, \tag{4.4}$$

where $\delta P^{\parallel}_{zz}$ and $\delta P^{\perp}_{zz}$ represent the uncertainties in the measured polarizations.

The extracted value of P_{zz} depends on the spin angle; therefore, the uncertainty in θ_S propagates into the polarizations. However, the spin angle sensitivity largely

[12] It is estimated that the neuron charge form factor, G^n_E, simultaneously measured from $D(e,e'n)$ channel has a sensitivity to spin orientation of 12%/degree.

[13] The actual fit procedure minimizes,

$$\chi^2_{\parallel,\perp} = \left(\frac{A^{\parallel,\perp}_{raw}(Q^2_1) - P^{\parallel,\perp}_{zz}A^{\parallel,\perp}_{MC}(Q^2_1)}{\delta A^{\parallel,\perp}_{raw}(Q^2_1)}\right)^2 + \left(\frac{A^{\parallel,\perp}_{raw}(Q^2_2) - P^{\parallel,\perp}_{zz}A^{\parallel,\perp}_{MC}(Q^2_2)}{\delta A^{\parallel,\perp}_{raw}(Q^2_2)}\right)^2,$$

where $Q^2_{1,2}$ are the Q^2 for the 1^{st} and 2^{nd} bins.

cancels out when the difference $A^{\perp}_{raw} - A^{\parallel}_{raw}$ is used to measure the polarization [14],

$$P^{\perp-\parallel}_{zz} = \frac{A^{\perp}_{raw} - A^{\parallel}_{raw}}{A^{\perp}_{MC}(\overline{\theta}_S) - A^{\parallel}_{MC}(\overline{\theta}_S)}. \tag{4.5}$$

The procedure is illustrated in Fig. 4-12. The tensor polarizations and average spin

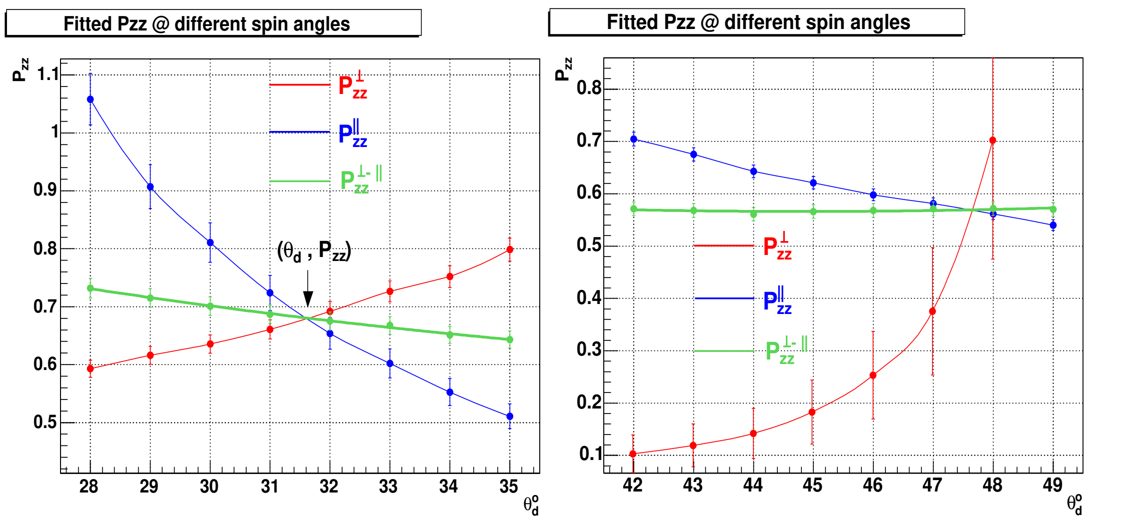

Figure 4-12: The polarization and spin angle measurements for 2004 (left) and 2005 (right) data sets. P_{zz} is extracted in both parallel and perpendicular kinematics for a range of θ_S. Self-consistent measurements of both P_{zz} and θ_S are obtained simultaneously. The P^{diff}_{zz} fit from $A^{\perp-\parallel}_{raw} = A^{\perp}_{raw} - A^{\parallel}_{raw}$ is not sensitive to uncertainties in θ_S. The Monte Carlo asymmetry A_{MC} has opposite sign to the observed A_{raw} in the perpendicular kinematics for θ_S above 49°, resulting in negative P_{zz} which is unphysical due to the definition of target polarization. This provides an additional bound of error by constraining θ_S to be below 49°. The procedure was also applied with vertex cuts selecting subranges along the target cell to measure spin angle and tensor polarization profiles. The spin angle profiles are compared to target field surveys and TOSCA simulations (Sec. 3.2.2).

angles thus determined are, $P_{zz} = 0.683 \pm 0.015$, $\theta_S = 31.72 \pm 0.35$ in 2004 and $P_{zz} = 0.563 \pm 0.013$, $\theta_S = 47.74 \pm 0.42$ in 2005. The uncertainties are statistical only and systematic errors are discussed in detail in Sec. 4.5. The procedure was also applied with vertex cuts selecting subranges along the target cell to measure z-dependence of the spin angle (Fig. 3-9) and the tensor polarization (Fig. 3-10). The spin angle profiles are compared to target field surveys and TOSCA simulations

[14]The average of $P^{\parallel}_{zz}$ and $P^{\perp}_{zz}$ does not have any physical significance as the two are forced to be the same by shifting θ_S.

(Sec. 3.2.2). There are discrepancies between the target field surveys and the spin angle measured with tensor ed-elastic asymmetries, as described in this section. The differences and their significance are discussed in detail in Sec. 4.5.3.

There are two major approximations in the Monte Carlo (MC) asymmetry A_{MC} used in Eqs. 4.3 and 4.5: 1) The MC assumed a constant spin angle, while the actual holding field direction varies within the ± 20 cm range along the target cell; 2) The polynomial fit of A_{MC} may introduce a fit error. Because P_{zz} and θ_S are of great importance to not only ed-elastic analysis but several other channels as well [54, 55], a discussion is devoted to the impact of these approximations in Sec. 4.5.3.

4.4 T_{20} and T_{21}

To extract T_{20} and T_{21}, the asymmetries must be measured at the same Q^2 in the left and right sectors. The raw asymmetries are adjusted to the average Q^2 of the left and right sector according to Monte Carlo simulations,

$$A^{l,r}_{raw}(Q^2) = A^{l,r}_{raw}(Q^2_{l,r})\frac{A^{l,r}_{MC}(Q^2)}{A^{l,r}_{MC}(Q^2_{l,r})}. \tag{4.6}$$

Here $Q^2_{l.r}$ are the mean Q^2 in each bin with electron scattered into the left and right sector respectively (The values are tabulated in Tab. 4.2), Q^2 is the average Q^2 in each bin for all the events in both left and right sectors, $A^{l,r}_{raw}$ if defined by Eq. 4.2 with the superscript l, r denoting the case where the electron is detected in the left and right sector respectively, and $A^{l,r}_{MC}$ is the asymmetry extracted from Monte Carlo simulation. The correction is less than 1% except for the highest Q^2 bin, where it is about 1-2%, which is much smaller than the statistical errors.

A_{raw} is converted to,

$$A_{exp} = \frac{A_{raw}}{P_{zz}}. \tag{4.7}$$

For each bin, A_{exp} can be expressed as combinations of T_{20}, T_{21} and T_{22} modulated by kinematic coefficients:

$$\begin{aligned}
A_{exp} &= \left\langle d^2_{00}(\theta^*)T_{20} + 2d^2_{10}(\theta^*)\cos\phi^* T_{21} + 2d^2_{20}(\theta^*)\cos2\phi^* T_{22}\right\rangle \\
&\approx \left\langle d^2_{00}(\theta^*)\right\rangle \langle T_{20}\rangle + 2\left\langle d^2_{10}(\theta^*)\cos\phi^*\right\rangle \langle T_{21}\rangle + 2\left\langle d^2_{20}(\theta^*)\cos2\phi^*\right\rangle \langle T_{22}\rangle \\
&= c_{20}T_{20} + c_{21}T_{21} + c_{22}T_{22}, \qquad (4.8)
\end{aligned}$$

where $d^2_{00}(\theta^*) = \frac{3}{2}\cos^2\theta^* - \frac{1}{2}$, $d^2_{10}(\theta^*) = -\frac{\sqrt{3}}{2}\cos\theta^*\sin\theta^*$, and $d^2_{20}(\theta^*) = \frac{3}{8}\sin^2\theta^*$. The averages are separated in the second step [15], and the kinematic coefficients are defined in the third step as $c_{20} = \langle d^2_{00}(\theta^*)\rangle$, $c_{21} = 2\langle d^2_{10}(\theta^*)\cos\phi^*\rangle$ and $c_{22} = 2\langle d^2_{20}(\theta^*)\cos2\phi^*\rangle$. For each Q^2 bin, there are two A_{exp}: $A^{\parallel}_{exp}$ for the parallel and $A^{\perp}_{exp}$ for the perpendicular kinematics.

4.4.1 The Kinematic Coefficients

The values of the kinematic coefficients are calculated for each event, with the direction of the momentum transfer (θ_q, ϕ_q) calculated from (θ_e, ϕ_e), and the spin angle $\theta_S(z)$ in the Lab frame interpolated from the surveyed holding field maps.

It is crucial to recognize that there are discrepancies among the several spin angle surveys at different times, and between the spin angle measured by the tensor ed-elastic asymmetry and any of the surveys. These discrepancies are discussed in detail in Sec. 4.5.3. However, the shape of the spin angle profile, $\theta_S(z)$, obtained from the several surveys are consistent with each other. Therefore, to be self-consistent, the

[15]It can be shown that

$$\begin{aligned}
\langle Y_1(X)Y_2(X)\rangle &= \langle Y_1\rangle\langle Y_2\rangle + \mathrm{Cov}(Y_1, Y_2) \\
&= \langle Y_1\rangle\langle Y_2\rangle + \frac{dY_1}{dX}\frac{dY_2}{dX}\langle dX \cdot dX\rangle \\
&= \langle Y_1\rangle\langle Y_2\rangle + \frac{dY_1}{dX}\frac{dY_2}{dX}\mathrm{Var}(X),
\end{aligned}$$

where $\mathrm{Cov}(Y_1, Y_2)$ is the covariance between the two variables, and $\mathrm{Var}(X)$ is the variance of the variable X. Typically, for low Q^2 bins, $\mathrm{Var}(Q^2) \lesssim 10^{-9}$ (GeV/c)^2 and $|dA/dQ^2| \lesssim 1$. For high Q^2 bins, $\mathrm{Var}(Q^2) \lesssim 10^{-6}$ (GeV/c)^2 and $|dA/dQ^2| \sim 0.1$. Therefore the error introduced is less than 10^{-8} level.

spin angle profile in the ed-elastic analysis is corrected according to,

$$\frac{\tan\left(\theta_S(z)\right)}{\tan\left(\theta_S^{prof}(z)\right)} = \frac{\tan\left(\left\langle\theta_S^{ed}\right\rangle\right)}{\tan\left(\left\langle\theta_S^{prof}\right\rangle\right)}, \tag{4.9}$$

where $\theta_S^{prof}(z)$ is the spin angle at vertex position z determined by the surveyed holding field profile, $\left\langle\theta_S^{ed}\right\rangle$ is the average spin angles obtained from elastic tensor asymmetries, and

$$\left\langle\theta_S^{prof}\right\rangle = \frac{1}{N}\sum_{i=1}^{N}\theta_S(z_i), \tag{4.10}$$

with i running over all the ed-elastic events [16], is the average spin angle profile from the surveys weighted by the ed-elastic z-vertex distribution. The resulted spin angle $\theta_S(z)$ is not sensitive to the choice of survey and the January 2005 survey is used in this work. This survey includes both 32° and 47° nominal configurations. The discrepancy with the spin angle determined by ed-elastic asymmetry is the smallest among all surveyed profiles for both configurations (See Tab. 4.9). The kinematic coefficients are histogramed and the mean values are obtained for each bin. To correct for the difference in the $Q^2_{l,r}$, the coefficients are linearly interpolated between the measured points to the average Q^2. The corrections are less than 1% except for c_{21} and c_{22} at high Q^2 in the 2005 data set, where these coefficients themselves are small in size. For this region, the asymmetry is dominated by $c_{20}T_{20}$ due to the small size of c_{21}, c_{22} and T_{22}. Therefore the corrections to c_{21} and c_{22}, that are slightly larger than 1%, do not affect the final results in any significant manner. Fig. 4-13 shows the distribution of the coefficients for both spin angle orientations in parallel and perpendicular kinematics. The values of average Q^2 and the kinematic coefficients are tabulated in Tab. 4.3.

[16] N is about 100,000 for either 2004 or 2005 data set for the region of $Q < 2$ fm^{-1} which is used in the extraction of P_{zz} and θ_S.

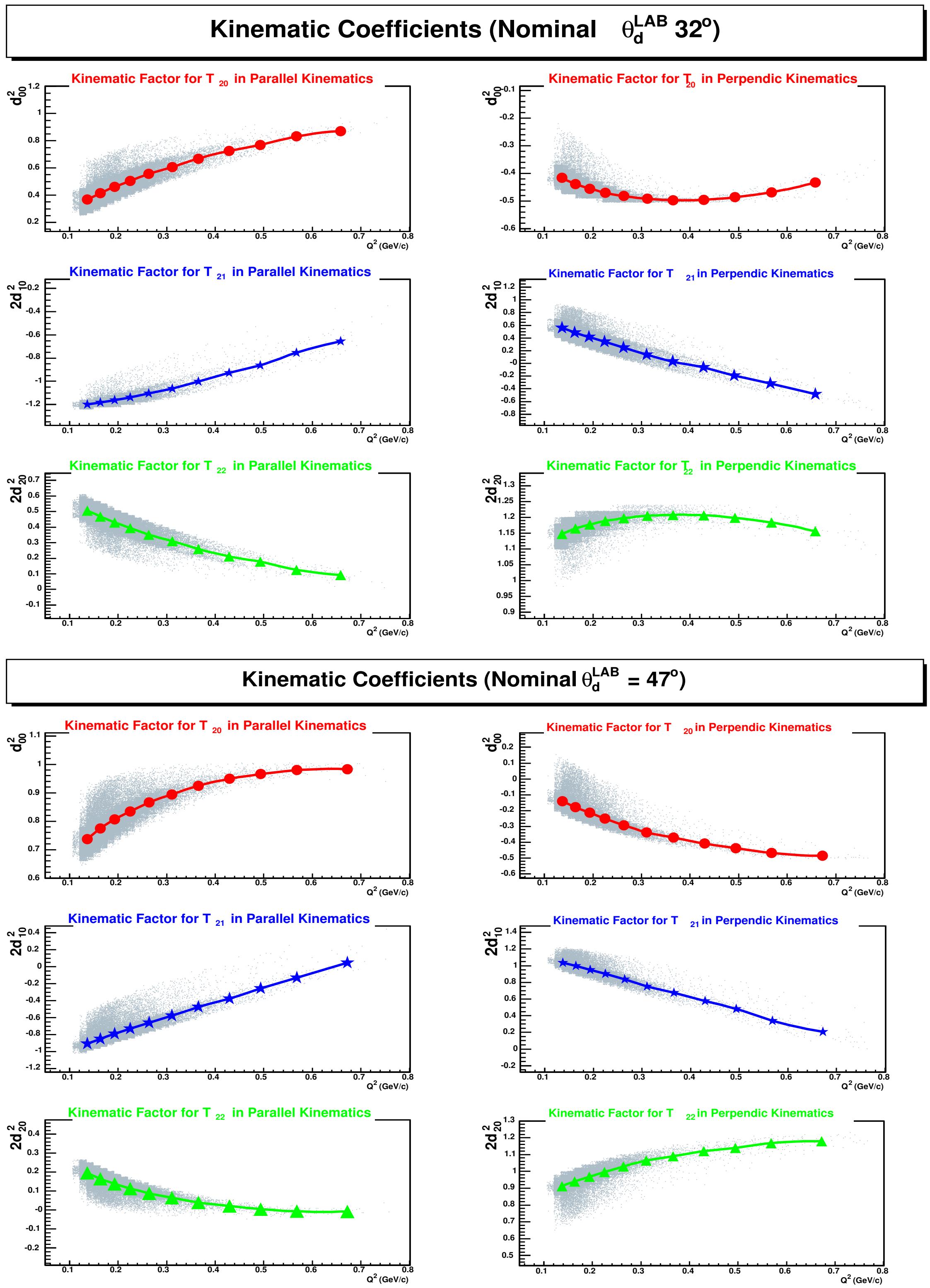

Figure 4-13: The distribution of kinematic coefficients for 2004 (top) and 2005 (bottom) data sets, in parallel (left) and perpendicular (right) kinematics. The distributions are fit to polynomials and the mean values for each in each Q^2 bin is marked. The spread in the distribution is due to the variation in target spin angle along the cell.

2004		Perpendicular Kinematics (e' left)							Parallel Kinematics (e' right)						
Q^2 (GeV/c)^2	θ_q (°)	θ^* (°)	c_{20}	δc_{21} (10^{-4})	c_{21}	δc_{21} (10^{-4})	c_{22}	δc_{22} (10^{-4})	θ^* (°)	d_{20}	δc_{20} (10^{-4})	d_{21}	δc_{21} (10^{-4})	d_{22}	δc_{22} (10^{-4})
0.137	71.68	103.5	-0.417	0.31	0.551	1.1	1.148	0.37	40.4	0.368	0.94	-1.201	0.26	0.507	0.74
0.164	69.90	101.4	-0.438	0.29	0.472	1.3	1.164	0.44	38.6	0.416	0.94	-1.184	0.32	0.467	0.70
0.193	68.08	99.6	-0.456	0.31	0.401	1.7	1.177	0.64	36.7	0.462	1.2	-1.163	0.48	0.429	0.85
0.225	66.28	97.7	-0.470	0.36	0.324	2.5	1.188	0.96	35.0	0.504	1.7	-1.140	0.83	0.395	1.2
0.264	64.23	95.7	-0.482	0.38	0.240	3.8	1.198	1.4	32.9	0.557	2.5	-1.104	1.5	0.351	1.8
0.312	61.83	93.3	-0.492	0.32	0.135	6.8	1.205	2.4	30.7	0.605	4.1	-1.064	3.1	0.312	3.0
0.365	59.35	90.7	-0.497	1.2	0.031	9.3	1.208	3.2	28.0	0.670	6.2	-1.000	5.8	0.259	4.6
0.428	56.56	88.2	-0.496	1.1	-0.077	17	1.207	5.8	25.2	0.726	11	-0.928	12	0.212	7.8
0.493	53.87	85.2	-0.487	3.2	-0.203	25	1.199	10	22.9	0.770	14	-0.864	20	0.178	11
0.570	50.76	82.1	-0.468	9.1	-0.335	46	1.183	16	19.5	0.832	22	-0.751	39	0.125	18
0.661	47.21	78.1	-0.436	27	-0.494	89	1.165	29	16.6	0.871	29	-0.656	65	0.093	20

2005		Perpendicular Kinematics (e' left)							Parallel Kinematics (e' right)						
Q^2 (GeV/c)^2	θ_q (°)	θ^* (°)	c_{20}	δc_{21} (10^{-4})	c_{21}	δc_{21} (10^{-4})	c_{22}	δc_{22} (10^{-4})	θ^* (°)	c_{20}	δc_{20} (10^{-4})	c_{21}	δc_{21} (10^{-4})	c_{22}	δc_{22} (10^{-4})
0.137	71.66	118.4	-0.141	0.62	1.037	0.78	0.913	0.64	24.7	0.736	0.85	-0.910	0.86	0.197	0.64
0.164	69.89	117.0	-0.177	0.62	0.996	0.90	0.941	0.73	22.7	0.774	0.88	-0.847	0.87	0.165	0.60
0.193	68.09	115.4	-0.213	0.80	0.952	1.3	0.968	1.1	20.8	0.806	1.1	-0.789	1.1	0.138	0.74
0.225	66.28	113.7	-0.251	1.1	0.900	2.0	0.996	1.7	19.2	0.834	1.6	-0.730	1.8	0.114	1.0
0.264	64.21	111.6	-0.293	1.6	0.834	3.2	1.030	2.4	17.2	0.866	2.0	-0.658	2.8	0.0885	1.4
0.310	61.89	109.2	-0.337	2.5	0.753	5.8	1.065	4.2	15.1	0.894	3.2	-0.578	4.9	0.0649	2.1
0.366	59.31	107.1	-0.370	4.2	0.675	12	1.090	7.8	12.7	0.925	4.5	-0.475	8.5	0.0398	3.0
0.430	56.50	104.3	-0.410	5.0	0.572	17	1.121	13	10.4	0.948	7.8	-0.377	18	0.0220	5.1
0.494	53.80	101.6	-0.437	4.6	0.479	21	1.141	14	8.4	0.966	9.6	-0.258	24	0.0053	7.1
0.569	50.82	98.2	-0.468	5.1	0.335	33	1.169	18	6.4	0.979	13	-0.136	39	-0.0059	8.5
0.674	46.71	94.9	-0.487	5.6	0.206	94	1.187	28	5.5	0.982	18	0.033	111	-0.0069	14

Table 4.3: The mean values for the kinematic coefficients and their statistical uncertainties. The direction of three-momentum transfer θ_q and the target spin angle θ^* with respect to $\boldsymbol{q}$ are indicated. When $\boldsymbol{q}$ is in the plane spanned by the beam line and the target spin quantization axis, $\theta^* \approx \theta_q \pm \theta_S$. The small deviation from the relationship is caused by the spread in θ_S and ϕ_q.

4.4.2 T_{20} and T_{21} Extraction

The T_{22} contributions are subtracted and the statistical uncertainties in Q^2 are absorbed into the asymmetries,

$$
\begin{aligned}
A^* &= A_{exp} - c_{22}T_{22}, && (4.11)\\
\delta A^* &= \sqrt{\left(\frac{\delta A_{raw}}{P_{zz}}\right)^2 + \left(\frac{\partial A_{exp}}{\partial Q^2}\delta Q^2\right)^2 + (T_{22}\delta c_{22})^2 + (c_{22}\delta T_{22})^2}, && (4.12)
\end{aligned}
$$

where T_{22} is determined numerically from Abbott's parameterization III (Sec. 2.3.3) [61] and δT_{22} is the theoretical uncertainty in T_{22}. The contribution $c_{22}T_{22}$ is typically only a few percent of A_{exp}, as can be seen from Fig. 4-11. As expected, δA^* is dominated by the statistical uncertainties in A_{raw}, while the contribution from the other sources are insignificant.

It follows from Eq. 4.8 and the definition of A^* (Eq. 4.11), that A^* can be expressed in terms of T_{20}, T_{21} and the corresponding kinematic coefficients,

$$
\left\{
\begin{aligned}
A^*_{\parallel} &= c^{\parallel}_{20}T_{20} + c^{\parallel}_{21}T_{21}\\
A^*_{\perp} &= c^{\perp}_{20}T_{20} + c^{\perp}_{21}T_{21}
\end{aligned}
\right. . \qquad (4.13)
$$

With the kinematic coefficients known (Sec. 4.4.1 and Tab. 4.3), T_{20} and T_{21} are found as the root to the linear equations Eq. 4.13.

$$
\left\{
\begin{aligned}
T_{20} &= \frac{c^{\perp}_{21}A^*_{\parallel} - c^{\parallel}_{21}A^*_{\perp}}{c^{\perp}_{21}c^{\parallel}_{20} - c^{\parallel}_{21}c^{\perp}_{20}}\\
T_{21} &= \frac{c^{\perp}_{20}A^*_{\parallel} - c^{\parallel}_{20}A^*_{\perp}}{c^{\perp}_{20}c^{\parallel}_{21} - c^{\parallel}_{20}c^{\perp}_{21}}
\end{aligned}
\right. , \qquad (4.14)
$$

where $c^{\parallel,\perp}_{20,21}$ are the kinematic coefficients for T_{20} and T_{21} in parallel and perpendicular kinematics respectively. In this method, A^* from both parallel and perpendicular kinematics contribute to both T_{20} and T_{21}. The results are shown in Fig. 4-14 and tabulated in Tab. 4.4.

4.4.3 Single T_{20} Extraction

Instead of solving for both T_{20} and T_{21} from the two asymmetries measured simultaneously in parallel and perpendicular kinematics, an alternative approach is to use the world data to subtract the T_{21} contribution in the asymmetries and use the data in both sectors to extract T_{20}.

$$T_{20}^{\|,\perp} = \frac{\left(A_{exp}^{\|,\perp} - c_{21}^{\|,\perp} T_{21} - c_{22}^{\|,\perp} T_{22}\right)}{c_{20}^{\|,\perp}}. \tag{4.15}$$

The T_{20} values extracted from the two sectors are then combined by weighted average,

$$T_{20}^{s} = \frac{\left(\frac{1}{\delta T_{20}^{\|}}\right)^2 T_{20}^{\|} + \left(\frac{1}{\delta T_{20}^{\perp}}\right)^2 T_{20}^{\perp}}{\left(\frac{1}{\delta T_{20}^{\|}}\right)^2 + \left(\frac{1}{\delta T_{20}^{\perp}}\right)^2}. \tag{4.16}$$

The results are shown in Fig. 4-15 and included in Tab. 4.4 also. The subtraction of the T_{21} contribution introduces an additional amount of uncertainty, which is discussed in Sec. 4.5.4. The results are generally in agreement with the T_{20} extracted simultaneously with T_{21} as described in Sec. 4.4.2. The consistency and differences are discussed in detail in Sec. 4.5.4 also.

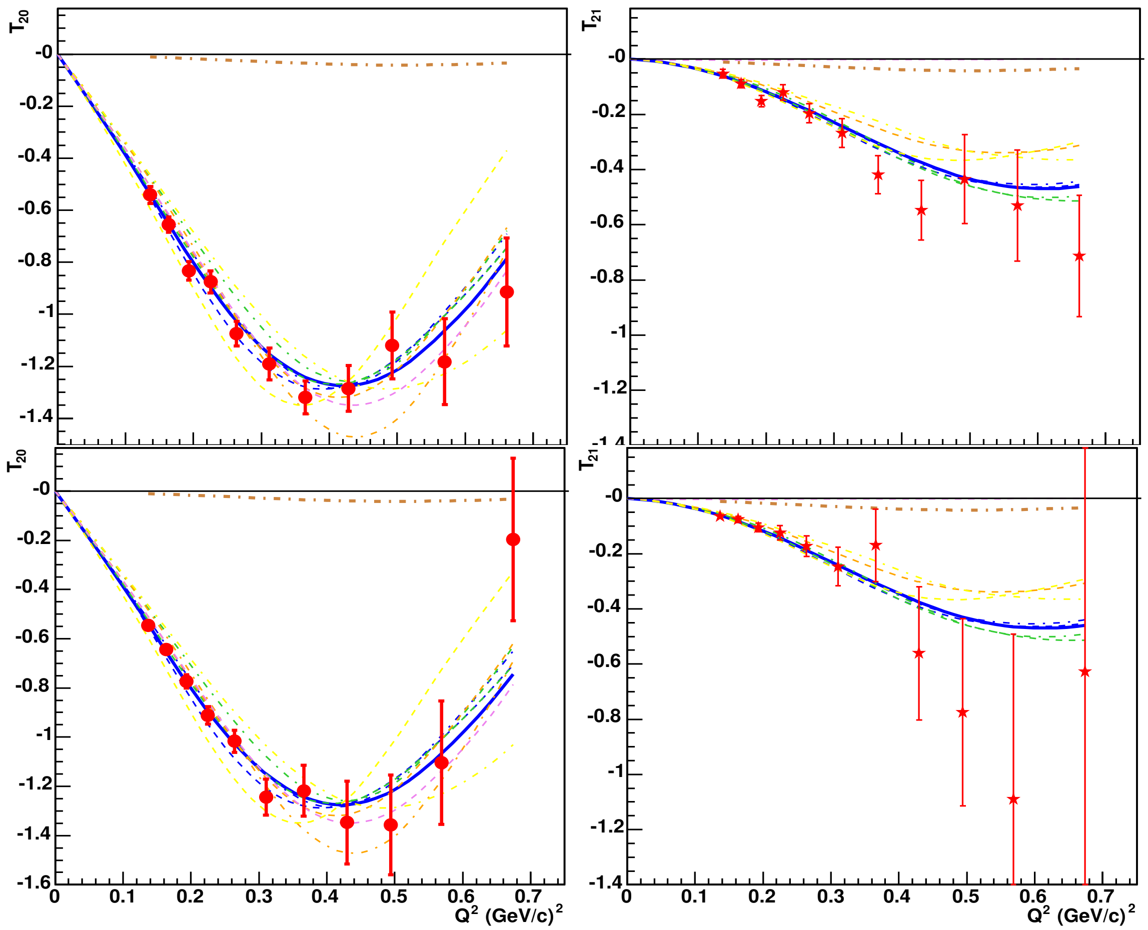

Figure 4-14: T_{20} and T_{21} measured from 2004 (top) and 2005 (bottom) data sets. The curves are: Abbott's parameterization I (blue, dashed), II (blue, dash-dot), III (blue, solid), Arenhövel (green, dashed), van Orden (green, dash-dotted), Schiavilla (orange, dashed), LP2 (violet, dashed), Krutov (violet, dash-dotted), Buchmann full (yellow, dashed), and Tjon (yellow, dash-dotted). The brown dash-dotted curve shows the size of T_{22} for comparison.

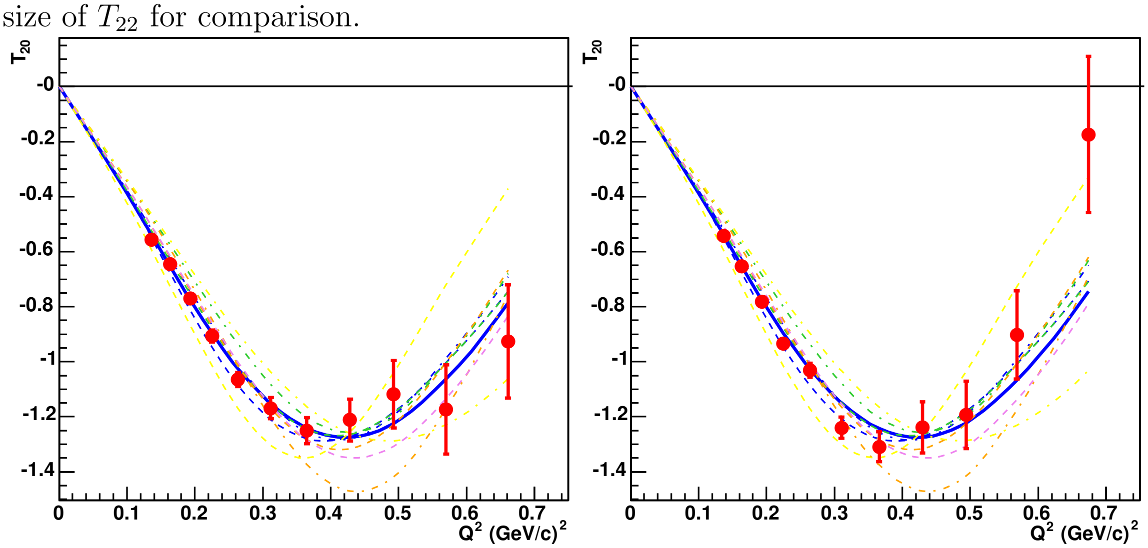

Figure 4-15: Single T_{20} extraction from 2004 (left) and 2005 (right) data sets. The curves as in Fig. 4-14.

	Q^2 $(GeV/c)^2$	θ_e $(^\circ)$	$A^*_\parallel$	$\delta A^*_\parallel$	$A^*_\perp$	$\delta A^*_\perp$	T_{20}	δT_{20}	T_{21}	δT_{21}	T^s_{20}	δT^s_{20}
2004	0.137 [a]	25.67	-0.1359	0.0091	0.1959	0.0069	-0.541	0.033	-0.053	0.015	-0.557	0.014
	0.164 [a]	28.28	-0.1677	0.0093	0.2448	0.0073	-0.655	0.030	-0.089	0.016	-0.646	0.013
	0.193	30.95	-0.208	0.012	0.3185	0.0098	-0.833	0.036	-0.152	0.021	-0.770	0.017
	0.225	33.65	-0.304	0.017	0.372	0.013	-0.875	0.042	-0.120	0.027	-0.906	0.021
	0.264	36.75	-0.383	0.022	0.472	0.016	-1.075	0.047	-0.196	0.035	-1.064	0.026
	0.312	40.46	-0.436	0.035	0.550	0.025	-1.191	0.061	-0.268	0.052	-1.169	0.038
	0.365	44.37	-0.465	0.052	0.642	0.030	-1.319	0.063	-0.419	0.068	-1.251	0.048
	0.428	48.88	-0.425	0.087	0.679	0.049	-1.285	0.089	-0.55	0.11	-1.212	0.076
	0.493	55.35	-0.49	0.14	0.633	0.079	-1.12	0.13	-0.44	0.16	-1.12	0.12
	0.570	58.68	-0.59	0.19	0.73	0.11	-1.18	0.17	-0.53	0.20	-1.17	0.16
	0.661	65.00	-0.33	0.24	0.75	0.14	-0.91	0.21	-0.71	0.22	-0.93	0.21
	Q^2 $(GeV/c)^2$	θ_e $(^\circ)$	$A^*_\parallel$	$\delta A^*_\parallel$	$A^*_\perp$	$\delta A^*_\perp$	T_{20}	δT_{20}	T_{21}	δT_{21}	T^s_{20}	δT^s_{20}
2005	0.137 [a]	25.70	-0.345	0.010	0.0110	0.0082	-0.548	0.021	-0.064	0.010	-0.544	0.014
	0.164 [a]	28.28	-0.434	0.010	0.0375	0.0084	-0.645	0.020	-0.076	0.011	-0.654	0.013
	0.193	30.95	-0.542	0.014	0.066	0.012	-0.775	0.027	-0.105	0.017	-0.783	0.016
	0.225	33.63	-0.671	0.018	0.117	0.016	-0.914	0.036	-0.125	0.025	-0.935	0.021
	0.264	36.79	-0.769	0.023	0.154	0.021	-1.020	0.045	-0.173	0.037	-1.034	0.025
	0.310	40.36	-0.972	0.038	0.234	0.035	-1.247	0.073	-0.247	0.071	-1.242	0.039
	0.366	44.43	-1.048	0.054	0.337	0.060	-1.22	0.10	-0.17	0.13	-1.311	0.055
	0.430	48.98	-1.067	0.098	0.232	0.089	-1.35	0.17	-0.56	0.24	-1.241	0.093
	0.494	53.46	-1.11	0.14	0.22	0.11	-1.36	0.20	-0.78	0.34	-1.20	0.12
	0.569	58.58	-0.93	0.19	0.15	0.13	-1.11	0.25	-1.09	0.60	-0.90	0.16
	0.674	65.91	-0.21	0.35	-0.03	0.23	-0.20	0.33	-0.6	1.3	-0.17	0.28

[a] The first two bins are used for normalization hence do not present new measurements.

Table 4.4: The asymmetries A^* with T_{22} components subtracted are shown. Combined with the kinematic coefficients in Tab. 4.3, T_{20} and T_{21} are extracted. The single extractions of T_{20}, as explained in Sec. 4.4.3, are shown as T^s_{20}.

4.5 Systematic Uncertainties

The systematic errors have several origins. The reconstruction of θ_e is not perfectly accurate (Sec. 4.5.1). This error enters into both the momentum transfer Q^2 and the target spin orientation θ^* relative to the momentum transfer. The analysis assumes that the tensor plus and minus ($P_{zz} = 1$ and -2 respectively) states are equally polarized, any deviation from this assumption causes errors in the results (Sec. 4.5.2). The target spin orientation θ_S in the LAB is not accurately known either, which affects the determination of the target tensor polarization P_{zz} and θ^* (Sec. 4.5.3). The statistical and systematic errors in the low Q^2 data affect the determination of P_{zz} and the spin angle θ_S (Sec. 4.5.3), which in turn propagate into the high Q^2 data points. Systematic errors in these important variables all contribute to the errors in T_{20} and T_{21} (Sec. 4.5.4). Whenever possible, both analytical error estimations and Monte Carlo verifications are provided.

In this section, the following notation will be adopted: 1) The superscript $\tilde{}$ indicates that the variable is measured in the low Q^2 bins used for the measurement of P_{zz} and θ_S; 2) $\Delta X(\Delta Y)$ denotes the error in X caused by the error in Y, for example $\Delta A_{exp}(\Delta\theta_e)$ means the error in the asymmetry A_{exp} due to the error in the reconstruction of the electron scattering angle θ_e; 3) Statistical errors are denoted by δ, while systematic errors are denoted with Δ. For example, δP_{zz} stands for the statistical error in the tensor polarization, and $\Delta P_{zz}(\Delta\tilde{\theta}_e)$ is the uncertainty in P_{zz} caused by the reconstruction error in $\tilde{\theta}_e$.

4.5.1 Errors in θ_e and Q^2

It is not possible to determine exactly the error in θ_e, which is used to calculate both Q^2 and θ^*. Estimations, however, can be made. In the elastic $H(e,e'p)$ reaction from hydrogen target, Q^2 can be calculated from either electron scattering angle θ_e or the proton scattering angle θ_p. The energy loss by the proton along its trajectory was less than 3-4 MeV/c, therefore reconstruction for protons is sufficiently accurate and reliable [17]. With two independent sources to determine Q^2, the discrepancy between $Q^2(\theta_e)$ and $Q^2(\theta_p)$ provides information on the systematic reconstruction errors in θ_e and θ_p. The error in θ_e can be estimated if the error in θ_p is ignored. The Q^2 calculated from θ_e and θ_p differ by about 0.0025 (GeV/c)^2 below Q^2 of 0.28 (GeV/c)^2, which corresponds to $\Delta\theta_e \approx 0.2°$. At higher Q^2, $\left|Q^2(\theta_e) - Q^2(\theta_p)\right| \approx 0.004\ (\mathrm{GeV/c})^2$, which corresponds to $\Delta\theta_e \approx 0.4°$ [83].

Although the ep-elastic kinematics are different from the elastic scattering from the deuteron, these observations from hydrogen target data are used to estimate the tracking error, i.e., the systematic error in the electron scattering angle θ_e. Throughout the analysis, the estimate is used that $\Delta\theta_e = 0.2°$ for the first four bins ($Q^2 < 0.25$) and $\Delta\theta_e = 0.4°$ in the rest of the acceptance.

The tracking errors are likely to be independent, between the two sectors and between different Q^2 bins, as the particles travel through different geometric regions in the drift chambers. However, an overall error in the BLAST toroidal field measurement or an error in the position of the chambers could cause uniform shifts in tracking across the entire acceptance. Denote $\Delta\theta_e$ as the error in θ_e that are independent from each other, and $\Delta\theta_e^*$ as the errors that are correlated between Q^2 bins. The error in A_{exp} due to $\Delta\theta_e$ can simply be estimated by,

$$\Delta A_{exp}(\Delta\theta_e) = \frac{\partial A_{exp}}{\partial\theta_e}\Delta\theta_e. \tag{4.17}$$

The effect of $\Delta\theta_e^*$ is more subtle because it affects the asymmetries at low and high Q^2 in a correlated manner. At low Q^2 used for normalization, it causes an error in P_{zz}: $\Delta P_{zz}(\Delta\theta_e^*) = \dfrac{P_{zz}}{\tilde{A}_{exp}}\dfrac{\partial\tilde{A}_{exp}}{\partial\theta_e}\Delta\theta_e^*$, where $\tilde{A}_{exp}$ stands for the asymmetry in the low Q^2 bins used for the normalization. Since $A_{exp} = \dfrac{A_{raw}}{P_{zz}}$ for the high Q^2 bins, (Eq. 4.7),

[17] Unfortunately the deuteron reconstruction suffered poor resolution and uncorrected energy loss which prevented the application of the same procedure. Nevertheless, the energy loss of deuteron is largely irrelevant in the ed-elastic analysis, as the Q^2 is determined purely from electron scattering angle θ_e.

		2004		2005	
		kinematics			
θ_e		$\parallel$	$\perp$	$\parallel$	$\perp$
27°	$\tilde{A}_{exp}$	−0.166	0.203	−0.389	0.020
	$\dfrac{\partial \tilde{A}_{exp}}{\partial \theta_e}$ (/°)	−0.020	0.020	−0.035	0.008
34°	A_{exp}	−0.323	0.355	−0.657	0.095
	$\dfrac{\partial A_{exp}}{\partial \theta_e}$ (/°)	−0.024	0.022	−0.039	0.013
	δA_{exp}	0.017	0.013	0.018	0.016
	$\Delta A_{exp}(\Delta\theta_e)$	0.0048	0.0044	0.0078	0.0026
	$\Delta A_{exp}(\Delta\theta_e^*)$	0.0026	−0.0026	0.0040	−0.0049
45°	A_{exp}	−0.563	0.569	−1.016	0.24
	$\dfrac{\partial A_{exp}}{\partial \theta_e}$ (/°)	−0.014	0.013	−0.020	0.01
	δA_{exp}	0.052	0.030	0.054	0.060
	$\Delta A_{exp}(\Delta\theta_e)$	0.0056	0.0052	0.0080	0.0048
	$\Delta A_{exp}(\Delta\theta_e^*)$	0.010	−0.0086	0.014	−0.017

Table 4.5: Variables in Eqs. 4.17 and 4.18 and the resulting systematic uncertainty in A_{exp}. The asymmetry $\tilde{A}_{exp}$ at $\theta_e = 27°$ is used for the measurement of P_{zz} and the spin angle θ_S. The errors in two high Q^2 bins are shown, one at $\theta_e = 34°$ (the 4^{th} bin, $Q^2 \approx 0.23$ (GeV/c)^2), and one at $\theta_e = 45°$ (the 7^{th} bin, $Q^2 \approx 0.37$ (GeV/c)^2). $\Delta A(\Delta\theta_e)$ stands for the errors caused by the tracking error that are independent across Q^2 bins, and $\Delta A(\Delta\theta_e^*)$ stands for the errors caused by the tracking error that are correlated between bins. $\Delta\theta_e^*$ is assumed to be 0.2° for all bins, while $\Delta\theta_e$ is 0.2° for the 34° bin and 0.4° for the 45° bin. The statistical error δA_{exp} are shown for reference.

it follows that the error in A_{exp} due to $\Delta\theta_e^*$ is,

$$\Delta A_{exp}(\Delta\theta_e^*) = \frac{\partial A_{exp}}{\partial \theta_e}\Delta\theta_e^* - \frac{A_{raw}}{P_{zz}^2}\Delta P_{zz}(\Delta\theta_e^*) = \left(\frac{\partial A_{exp}}{\partial \theta_e} - \frac{A_{exp}}{\tilde{A}_{exp}}\frac{\partial \tilde{A}_{exp}}{\partial \theta_e}\right)\Delta\theta_e^*. \quad (4.18)$$

The variables in Eqs. 4.17 and 4.18 are listed in Tab. 4.5 for two bins $\theta_e = 34°$ and $\theta_e = 45°$. $\tilde{A}_{exp}$ and $\dfrac{\partial \tilde{A}_{exp}}{\partial \theta_e}$ are measured at $\theta_e = 27°$ and are also shown in Tab. 4.5. It can be seen that at medium Q^2 (the $\theta_e = 34°$ bin), A_{exp} is not much larger is size than $\tilde{A}_{exp}$. In the mean time, $\dfrac{\partial A_{exp}}{\partial \theta_e}$ is of similar size as $\dfrac{\partial \tilde{A}_{exp}}{\partial \theta_e}$. This leads to strong cancellation in Eq. 4.18. As a result, the effect of correlated reconstruction error $\Delta A_{exp}(\Delta\theta_e^*)$ is about half the size of the uncorrelated $\Delta A_{exp}(\Delta\theta_e)$. At high Q^2,

$\dfrac{\partial A_{exp}}{\partial \theta_e}$ becomes small while A_{exp} is large. Therefore $\Delta A_{exp}(\Delta\theta_e^*)$ is large. In any case the statistical uncertainty dominates the reconstruction error by a factor of two to five, especially at high Q^2, where the statistical the uncertainties dominate any tracking error by a factor of four. Therefore, in the following analysis, the reconstruction error $\Delta\theta_e$ will simply be considered independent between Q^2 bins and the two sectors, with all possible correlations ignored.

4.5.2 False Asymmetries

The analysis relies on the assumption that $P_{zz}^- = -2 \times P_{zz}^+$. Any deviation from this assumption causes errors in the measured P_{zz}, θ_S, T_{20} and T_{21}. These errors will be referred to as errors due to "false asymmetries".

Let $\overline{P}_{zz} = \dfrac{P_{zz}^+ - P_{zz}^-}{3}$ be the average polarization. Define ΔR as the measure of the false asymmetry. Then,

$$P_{zz}^+ = \overline{P}_{zz}(1+\Delta R), \quad P_{zz}^- = -2\overline{P}_{zz}(1-0.5\Delta R), \quad \text{and} \quad \Delta R = \frac{2}{3}\left(\frac{P_{zz}^-}{P_{zz}^+} + 2\right). \tag{4.19}$$

The assumption of equal tensor polarization, $P_{zz}^- = -2P_{zz}^+$, is equivalent to $\Delta R = 0$.

The measured yields are proportional to, $\sigma^\pm = \sigma_0(1 + P_{zz}^\pm A_d^T)$, where A_d^T is the theoretical tensor asymmetry given by the models. Therefore, when the assumption $\Delta R = 0$ is violated, the observed asymmetries are,

$$A_{raw} = \frac{\sigma^+ - \sigma^-}{2\sigma^+ + \sigma^-} = \frac{(P_{zz}^+ - P_{zz}^-)A_d^T}{3 + (2P_{zz}^+ + P_{zz}^-)A_d^T} = \frac{\overline{P}_{zz}A_d^T}{1 + \overline{P}_{zz}A_d^T\Delta R}.$$

As a result the measured tensor polarization, and its deviation ΔP_{zz} from $\overline{P}_{zz}$ is,

$$\begin{aligned} P_{zz} &= \frac{\frac{\overline{P}_{zz}\tilde{A}_\perp^T}{1+\overline{P}_{zz}\tilde{A}_\perp^T\Delta R} - \frac{\overline{P}_{zz}\tilde{A}_\parallel^T}{1+\overline{P}_{zz}\tilde{A}_\parallel^T\Delta R}}{\tilde{A}_\perp^T - \tilde{A}_\parallel^T} = \frac{\overline{P}_{zz}}{1 + \overline{P}_{zz}\Delta R(\tilde{A}_\parallel^T + \tilde{A}_\perp^T)} \\ \Delta P_{zz} &= P_{zz} - \overline{P}_{zz} = \overline{P}_{zz}^2\Delta R\left(\tilde{A}_\perp^T + \tilde{A}_\parallel^T\right), \end{aligned} \tag{4.20}$$

where $\tilde{A}_{\parallel,\perp}^T$ represent the tensor asymmetries in parallel and perpendicular kinematics respectively at low Q^2, where the normalization to the models is performed [18]. At higher Q^2, P_{zz} is used to compute A_{exp} from A_{raw} according to Eq. 4.7. It is easy to show that when ΔR is not zero, the measured A_{exp}, and the error incurred is,

$$
\begin{aligned}
A_{exp} &= \frac{A_{raw}}{P_{zz}} \approx A_d^T \left[1 + \overline{P}_{zz}\Delta R(\tilde{A}_{\parallel}^T + \tilde{A}_{\perp}^T - A_d^T)\right], \\
\Delta A_{exp}(\Delta R) &= A_{exp} - A_d^T = P_{zz}\Delta R A^T(\tilde{A}_{\parallel}^T + \tilde{A}_{\perp}^T - A_d^T). \qquad (4.21)
\end{aligned}
$$

There are two additional assumptions. First, the vector polarization P_z' in the $P_{zz} = -2$ state is assumed to be 0. From the definition of $P_z = n_+ - n_-$, $P_{zz} = 1 - 3n_0$, and the constraint $n_+ + n_- + N_0 = 1$ (Sec. 2.1.3), P_z' must be small when P_{zz}^- is highly negative. In fact, the following constraint is always true, $|P_z'| \leq \frac{P_{zz}^- + 2}{3}$. Nevertheless, with $P_{zz}^- \approx -1.2$ (0.683×-2 in 2004 and 0.563×-2 in 2005, as observed with BLAST ABS, as described in Sec. 4.3.3), $|P_z'|$ could be as large as 0.25. In addition, the degree of vector polarization on the two vector target states $(P_z, P_{zz}) = (+,+)$ and $(-,+)$ are assumed to be equal, i.e., $P_z^- = -P_z^+$. Both assumptions are verified in the following.

Without an independent polarimeter, it is not possible to verify directly the assumption that $\Delta R = 0$. Neither is there any guarantee from the target design principles [77]. Nevertheless, it is possible to make indirect estimates of the size of ΔR. A tensor asymmetry was built between the two target states with positive tensor polarizations ($(P_z, P_{zz}) = (+,+)$ and $(-,+)$),

$$
\begin{aligned}
A_+^T &= \frac{\sigma(+,+,+) + \sigma(-,+,+) - \sigma(+,-,+) - \sigma(-,-,+)}{4\Sigma_0} \\
&\approx \frac{1}{4}(h^+ + h^-)(P_z^+ - P_z^-)A_{ed}^V + \frac{1}{2}(P_{zz}^{++} - P_{zz}^{-+})A_d^T \\
&= \frac{1}{2}(P_{zz}^{++} - P_{zz}^{-+})A_d^T, \qquad (4.22)
\end{aligned}
$$

where $\sigma(h, P_z, P_{zz}) = \sigma_0 \times \left(1 + hP_zA_{ed}^V + P_{zz}A_d^T\right)$, is the cross section in the corresponding helicity-target polarization state combination [19], $h^{\pm}$ is the beam polarization

[18] High Q^2 data are not used to measure P_{zz}.

[19] For example $\sigma(+,+,+)$ represents the cross section in the state of positive beam helicity $h = +$, positive target vector polarization $P_z = +$ and positive target tensor polarization $P_{zz} = +$.

in the $+$ and $-$ helicity states respectively, P_z^+, P_z^-, stand for the vector polarization in the two target vector spin states, P_{zz}^{++} and P_{zz}^{-+} stand for the tensor polarization in those two target vector spin states $(+,+)$ and $(-,+)$, whose tensor polarizations are both positive. Ideally, $h^- = -h^+$, $P_z^- = -P_z^+$ and $P_{zz}^{++} = P_{zz}^{-+}$. A_{ed}^V is the theoretical asymmetries related to the product of beam helicity and target vector polarization, and A_d^T, again, is the theoretical asymmetry related to target tensor polarization only. Σ_0 is the unpolarized cross section determined by the total counts normalized by the total charge,

$$\begin{aligned}\Sigma_0 &= \frac{\sigma(+,+,+)+\sigma(-,+,+)+\sigma(+,-,+)+\sigma(-,-,+)+\sigma(+,0,-2)+\sigma(-,0,-2)}{6} \\ &= \sigma_0 \times \left[1+\frac{1}{6}(h^+ + h^-)(P_z^+ + P_z^- + P_z')A_{ed}^V + \frac{1}{3}(P_{zz}^{++} + P_{zz}^{-+} + P_{zz}^-)A_d^T\right], \qquad (4.23)\end{aligned}$$

where σ_0 is the theoretical unpolarized cross section (Eq. 2.2) [20].

In the last step of Eq. 4.22, the term proportional to $(h^+ + h^-)$ is neglected as the Compton Polarimeter measurements showed that $\Delta h = (h^+ + h^-)/2 = 0.00075 \pm 0.0068$ (Sec. 3.1.3). The asymmetries, shown in Fig. 4-16, are fit to Monte Carlo asymmetries, A_{MC}, to extract $\Delta P_{zz}^+ = (P_{zz}^{++} - P_{zz}^{-+})/2$. The procedure is identical to that described in Sec. 4.3.3. It is found that $\Delta P_{zz}^+ = 0.102 \pm 0.016$ in 2004 and $\Delta P_{zz}^+ = 0.092 \pm 0.012$ in 2005, both of which correspond to $\dfrac{\Delta P_{zz}^+}{\overline{P}_{zz}} \sim 15\%$.

ΔP_{zz}^+ represents the difference in the degree of polarization between the two states with positive tensor polarization (the two states: $(P_z, P_{zz}) = (+,+)$ and $(-,+)$), and therefore does not provide a direct measurement of ΔR which measures the difference in polarization of the positive and negative tensor states (the states: $P_{zz} = +$ and $P_{zz} = -2$). Nevertheless, it does provide a general estimation on the degree of disparity between different polarization states.

[20] When ΔR is not zero, Σ_0 constructed in this manner has an error of:

$$\Sigma_0 = \sigma_0 \times \left[1 + \Delta R \overline{P}_{zz} A_d^T\right].$$

$\Delta R \overline{P}_{zz} A_d^T$. Given the typical P_{zz} and A_d^T, the error is 3-5%. This error affects vector asymmetry measurements. This applies to the vector asymmetries in the electro-disintegration channel also, where A_d^T should be taken as the target tensor asymmetry in that channel. This error affects the ΔP_{zz}^+ results listed in the text, and with this systematic uncertainty included, one has $\Delta P_{zz}^+ = 0.102 \pm 0.016 \pm 0.005$ for 2004 and $0.092 \pm 0.012 \pm 0.005$.

NIKHEF used an ion-extraction polarimeter to measure $P_{zz}^+ = 0.526 \pm 0.007$ and $P_{zz}^- = -1.038 \pm 0.014$ [80], consistent with $\Delta R = 0.02$. It must be pointed out that NIKHEF operated with a different set of target spin states, where the positive tensor state was not simultaneously vector polarized. The VEPP-3 collaboration assumed a 15% systematic error due to the unknown difference in polarization between target spin states in their internal target [91], which is incidentally equal to the $\frac{\Delta P_{zz}^+}{\overline{P}_{zz}}$ discovered here for BLAST deuterium target. It will be assumed that $\Delta R = 0.15$ in this work. With $P_{zz} \approx 0.6$ and $A_d^T \lesssim 0.3$ at the Q^2 used for polarization measurement, the systematic uncertainties induced are $\Delta P_{zz}(\Delta R) = 0.003$ for the 2004 data set, and $\Delta P_{zz}(\Delta R) = 0.019$ for 2005.

The effect of the false asymmetry ΔR were also studied by a Monte Carlo simulation, where ed-elastic events with different polarization in the three spin states were generated but analyzed under the assumption of equal polarization. The difference between extracted P_{zz} and the average value assumed in the simulation is consistent with Eq. 4.20. The difference between the extracted asymmetry A_{exp} and the true model value is also consistent with Eq. 4.21. The same Monte Carlo is also used to study the systematic error in the measured θ_S caused by the false asymmetry.

There does not seem to be a large difference in the vector polarizations between the vector plus and minus ($P_z = 1$ and -1 respectively) states, nor does the tensor minus state seem be significantly vector polarized. These false asymmetries are calculated by

$$\begin{aligned} A_h^+ &= \frac{\sigma(+,+,+) + \sigma(+,-,+) - \sigma(-,+,+) - \sigma(-,-,+)}{4\Sigma_0} = \frac{1}{2} h (P_z^+ + P_z^-) A_{ed}^V, \\ A_h^- &= \frac{\sigma(+,0,-) + \sigma(-,0,-)}{2\Sigma_0} = h P_z' A_{ed}^V. \end{aligned}$$

Any non-zero value in A_h^+ indicates non-zero $\Delta P_z = \frac{1}{2}(P_z^+ + P_z^-)$, and A_h^- reflects P_z'. The observed $A_h^\pm$ are also included in Fig. 4-16, which indicate that ΔP_z and P_z' are consistent with 0. These false asymmetries were more precisely verified by the electro-disintegration channel [53], and the results were consistent with zero.

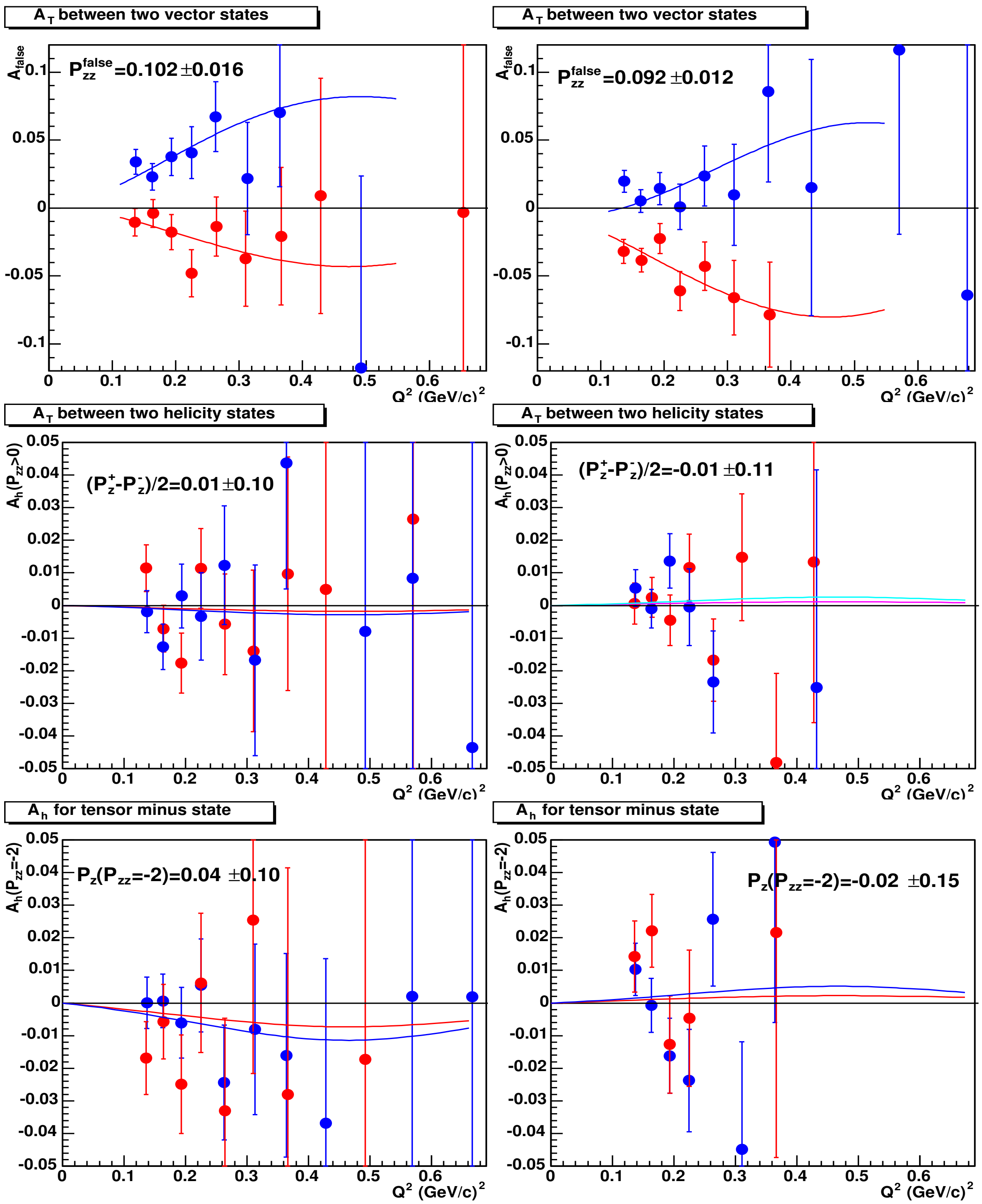

Figure 4-16: False asymmetries in the 2004 (left) and 2005 (right) data sets. The tensor asymmetries between the two tensor + states are shown at the top and fit to Monte Carlo. The difference in the tensor polarization ΔP_{zz}^{+} is extracted from the fit and used to estimate the difference in polarization among different target states in general. In the middle, the helicity only asymmetries for tensor plus states are shown, which measures the difference in the vector polarization between the two vector plus states. On the bottom, the helicity only asymmetries for tensor minus states are shown. The vector polarization for this state should be zero.

4.5.3 Errors in P_{zz} and θ_S

The reconstruction errors in low Q^2 bin cause systematic uncertainties in the measured polarization and spin orientation. It is easy to show from Eq. 4.5, that, assuming the reconstruction errors are independent in the left and right sectors, the error in P_{zz} caused by the error in the low Q^2 electron scattering angle $\Delta\tilde{\theta}_e$ is,

$$\Delta P_{zz}(\Delta\tilde{\theta}_e) = \frac{\sqrt{\left(\frac{\partial A^{\perp}}{\partial \theta_e}\right)^2 + \left(\frac{\partial A^{\parallel}}{\partial \theta_e}\right)^2}}{\left|A^{\perp}_{MC} - A^{\parallel}_{MC}\right|}\Delta\tilde{\theta}_e, \tag{4.24}$$

where $\Delta\tilde{\theta}_e \approx 0.2°$ stands for the tracking error in $\tilde{\theta}_e$ in the low Q^2 bins. The systematic error in spin angle $\Delta\theta_S(\Delta\tilde{\theta}_e)$ is estimated by noticing that the measured spin angle $\overline{\theta}_S$ is the root of $P^{\parallel}_{zz}(\overline{\theta}_S) - P^{\perp}_{zz}(\overline{\theta}_S) = 0$. The analysis procedure implies that the error $\Delta\theta_S(\Delta\tilde{\theta}_e)$ is such that the following holds,

$$\begin{aligned} & P^{\parallel}_{zz}(\overline{\theta}_S + \Delta\theta_S) + \frac{\partial P^{\parallel}_{zz}}{\partial \theta_e}\Delta\tilde{\theta}_e - P^{\perp}_{zz}(\overline{\theta}_S + \Delta\theta_S) - \frac{\partial P^{\perp}_{zz}}{\partial \theta_e}\Delta\tilde{\theta}_e \\ & = P^{\parallel}_{zz}(\overline{\theta}_S) + \frac{\partial P^{\parallel}_{zz}}{\partial \theta_S}\Delta\theta_S + \frac{\partial P^{\parallel}_{zz}}{\partial \theta_e}\Delta\tilde{\theta}_e - P^{\perp}_{zz}(\overline{\theta}_S) - \frac{\partial P^{\perp}_{zz}}{\partial \theta_S}\Delta\theta_S - \frac{\partial P^{\perp}_{zz}}{\partial \theta_e}\Delta\tilde{\theta}_e \quad = \quad 0, \end{aligned}$$

which, assuming, again, the reconstruction errors are independent in the two sectors, leads to,

$$\Delta\theta_S = \frac{\sqrt{\left(\frac{\partial P^{\parallel}_{zz}}{\partial \theta_e}\right)^2 + \left(\frac{\partial P^{\perp}_{zz}}{\partial \theta_e}\right)^2}}{\left|\frac{\partial P^{\parallel}_{zz}}{\partial \theta_S} - \frac{\partial P^{\perp}_{zz}}{\partial \theta_S}\right|}\Delta\tilde{\theta}_e, \tag{4.25}$$

where again, $\Delta\tilde{\theta}_e \approx 0.2°$. The partial derivative of P_{zz} over θ_e is estimated by $\dfrac{\partial P_{zz}/\partial \theta_e}{P_{zz}} = \dfrac{\partial A_{exp}/\partial \theta_e}{A_{exp}}$, and the partial derivatives $\dfrac{\partial P^{\parallel}_{zz}}{\partial \theta_S}$ are measured from Fig. 4-12. The variables in Eqs. 4.24 and 4.25 are tabulated in Tab. 4.6. The error arises from reconstruction error is 0.02 in P_{zz} and about 0.2° in θ_S.

The effects were verified by refitting both polarization P_{zz} and θ_S with the Q^2 shifted by the amount corresponding to $\Delta\tilde{\theta}_e = 0.2°$. One can shift the Q^2 in each sector higher or lower, giving a total of four directional combinations. Since there are two Q^2 bins in each sector used for the normalization and the tracking errors are not

	2004		2005	
kinematics	$\parallel$	$\perp$	$\parallel$	$\perp$
A_{MC}	-0.17	0.21	-0.40	0.025
$\dfrac{\partial A}{\partial\theta_e}$ (/°)	-0.020	0.020	-0.036	0.008
$\dfrac{\partial A/\partial\theta_e}{A}$ (/°)	0.1	0.1	0.1	0.3
$\dfrac{\partial P_{zz}}{\partial\theta_S}$ (/°)	0.03	-0.07	0.34	0.02
P_{zz}	0.683		0.563	
$\Delta P_{zz}(\Delta\tilde{\theta}_e)$	0.02		0.02	
$\Delta\theta_S(\Delta\tilde{\theta}_e)$ (°)	0.20		0.12	

Table 4.6: Variables in Eqs. 4.24 and 4.25 and the resulting systematic uncertainty in P_{zz} and θ_S due to tracking error in θ_e.

		2004		2005	
Q'_l	Q'_r	ΔP_{zz}	$\Delta\theta_S$	ΔP_{zz}	$\Delta\theta_S$
$Q_l + \Delta Q_l$	$Q_r + \Delta Q_r$	-0.008	$-0.04°$	-0.008	$+0.09°$
$Q_l + \Delta Q_l$	$Q_r - \Delta Q_r$	-0.011	$+0.18°$	-0.008	$+0.10°$
$Q_l - \Delta Q_l$	$Q_r + \Delta Q_r$	+0.011	$-0.18°$	+0.007	$-0.08°$
$Q_l - \Delta Q_l$	$Q_r - \Delta Q_r$	+0.008	$+0.04°$	+0.007	$-0.07°$

Table 4.7: Systematic errors in P_{zz} and θ_S caused by tracking errors, estimated by shifting the Q^2 of measured asymmetry data. ΔQ^2 are determined for the low Q^2 bins by $\dfrac{\partial Q^2}{\partial\tilde{\theta}_e}\Delta\tilde{\theta}_e$ where $\Delta\tilde{\theta}_e = 0.2°$ is the systematic error in electron scattering angle discussed in Sec. 4.5.1. Asymmetry data points are shifted by $\pm\Delta Q^2$ and P_{zz} and θ_S refit. All four possible directional combinations in the two sectors are performed and the changes in P_{zz} and θ_S are shown.

considered strongly correlated between the Q^2 bins, only the second bin, which has larger impact on P_{zz} and θ_S, was shifted. The effects on P_{zz} and θ_S are tabulated in Tab. 4.7. All the methods give consistent estimations on the uncertainties in P_{zz} and θ_S. ΔP_{zz} and $\Delta\theta_S$ estimated in Tab. 4.7 are slightly smaller than those shown in Tab. 4.6 obtained from analytical estimations: Eqs. 4.24 and 4.25. This is because Eqs. 4.24 and 4.25 assume the reconstruction error in both low Q^2 bins are perfectly correlated while Tab. 4.7 assumes the two bins are independent.

Tab. 4.8 lists the major systematic errors in P_{zz} and θ_S. P_{zz} measured from $A^{\perp}_{raw} - A^{\parallel}_{raw}$ is not sensitive to the errors in the spin angle θ_S, as can be seen from

Fig. 4-12. The effect from the false asymmetry on P_{zz} is discussed in Sec. 4.5.2, while its effect on θ_S is studied with Monte Carlo. The total uncertainties in spin angle $\Delta\theta_S$ is $\lesssim 0.5°$ for both data sets.

	2004		2005	
source	ΔP_{zz}	$\Delta\theta_S$	ΔP_{zz}	$\Delta\theta_S$
Statistics	0.015	0.35°	0.013	0.42°
$\Delta\theta_e$	0.015	0.20°	0.018	0.12°
$\Delta\theta_S$	0.004		0.002	
ΔR	0.002	0.10°	0.019	0.01°
theory	0.034	0.10°	0.028	0.10°
total	0.040	0.43°	0.040	0.45°

Table 4.8: Systematic errors in P_{zz} and θ_S from various sources. The statistical errors are listed too for comparison. The effect of tracking error $\Delta\tilde{\theta}_e$ is estimated with Eqs. 4.24 and 4.25. The effect from the false asymmetry on P_{zz} is discussed in Sec. 4.5.2, while its effect on θ_S is studied with Monte Carlo. The theoretical uncertainties are discussed in Sec. 4.6.

There are several measurements on the spin angle. Several surveys were performed with Hall Probes. Apart from the elastic electron deuteron scattering analyzed in this work, the elastic electron proton scattering was used to measure the spin angle with a similar procedure for the hydrogen target data taken in the winter of 2004 between the two deuterium data sets [83].

The ed-elastic tensor asymmetry measures the average spin angle for all the ed-elastic events originated from the entire length of the target [21]. To better compare the surveyed spin angle profiles to the average spin angle measured by ed-elastic and ep-elastic asymmetries, a z-vertex weighted average spin angle $\left\langle \theta_S^{prof} \right\rangle$ is calculated for each survey using Eq.4.10.

Average spin angle from all the measurements are tabulated in Tab. 4.9. A few observations are in order. First, the agreement between the three holding field surveys are less than ideal. More importantly, a strict decreasing trend in time is obvious. For example, the Jan. 2005 survey for the nominal 32° setup is 1.3° higher than the March 2006 survey, and the July 2004 survey for the nominal 47° setup is 0.8° higher than

[21]Though the technique can be applied to bins along z-vertex, as shown in Fig. 3.2.2, the statistical precision is lower for individual z-bin.

	2004	2005
Holding field map July 2004		$47.0 \pm 1.0°$
Holding field map Jan. 2005	$31.3 \pm 1.0°$	$46.8 \pm 1.0°$
Holding field map June 2005	$30.7 \pm 1.0°$	$46.2 \pm 1.0°$
Holding field map Mar. 2006	$30.0 \pm 0.5°$	
$H(e, e'p)$		$45.8 \pm 0.8 \pm 2°$
$D(e, e'd)$ (this work)	$31.7 \pm 0.5°$	$47.8 \pm 0.5°$

Table 4.9: Average spin angle from various measurements. For the four holding field maps, the $D(e, e'd)$ events were used to weight the surveyed profile along the target cell. The strictly decreasing trend from July 2004 to March 2006 holding field surveys is obvious, which indicates unknown systematic errors. The 45.8° value measured $H(e, e'p)$ vector asymmetry suffers large systematic error of $\pm 2°$, due to its high sensitivity to tracking error in electron scattering angle θ_e. The $\pm 0.5°$ uncertainty shown for the spin angles measured by the tensor $D(e, e'd)$ asymmetry includes all statistical and systematic errors (Tab. 4.8). The Jan. 2005 survey is used in this work and corrected to match the $D(e, e'd)$ measured spin angle according to Eq. 4.9. This spin angle map requires the least correction for both 32° and 47° nominal configuration.

the June 2005 results. This indicates unknown systematics [22]. In addition, in order to make room for the apparatus, all the holding field surveys were taken with the detector frame open. On the other hand, the $D(e, e'd)$ and $H(e, e'p)$ measurements were truly real time and in-situ. Finally, the spin angle measured by the ep-elastic channel during the hydrogen target runs suffered large sensitivity to the systematic reconstruction errors in θ_e. The systematic error in θ_S measured by ep-elastic channel is estimated to be about $\pm 2°$, even though the systematic error in θ_e itself is estimated to be only 0.2-0.4°. This uncertainty is estimated with a procedure similar to Eq. 4.25. The reason for such a large sensitivity is that $\frac{\partial P_z}{\partial \theta_S}$ (with θ_S standing for the hydrogen target spin angle, and P_z standing for the hydrogen target polarization) in both parallel and perpendicular kinematics are positive and similar in size (Fig.3-11 in Ref. [83]), resulting in a small denominator in Eq. 4.25. On the contrary, for ed-elastic, the two partial derivatives $\frac{\partial p_{zz}}{\partial \theta_S}$ are always opposite in signs. Therefore, the mean spin angles measured by ed-elastic tensor asymmetry are the most accurate, reliable and robust.

[22]The conjecture of misalignment in the Hall Probes could not explain such a monotonic trend, because the alignment error should be independent between surveys taken at different times.

As pointed out at the end of Sec. 4.3.3, there are two important approximations in the analysis procedure to extract P_{zz} and θ_S. First, the Monte Carlo simulation assumed constant spin angle along the cell rather than the measured vertex dependent holding field map. In addition, The Monte Carlo simulated asymmetries were parameterized into polynomials in order to facilitate the fitter procedures. Special care has been taken to verify that the impact of these approximations are insignificant compared to the statistical uncertainty and other systematic errors.

If the proper spin angle profile was taken into consideration in the Monte Carlo, then it must hold that the P_{zz} obtained with Eq. 4.3 in the parallel and perpendicular kinematics are the same,

$$\frac{P_{zz}^{\perp}}{P_{zz}^{\parallel}} = \frac{A_{raw}^{\perp}/\left\langle A_{MC}^{\perp}(\theta_S)\right\rangle}{A_{raw}^{\parallel}/\left\langle A_{MC}^{\parallel}(\theta_S)\right\rangle} = 1, \tag{4.26}$$

where $\langle . \rangle$ stands for the average operator for given Q^2 bin. Since only the average spin angle $\langle \theta_S \rangle$ was used in the simulations, $\langle A_{MC}(\theta_S)\rangle$ is approximated by $A_{MC}(\langle \theta_S \rangle)$, and Eq. 4.26 becomes,

$$\begin{aligned}
\frac{P_{zz}^{\perp}(\langle\theta_S\rangle)}{P_{zz}^{\parallel}(\langle\theta_S\rangle)} &= \frac{A_{raw}^{\perp}/A_{MC}^{\perp}(\langle\theta_S\rangle)}{A_{raw}^{\parallel}/A_{MC}^{\parallel}(\langle\theta_S\rangle)} \\
&\approx \frac{A_{raw}^{\perp}/\left\langle A_{MC}^{\perp}(\theta_S)\right\rangle}{A_{raw}^{\parallel}/\left\langle A_{MC}^{\parallel}(\theta_S)\right\rangle} \times \left[1 + \frac{1}{2}\left(\frac{d^2A_{raw}^{\parallel}/d\theta_S^2}{A_{MC}^{\parallel}} - \frac{d^2A_{raw}^{\perp}/d\theta_S^2}{A_{MC}^{\perp}}\right)\Delta\theta_S^2\right] \\
&= 1,
\end{aligned} \tag{4.27}$$

where $\Delta\theta_S^2 = \langle\theta_S^2\rangle - \langle\theta_S\rangle^2$ is the Mean Square Error (MSE) of θ_S [23]. Denote, $f(\theta_S) = \dfrac{A_{raw}^{\perp}/\left\langle A_{MC}^{\perp}(\theta_S)\right\rangle}{A_{raw}^{\parallel}/\left\langle A_{MC}^{\parallel}(\theta_S)\right\rangle}$. Then Eq. 4.26 can be rewritten as,

$$f(\langle\theta_S\rangle) = 1, \tag{4.28}$$

and the true $\langle\theta_S\rangle$ is the root of this equation.

[23] The approximation that $\langle A(\theta_S)\rangle = A(\langle\theta_S\rangle) + \frac{1}{2}A''(\langle\theta_S\rangle)\Delta\theta_S^2$, is used, where A'' is the second derivative of A over θ_S. The first order term $A'(\langle\theta_S\rangle)\langle\theta_S - \langle\theta_S\rangle\rangle$ is zero.

By using only constant spin angles in the Monte Carlo, the spin angle obtained from tensor ed-elastic asymmetries is in fact the solution to the approximation Eq. 4.27 rather than Eq. 4.28. Let $\delta\theta_S$ be the error introduced by this approximation, $\langle\theta_S\rangle+\delta\theta_S$ is then the root of Eq. 4.27:

$$f(\langle\theta_S\rangle+\delta\theta_S)\times\left[1+\frac{1}{2}\left(\frac{d^2A^{\|}_{raw}/d\theta_S^2}{A^{\|}_{MC}}-\frac{d^2A^{\perp}_{raw}/d\theta_S^2}{A^{\perp}_{MC}}\right)\Delta\theta_S^2\right]=1.$$

It immediately follows by Taylor expansion that,

$$f(\langle\theta_S\rangle)+f'(\langle\theta_S\rangle)\delta\theta_S=1-\frac{1}{2}\left(\frac{d^2A^{\|}_{raw}/d\theta_S^2}{A^{\|}_{MC}}-\frac{d^2A^{\perp}_{raw}/d\theta_S^2}{A^{\perp}_{MC}}\right)\Delta\theta_S^2.$$

Using Eq. 4.28,

$$f'(\langle\theta_S\rangle)\delta\theta_S=-\frac{1}{2}\left(\frac{d^2A^{\|}_{raw}/d\theta_S^2}{A^{\|}_{MC}}-\frac{d^2A^{\perp}_{raw}/d\theta_S^2}{A^{\perp}_{MC}}\right)\Delta\theta_S^2,$$

which yields,

$$\delta\theta_S\le\frac{1}{2|f'(\langle\theta_S\rangle)|}\left(\left|\frac{d^2A^{\|}_{raw}/d\theta_S^2}{A^{\|}_{MC}}\right|+\left|\frac{d^2A^{\perp}_{raw}/d\theta_S^2}{A^{\perp}_{MC}}\right|\right)\Delta\theta_S^2. \tag{4.29}$$

The various terms in Eq. 4.29, were estimated using Monte Carlo or data: $A_{MC}\sim 0.5$, $f'\sim 10$ rad^{-1}, and $\left|\frac{d^2A^{\|,\perp}_{raw}}{d\theta_S^2}\right|\sim 1$ rad^{-2} [24]. $\Delta\theta_S\sim 10^{-3}$ rad^2 is estimated using the surveyed holding field map. These yield, $\delta\theta_S\sim 0.05^\circ$ which is one order of magnitude smaller than the statistical uncertainty.

The conclusion of the above analysis was confirmed by another approach where the analysis procedure in Sec. 4.4 is applied to the Q^2 bins used for the normalization. The shape of the surveyed spin angle profile was incorporated through Eq. 4.9. The

[24]Notice that only rough estimations of these quantities are needed, and therefore it is not a concern that the true value of $\langle\theta_S\rangle$ is not known exactly.

T_{20} and T_{21} obtained are compared to model calculations. Define

$$\chi^2 = \frac{1}{2}\sum_1^2 \left[\left(\frac{T_{20} - T_{20}^{model}}{\Delta T_{20}} \right)^2 + \left(\frac{T_{21} - T_{21}^{model}}{\Delta T_{21}} \right)^2 \right], \tag{4.30}$$

where $\Delta T_{2i} = \sqrt{\delta T_{2i}^2 + \Delta T_{2i}(\Delta\theta_e)^2}$, in which, δT_{2i} is the statistical uncertainty, and $\Delta T_{2i}(\Delta\theta_e)$ is the systematic uncertainty in T_{20} and T_{21} caused by tracking errors. The systematic errors caused by uncertainties in P_{zz} and θ_S are not included. The sum runs over the first two Q bins, which are below 2 fm^{-1}. The degree of freedom is 2, since there are four data points to fit for two parameters. A grid of steps $0.1°$ in $\langle\theta_S\rangle$, and 0.001 in P_{zz} was searched, and it was confirmed that χ^2 for Abbott's parameterization III was indeed minimized by the P_{zz} and θ_S obtained by comparing data to Monte Carlo.

It can therefore be concluded that the Monte Carlo with constant spin angle are sufficient in the determination of P_{zz} and θ_S. The errors introduced by not considering the spin angle variation along the cell are much smaller than the statistical uncertainties.

One million events were simulated in each Monte Carlo simulation. Compare to the total number of two to three hundred thousand events collected in experiment, the statistical error in the Monte Carlo is very small. In addition, the use of low-discrepancy sequence (Sec. 3.5) further reduces the statistical error in the Monte Carlo. Therefore the polynomial fits described in Sec. 4.1 were very well constrained, especially at the low Q^2, where the normalization to model was performed.

4.5.4 Errors in T_{20} and T_{21}

T_{20} and T_{21} are calculated from the experimental asymmetries A_{exp}. Since $A_{exp} = \dfrac{A_{raw}}{P_{zz}}$, the uncertainties in P_{zz} propagate into A_{exp},

$$\Delta A_{exp} = -\frac{A_{raw}}{P_{zz}^2}\Delta P_{zz} = -\frac{A_{exp}}{P_{zz}}\Delta P_{zz}.$$

As discussed in Sec. 4.5.3, the error in P_{zz} includes contributions from several sources: 1) The statistical uncertainty δP_{zz}; 2) The error caused by the tracking error in the electron scattering angle, $\Delta\tilde{\theta}_e$, in the low Q^2 bins; 3) The error caused by uncertainty in spin angle $\Delta\theta_S$; 4) The error caused by the false asymmetry ΔR. The effect of ΔR is correlated across all Q^2 bins, and is treated separately in Eq. 4.21. ΔA_{exp} from the other three sources can be determined by,

$$\begin{aligned}
\Delta A_{exp}(\delta P_{zz}) &= -\frac{A_{exp}}{P_{zz}}\delta P_{zz} && (4.31)\\
\Delta A_{exp}(\Delta\theta_S) &= -\frac{A_{exp}}{P_{zz}}\Delta P_{zz}(\Delta\theta_S) && (4.32)\\
\Delta A_{exp}(\Delta P_{zz}) &= -\frac{A_{exp}}{P_{zz}}\Delta P_{zz}(\Delta\tilde{\theta}_e) && (4.33)
\end{aligned}$$

where $\tilde{\theta}_e$ is the electron scattering angle in the low Q^2 bins used for the normalization as oppose to the scattering angle at which T_{20} and T_{21} are measured. The signs are preserved in order to properly take into consideration the correlation between the left and right sectors in Eqs. 4.31 and 4.32.

The kinematic coefficients are functions of target spin direction θ^* relative to the three-momentum transfer $\boldsymbol{q}$. θ^* is calculated from $(\theta_q,\, \phi_q)$ and θ_S, and the direction of the three-momentum transfer (θ_q, ϕ_q) is in turn a function of θ_e and ϕ_e. Therefore, the systematic errors in the kinematic coefficients $c(\theta^*)$, defined in Sec. 4.4 below Eq. 4.8, have contributions from both $\Delta\theta_e$ and $\Delta\theta_S$ and are estimated as,

$$\Delta c(\Delta\theta_e) = \frac{\partial c}{\partial\theta^*}\frac{\partial\theta^*}{\partial\theta_e}\Delta\theta_e, \quad \text{and} \quad \Delta c(\Delta\theta_S) = \frac{\partial c}{\partial\theta^*}\frac{\partial\theta^*}{\partial\theta_S}\Delta\theta_S,$$

where $\Delta\theta_e$ and $\Delta\theta_S$ are the uncertainty in the reconstructed electron scattering angle and spin angle respectively.

The systematic uncertainties in T_{20} and T_{21} are estimated through error propagations in Eqs. 4.34 to 4.38,

$$
\begin{aligned}
\Delta T_{20}(\Delta\theta_e) &= \frac{1}{c_{21}^{\perp}c_{20}^{\parallel} - c_{21}^{\parallel}c_{20}^{\perp}} \left\{ \left[c_{21}^{\perp} \left(\Delta A_{exp}^{\parallel}(\Delta\theta_e) - T_{20}\Delta c_{20}^{\parallel}(\Delta\theta_e) - T_{21}\Delta c_{21}^{\parallel}(\Delta\theta_e) \right) \right]^2 \right. \\
&\quad \left. + \left[c_{21}^{\parallel} \left(-\Delta A_{exp}^{\perp}(\Delta\theta_e) + T_{20}\Delta c_{20}^{\perp}(\Delta\theta_e) + T_{21}\Delta c_{21}^{\perp}(\Delta\theta_e) \right) \right]^2 \right\}^{1/2}, \quad (4.34) \\
\Delta T_{20}(\Delta\theta_S) &= \frac{1}{c_{21}^{\perp}c_{20}^{\parallel} - c_{21}^{\parallel}c_{20}^{\perp}} \left\{ c_{21}^{\perp} \left(\Delta A_{exp}^{\parallel}(\Delta\theta_S) - T_{20}\Delta c_{20}^{\parallel}(\Delta\theta_S) - T_{21}\Delta c_{21}^{\parallel}(\Delta\theta_S) \right) \right. \\
&\quad \left. + c_{21}^{\parallel} \left(-\Delta A_{exp}^{\perp}(\Delta\theta_S) + T_{20}\Delta c_{20}^{\parallel}(\Delta\theta_S) + T_{21}\Delta c_{21}^{\parallel}(\Delta\theta_S) \right) \right\}, \quad (4.35) \\
\Delta T_{20}(\delta P_{zz}) &= \frac{c_{21}^{\perp}\Delta A_{exp}^{\parallel}(\delta P_{zz}) - c_{21}^{\parallel}\Delta A_{exp}^{\perp}(\delta P_{zz})}{c_{21}^{\perp}c_{20}^{\parallel} - c_{21}^{\parallel}c_{20}^{\perp}}, \quad (4.36) \\
\Delta T_{20}(\Delta P_{zz}) &= \frac{c_{21}^{\perp}\Delta A_{exp}^{\parallel}(\Delta P_{zz}) - c_{21}^{\parallel}\Delta A_{exp}^{\perp}(\Delta P_{zz})}{c_{21}^{\perp}c_{20}^{\parallel} - c_{21}^{\parallel}c_{20}^{\perp}}, \quad (4.37) \\
\Delta T_{20}(\Delta R) &= \frac{c_{21}^{\perp}\Delta A_{exp}^{\parallel}(\Delta R) - c_{21}^{\parallel}\Delta A_{exp}^{\perp}(\Delta R)}{c_{21}^{\perp}c_{20}^{\parallel} - c_{21}^{\parallel}c_{20}^{\perp}}, \quad (4.38)
\end{aligned}
$$

where $\Delta A_{exp}^{\parallel,\perp}(\Delta\theta_e)$, $\Delta A_{exp}^{\parallel,\perp}(\Delta\theta_S)$, $\Delta A_{exp}^{\parallel,\perp}(\delta P_{zz})$, $\Delta A_{exp}^{\parallel,\perp}(\Delta P_{zz})$, and $\Delta A_{exp}^{\parallel,\perp}(\Delta R)$ are determined by Eqs. 4.17, 4.32, 4.31, 4.33, and 4.21 respectively [25]. The errors $\Delta\theta_e$ are assumed to be independent in each bin and between the two sectors while the errors in θ_S and P_{zz} are 100% correlated across the entire Q^2 acceptance and the two sectors. Similar rules apply to T_{21}.

The effect of $\Delta\theta_S$ is verified by reanalysis of the data assuming a θ_S value which differs by 0.5° from the measured values. The effect of ΔR is verified with Monte Carlo, where ed-elastic events with different polarization in the three tensor states were generated but analyzed under the assumption of equal polarization (Sec. 4.5.2). The resulting T_{20} and T_{21} were compared to the model calculation used in the event generation and the differences are consistent with the results of the analytical estimation in Eq. 4.38.

The error $\Delta T_{20}(\Delta\theta_e)$ is considered to be independent between different Q^2 bins.

[25] Though it is A^* directly used in Rq. 4.14, the systematic uncertainties in A^* are equal to those of A_{exp} which is the result of the definition of A^* (Eq. 4.11).

Although there could be reconstruction errors that are correlated over the entire acceptance, Sec. 4.5.1 showed that the effect of such errors is small at low to medium Q^2. At high Q^2, the statistical error dominates in any case. All other errors, $\Delta T_{20}(\Delta\theta_S)$, $\Delta T_{20}(\delta P_{zz})$, $\Delta T_{20}(\Delta P_{zz})$, and $\Delta T_{20}(\Delta R)$, are correlated between bins and sectors. The systematic errors are tabulate in Tab. 4.10.

The systematic uncertainties in the T_{20} measured by the procedure described in Sec. 4.4.3 is easily estimated through Eq. 4.15,

$$\Delta T_{20}^{\parallel,\perp} = \frac{\Delta A_{exp}^{\parallel,\perp} - T_{20}\Delta c_{20}^{\parallel,\perp} - T_{21}\Delta c_{21}^{\parallel,\perp} - T_{22}\Delta c_{22}^{\parallel,\perp}}{c_{20}^{\parallel,\perp}}. \tag{4.39}$$

$\Delta T_{20}^{\parallel,\perp}$ are then combined accordingly to Eq. 4.16. The results are tabulated in Tab. 4.11.

The subtraction of T_{21} using world data in Eq. 4.15 introduced an additional systematic error. A 10% error in T_{21} is assumed. This estimation is consistent with Ref. [72], and consistent with the dispersion among the three parameterizations of the world data. Within one statistical standard deviation, the measured T_{21} from the data (Sec. 4.4.2), are also consistent with the parameterizations of world data within $\pm 10\%$.

2004

T_{20}	δT_{20}	ΔT_{20}						T_{21}	δT_{21}	ΔT_{21}					
		$\Delta\theta_e$	$\Delta\theta_S$	δP_{zz}	ΔP_{zz}	ΔR	norm			$\Delta\theta_e$	$\Delta\theta_S$	δP_{zz}	ΔP_{zz}	ΔR	norm
-0.541	0.033	0.023	-0.030			0.015	0.024	-0.053	0.015	0.010	-0.015			0.007	0.002
-0.655	0.030	0.023	-0.030			0.023	0.025	-0.089	0.016	0.012	-0.018			0.012	0.002
-0.833	0.036	0.022	-0.034	0.015	0.012	0.033	0.035	-0.152	0.021	0.013	-0.021	0.001	0.001	0.019	0.003
-0.875	0.042	0.020	-0.033	0.018	0.014	0.043	0.040	-0.120	0.027	0.013	-0.023	0.002	0.002	0.029	0.004
-1.075	0.047	0.035	-0.032	0.021	0.016	0.055	0.047	-0.196	0.035	0.027	-0.026	0.003	0.002	0.043	0.006
-1.191	0.061	0.027	-0.027	0.024	0.018	0.063	0.053	-0.268	0.052	0.024	-0.027	0.004	0.003	0.059	0.008
-1.319	0.063	0.019	-0.022	0.026	0.020	0.065	0.057	-0.419	0.068	0.020	-0.028	0.005	0.004	0.076	0.011
-1.285	0.089	0.011	-0.017	0.027	0.021	0.059	0.060	-0.55	0.11	0.014	-0.028	0.007	0.005	0.088	0.015
-1.12	0.13	0.004	-0.011	0.026	0.020	0.043	0.058	-0.44	0.16	0.006	-0.025	0.007	0.006	0.085	0.017
-1.18	0.17	0.002	-0.004	0.023	0.018	0.024	0.051	-0.53	0.20	0.002	-0.023	0.009	0.007	0.070	0.020
-0.91	0.21	0.004	-0.000	0.017	0.013	0.010	0.038	-0.71	0.22	0.005	-0.016	0.009	0.007	0.043	0.019

2005

T_{20}	δT_{20}	ΔT_{20}						T_{21}	δT_{21}	ΔT_{20}					
		$\Delta\theta_e$	$\Delta\theta_S$	δP_{zz}	ΔP_{zz}	ΔR	norm			$\Delta\theta_e$	$\Delta\theta_S$	δP_{zz}	ΔP_{zz}	ΔR	norm
-0.548	0.021	0.015	0.019			0.002	0.029	-0.064	0.010	0.004	0.009			0.000	0.004
-0.645	0.020	0.016	0.022			-0.004	0.034	-0.076	0.011	0.006	0.012			-0.001	0.005
-0.775	0.027	0.018	0.027	0.019	0.017	-0.014	0.041	-0.105	0.017	0.007	0.016	0.003	0.003	-0.005	0.007
-0.914	0.036	0.018	0.030	0.022	0.020	-0.027	0.047	-0.125	0.025	0.009	0.020	0.004	0.004	-0.011	0.009
-1.020	0.045	0.036	0.034	0.025	0.023	-0.047	0.055	-0.173	0.037	0.022	0.026	0.006	0.005	-0.022	0.012
-1.247	0.073	0.033	0.037	0.029	0.026	-0.072	0.062	-0.247	0.071	0.027	0.033	0.008	0.007	-0.042	0.017
-1.22	0.10	0.026	0.036	0.030	0.028	-0.094	0.066	-0.17	0.13	0.028	0.040	0.009	0.009	-0.067	0.020
-1.35	0.17	0.016	0.036	0.032	0.029	-0.110	0.068	-0.56	0.24	0.027	0.050	0.012	0.011	-0.103	0.027
-1.36	0.20	0.006	0.030	0.030	0.028	-0.100	0.064	-0.78	0.34	0.023	0.056	0.014	0.013	-0.124	0.029
-1.11	0.25	0.007	0.024	0.026	0.024	-0.074	0.056	-1.09	0.60	0.021	0.070	0.017	0.016	-0.151	0.037
-0.20	0.33	0.010	0.009	0.018	0.016	-0.021	0.038	-0.6	1.3	0.025	0.071	0.015	0.014	-0.010	0.032

Table 4.10: Systematic errors in T_{20} and T_{21}. The columns are the systematic errors calculated from Eqs 4.34 to 4.38. $\Delta\theta_e$: Eq. 4.34; $\Delta\theta_S$: Eq. 4.35; δP_{zz}: Eq. 4.36; ΔP_{zz}: Eq. 4.37; ΔR: Eq. 4.38. The normalization uncertainties ("norm") are discussed in detail in Sec. 4.6. The polarization related errors are not applicable to the first two bins as they are used for the normalization themselves. The sign of the errors are preserved whenever possible for the combination of the data sets. The values and statistical errors in T_{20} and T_{21} are included for comparison.

2004

T_{20}	δT_{20}	ΔT_{20}						
		$\Delta\theta_e$	$\Delta\theta_S$	δP_{zz}	ΔP_{zz}	ΔR	ΔT_{21}	norm
-0.557	0.014	0.010	-0.001			-0.007	0.012	0.021
-0.646	0.013	0.010	-0.000			-0.011	0.014	0.025
-0.770	0.017	0.010	-0.002	0.013	0.010	-0.016	0.017	0.030
-0.906	0.021	0.010	-0.002	0.015	0.012	-0.022	0.019	0.034
-1.064	0.026	0.020	-0.002	0.018	0.014	-0.029	0.021	0.040
-1.169	0.038	0.018	-0.002	0.020	0.016	-0.039	0.022	0.045
-1.251	0.048	0.014	-0.005	0.023	0.018	-0.046	0.019	0.051
-1.212	0.076	0.020	-0.005	0.024	0.019	-0.051	0.016	0.054
-1.12	0.12	0.005	-0.004	0.024	0.019	-0.041	0.006	0.048
-1.17	0.16	0.002	-0.002	0.021	0.017	-0.041	0.006	0.048
-0.93	0.21	0.004	-0.001	0.018	0.014	-0.025	0.002	0.039

2005

T_{20}	δT_{20}	ΔT_{20}						
		$\Delta\theta_e$	$\Delta\theta_S$	δP_{zz}	ΔP_{zz}	ΔR	ΔT_{21}	norm
-0.554	0.014	0.011	0.005			0.001	0.010	0.023
-0.654	0.013	0.012	0.005			-0.003	0.012	0.027
-0.783	0.016	0.012	0.007	0.015	0.014	-0.009	0.014	0.032
-0.935	0.021	0.012	0.008	0.017	0.016	-0.016	0.017	0.037
-1.034	0.025	0.022	0.008	0.019	0.018	-0.027	0.019	0.042
-1.242	0.039	0.019	0.008	0.022	0.020	-0.039	0.021	0.047
-1.311	0.055	0.015	0.010	0.024	0.022	-0.054	0.020	0.052
-1.241	0.093	0.009	0.007	0.024	0.023	-0.059	0.022	0.053
-1.20	0.12	0.005	0.004	0.023	0.021	-0.054	0.021	0.050
-0.90	0.16	0.005	0.001	0.021	0.019	-0.041	0.015	0.045
-0.17	0.28	0.007	-0.001	0.016	0.014	-0.020	0.006	0.034

Table 4.11: Systematic errors in single T_{20} Extraction discussed in Sec. 4.4.3.

4.6 Normalization Uncertainties

Due to the lack of independent tensor polarimetry, the tensor polarization must be extracted by comparing the data at low Q^2 to theoretical or phenomenological models (Sec. 4.3.3). This procedure introduces an uncertainty due to the inaccuracy of the theoretical model used for the normalization.

4.6.1 World Data

On average the data used for normalization is at $Q = 1.96\ \mathrm{fm}^{-1}$. There are two prior measurements at $Q = 2.03\ \mathrm{fm}^{-1}$ which are very close to the normalization points. The values for $T_{20}(\theta_e = 70°)$ are -0.59 ± 0.13 measured by Bates in 1984 [30] and $-0.713 \pm 0.082 \pm 0.036$ obtained by NIKHEF collaboration in 1999 [37]. The difference between the two measurements is 0.12 which is about 1-σ from each other. The weighted average is -0.674 ± 0.073 which is a $\pm 10\%$ accuracy. additionally, in the region of $1.5 < Q < 3\ \mathrm{fm}^{-1}$, all the NIKHEF data with polarized target and ion-extraction polarimeter [36, 37] are consistently larger in size (more negative) than the Bates recoil polarimetry measurement in 1984 [30].

JLab T_{20} collaboration performed three global parameterizations of world electron deuteron elastic scattering data published up to 2000 (Sec. 2.3.3) [61]. The three form factors and T_{20} at $Q = 1.96\ \mathrm{fm}^{-1}$ calculated from the three parameterizations are shown in Tab. 4.12. The uncertainties in the fits give another estimation of the errors in the normalization. The error in T_{20} from parameterization I and III are both about 6% by adding the errors in form factors independently [26]. The three parameterizations give different T_{20} value at this Q also. The absolute value given by parameterization III is larger than parameterization II but smaller than parameterization I. The dispersion between the three parameterizations is about $\pm 5\%$.

Parameterization I is refit with Bates-84 or NIKHEF-96/99 data excluded, to judge the impact on the parameterizations by the difference between these data sets.

[26] At low Q^2, the cross section is dominated by $G_C^2 + \frac{8}{9} G_Q^2$. Therefore, the cross section data induce strong correlation between the errors in G_C and G_Q.

	G_C	G_C	G_C	T_{20}	χ^2
Parameterization I	0.177 ± 0.001	0.364 ± 0.006	5.4 ± 0.4	-0.607	1.5
Parameterization II	0.178	0.372	5.0	-0.563	1.8
Parameterization III	0.180 ± 0.001	0.371 ± 0.005	5.3 ± 0.3	-0.589	1.5
I with Bates-84 excluded	0.177 ± 0.001	0.363 ± 0.006	5.6 ± 0.4	-0.627	1.2
I with NIKHEF excluded	0.179 ± 0.001	0.364 ± 0.006	4.7 ± 0.4	-0.534	1.2

Table 4.12: Parameterization I refit with Bates-84 or NIKHEF-96/99 data excluded. G_C, G_M, G_Q and T_{20} at $Q = 1.96$ fm^{-1} are shown as well as the reduced χ^2.

The results are also listed in Tab. 4.12. The exclusion of either data set results in significant change in the calculated T_{20} value. T_{20} from these two fits, one excludes Bates-84 data while the other excludes all NIKHEF data differ by 15%, or ±8% about their average.

Significant discrepancies exist between the cross section measurements by Mainz [22] and Saclay [26] in the region of $Q \approx 1 \sim 2$ fm^{-1} [60]. For example at $Q^2 = 3.96$ fm^{-2} and $\theta_e = 90°$, Mainz measured $\frac{d\sigma}{d\Omega} = 0.00384 \pm 0.00006 \times 10^{-30}$ cm^{-2}/sr, while Saclay measured $\frac{d\sigma}{d\Omega} = 0.003417 \pm 0.000058 \times 10^{-30}$ cm^{-2}/sr. The difference is about 10% and larger than 5-σ. As pointed out in Sec. 2.3.3, Abbott's parameterizations [61] favored Saclay data and excluded some of the Mainz data points. This inconsistency further limits the accuracy of the parameterizations at this Q neighborhood.

To summarize, the world data on deuteron form factors at $Q \sim 2$ fm^{-1} are hardly satisfactory. The two direct T_{20} measurements provide only ±10% level constraint and the consistency is only marginal. The prediction by parameterizations of world data have ±6% uncertainty. The difference between the three parameterizations is ±5%. Excluding Bates or NIKHEF data shifts the parameterization by 7-8%. In conclusion, the accuracy of T_{20} at about 2 fm^{-1} given by the world data is at best ±5%, and the discrepancy in Mainz and Saclay cross section data presents additional difficulties in precise determination of T_{20} at this Q^2 using world data. The world data and a few theoretical calculations at $Q \approx 2$ fm^{-1} are presented in the top left panel of Fig. 4-17.

4.6.2 Theoretical Calculations

There are many theoretical models on the deuteron structure. Tab. 4.13 lists several important predictions by an array of models: 1) The static deuteron electric-magnetic moments, and the quadrupole moment. These values are obtained by extrapolating the form factors G_C, G_M and G_Q to $Q = 0$; 2) The position Q_C^0 of the first node in G_C, the momentum transfer Q_{min} where T_{20} reaches its minimum, as well as the minimum value T_{20}^{min}; 3) T_{20} and T_{21} evaluated at ($Q = 1.96$ fm$^{-1}, \theta_e = 70°$) [27]. In principle, the form factors G_C, G_M and G_Q, when extrapolated to $Q = 0$, should be equal to the static charge, magnetic and quadrupole moment respectively. However, it is interesting to note that despite the tremendous effort, none of the theories reproduce the static magnetic and quadrupole moment of deuteron, as can be seen from Tab. 4.13. The three parameterizations, on the other hand, are constrained to reproduce the experimental value of static moments [61]: $\mu_d = 1.714 \dfrac{M_p}{M_d}\mu_d$ and $Q_d = 25.83\ \mathrm{M_d^{-2}}$.

Some of the model predictions in G_M differ significantly from the experimental data. As discussed in Sec. 2.1.3, neglecting the G_M contribution, $\tilde{T}_{20}$ defined by Eq. 2.15 reaches its minimum of $-\sqrt{2}$ when $2\eta G_Q/3G_C = 1$. The difference between the actual minimum value of T_{20} and $-\sqrt{2}$ is caused by the non-zero value of G_M. Therefore T_{20}^{min} in Tab. 4.13 is sensitive to G_M at Q_{min}. To quantify the effect of the model errors on the magnetic form factor, the parameterization III of world data was used to replace the model calculation of G_M in several models [28] to calculate T_{20} from Eq. 2.9,

$$T_{20}(Q^2, \theta_e) = -\frac{1}{\sqrt{2}S}\left[\frac{8}{3}\eta G_C G_Q + \frac{8}{9}\eta^2 G_Q^2 + \frac{1}{3}\eta\left[1 + 2(1+\eta)\tan^2\frac{\theta_e}{2}\right] {G_M^*}^2\right],$$

with G_C and G_Q calculated from the model, while G_M^* represents the magnetic form

[27] The choice of $\theta_e = 70°$ is simply by convention. Since the very first T_{20} measurements carried out by Bates collaboration in 1984 were at $\theta_e = 70°$, it has been customary to correct the T_{20} values measured at different θ_e to 70° in order to compare the data. The correction is very small, typically about one percent of T_{20}.

[28] All three form factors are provided in these three model while the value of form factors must be calculated from other observables in other models. The extrapolation to static property for other models thus are not as reliable.

factor calculated from Parameterization III of world data. The results are also listed in Tab. 4.13. It can be seen that the effect of model errors in G_M is indeed small. The location, Q_{min}, of the minimum in T_{20} is shifted by ≤ 0.05 fm^{-1}, and the minimal value T_{20}^{min} itself is changed by a few percent. At 1.96 fm^{-1} where the normalization to model takes place, the effect is typically 0.2%.

theory	G_C	G_M ($Q=0$)	G_Q	Q_C^0	Q_{min} (fm^{-1})	T_{20}^{min}	T_{20}	T_{21} ($1.96\mathrm{fm}^{-1}, 70°$)	P_{zz}	θ_S (2004 setup)	χ^2	P_{zz}	θ_S (2005 setup)	χ^2
Abbott I [61]	1.000	1.714	25.83	4.215	3.175	-1.240	-0.605	-0.084	0.658	31.7°	0.93	0.557	47.5°	0.57
Abbott II	1.000	1.714	25.83	4.145	3.255	-1.240	-0.565	-0.080	0.717	31.7°	0.81	0.589	47.6°	0.48
Abbott III	1.000	1.714	25.83	4.245	3.305	-1.229	-0.589	-0.083	0.683	31.7°	0.95	0.563	47.7°	0.54
Arenhövel [42, 92] [a]	1.000	1.765	26.08	4.235	3.245	-1.219	-0.572	-0.082	0.709	31.7°	0.67	0.585	47.5°	0.48
(G_M^*)					3.275	-1.259	-0.573	-0.078	0.709	31.8°	0.93	0.580	47.7°	0.51
van Orden [49] [a]	1.000	1.755	23.97	4.145	3.325	-1.207	-0.518	-0.075	0.796	31.7°	0.95	0.635	47.6°	0.51
(G_M^*)					3.335	-1.229	-0.519	-0.072	0.796	31.8°	1.2	0.637	47.7°	0.51
Schiavilla(IA) [45, 46]	0.999	1.622	24.18	4.845	3.655	-1.274	-0.503	-0.053	0.765	31.3°	1.6	0.637	48.2°	1.1
Schiavilla(+MEC)	0.999	1.618	24.95	4.115	3.275	-1.284	-0.558	-0.059	0.698	31.5°	1.2	0.578	48.2°	0.51
(G_M^*)					3.255	-1.246	-0.557	-0.077	0.725	31.7°	0.83	0.582	47.9°	0.46
PWD [48, 93]	0.997	1.709	24.93	4.205	3.335	-1.261	-0.553	-0.074	0.736	31.5°	1.0	0.607	47.8°	0.52
(G_M^*)					3.285	-1.191	-0.541	-0.081	0.765	31.6°	0.65	0.627	47.2°	0.46
Krutov [94]	0.998	1.675	24.45	4.245	3.375	-1.313	-0.535	-0.065	0.723	31.5°	1.7	0.597	48.4°	0.73
(G_M^*)					3.345	-1.254	-0.534	-0.071	0.746	31.6°	1.1	0.599	48.2°	0.57
Tjon [95]	1.000	1.708	24.48	4.605	3.555	-1.253	-0.505	-0.056	0.788	31.5°	1.8	0.648	47.9°	1.0
LP2 [96]					3.365	-1.282	-0.547	-0.004	0.568	29.8°	5.4	0.470	52.9°	1.4
Buchmann [97]					3.035	-1.295	-0.649	-0.088	0.613	31.8°	2.1	0.504	47.9°	1.0
Phillips χPT [98] [b]			24.97				-0.554	-0.080						
χPT [c]			25.16				-0.566	-0.082						

aValue of static moments provided by the theorist.

bWith MMD nuclear form factor.

cWith Nijmegen nuclear form factor.

Table 4.13: Deuteron form factors from various theoretical models. The χPT calculation is done with both MMD and NIJMEGEN nucleon form factors. The static moments are extrapolated from the calculation for each model, except for the models by Arenhövel and Van Orden where the theorists provided the model value of μ_d and Q_d. (G_M^*) stands for corresponding models with Abbott parameterization III replacing the model prediction of magnetic form factor. Both BLAST data sets are fit to the models for P_{zz} and θ_S.

4.6.3 The Q_d Corrections

At low Q^2, T_{20} is dominated by the interference between G_C and G_Q. As the static quadrupole moment of deuteron is measured with fairly high accuracy, attempts can be made to correct for the discrepancy between the extrapolated $G_Q(0)$ and the measured static quadrupole moment Q_d in an ad hoc manner. That is, to correct the quadrupole form factor $G_Q(Q)$,

$$G_Q^*(Q) = G_Q^0(Q) + \Delta Q_d(Q),$$

where $G_Q^0(Q)$ is the original model calculation of the quadrupole form factor and $\Delta Q_d(Q)$ is an ad hoc correction that satisfies $\Delta Q_d(0) + G_Q^0(0) = Q_d$.

Correction I: It is suggested [98] that the short range processes missing in the calculations that are responsible to the Q_d discrepancy should be fairly constant at low Q. Therefore a constant correction,

$$\Delta Q_d = Q_d - G_Q^0(0), \tag{4.40}$$

can be added to G_Q over the entire Q range. However it appears that for most models $|\Delta Q_d| \approx 1$, which is an extremely large correction to G_Q considering that $G_Q(Q)$ itself assumes values of only about 5 at $Q \approx 2$ fm^{-1}. This suggests that a Q dependence in play which suppresses the correction term as Q gets larger.

Correction II: There is no conclusions on this Q behavior as the nature of the correction itself is yet to be understood. Only ad hoc models can be suggested. For example, the contribution of MEC involves two meson and one nucleon propagator, two πNN and one $\pi\rho\gamma$ vertices. Simple power counting suggests a $(Q^2)^{-5}$ behavior,

$$\Delta Q_d(Q) = \frac{Q_d - G_Q^0(0)}{(1 + Q^2/M^2)^5}, \tag{4.41}$$

where $M \sim 1$ GeV/c^2 is the energy scale in effective field theory.

Correction III: Another possible Q^2 dependence is

$$\Delta Q_d(Q) = \left(Q_d - G_Q^0(0)\right) \frac{G_Q(Q)}{Q_d}, \tag{4.42}$$

which simply assumes that the correction varies in the same way as $G_Q(Q)$ itself.

All three corrections were applied to a few models to quantify the effect. T_{20} is calculated from Eq. 2.9,

$$T_{20}(Q^2, \theta_e) = -\frac{1}{\sqrt{2}S}\left[\frac{8}{3}\eta G_C G_Q^* + \frac{8}{9}\eta^2 {G_Q^*}^2 + \frac{1}{3}\eta\left[1 + 2(1+\eta)\tan^2\frac{\theta_e}{2}\right]{G_M}^2\right],$$

where G_C and G_M are the charge and magnetic form factors calculated by the models, and G_Q^* is the quadrupole form factor from the model corrected by one of the three ΔQ_d corrections.

The resulting T_{20} for $1.5 < Q < 2.5$ fm^{-1} are shown in Fig. 4-17 and Tab. 4.14. Because all models but Arenhövel under predicts Q_d, the corrections increase the size of T_{20} predicted by these models. It is easy to estimate that Correction I defined by Eq. 4.40 is the largest among the three. The Q_d correction given by Eq. 4.41 at 2 fm^{-1} is reduced by about 50%, and Eq. 4.42 is about 20% in the size of the correction from Eq. 4.40. Judging from the bottom right of Fig. 4-17, Eq. 4.40 clearly "over corrects". The predicted T_{20} lie below the range depicted by the three green curves, which represent the parameterizations of the world data, and are more than one standard deviation below Bate-84 data. Tab. 4.14 shows that Q_{min} also is dramatically shifted to lower values that are not compatible with experimental observations. For instance, the Q_{min} by the three parameterizations of world data shown in Tab. 4.14 indicate that T_{20} reaches its minimum at about 3.2 fm−1, while Correction I applied to Van Orden and Schiavilla (indicated by $(+\Delta Q_d^{**})$ in the table) shifted Q_{min} from 3.3 fm^{-1} down to about 2.9 fm^{-1}.

The Q_d corrections change the predicted structure function $A(Q)$ as well. Fig. 4-18 shows the $A(Q)$ world data below 2.5 fm^{-1} along with a few models. Original models and those corrected with Eqs. 4.41 and 4.40 are shown. The discrepancy between Mainz (blue circle) and Saclay (black diamond) data at 1.8 and 2 fm^{-1} is clearly

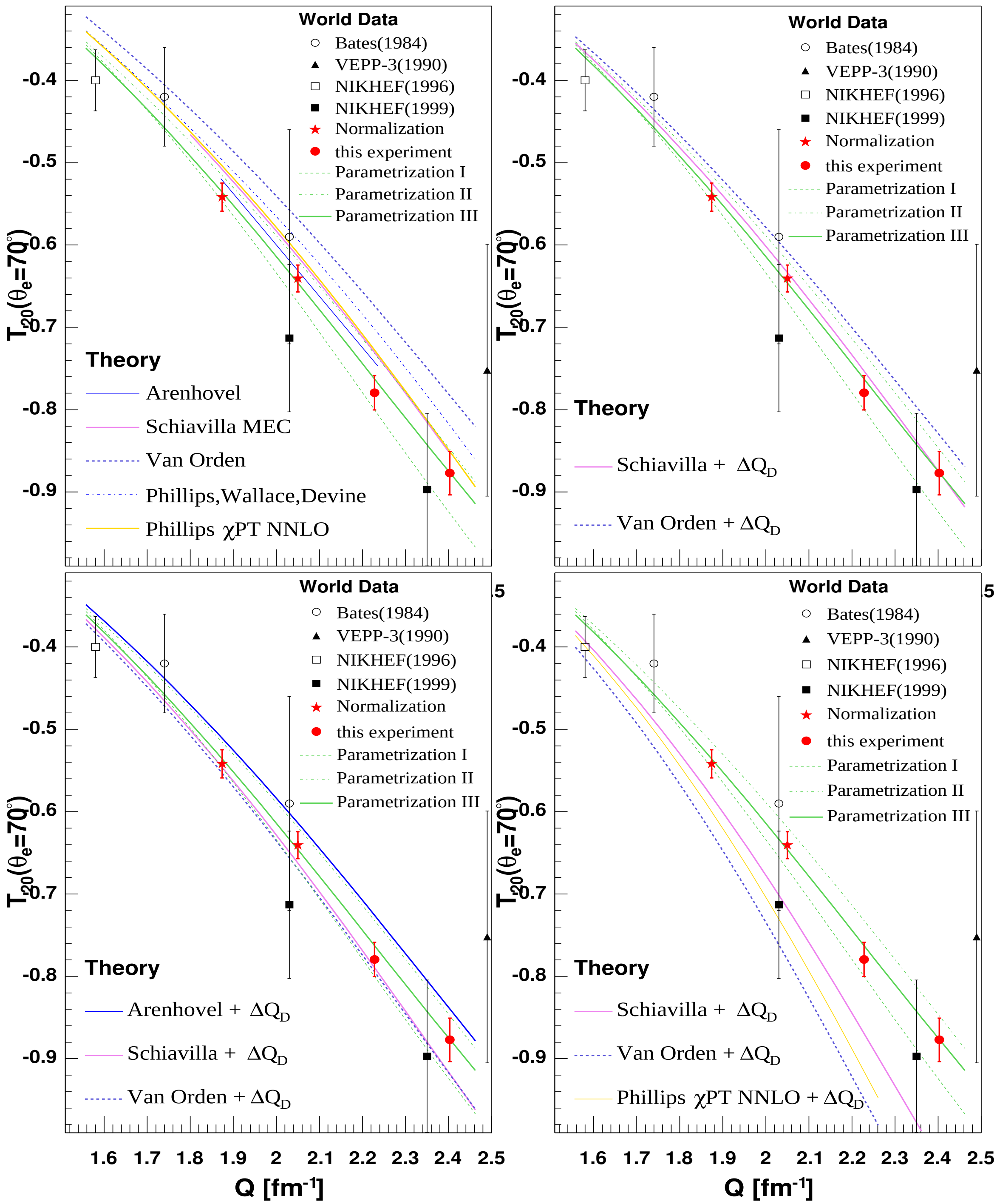

Figure 4-17: World T_{20} data and theoretical calculations in the region of $1.5 < Q < 2.5$ fm^{-1} which is around the momentum transfer region used for the normalization. The original calculations are shown on top left. The other three figures show calculations with G_Q corrected at low Q^2 by Eq. 4.42 (top right), Eq. 4.41 (bottom left) and the constant Eq. 4.40 (bottom right). Eq. 4.41 (bottom left) best reduces the discrepancy between van Orden and Schiavilla however, both curves moved beyond the range defined by the three Abbott's parameterizations. The constant Q_d correction (bottom right) is a 20% modification of G_Q at 1.96 fm^{-1} which moves the predictions rather dramatically.

theory	G_C	G_M	G_Q	Q_{min}	T_{20}^{min}	T_{20}	T_{21}	P_{zz}	θ_S	χ^2	P_{zz}	θ_S	χ^2
		$(Q=0)$		(fm^{-1})		(1.96fm^{-1}, 70°)			2004 setup			2005 setup	
Abbott I	1.000	1.714	25.83	3.175	-1.240	-0.605	-0.084	0.658	31.7°	0.93	0.557	47.5°	0.57
Abbott II	1.000	1.714	25.83	3.255	-1.240	-0.565	-0.080	0.717	31.7°	0.81	0.589	47.6°	0.48
Abbott III	1.000	1.714	25.83	3.305	-1.229	-0.589	-0.083	0.683	31.7°	0.95	0.563	47.7°	0.54
Arenhövel	1.000	1.765	26.08	3.245	-1.219	-0.572	-0.082	0.709	31.7°	0.73	0.585	47.5°	0.48
$(+\Delta Q_d^*)$				3.265	-1.209	-0.560	-0.080	0.727	31.7°	0.64	0.602	47.4°	0.44
van Orden	1.000	1.753	24.05	3.325	-1.207	-0.518	-0.075	0.796	31.7°	0.95	0.635	47.6°	0.51
$(+\Delta Q_d)$				3.285	-1.226	-0.555	-0.080	0.744	31.8°	0.79	0.602	47.5°	0.43
$(+\Delta Q_d^*)$				3.175	-1.267	-0.609	-0.087	0.667	31.8°	0.91	0.556	47.4°	0.59
$(+\Delta Q_d^{**})$				2.845	-1.337	-0.698	-0.099						
Schiavilla	0.999	1.618	24.95	3.275	-1.284	-0.558	-0.059	0.698	31.5°	1.2	0.578	48.2°	0.51
$(+\Delta Q_d)$				3.245	-1.290	-0.576	-0.075	0.697	31.7°	1.1	0.568	48.0°	0.49
$(+\Delta Q_d^*)$				3.195	-1.304	-0.601	-0.078	0.656	31.7°	1.1	0.541	48.1°	0.58
$(+\Delta Q_d^{**})$				2.985	-1.341	-0.646	-0.083						
PWD	0.997	1.709	24.93	3.335	-1.261	-0.553	-0.074	0.736	31.5°	1.0	0.607	47.8°	0.52
$(+\Delta Q_d^*)$				3.245	-1.288	-0.591	-0.080	0.684	31.8°	1.0	0.564	47.7°	0.58
Krutov	0.998	1.675	24.45	3.375	-1.313	-0.535	-0.065	0.723	31.5°	1.7	0.597	48.4°	0.73
$(+\Delta Q_d^*)$				3.255	-1.334	-0.601	-0.073	0.637	31.6°	1.3	0.527	48.7°	0.53
Phillips χPT MMD			24.97			-0.554	-0.080						
$\chi PT + \Delta Q_d^{**}$			25.83			-0.669	-0.096						
χPT(Nijmegen)			25.16			-0.566	-0.082						
$\chi PT + \Delta Q_d^{**}$			25.83			-0.638	-0.092						

Table 4.14: Theoretical calculations with various Q_d corrections. $(+\Delta Q_d)$ stands for models corrected for static Q_d as with Correction III defined in Eq. 4.41. $(+\Delta Q_d^*)$ stands for the Correction II defined in Eq. 4.42. $(+\Delta Q_d^{**})$ stands for correction I, defined in Eq. 4.40 which is a constant amount of $Q_d - G_Q^0(0)$. The three Abbott's parameterizations and the original models are listed for reference. The constant Q_d correction changes Q_{min} dramatically therefore is deemed an over correction. Arenhövel over predicts Q_d while all others under predict. It is suggested that the Q_d correction should be then different for Arenhövel so only one correction to Arenhövel is listed for illustration purpose only. Only G_C/G_Q is available for the χPT, the static ΔQ_d^{**} correction were provided by Phillips himself. ΔQ_d^{**} is the strongest correction at 1.96fm^{-1},ΔQ_d^* is suppressed by about 50% at this Q^2 while ΔQ_d is suppressed by 80% compared to the constant correction.

visible. The Q_d corrections shift Schiavilla, Van Orden, and Phillips χPT upward while moving Arenhövel slightly downward. The original Schiavilla and Phillips χPT calculations appear to agree with Saclay data (black diamond), yet after the constant Q_d correction (bottom panel of Fig. 4-18), they seem more in favor of Mainz data. Due to the ambiguity between the Mainz and Saclay $A(Q)$ data, it is hard to decide if any of the corrections can be rejected.

To summarize, though all three Q_d corrections are motivated by some physics consideration, there is no good criteria to compare the quality of each correction. It is therefore inappropriate to rely upon any of the corrected models for the normalization of BLAST data.

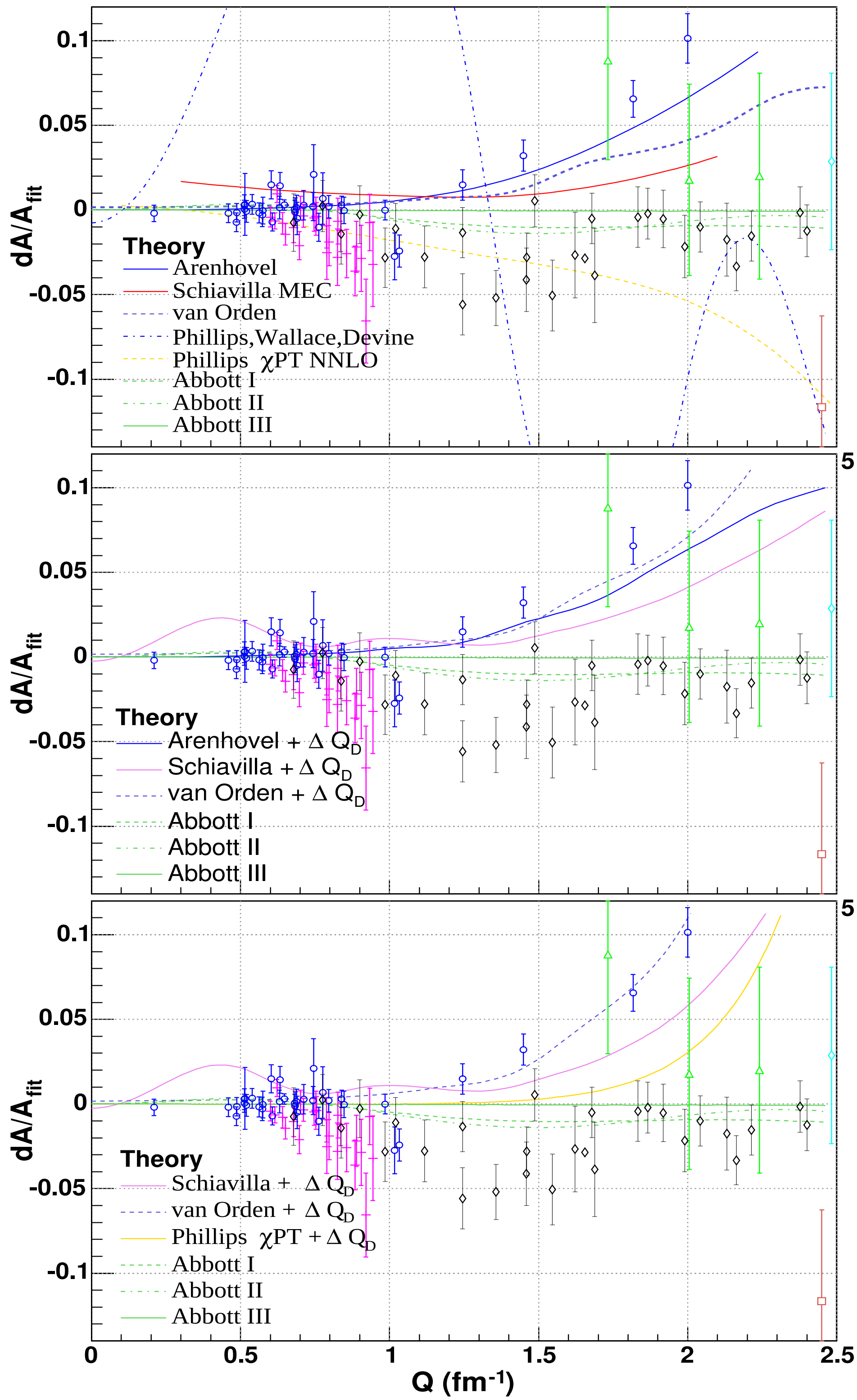

Figure 4-18: $A(Q)$ world data and model calculations. The relative deviations from Abbott's parameterization III $(A - A_{fit})/A_{fit}$ are shown, where A_{fit} is the value calculated from Abbott's parameterization III. On the top, the original calculations are shown. G_Q at low Q^2 is corrected by Eq. 4.41 in the middle panel. On the bottom, G_Q is corrected by Eq. 4.40 which is a constant amount.

4.6.4 Comparison with BLAST Data

Covering a wide range in Q^2, BLAST data have unique discriminating power in the Q^2 evolution of the tensor analyzing powers. To take full advantage of this discriminating power, both BLAST data sets are "renormalized" to each theory for P_{zz} and θ_S. A grid of steps 0.1° in $\langle\theta_S\rangle$, and 0.001 in P_{zz} was searched and the (P_{zz}, θ_S) pair that minimized the χ^2 defined by Eq. 4.30 for each theoretical model was determined. T_{20} and T_{21} at higher Q^2 were then extracted for each model using the corresponding P_{zz} and θ_S. When T_{20} and T_{21} are compared to the models following this procedure, it essentially compares $\frac{T_{2i}(Q)}{T_{2i}(Q = 1.96 \text{ fm}^{-1})}$, where the effect of normalization cancels out, as a common scaling factor to both the numerator and the denominator. The information carried by this ratio can be interpreted as the "shape" of the T_{20} curve.

A χ^2 is constructed for each theory,

$$\chi^2 = \frac{1}{18}\sum_1^9 \left[\left(\frac{T_{20} - \overline{T}_{20}}{\Delta T_{20}}\right)^2 + \left(\frac{T_{21} - \overline{T}_{21}}{\Delta T_{21}}\right)^2\right], \tag{4.43}$$

with the T_{20} and T_{21} obtained by the procedure describe above using the model to be compared to. The summation runs over the nine Q^2 bins not including the ones for normalization, $\overline{T}_{20}$ and $\overline{T}_{21}$ in Eq. 4.43 are the predicted values by the models, ΔT_{20} and ΔT_{21} are the quadratic sum of the statistical and systematic uncertainties caused by tracking error, i.e., the errors that are mutually independent. The other systematic errors are polarization related, therefore are not included. The degrees of freedom are 18 as there are 9 data points for T_{20} and T_{21} each. The χ^2 defined by Eq. 4.43 measures the agreement in the shape of the T_{20} curve, not the absolute size. The P_{zz}, θ_S and resulting χ^2 are included in the rightmost columns of Tabs. 4.13 and 4.14.

The models that result in large χ^2 predict poorly the shape of T_{20} and T_{21}. It can be argued that the confidence level that these theories predict the size of T_{2i} at low Q is also low, therefore only the models leading to reasonable χ^2 in Tabs. 4.13 and 4.14 should be considered as candidates whom BLAST data shall be normalized to. The dispersion in the resulting P_{zz} and θ_S shall be used to gauge the theoretical uncertainty in these quantities.

If one considers models with $\chi^2 \lesssim 1.5$ for 2004 data and $\chi^2 \lesssim 1$ for 2005 [29], only the "state of art" models by Arenhövel, Van Orden, Schiavilla and Phillips-Wallace-Devine(PWD) fit the shape of BLAST T_{20} and T_{21} data. The three phenomenological parameterizations fit the shape of BLAST data also. From the top-left panel of Fig. 4-17, T_{20} by Van Orden lies consistently above both Bates 84 data points and is in fairly poor agreement with the NIKHEF measurements. Therefore, this model can also be excluded from consideration for the normalization. Arenhövel [42, 92] and PWD [48, 93] used the old πN coupling constant. The value has since been updated by the Particle Data Group. Hence these two models need to be considered with caution.

4.6.5 Choice of Model for Normalization

The three parameterizations were fit to previous data, which in most cases are measured with absolute target or recoil polarimetry. The sole exceptions the VEPP-3(1990) [33] measurements which were normalized to theoretical calculations based on the Paris potential [30]. The two data points in Ref. [33] lie beyond $Q = 2.49$ and 2.93 fm^{-1}, and have 23% and 26% uncertainty respectively. Therefore these two data points had very small impact on the predicted value at $Q < 2$ fm^{-1} by the parameterizations This was confirmed by refitting the parameterizations with the data from Ref. [33] excluded, and the predicted T_{20} value at $Q = 1.96$ fm^{-1} changed by less than 1%. It is therefore concluded that these parameterizations are not biased toward any of the theoretical calculations.

The elaborated comparisons with various theories and the three plausible Q_d corrections do not improve the uncertainty in P_{zz}! As can been see from Tabs. 4.13 and 4.14, the three parameterizations along with calculations by Arenhövel [42, 92]

[29] The χ^2s for 2005 data are about 0.5 to 0.6 which is lower than the expected value 1. This is because the experimental asymmetries for this data set are much smaller in the perpendicular kinematics than in the parallel kinematics. As a result, most information comes from the parallel kinematics only, effectively reduces the degree of freedom.

[30] The VEPP-3(2003) [39] data, normalized to calculations by D. Phillips, were not published at the time of the original fit of the parameterizations [61].

and Schiavilla [45, 46] give P_{zz} measurements spanning from 0.658 to 0.717 for the 2004 data set, and 0.557 to 0.589 for 2005 (or -4% to $+5\%$ for 2004, and -2% to $+5\%$ for 2005, centered at Abbott's parameterization III). Both the upper and lower bounds are limited by Abbott's parameterization I and II for both data sets. After the Q_d correction, Schiavilla corrected by Eq. 4.41 sets the lower bounds of P_{zz}, which ranges from 0.656 to 0.717 for 2004 and 0.541 to 0.589 for 2005 (or -4% to $+5\%$ for both data sets centered at Abbott's parameterization III).

Because Abbott's parameterization III seems to lie in the middle of various theoretical and phenomenological models. It is decided to normalize BLAST data below 2 fm^{-1} to this particular parameterization. The normalizations with the three parameterizations of world data differ from each other by 4-5%. It is therefore decided that the relative uncertainty in the normalization is $\Delta P_{zz}/Pzz = \pm 5\%$.

4.6.6 The Electro-disintegration Channel

The data collected in the $D(e, e'p)$ channel simultaneously with elastic reaction show sizable tensor asymmetries [53]. Unfortunately, there are several difficulties in using the electro-disintegration channel as a semi-independent tensor polarimeter.

First of all, only models by Arenhövel [99, 100] are available for this channel. Although calculations using several N-N potential and the effects by final state interactions, meson exchange currents and relativistic corrections were provided separately, the lack of independent models makes it hard to quantify the theoretical uncertainties.

In addition, the analysis in electro-disintegration channel relies on the accurate reconstruction of the scattering angle, as well as the momentum of both the electrons and protons. As a result, it is highly susceptible to any reconstruction errors presented. It is in fact discovered that significant corrections on kinematic variables must be applied in order to match the missing mass and missing momentum spectra to the Monte Carlo predictions [53]. Significant deviation from model predictions in the tensor asymmetries are also observed at missing momentum $P_m > 0.2$ GeV/c over the entire Q^2 acceptance. Fig. 4-19, taken from Ref. [53] is an example. The data are normalized by the P_{zz} value obtained from ed-elastic channel described in this work.

In the right panel of the figure, the asymmetries agree with the model reasonably at low missing momentum $p_M < 0.13$ GeV/c. However, starting from $p_M \sim 0.15$ GeV/c, the size of the asymmetry is significantly larger than the model. The measured asymmetry becomes smaller than the model again at $p_M > 0.35$ GeV/c. This means that the P_{zz} obtained using data at $p_M \sim 0.2$ GeV/c will be significantly larger than the P_{zz} from low p_M asymmetries, while the p_{zz} calculated using data at $p_M \sim 0.2$ or 0.4 GeV/c will, again, be significantly different from each other. As a result, these deviations from the model preclude the possibility of using the entire p_M range as a tensor polarimetry.

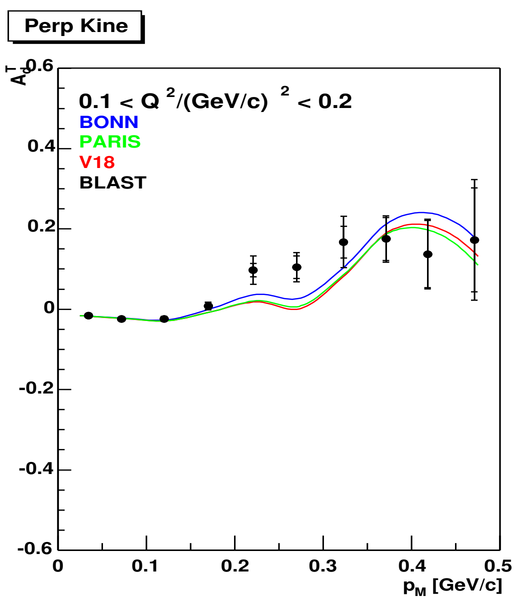

Figure 4-19: Tensor asymmetries A_d^T in the $D(e, e'p)$ channel in 2004 data set. Figure taken from Ref. [53]. Calculation by Ref. [99, 100] are shown using three different NN-potentials: BONN [101], Paris [4] and V18 [7]. Data are normalized by the P_{zz} value measured in elastic channel. The agreement between data and model is good at low missing momentum P_M, while significant deviations from the theory exist at high missing momentum. The deviations can not be explained by errors in P_{zz} which only scales the data in the vertical direction in the entire P_M range.

At low missing momentum, however, tensor asymmetries in electro-disintegration channel are prohibited in the impulse approximation and acquire non-zero values only through additional reaction mechanism. As a result, the asymmetries are small in

Q^2	P_{zz}	
$(\mathrm{GeV/c})^2$	all	$p_{miss} < 0.2$ GeV/c
0.1-0.5	0.5771 ± 0.0086	0.600 ± 0.011
0.1-0.2	0.535 ± 0.011	0.466 ± 0.011
0.2-0.3	0.605 ± 0.017	0.534 ± 0.017
0.3-0.4	0.757 ± 0.038	0.619 ± 0.040
0.4-0.5	0.790 ± 0.074	0.683 ± 0.071

Table 4.15: The tensor polarization extracted by fitting tensor asymmetries in $D(e, e'p)$ channel to calculations by Arenhövel [99, 100]. Results for the 2005 data set provided by Renee Fatemi [102, 53]. Fits to all data and the range with missing momentum $p_{miss} < 0.2$ GeV/c are shown. Errors are purely statistical. The reduced χ^2 for the fits are about 3 for all the data, and about 2 for $p_{miss} < 0.2$ GeV/c. The improved fit with limited p_{miss} range leads to reduced uncertainties even with less statistics. There are significant discrepancies between Q^2 bins and between p_{miss} regions.

size. As a result, low missing momentum $D(e, e'p)$ does not have advantage as a tensor polarimetry compared to the low Q^2 ed-elastic channel.

The P_{zz} measured by fitting $D(e, e'p)$ data to the model in different Q^2 and missing momentum ranges for the 2005 data set are tabulated in Tab. 4.15 [102, 53]. P_{zz} from electro-disintegration channel differ significantly across Q^2 bins, even with missing momentum limited to be below 0.2 GeV/c. This could be due to the errors in kinematic reconstructions that were not properly corrected, or intrinsic deficiencies in the model itself. Regardless the causes, this internal discrepancy indicates large systematic errors in the polarization measurement.

Chapter 5

Results and Discussions

5.1 Combination of Data Sets

The tensor analyzing powers from the two data sets can be combined by averaging, in each bin, the T_{20} and T_{21} obtained in the two data sets. Each data set is weighted by $1/(\delta T_{2i})^2$ with $i = 0$ or 1. The Q^2 values are slightly different in the two data sets especially at large Q^2. The Q^2 are corrected to the average value, which means shifting T_{20} and T_{21} values by the amount calculated from Abbott's parameterization III [61]. The shift is less than 1% except for the last bin, where the shift is about 2%, which is still far less that the statistical uncertainty. The T_{20} and T_{21} are corrected to $\theta_e = 70^\circ$ to facilitate the comparison with the theories and the previous world data [1]. The combined results obtained are shown in Tab. 5.1, and Fig. 5-1 to 5-4. The T_{20} results by the single extraction extraction procedure described in Sec. 4.4.3 are shown in Fig. 5-2. The $\tilde{T}_{20R}$ (Sec. 2.3.4) [51] are obtained from the BLAST results shown in Fig. 5-1, and shown in Fig. 5-3. From Fig. 5-4, the few BLAST data T_{21} points between 2 and 3 fm^{-1} are unique at this low Q.

Although it is possible that the systematic errors, $\Delta\theta_e$, in the reconstruction of the electron scattering angle were in fact correlated between the two data sets, it is difficult to determine the exact degree of the correlation. The systematic errors

[1]This convention was established as the very frist T_{20} measurement at Bates in 1984 [30] was carried out at this electron scattering angle. The electron scattering angle only enters in the coefficient in front of G_M, which it a small contribution to T_{20}.

in reconstruction of θ_e are assumed to be independent between the two data sets. The systematic errors due to the statistical error δP_{zz} in tensor polarization are independent between the two sets of data. The errors in spin angle θ_S are also independent in the two data sets as they are dominated by the fitting errors which are largely statistical.

Although, as discussed in Sec. 4.5.2, in both data sets the tensor polarization in the $(P_z, P_{zz}) = (+,+)$ state was higher than the $(-,+)$ state, indicating a positive correlation between the ΔR as defined in Eq. 4.19, there is no direct determination of ΔR which measures the difference in polarization between tensor plus and minus states. The effect would partially cancel when $\Delta R = +15\%$ in both data sets. The false asymmetries ΔR will be assumed to be independent. The normalization errors, on the other hand, are of course totally correlated between the two data sets.

It is noticed in Fig. 5-4 that the T_{21} data lie consistently below any of the theoretical or phenomenological models at momentum transfer above 3 fm^{-1} [2]. The deviation could largely be explained by the false asymmetry ΔR described in Sec. 4.5.2, which is represented by the yellow area in the top systematic error band in Fig. 5-4. Shifting all data points up by the distance corresponding to the width of the yellow area would bring the data to agreement within 1-σ with Abbott's parameterization III.

[2]The apparent agreement with Arenhövel [43] must be taken with caution as the model overpredicts G_M (Fig. 2-10) which leads to large value of T_{21}, which is proportional to $G_M G_Q$.

Q^2 $(GeV/c)^2$	Q fm^{-1}	θ_e $(^\circ)$	T_{20}	δT_{20}	ΔT_{20}					
					$\Delta\theta_e$	$\Delta\theta_S$	δP_{zz}	ΔP_{zz}	ΔR	norm
0.137	1.874	25.7	-0.542	0.017	0.017	0.016			0.004	0.027
0.164	2.050	28.3	-0.641	0.016	0.018	0.017			0.007	0.032
0.193	2.228	31.0	-0.780	0.021	0.019	0.021	0.013	0.015	0.014	0.037
0.225	2.404	33.6	-0.877	0.026	0.018	0.022	0.014	0.017	0.023	0.043
0.264	2.603	36.8	-1.016	0.031	0.034	0.022	0.016	0.019	0.034	0.049
0.311	2.827	40.4	-1.172	0.044	0.028	0.021	0.017	0.021	0.045	0.054
0.365	3.063	44.4	-1.244	0.051	0.020	0.018	0.019	0.021	0.051	0.057
0.429	3.319	48.9	-1.251	0.074	0.012	0.015	0.021	0.022	0.049	0.059
0.493	3.560	53.4	-1.15	0.10	0.005	0.011	0.019	0.021	0.040	0.058
0.569	3.823	58.6	-1.13	0.13	0.003	0.008	0.017	0.019	0.027	0.052
0.667	4.140	65.4	-0.70	0.17	0.006	0.003	0.013	0.014	0.009	0.039

Q^2 $(GeV/c)^2$	Q fm^{-1}	θ_e $(^\circ)$	T_{21}	δT_{21}	ΔT_{21}					
					$\Delta\theta_e$	$\Delta\theta_S$	δP_{zz}	ΔP_{zz}	ΔR	norm
0.137	1.874	25.7	-0.074	0.010	0.007	0.009			0.002	0.004
0.164	2.050	28.3	-0.098	0.011	0.009	0.012			0.005	0.005
0.193	2.228	31.0	-0.149	0.016	0.012	0.015	0.002	0.003	0.010	0.006
0.225	2.404	33.6	-0.148	0.023	0.013	0.018	0.003	0.003	0.018	0.008
0.264	2.603	36.8	-0.224	0.031	0.030	0.022	0.004	0.004	0.030	0.011
0.311	2.827	40.4	-0.312	0.050	0.030	0.025	0.004	0.005	0.049	0.013
0.365	3.063	44.4	-0.433	0.072	0.026	0.028	0.005	0.006	0.073	0.016
0.429	3.319	48.9	-0.64	0.12	0.019	0.029	0.007	0.007	0.088	0.020
0.493	3.560	53.4	-0.57	0.17	0.011	0.026	0.008	0.008	0.083	0.022
0.569	3.823	58.6	-0.65	0.21	0.004	0.023	0.009	0.009	0.071	0.024
0.667	4.140	65.4	-0.74	0.23	0.006	0.017	0.009	0.007	0.044	0.022

Q^2 $(GeV/c)^2$	θ_e $(^\circ)$	T^s_{20}	δT^s_{20}	ΔT^s_{20}						
				$\Delta\theta_e$	$\Delta\theta_S$	δP_{zz}	ΔP_{zz}	ΔR	norm	T_{21}
0.137	25.7	-0.547	0.010	0.010	0.010	0.003			0.003	0.021
0.164	28.3	-0.643	0.009	0.011	0.013	0.003			0.005	0.025
0.193	31.0	-0.761	0.011	0.011	0.015	0.004	0.010	0.012	0.009	0.030
0.225	33.6	-0.900	0.014	0.011	0.017	0.004	0.011	0.013	0.013	0.034
0.264	36.8	-1.019	0.017	0.020	0.019	0.004	0.013	0.015	0.019	0.039
0.311	40.4	-1.163	0.026	0.017	0.021	0.004	0.014	0.017	0.027	0.044
0.365	44.4	-1.228	0.034	0.014	0.018	0.005	0.016	0.019	0.033	0.049
0.429	48.9	-1.178	0.056	0.009	0.017	0.004	0.017	0.019	0.037	0.051
0.493	53.4	-1.119	0.083	0.005	0.015	0.003	0.016	0.019	0.035	0.050
0.569	58.6	-1.01	0.11	0.003	0.010	0.001	0.014	0.017	0.028	0.045
0.667	65.4	-0.66	0.16	0.005	0.005	0.000	0.013	0.014	0.018	0.038

Table 5.1: T_{20} and T_{21} from combined data sets. T^s_{20} is the result from the single extraction method. All are corrected to $\theta_e = 70^\circ$.

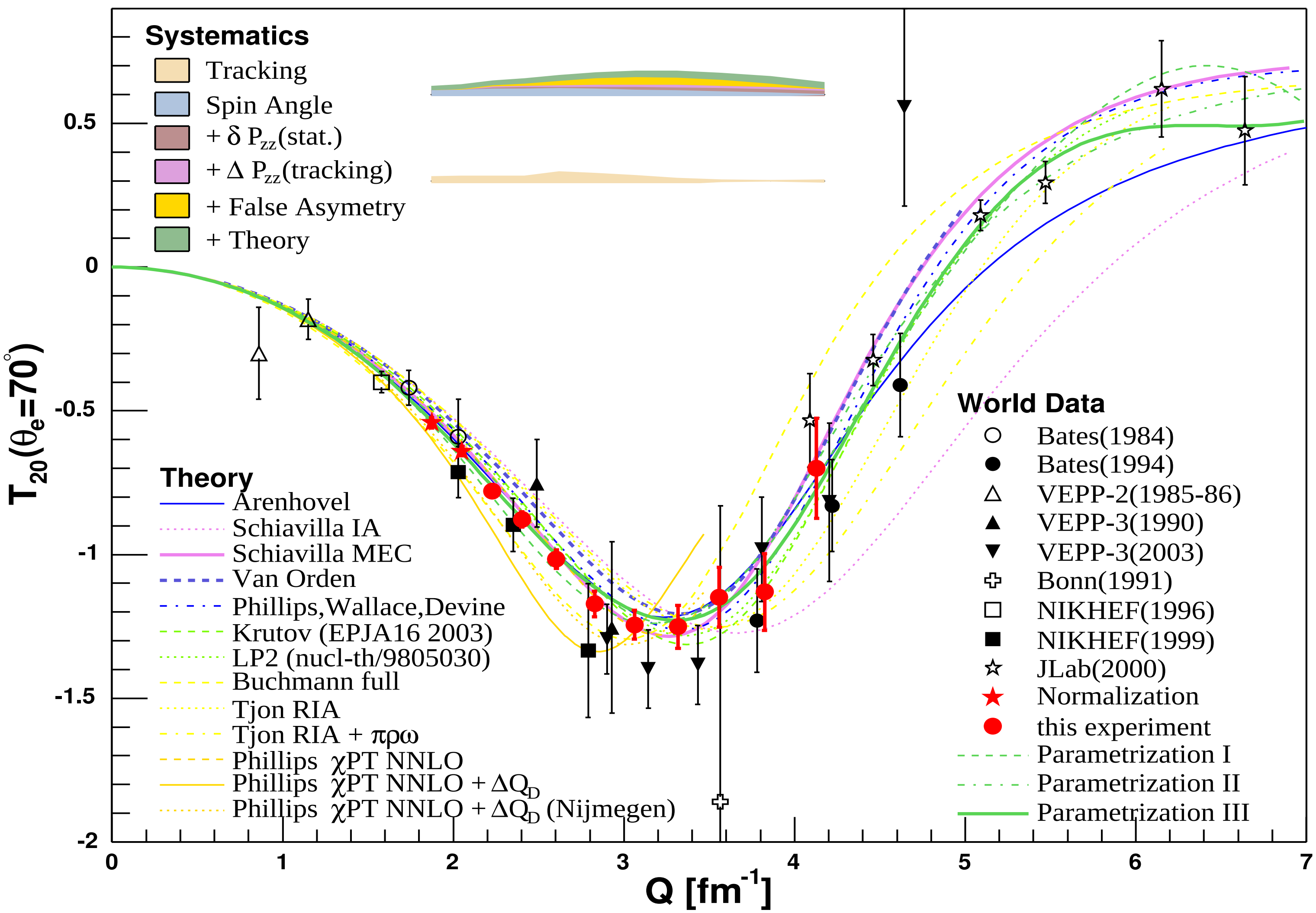

Figure 5-1: T_{20} from combined data sets simultaneously extracted with T_{21} as described in Sec. 4.4.2. Corrected to $\theta_e = 70°$ for the comparison with theory and world data. Systematic errors are represented in the two bands. The top band represents the systematic errors that are correlated between Q bins (the columns $\Delta\theta_S$, δP_{zz}, ΔP_{zz}, ΔR and "norm" in Tab. 5.1), while the bottom band is the systematic errors that are independent across Q bins (The $\Delta\theta_e$ column in Tab. 5.1).

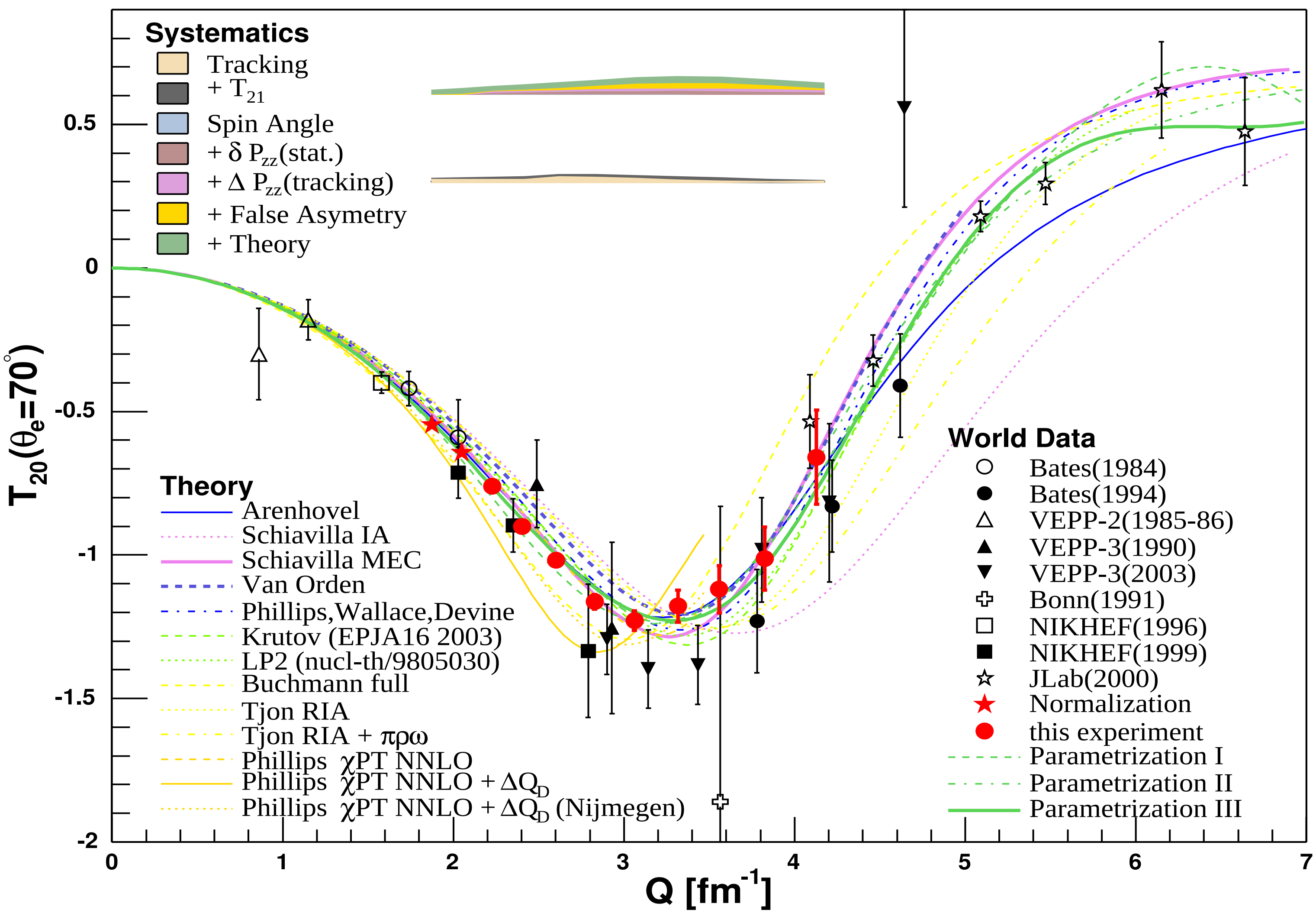

Figure 5-2: T_{20} from combined data sets from single extraction as described in Sec. 4.4.3. Corrected to $\theta_e = 70°$ for the comparison with theory and world data. Systematic errors are represented in the two bands (see caption of Fig. 5-1).

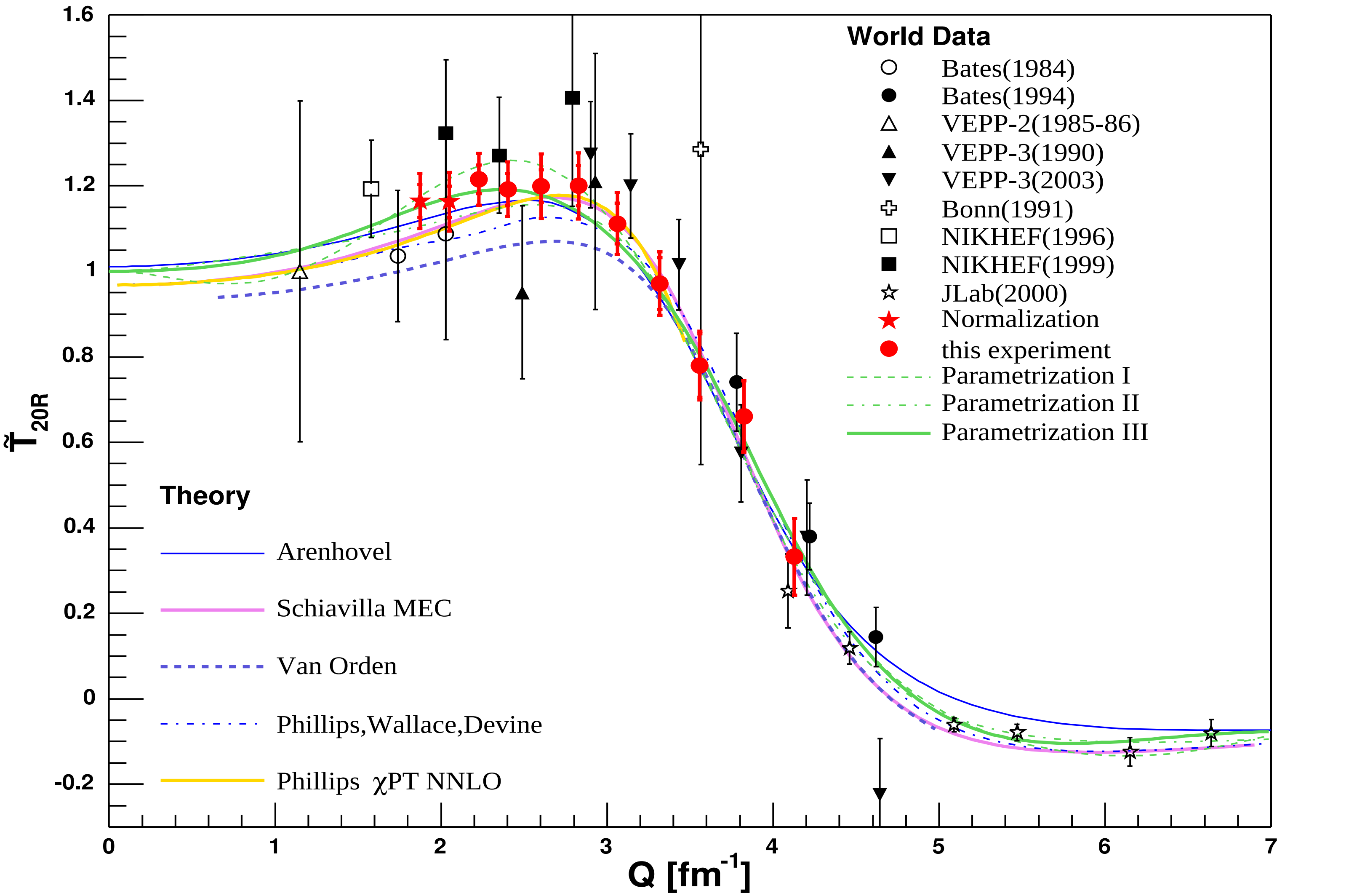

Figure 5-3: $\tilde{T}_{20R}$ [51] (Sec. 2.3.4) from BLAST results. The systematic errors are added to statistical uncertainties in quadrature, as with the rest of the world data.

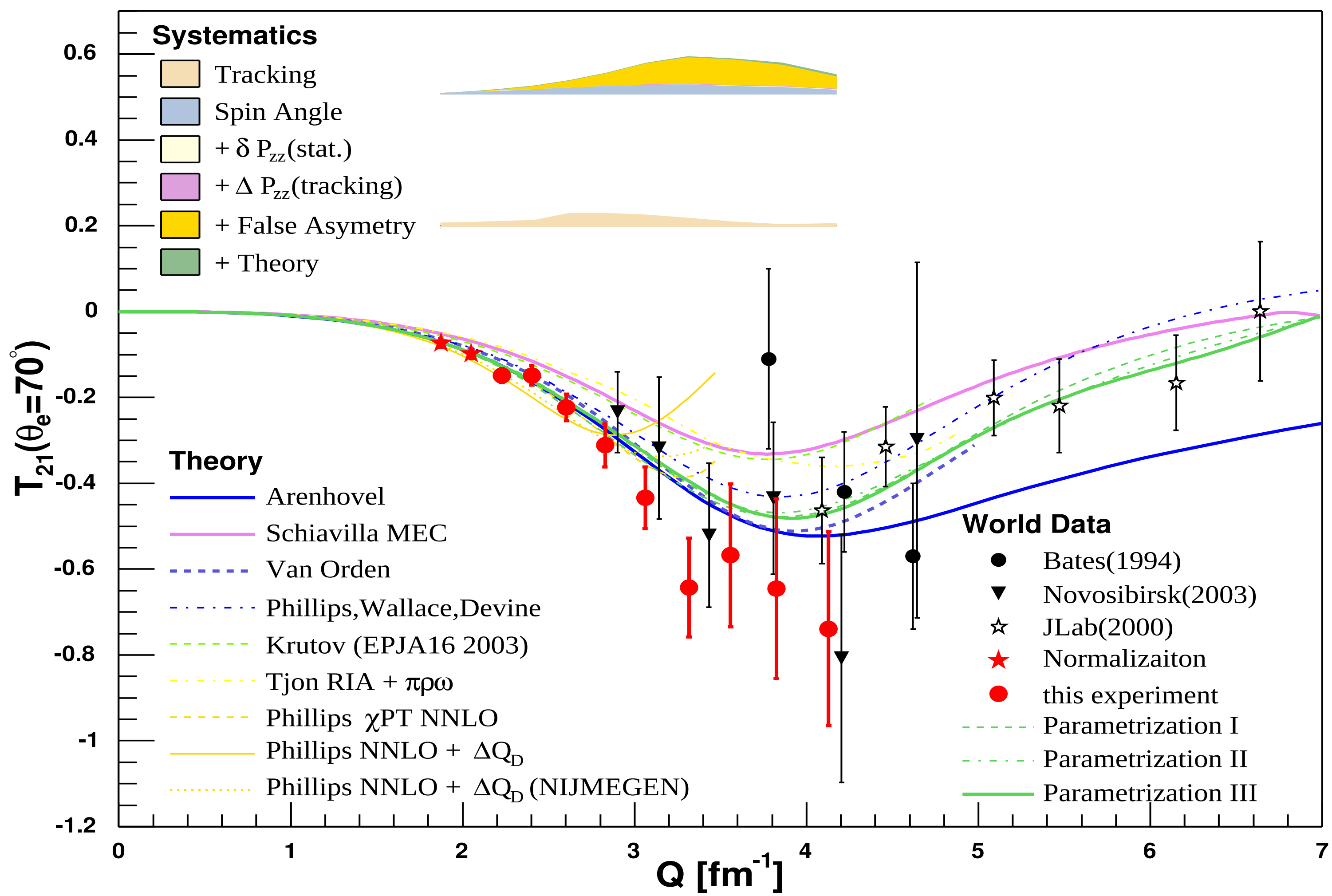

Figure 5-4: T_{21} from combined data sets simultaneously extracted with T_{20} as described in Sec. 4.4.2. Systematic errors are represented in the two bands (see caption of Fig. 5-1). The T_{21} data lie consistently below any of the theoretical or phenomenological models. The deviation could largely be explained by the "ΔR-error" described in Sec. 4.5.2, which is represented by the yellow area in the top systematic error band. Shifting all data points up by the distance corresponding to the width of the yellow area brings the data to agreement within 1-σ with Abbott's parameterization.

5.2 Comparison with Theories

The BLAST T_{20} and T_{21} data are compared to several theoretical models. The agreement with the theories is quantified with χ^2s shown in Tab. 5.2. Two kinds of χ^2s are constructed for each model, denoted in Tab. 5.2 as "floating" and "fixed", for T_{20} and T_{21} respectively.

The "fixed" χ^2 is computed as,

$$\chi^2_{20} = \frac{1}{9}\sum_1^9 \left(\frac{T_{20} - \overline{T}_{20}}{\Delta T_{20}}\right)^2, \quad \text{and} \quad \chi^2_{21} = \frac{1}{9}\sum_1^9 \left(\frac{T_{21} - \overline{T}_{21}}{\Delta T_{21}}\right)^2, \tag{5.1}$$

where T_{2i} are the BLAST data as listed in Tab. 5.1, $\overline{T}_{2i}$ are the values calculated from the model to be compared to, and ΔT_{2i} are the quadratic sum of all the uncertainties, statistical and systematic. The name "fixed" reflects the fact that the normalization is fixed by Parameterization III.

As the "fixed" χ^2 is computed with BLAST data normalized to Parameterization III, and the parameterization does not necessarily reflect the values of the tensor analyzing powers accurately at $Q \lesssim 2$ fm^{-1}. Hence it can be argued that the comparison with theories based on this normalization might be biased.

As described in Sec. 4.6.4, the effect of the "fixed" normalization can be eliminated by normalizing the data to the model with which they are to be compared, i.e., using the model concerned to refit target polarization and spin angle instead of the parameterization III. T_{20} and T_{21} are then extracted using the refit value of P_{zz} and θ_S. This procedure is described at the beginning of Sec. 4.6.4, P_{zz} and θ_S from each model can be found in Tab. 4.13 and 4.14. The χ^2s are then constructed as Eqs. 5.1, but with,

$$\Delta T_{2i} = \sqrt{\delta T_{2i}^2 + \Delta T_{2i}^2(\Delta\theta_e)},$$

where δT_{2i} are the statistical uncertainties, and $\Delta T_{2i}(\Delta\theta_e)$ are the systematic uncertainties due to the reconstruction error in θ_e. The rest of the systematic errors are all related to the normalization, and therefore are not included when data are normalized to each model separately. This approach effectively allows BLAST data to float up and down according to the theoretical calculations at low Q, hence the name "floating".

The "floating" χ^2 tests the agreement of, $\dfrac{T_{20}(Q)}{\left|T_{20}(Q = 1.96\ \mathrm{fm}^{-1})\right|}$, where the effect of normalization cancels out as a common scaling factor to both the numerator and the denominator. The information carried by this ratio can be interpreted as the "shape" of the T_{20} curve. This methodology is illustrated in Fig. 5-5. The figure shows that Arenhövel's caculation [43] best fit the shape of BLAST data. Schiavilla [45], Van Orden [49] and PWD [48] all seem to overpredict the size of the "dip" from $Q = 1.96\ \mathrm{fm}^{-1}$ to the minimum. The BLAST data lie systemtaically higher than these three model predictions between $Q = 3$ and $3.6\ \mathrm{fm}^{-1}$. This region contributes the most to the χ^2_{floating} in Tab. 5.2.

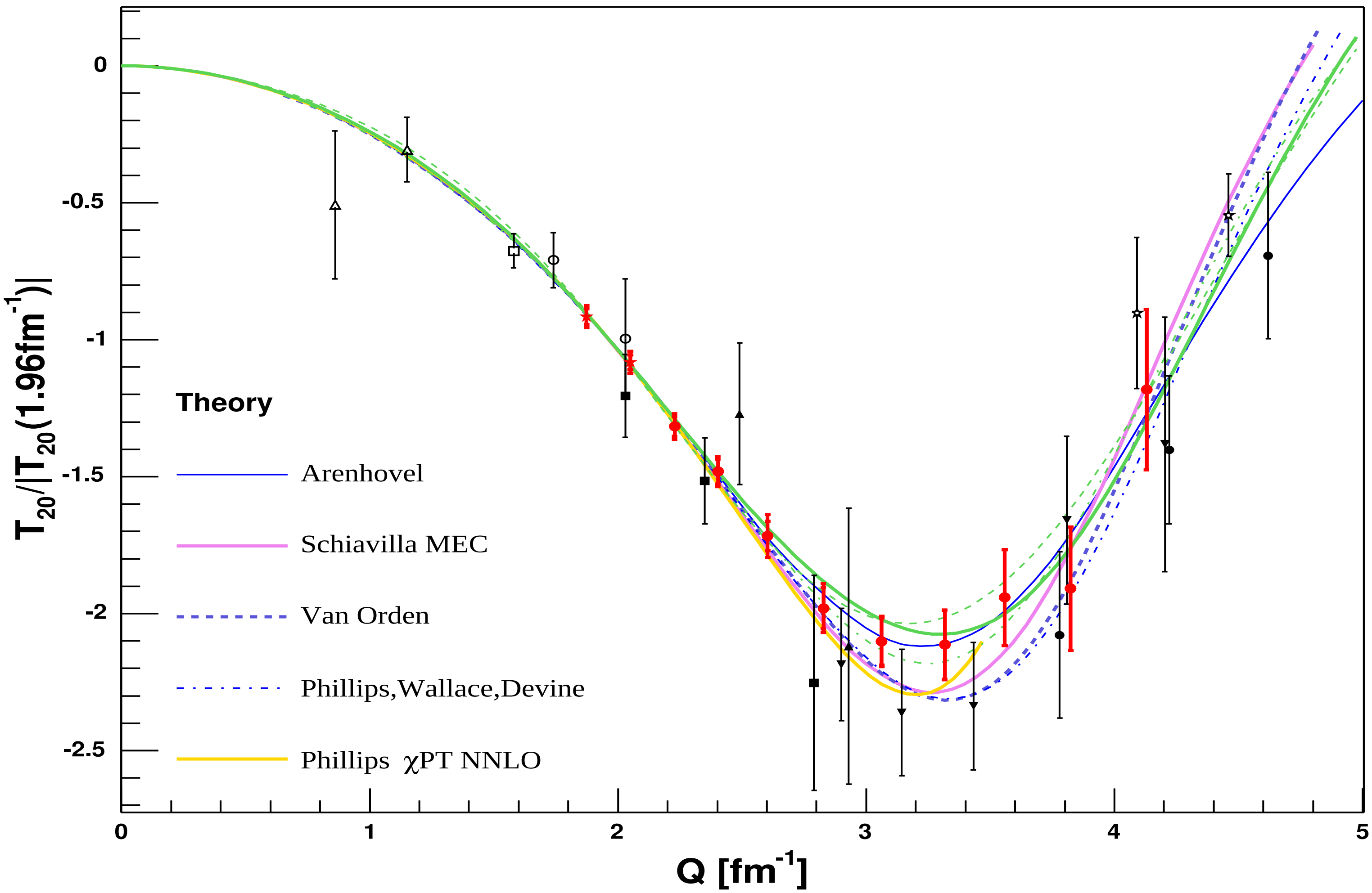

Figure 5-5: Illustration of the "floating" comparison between the BLAST data and the models as well as world data. $T_{20}(Q)/\left|T_{20}^{III}(1.96\ \mathrm{fm}^{-1})\right|$ is shown for BLAST, as well as the world data, where $T_{20}^{III}(Q)$ is the T_{20} predicted by the parameterization III. For the theoretical models, the ratio of T_{20} over the value predicted at $Q = 1.96\ \mathrm{fm}^{-1}$, $T_{20}(Q)/\left|T_{20}(1.96\ \mathrm{fm}^{-1})\right|$ is shown. As a result, at $Q = 1.96\ \mathrm{fm}^{-1}$, all theoretical curves cross the level -1. The systematic error due to tracking (the column $\Delta\theta_e$ in Tab. 5.1) are added to the statistical uncertainty in quadrature. This approach compares the shape of T_{20} as a function of Q.

For the χPT models, only calculations of T_{20} are available for comparison. In addition χPT models are not valid for $Q > 0.6$ GeV/c (or 3 fm^{-1}) since the energy scale used was about 1 GeV. Therefore the summation only runs across the first 5 bins in Eq. 5.1, which cover the range $2.23 < Q < 3.06$ fm^{-1}. χPT calculations were provided [98] with MMD [103] and Nijmegen [6] parameterizations of nucleon form factors, also with corrections for static quadrupole moment [98].

The impulse approximation (IA) by Schiavilla is compared to BLAST data to investigate the significance of MEC. The comparison is done over the entire BLAST Q acceptance as well as for the low-Q region below $Q = 3.06$ fm^{-1}.

Several observations can be made from Tab. 5.2:

- In general the floating χ^2 is slightly less than the fixed. Should the BLAST data have been normalized absolutely with independent tensor polarimetry, this could be interpreted as an indication that the theoretical models predict the shape of the T_{20}, as a function of Q, better than the absolute size. However, due to the normalization to the model, this slight increase in χ^2 when data were normalized to Parameterization III, instead of being determined by an independent polarimeter, only reflects that the theoretical models lie slightly further from Parameterization III than the ±5% theoretical uncertainty quoted in P_{zz}.

- The Q_d correction provided for the χPT theory [98] clearly needs more careful examination. It leads to an increase in the χ^2 from 0.24 to 5.4. This shows that more investigation is still in order before the theoretical calculations could reproduce the static quadrupole moment of the deuteron.

- In general the χ^2 for T_{20} is less than for T_{21}, with the exception of Van Orden's. As discussed in Sec. 5.1, BLAST T_{21} data might suffer systematic errors due to uneven degree of tensor polarization between target spin states (Sec. 4.5.2). Therefore, the larger χ^2 for T_{21} could well be the result of systematic errors, instead of inadequacy in the models. In fact, when all systematic errors are added quadratically, χ^2_{fixed} for Arenhövel, Van Orden, as well as Parameterization III are less than one.

theory	BLAST				Bates	VEPP2	VEPP3	NIKHEF		Bates	JLAB	VEPP3
	χ^2_{floating}		χ^2_{fixed}		[30]	[31, 32]	[33]	[36]	[37]	[35, 104]	[38]	[39]
	T_{20}	T_{21}	T_{20}	T_{21}	(84)	(85/86)	(90)	(96)	(99)	(94)	(2000)	(2003)
d.o.f.	9	9	9	9	2	2	2	1	3	3	6	5 [d]
Abbott III [61]			0.15	0.79	0.25	0.75	0.75	0.57	0.73	0.80	0.98	1.0
Arenhövel [43]	0.21	1.0	0.27	0.61	0.12	0.75	0.60	0.86	0.97	0.94	4.2	1.1
Schiavilla (IA) [45]	1.3	3.5	2.9	3.4	0.15	0.80	0.28	3.9	3.3	3.0	47.0	2.4
Schiavilla (+MEC) [45]	0.32	3.2	0.26	2.7	0.03	0.80	0.60	1.6	1.1	2.3	1.4	0.70
Van Orden [49]	0.94	0.77	1.2	0.82	0.06	2.3	0.80	3.3	2.4	2.3		1.6
PWD [48]	0.47	1.5	0.52	1.3	0.01	1.1	0.80	1.8	1.6	0.42	1.1	0.42
Schiavilla (IA) [a]	0.87	4.2	3.5	3.8								
Schiavilla (+MEC) [a]	0.31	3.8	0.21	2.4								
Phillips χPT [50, 98] [a,b]			0.24									
Phillips χPT [a,c]			0.23									
$\chi PT + \Delta Q_d$ [a,b]			5.4									

[a] Compared to the first 5 out of the 9 bins: $2.23 < Q < 3.06$ fm^{-1}.

[b] With MMD nucleon form factor.

[c] With Nijmegen nucleon form factor.

[d] The data point at 4.6 fm^{-1} is excluded. It deviates from all theoretical curves significantly and dominates the χ^2 when included.

Table 5.2: Reduced χ^2s for comparison between BLAST data and theoretical models. The χ^2s compared to Parameterization III, and for previous world data are show for reference. χPT models are only compared to data up to 3 fm^{-1}. The lower part of the table shows comparisons between BLAST data and theories for the first five bins, which cover $2.23 < Q < 3.06$ fm^{-1}. The Bates-84 data agree very well with the relativistic models (Van Orden and PWD). On the other hand, the NIKHEF(96,99) data agree better with nonrelativistic models with MEC (Arenhövel and Schiavilla MEC). BLAST data seem to agree better with nonrelativistic models with MEC corrections.

- In general, the nonrelativistic approach with MEC corrections (Arenhövel [43] and Schiavilla [45, 46]) fits better to BLAST data, in both the shape (χ^2_{float}) and the size (χ^2_{fixed}), compared to the relativistic models [49, 48]. Compared with previous world data, Bates-84 data agree better with relativistic models, while all NIKHEF data agree better with nonrelativistic models with MEC.
- Van Orden fits T_{20} the worst among the models listed except for the $\chi PT{+}\Delta Q_d$. Further examine showed that the floating χ^2 is dominated by the difference between Van Orden and data at $Q = 3.06$, 3.32 and 3.56 fm^{-1}. As can be seen from the lower panel of Fig. 5-5, there is significant deviation in the shape of T_{20} between this model and BLAST T_{20} data in this Q range, which happens to be around the minimum.
- The fixed χ^2 for the IA is much larger than the corresponding model with MEC included. This reflects the fact that the T_{20} derived from the IA is much smaller than the full MEC model for $Q < 2$ fm^{-1} where the normalization takes place. The agreement between T_{20} and the IA model at low Q is much better than for the entire Q range. This is also obvious from Fig. 5-1 which shows that the IA model (purple dotted curve) deviates from all the data beyond 3.5 fm^{-1}. Limited to the low Q region, the χ^2 for the full model is much smaller than the IA. This is true even for the floating χ^2 where data are normalized to MEC and IA respectively for comparison to the two models. This is evidence that MEC plays an important role in T_{20} even at low momentum transfer.

A third approach to compare BLAST data with theoretical calculations is to compare with the ratio $\frac{T_{21}}{T_{20}}$. As can be obviously seen from Eqs. 4.14, a common scaling in $A^*_{\parallel}$ and $A^*_{\perp}$ would not affect the T_{21} to T_{20} ratio. As a result, this ratio is insensitive to any uncertainty in P_{zz}. The result is shown in Fig. 5-6. The T_{21}/T_{20} ratio displays a systematic deviation from all of the models and previous world data as well. This deviation is largely driven by the systematic deviation in T_{21} from the models as can be seen in Fig. 5-4. The magnitude of the deviation is similar to the size of systematic uncertainty due to the uneven degree of tensor polarization between target spin states (Sec. 4.5.2), which is the dominating systematic error in T_{21}.

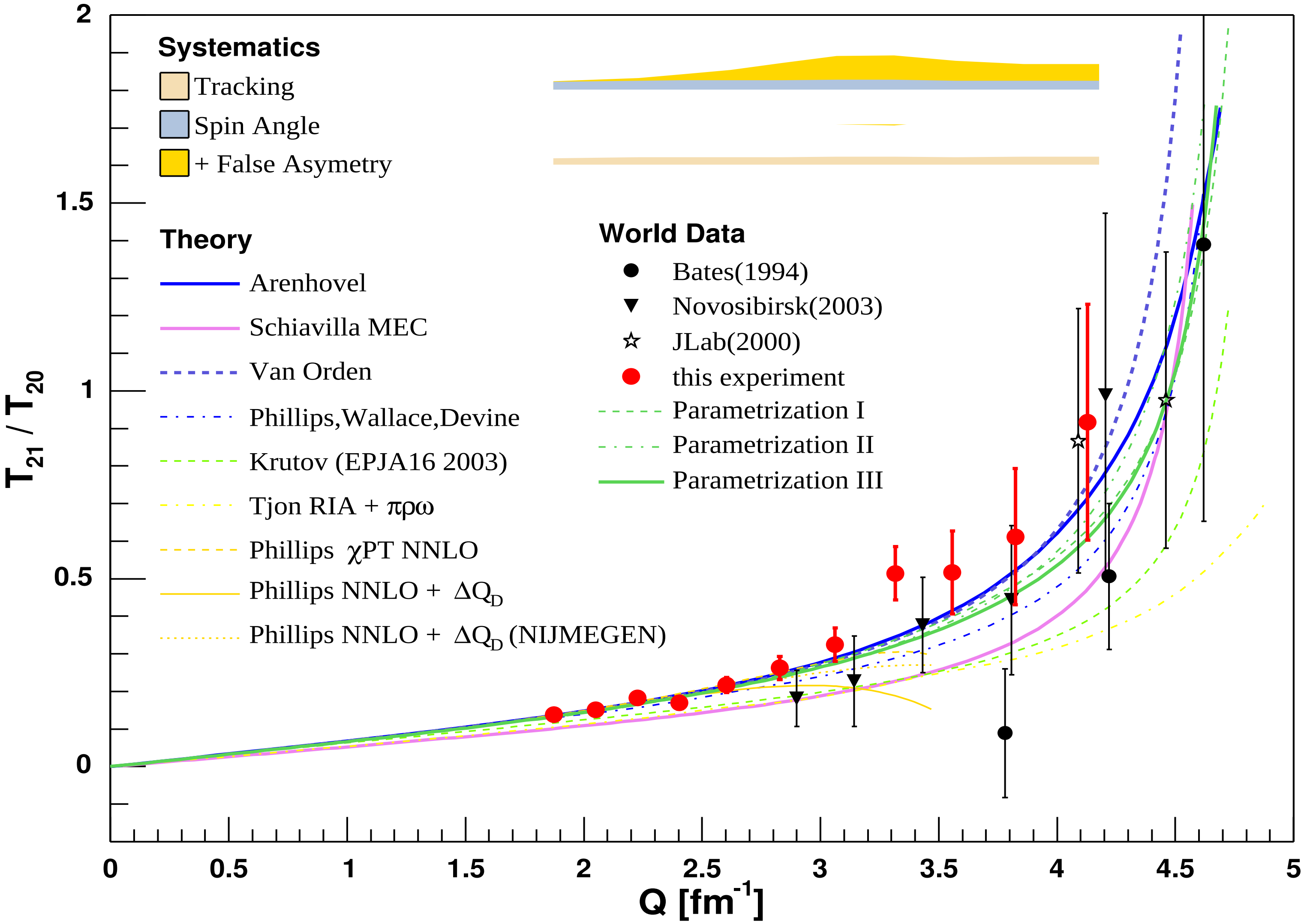

Figure 5-6: The T_{21}/T_{20} ratio compared to models and previous world data. A clear systematic deviation is obvious that the BLAST data lie consistently above all the models and previous data. This deviation is largely driven by the systematic deviation in T_{21} from the models as can be seen in Fig. 5-4. The magnitude of the deviation is similar to the size of the systematic uncertainty due to the "false asymmetry" discussed in Sec. 4.5.2, which is the dominating systematic error in T_{21}.

The significant difference among the theoretical models, for example between Arenhövel and Schiavilla, is again largely driven by the difference in T_{21} predicted by the models (Fig. 5-4). Because T_{21} is proportional to the product of G_M and G_Q, the difference between T_{21} is largely a result of the different G_M calculations by the models, again for example, Arenhövel's prediction of G_M is consistently higher than world data, while Schiavilla is consistently below world data. This is demonstrated in Fig. 2-10.

5.3 Refit of Parameterization I

Parameterization I [61] is refit with VEPP-3(2003) and BLAST data included [3]. This parameterization is chosen as it fits the first nodes of the form factors explicitly. The previous world data used are summarized in Tab. A.1 and A.2.

The fit minimizes $\chi^2 = \sum_I dy_I^T C_I^{-1} dy_I$, where dy_I is the vector of difference between the measured value and the model prediction for each experiment. C is the variance-covariance matrix [88]. The uncertainties in the cross section measurements are all considered independent therefore C is diagonal. The same is assumed for the recoil polarimeter experiments [4].

For experiments with polarized target, the uncertainties in P_{zz} dominate the systematic errors without exception, therefore the covariance matrices have non-zero

[3] Some of the systematic errors in the world data were not incorporated in the original fit in a consistent fashion. Due to the inadequate descriptions in some of the publications, it is probably not possible to include all the systematic errors correctly. For consistency, all the literature for data used in the fit were re-examined and systematic errors are included whenever possible. The fit results on the other hand were not affected significantly.

[4] For example, for Ref. [12], which is a cross section experiment with six data points,

$$dy = \begin{pmatrix} \sigma_1 - \sigma_1(\mathbf{a}) \\ \sigma_2 - \sigma_2(\mathbf{a}) \\ \sigma_3 - \sigma_3(\mathbf{a}) \\ \sigma_4 - \sigma_4(\mathbf{a}) \\ \sigma_5 - \sigma_5(\mathbf{a}) \\ \sigma_6 - \sigma_6(\mathbf{a}) \end{pmatrix}, \quad \text{and} \quad C = \begin{pmatrix} d\sigma_1^2 & 0 & 0 & 0 & 0 & 0 \\ 0 & d\sigma_2^2 & 0 & 0 & 0 & 0 \\ 0 & 0 & d\sigma_3^2 & 0 & 0 & 0 \\ 0 & 0 & 0 & d\sigma_4^2 & 0 & 0 \\ 0 & 0 & 0 & 0 & d\sigma_5^2 & 0 \\ 0 & 0 & 0 & 0 & 0 & d\sigma_6^2 \end{pmatrix},$$

where σ_i is the measured cross section, $\sigma_i(\mathbf{a})$ is the calculated cross section value from the parameterization with parameters $\mathbf{a}$. Parameterization I has 18 parameters, therefore $\mathbf{a} = (a_1, a_2, ..., a_{18})$. $d\sigma_i$ is the standard deviation of the measurement.

off-diagonal elements. For example, two BLAST data sets for T_{20} and T_{21} are used, leading to a 36×36 covariance matrix. As discussed in Sec. 5.1 the statistical and tracking errors are independent between Q^2 bins within each data set. The errors from P_{zz} and θ_S and false asymmetries are correlated within data sets but independent between the 2004 and 2005 data sets. The normalization errors are correlated across all the 36 BLAST data points.

The fit converges to χ^2 of 1.19 and gives the first nodes of the form factors,

$$Q_C^0 = 4.19 \pm 0.05 \text{ fm}^{-1}, \quad Q_M^0 = 7.30 \pm 0.15 \text{ fm}^{-1}, \quad Q_Q^0 = 10.5 \pm 7.7 \text{ fm}^{-1}.$$

The original fit gives $Q_C^0 = 4.21 \pm 0.08$ fm^{-1} [61] with world data up to 2001. Ref. [39] obtained $Q_C^0 = 4.17 \pm 0.04$ fm^{-1} with the 2003 VEPP-3 data included. It must be noted that the ± 0.08 fm^{-1} uncertainty in Ref. [61] includes the dispersion among the three parameterizations. On the other hand, the ± 0.04 fm^{-1} uncertainty in Ref. [39] is obtained by refitting parameterization I varying only Q_C^0, while keeping the remaining 17 parameters fixed at the original values found in Ref. [61]. These differences make direct comparisons between the Q_C^0 values difficult. G_Q^0 lies beyond 7 fm^{-1} where no polarized measurements exist; hence the uncertainty is large.

5.4 Separation of Form Factors

The T_{20} and T_{21} data are used in combination with world $A(Q)$ data to separate the form factor G_C and G_Q. Define for each Q point,

$$\begin{aligned}
dA &= G_C^2 + \frac{8}{9}\eta^2 G_Q^2 + \frac{2}{3}\eta G_M^2 - A(Q), \\
dT_{20} &= -\frac{1}{\sqrt{2}S}\left[\frac{8}{3}\eta G_C G_Q + \frac{8}{9}\eta^2 G_Q^2 + \frac{1}{3}\eta\left[1 + 2(1+\eta)\tan^2\frac{\theta_e}{2}\right] G_M^2\right] - T_{20}, \\
dT_{21} &= -\frac{2}{\sqrt{3}S}\eta\left[\eta + \eta^2 \sin^2\frac{\theta_e}{2}\right]^{1/2} G_M G_Q \sec\frac{\theta_e}{2} - T_{21},
\end{aligned}$$

Q	G_C	δG_C^{stat}	δG_C^{total}	G_Q	δG_Q^{stat}	ΔG_Q^{total}
2.228	0.1223	0.0009	0.0014	3.87	0.11	0.26
2.404	0.0953	0.0009	0.0014	2.985	0.095	0.20
2.603	0.0701	0.0010	0.0017	2.358	0.083	0.18
2.827	0.0479	0.0017	0.0021	1.839	0.096	0.15
3.063	0.0314	0.0033	0.0033	1.37	0.12	0.12
3.319	0.0139	0.0033	0.0033	1.091	0.055	0.055
3.560	0.0087	0.0026	0.0026	0.763	0.031	0.031
3.823	0.0065	0.0025	0.0015	0.522	0.024	0.024
4.140	0.0003	0.0016	0.0017	0.3637	0.0048	0.0048

Table 5.3: Separated deuteron form factors G_C and G_Q. The uncertainties are estimated with the fit, which produces the covariance matrix of the 18 parameters [88].

where $A(Q)$, S and G_M are fixed with Parameterization I obtained in Sec. 5.3. T_{20} and T_{21} are the measured values from BLAST. The residual vector is defined as,

$$dy = \left[dA(Q_1), ..., dA(Q_9), dT_{20}(Q_1), ..., dT_{20}(Q_9), dT_{21}(Q_1), ..., dT_{21}(Q_9)\right]^T,$$

and G_C and G_Q are determined by minimizing the $\chi^2 = dy^T C^{-1} dy$, with C the covariance matrix. The uncertainties in $A(Q)$ are calculated from the covariance matrix of the parameterization and are taken to be independent between Q values; therefore the upper-left 9 block of C is diagonal. The lower-right 18×18 block of C on the other hand has non-zero off-diagonal elements. The statistical uncertainties in G_C and G_Q are estimated by fitting with only a diagonal covariance matrix whose elements are the statistical variances of $A(Q)$, T_{20} and T_{21}. The results are tabulated in Tab. 5.3 and shown in Fig. 5-7, 5-8 and 5-9.

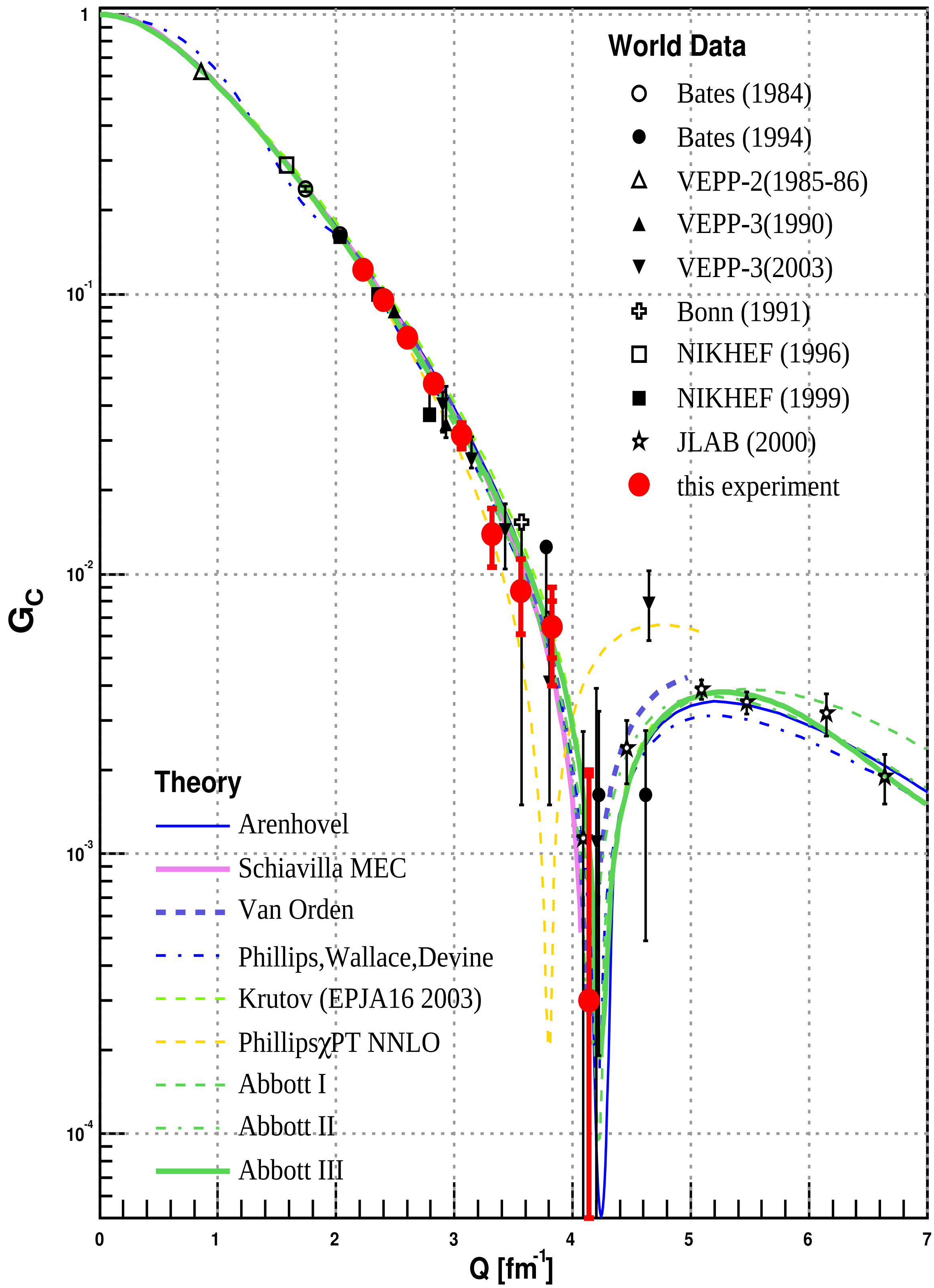

Figure 5-7: G_C separated with BLAST and world $A(Q)$ data. The error bars are quadratic sum of statistical uncertainties and all systematic errors.

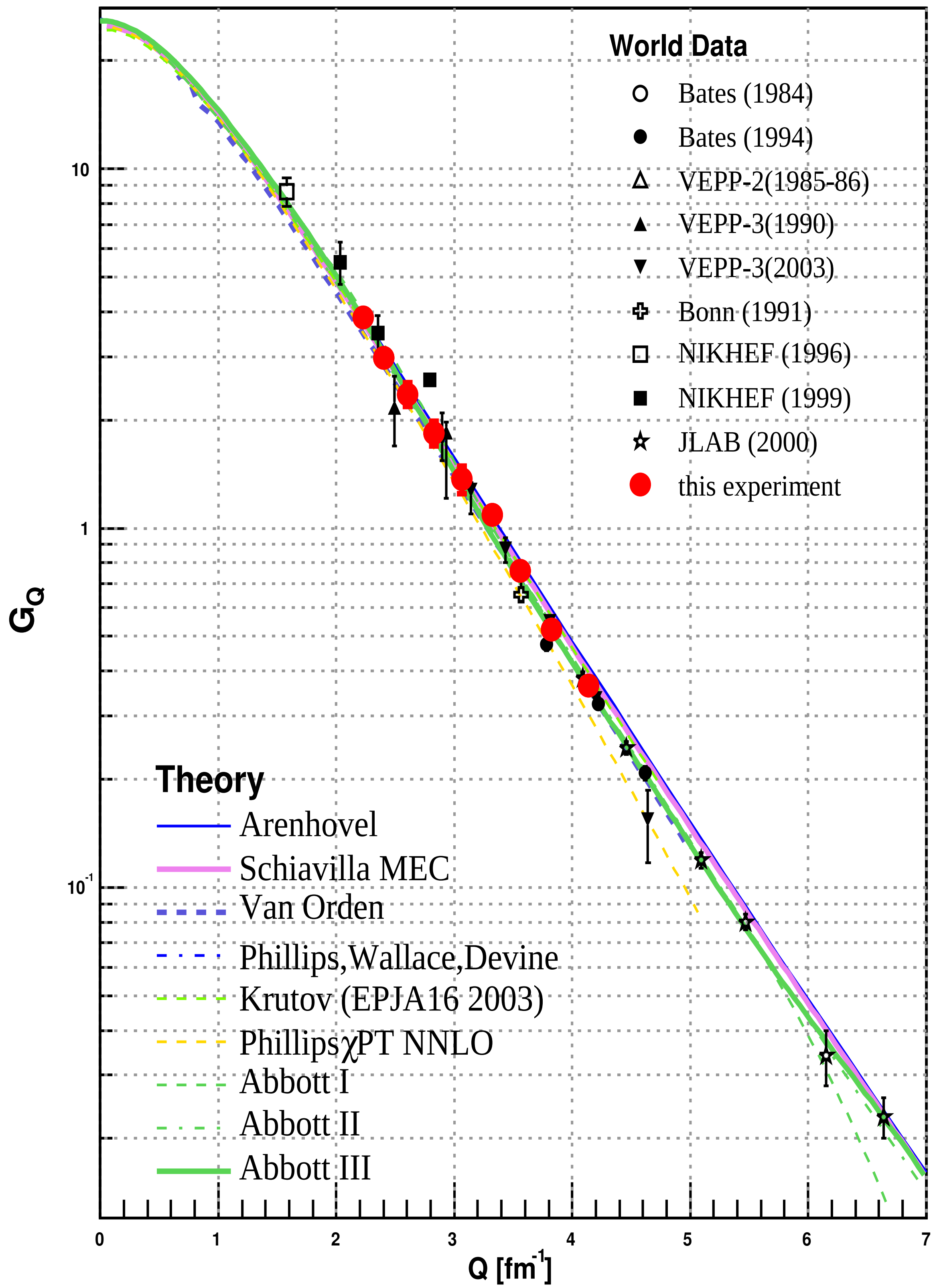

Figure 5-8: G_Q separated with BLAST and world $A(Q)$ data. The error bars are quadratic sum of statistical uncertainties and all systematic errors.

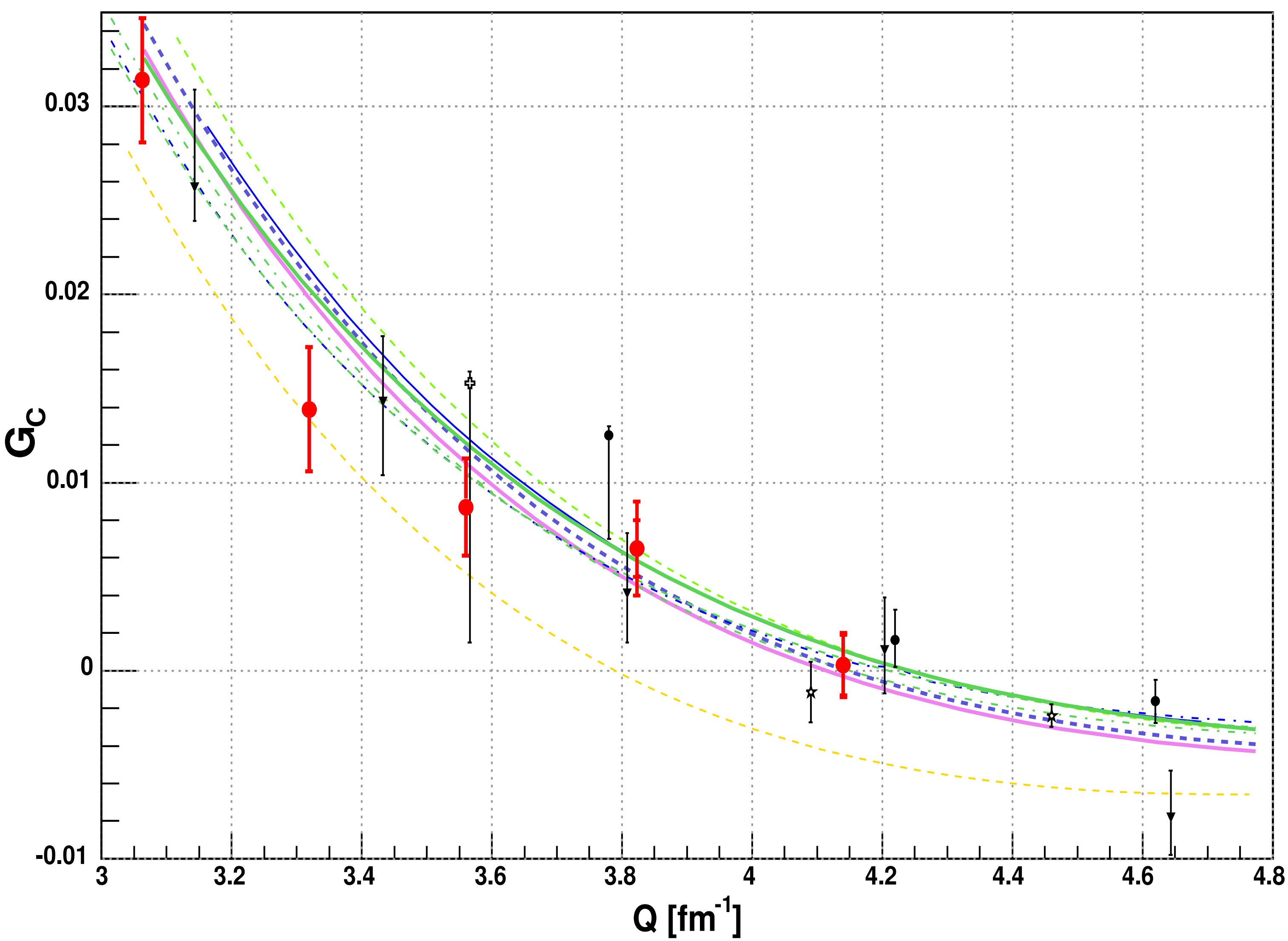

Figure 5-9: Linear scale plot of G_C is shown in the vicinity of its first node.

5.5 Outlook

This work substantially increased the statistical precision of deuteron tensor analyzing power data in a broad Q^2 range that covers the minimum of T_{20}, as well as the first node of G_C. Nine Q^2 bins were obtained compared with only a total of 26 data points measured from 1984 to 2003. T_{20} and T_{21} were measured simultaneously, which provides additional control on systematic errors.

Unfortunately, an independent tensor polarimeter was not implemented. One had to resort to the normalization at low Q^2 to theoretical calculations and previous world data. The direct effect is a dominating systematic error from the tensor polarization P_{zz}. The P_{zz} related uncertainties in T_{20} include statistical, tracking, false asymmetry and normalization errors (columns δP_{zz}, ΔP_{zz}, ΔR and "norm" in Tab. 5.1). At $Q^2 = 0.365\ (\mathrm{GeV/c})^2$, when these uncertainties are added in quadrature, the total error is ± 0.082 or 6.6% for T_{20} due to uncertainties in P_{zz}. NIKHEF achieved 5% relative uncertainty in tensor polarization in 1999 with a dedicated ion-extraction tensor polarimeter [71, 80]. It was proposed to install the same apparatus for BLAST and obtain a better than 5% measurement on P_{zz} [62]. However, the effort was not successful due to constraints in resources.

The ion-extraction polarimeter measures the tensor polarization on each target state individually [71, 80] as opposed to relying on the assumption that all states are equally polarized, as was done in this work (Sec. 4.3.3). This provides additional diagnostics on the target performance. More importantly, the ion-extraction polarimeter could completely eliminate the systematic error due to the false asymmetry discussed in Sec. 4.5.2. This error in listed in the ΔR columns in Tab. 5.1, and it can be seen that the effect of this error is almost as big as the normalization uncertainty, and is the dominating error in T_{21}. Even if the independent polarimeter could not achieve better precision on the absolute value of P_{zz} itself, being able to reduce the ΔR error could lead to significant improvement in the results. The ion-extraction polarimeter also measures the molecular fraction in the target gas stored in the target cell [71, 72, 80], providing valuable knowledge on the recombining process inside the cell (Sec. 3.2.2).

The Q^2 acceptance was reduced as the data below 2 fm^{-1} were used for tensor polarimetry. This means that BLAST T_{20} data cannot provide any information to better resolve the difference between Bates-84 and NIKHEF-96/99 measurements in this region of momentum transfer, where NIKHEF measurements are consistently lower (more negative) than the Bates-1984 data (Sec. 2.3.2).

The tensor ed-elastic asymmetries appeared to provide an very good measurement on the target spin angle θ_S (Sec. 4.3.3). However, without a dedicated tensor polarimetry, the target spin angle must be measured simultaneously with the tensor polarization P_{zz} by ed-elastic data also. With the help of an independent tensor polarimeter to constrain P_{zz}, the ed-elastic data could be used to obtain smaller statistical uncertainty and better understand the systematic errors in θ_S.

It must be noted that BLAST and the Novosibirsk 2003 data both are normalized to measurements at $Q = 1.96$ fm^{-1}. Therefore one future precise measurement of T_{20} at this momentum transfer with absolute tensor polarimetry could potentially improve the systematic errors in both sets of data. BLAST achieved 2% statistical uncertainty on T_{20} below 2 fm^{-1}, and the systematic uncertainty due to reconstruction error is also about 2%. With a lower beam energy, the event rate at this low Q will be much higher, therefore comparable or even higher statistical precision could be expected, while the challenge will be the control of systematic errors. It will be interesting to extend the Q coverage down to about 1.5 fm^{-1} as well. This will connect with the NIKHEF (96) measurement at 1.58 fm^{-1}.

The particle tracking with the BLAST drift chamber has room to improve. The design of the chambers left little of the redundancy which is desirable for precise calibration and diagnoses of systematic errors. Though not a major contributor of systematic errors, poor tracking resolution and accuracy caused confusion in the simultaneously measured electro-disintegration data which could have served as a good cross-check for this work. For example, the electro-disintegration channel could have been used to verify the P_{zz} extracted from elastic reaction. However, the large inconsistency within $D(e, e'p)$ data prevented an accurate comparison [53].

It is proposed to continue the BLAST physics program at other facilities [105], with a higher beam energy of about 1.5 GeV. Fig. 5-10 shows the Monte Carlo projected results for 1000 beam hours, under a luminosity of $\sim 5 \times 10^{31}$ /cm^2/sec and 60% target polarization. The measurement would provide even better statistical precision around the minimum of T_{20} [5].

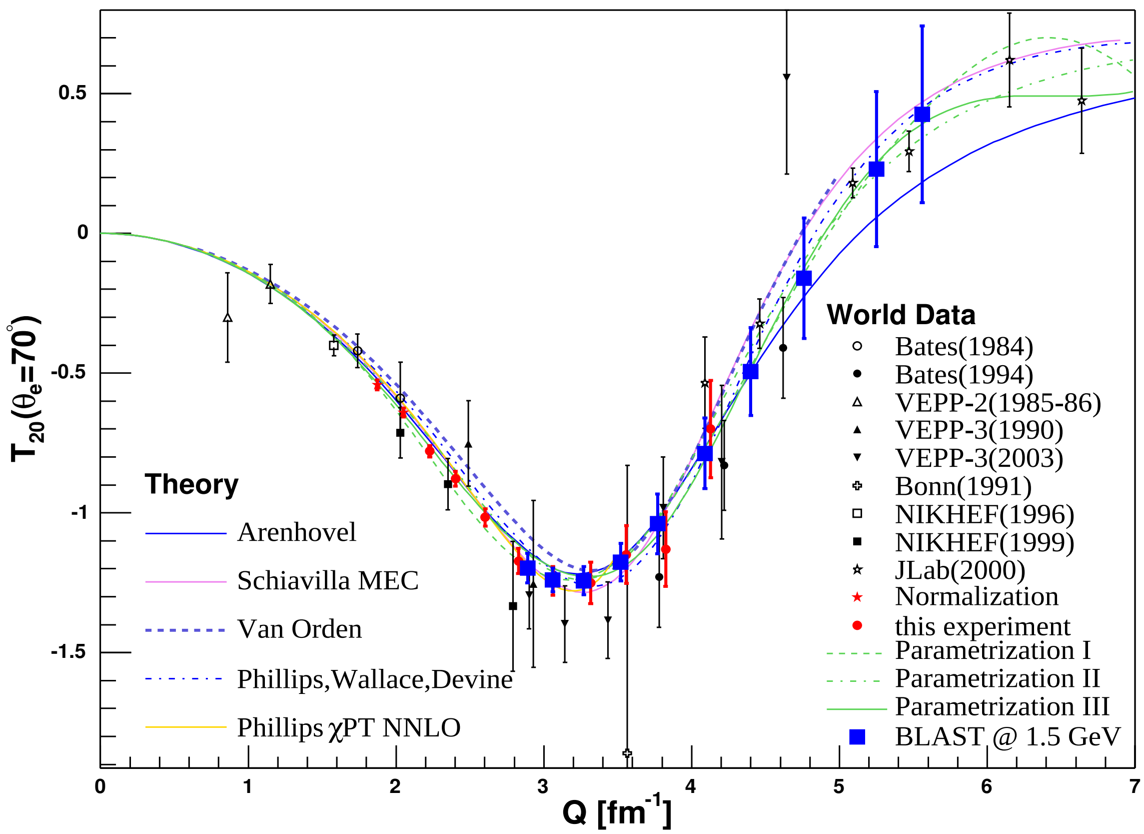

Figure 5-10: Projected statistical precision of T_{20} with 1.5 GeV beam. The projection is for 1000 beam hours with similar luminosity and target polarization as described in this work.

A few challenges must be answered under high beam energy. First, the measurement of target polarization must be addressed. With higher beam energy, the acceptance of the current BLAST detector package starts at almost 3 fm^{-1}. The absolute precision of data and models means that the precision in target polarization would be low if the data were to be normalized at this momentum transfer. Either an independent tensor polarimeter or a forward-angle detector for low Q^2 data must

[5] The detection efficiency is not taken into account in this projection. If the detection efficiency was not improved from the level of 50-60% described in Sec. 4.2.3, the statistical uncertainty will increase by about 40%.

be implemented. An independent polarimeter that can separately measure the polarization in each individual target state would be highly desirable. It would eliminate the systematic error due to the false asymmetry described in Sec. 4.5.2, which is the dominant error in T_{21} and the T_{21}/T_{20} ratio. In addition, at high Q^2 the deuteron identification must be treated with greater care. With the higher momentum of the recoil deuterons and knocked-out protons, their respective velocities become much closer to each other, leading to less separated time of flight peaks in Fig 4-2 and less separated distribution in Fig 3-22.

The discrepancy in world $A(Q)$ data at 2 fm^{-1}, described in Secs. 2.3.1 and 4.6.1, should be resolved in the near future as well [60]. It could potentially affect the normalization of BLAST data through the parameterizations.

A much better understanding of deuteron structure can be hoped for when the discrepancy in world $A(Q)$ data is resolved [60] and the absolute normalization in VEPP-3 and BLAST data are established.

Appendix A

Elastic Electron-Deuteron Scattering World Data

A.1 Cross Sections

Table A.1: World Cross Section Data. (Data below $Q = 10$ fm^{-1} are included. Data with (*) marked in front of the Q value are rejected from the fit due to inconsistency with the rest of the data.)

$Q(\text{fm}^{-1})$	$\theta_e(^\circ)$	$E_0(\text{GeV})$	$d\sigma/d\Omega(\text{cm}^2/\text{sr})$	error	Ref.
1.79	43.0	0.500	4.60×10^{-32}	0.45×10^{-32}	[11]
2.00	48.5	0.500	1.61×10^{-32}	0.15×10^{-32}	
2.22	55.0	0.500	0.726×10^{-32}	0.070×10^{-32}	
2.42	61.0	0.500	0.217×10^{-32}	0.020×10^{-32}	
2.62	67.5	0.500	0.0947×10^{-32}	0.010×10^{-32}	
2.82	75.0	0.500	0.0335×10^{-32}	0.0337×10^{-32}	
0.98	60.0	0.200	39.2×10^{-32}	3.7×10^{-32}	
1.07	70.0	0.190	20.1×10^{-32}	1.9×10^{-32}	
1.37	90.0	0.200	3.53×10^{-32}	0.34×10^{-32}	

Continued on next page

Table A.1 –continued from previous page

$Q(\mathrm{fm}^{-1})$	$\theta_e(^\circ)$	E_0(GeV)	$d\sigma/d\Omega(\mathrm{cm}^2/\mathrm{sr})$	error	Ref.
1.51	105.0	0.200	1.08×10^{-32}	0.10×10^{-32}	
1.60	145.0	0.179	0.185×10^{-32}	0.018×10^{-32}	
1.80	145.0	0.204	0.0825×10^{-32}	0.009×10^{-32}	
2.00	145.0	0.228	0.0579×10^{-32}	0.006×10^{-32}	
2.25	145.0	0.260	0.0192×10^{-32}	0.0023×10^{-32}	
0.548	45		674×10^{-32}	8.8×10^{-32}	[12]
0.775	45		225.4×10^{-32}	2.5×10^{-32}	
1.001	45		86.8×10^{-32}	0.955×10^{-32}	
1.268	60		15.95×10^{-32}	0.271×10^{-32}	
1.261	120		1.71×10^{-32}	0.0684×10^{-32}	
1.483	60		6.74×10^{-32}	0.148×10^{-32}	

Continued on next page

Table A.1 –continued from previous page

$Q(\text{fm}^{-1})$	$\theta_e(^\circ)$	$E_0(\text{GeV})$	$d\sigma/d\Omega(\text{cm}^2/\text{sr})$	error	Ref.
*2.450	90		617.00×10^{-36}	13.3×10^{-36}	[13] [1]
*2.450	120		221.00×10^{-36}	7.9×10^{-36}	
2.450	145		97.30×10^{-36}	5.8×10^{-36}	
*2.646	90		331.00×10^{-36}	8.2×10^{-36}	
2.646	120		119.00×10^{-36}	6.7×10^{-36}	
2.647	145		58.70×10^{-36}	6.0×10^{-36}	
*2.828	90		180.00×10^{-36}	5.2×10^{-36}	
2.828	120		68.70×10^{-36}	7.2×10^{-36}	
2.828	145		33.00×10^{-36}	6.1×10^{-36}	
3.464	90		29.00×10^{-36}	8.5×10^{-36}	
3.464	120		9.28×10^{-36}	14.9×10^{-36}	
3.464	145		5.81×10^{-36}	10.5×10^{-36}	
4.472	90		2.93×10^{-36}	19.0×10^{-36}	
0.939	60		59.400×10^{-32}	1.800×10^{-32}	[14]
0.999	60		44.700×10^{-32}	1.600×10^{-32}	
1.000	90		14.630×10^{-32}	0.280×10^{-32}	
1.005	130		3.241×10^{-32}	0.095×10^{-32}	
1.163	60		22.910×10^{-32}	0.760×10^{-32}	
1.162	60		23.890×10^{-32}	0.760×10^{-32}	
1.155	110		3.780×10^{-32}	0.110×10^{-32}	

Continued on next page

[1] Several of the data points are fit with large residuals, defined as the difference between the measured value σ and the value caluclated from the parameterization σ_{model}, divided by the uncertainty in the data $\delta\sigma$: $\frac{\sigma - \sigma_{model}}{\delta\sigma}$. The author estimated that the final results could differ from the published figures by up to 2%. An 2% error is added to the published uncertainties.

Table A.1 –continued from previous page

$Q(\mathrm{fm}^{-1})$	$\theta_e(^\circ)$	E_0(GeV)	$d\sigma/d\Omega(\mathrm{cm}^2/\mathrm{sr})$	error	Ref.
1.732	82.16		1.301×10^{-32}	0.070×10^{-32}	[15] [2]
2.005	80.84		4.61×10^{-33}	0.29×10^{-33}	
2.241	79.69		2.09×10^{-33}	0.12×10^{-33}	
1.723	180.00		2.855×10^{-34}	0.37×10^{-34}	
1.990	180.00		1.806×10^{-34}	0.18×10^{-34}	
2.220	180.00		7.81×10^{-35}	0.98×10^{-35}	
2.252	180.0		83.0×10^{-36}	9.0×10^{-36}	[16]
2.452	180.0		56.0×10^{-36}	7.0×10^{-36}	
2.839	180.0		24.5×10^{-36}	2.6×10^{-36}	
3.028	180.0		13.9×10^{-36}	2.4×10^{-36}	
3.177	180.0		6.9×10^{-36}	1.4×10^{-36}	

Continued on next page

[2] The authors used recoil angles.

Table A.1 –continued from previous page

$Q(\text{fm}^{-1})$	$\theta_e(^\circ)$	E_0(GeV)	$d\sigma/d\Omega(\text{cm}^2/\text{sr})$	error	Ref.
3.795	9.845	4.419	2.84919×10^{-33}	3.23374×10^{-34}	[17] [3]
3.847	10.028	4.419	1.69692×10^{-33}	1.45695×10^{-34}	
3.924	10.269	4.419	1.81863×10^{-33}	1.58504×10^{-34}	
4.000	10.496	4.419	1.37407×10^{-33}	1.30090×10^{-34}	
4.087	10.640	4.419	1.08135×10^{-33}	9.54129×10^{-35}	
4.159	10.851	4.419	8.93057×10^{-34}	9.31886×10^{-35}	
4.219	11.093	4.419	7.13201×10^{-34}	1.21396×10^{-34}	
4.025	10.493	4.419	1.10961×10^{-33}	2.18681×10^{-34}	
4.087	10.640	4.419	6.99695×10^{-34}	1.27217×10^{-34}	
4.159	10.933	4.419	8.11565×10^{-34}	1.15938×10^{-34}	
4.243	11.137	4.419	5.65526×10^{-34}	8.29438×10^{-35}	
4.324	11.339	4.419	5.15366×10^{-34}	1.10436×10^{-34}	
4.405	11.522	4.419	5.18295×10^{-34}	1.00780×10^{-34}	
4.472	11.746	4.419	5.55959×10^{-34}	9.14869×10^{-35}	
4.266	10.084	4.910	7.77695×10^{-34}	1.06583×10^{-34}	
*4.336	10.186	4.910	4.86592×10^{-34}	5.94921×10^{-35}	
4.427	10.391	4.910	5.63902×10^{-34}	6.48660×10^{-35}	
4.506	10.627	4.910	4.19633×10^{-34}	5.30861×10^{-35}	
4.594	10.812	4.910	3.29051×10^{-34}	4.11314×10^{-35}	
4.669	11.053	4.910	2.37409×10^{-34}	3.84987×10^{-35}	
4.743	11.219	4.910	1.94101×10^{-34}	4.40067×10^{-35}	
4.517	10.645	4.910	5.46233×10^{-34}	1.24373×10^{-34}	
4.583	10.815	4.910	3.58358×10^{-34}	7.24955×10^{-35}	
4.669	11.053	4.910	3.46489×10^{-34}	6.33625×10^{-35}	
4.754	11.278	4.910	2.23597×10^{-34}	5.31630×10^{-35}	
4.848	11.453	4.910	2.64995×10^{-34}	5.42209×10^{-35}	

Continued on next page

[3] The authors used recoil angles.

Table A.1 –continued from previous page

$Q(\mathrm{fm}^{-1})$	$\theta_e(^\circ)$	E_0(GeV)	$d\sigma/d\Omega(\mathrm{cm}^2/\mathrm{sr})$	error	Ref.
4.930	11.677	4.910	8.94092×10^{-35}	4.24694×10^{-35}	
5.010	11.833	4.910	1.13204×10^{-34}	5.47761×10^{-35}	
4.764	11.220	4.910	2.03705×10^{-34}	9.01002×10^{-35}	
4.827	11.410	4.910	1.81213×10^{-34}	5.22140×10^{-35}	
4.919	11.638	4.910	1.99703×10^{-34}	5.31046×10^{-35}	
5.010	11.853	4.910	1.35675×10^{-34}	4.59544×10^{-35}	
5.099	12.081	4.910	9.81396×10^{-35}	4.40917×10^{-35}	
5.187	12.276	4.910	1.11203×10^{-34}	4.72612×10^{-35}	
5.263	12.478	4.910	4.55621×10^{-35}	2.78813×10^{-35}	
5.560	13.321	4.910	6.07195×10^{-35}	1.67072×10^{-35}	
5.840	14.320	4.910	2.24917×10^{-35}	1.17002×10^{-35}	

Continued on next page

Table A.1 –continued from previous page

$Q(\mathrm{fm}^{-1})$	$\theta_e(^\circ)$	$E_0(\mathrm{GeV})$	$d\sigma/d\Omega(\mathrm{cm}^2/\mathrm{sr})$	error	Ref.
2.482	11.40		8.11×10^{-32}	0.41×10^{-32}	[18]
2.569	11.80		5.45×10^{-32}	0.32×10^{-32}	
2.653	12.20		4.00×10^{-32}	0.26×10^{-32}	
2.739	12.60		2.95×10^{-32}	0.21×10^{-32}	
3.123	13.35		7.54×10^{-33}	0.54×10^{-33}	
3.302	14.15		4.35×10^{-33}	0.36×10^{-33}	
3.321	14.25		3.63×10^{-33}	0.22×10^{-33}	
3.421	14.70		2.68×10^{-33}	0.16×10^{-33}	
3.524	15.15		2.05×10^{-33}	0.15×10^{-33}	
3.606	15.55		1.56×10^{-33}	0.13×10^{-33}	
0.686	180.	0.0701	279.0×10^{-35}	17.00×10^{-35}	[19]
1.288	180.	0.1353	85.7×10^{-35}	3.80×10^{-35}	
1.921	180.	0.2081	16.0×10^{-35}	2.30×10^{-35}	
2.431	180.	0.2763	6.35×10^{-35}	0.63×10^{-35}	
4.533	8.		0.114×10^{-32}	0.011×10^{-32}	[20]
5.068	8.		0.352×10^{-33}	0.030×10^{-33}	
6.207	8.		0.526×10^{-34}	0.042×10^{-34}	
6.704	8.		0.199×10^{-34}	0.017×10^{-34}	
7.167	8.		0.904×10^{-35}	0.071×10^{-35}	
8.013	8.		0.215×10^{-35}	0.020×10^{-35}	
8.778	8.		0.624×10^{-36}	0.068×10^{-36}	
0.136	8.		0.468×10^{-37}	0.106×10^{-37}	

Continued on next page

Table A.1 –continued from previous page

$Q(\mathrm{fm}^{-1})$	$\theta_e(^\circ)$	$E_0(\mathrm{GeV})$	$d\sigma/d\Omega(\mathrm{cm}^2/\mathrm{sr})$	error	Ref.
0.60000	1.50814		5.25791×10^{-27}	3.08785×10^{-29}	[21]
0.61563	1.54746		4.62621×10^{-27}	2.22991×10^{-29}	
0.62209	1.56372		4.46479×10^{-27}	2.22982×10^{-29}	
0.64109	1.61153		3.77998×10^{-27}	2.40107×10^{-29}	
0.65038	1.63491		3.49515×10^{-27}	2.22949×10^{-29}	
0.67823	1.70499		2.84120×10^{-27}	2.57199×10^{-29}	
0.69714	1.75257		2.44308×10^{-27}	2.05733×10^{-29}	
0.70143	1.76337		2.42073×10^{-27}	1.71440×10^{-29}	
0.71134	1.78831		2.24236×10^{-27}	1.54291×10^{-29}	
0.74699	1.87808		1.73618×10^{-27}	1.37112×10^{-29}	
0.75299	1.89318		1.66635×10^{-27}	1.88521×10^{-29}	
0.75498	1.89819		1.64272×10^{-27}	1.37108×10^{-29}	
0.78867	1.98301		1.29533×10^{-27}	1.71340×10^{-29}	
0.78930	1.98461		1.26890×10^{-27}	2.05601×10^{-29}	
0.79750	2.00524		1.20820×10^{-27}	1.71327×10^{-29}	
0.82523	2.07508		9.94518×10^{-28}	1.71292×10^{-29}	
0.82704	2.07966		1.00428×10^{-27}	1.37033×10^{-29}	
0.83606	2.10238		9.41147×10^{-28}	1.19891×10^{-29}	
0.85615	2.15299		8.13941×10^{-28}	1.19873×10^{-29}	
0.88431	2.22392		6.72183×10^{-28}	1.02728×10^{-29}	
0.88882	2.23529		6.62919×10^{-28}	1.02725×10^{-29}	
0.90499	2.27603		5.94519×10^{-28}	1.19829×10^{-29}	
0.92087	2.31606		5.17754×10^{-28}	1.36927×10^{-29}	
0.93328	2.34733		5.09146×10^{-28}	8.55705×10^{-30}	
0.94393	2.37418		4.65124×10^{-28}	1.19788×10^{-29}	

Continued on next page

Table A.1 –continued from previous page

$Q(\mathrm{fm}^{-1})$	$\theta_e(^\circ)$	E_0(GeV)	$d\sigma/d\Omega(\mathrm{cm}^2/\mathrm{sr})$	error	Ref.
0.210	30.0	0.0801	156.380×10^{-30}	0.761×10^{-30}	[22] [4]
0.459	70.0	0.0801	3.635×10^{-30}	0.020×10^{-30}	
0.487	75.0	0.0801	2.583×10^{-30}	0.014×10^{-30}	
0.513	80.0	0.0801	1.876×10^{-30}	0.010×10^{-30}	
0.539	85.0	0.0801	1.376×10^{-30}	0.008×10^{-30}	
0.562	90.0	0.0801	1.014×10^{-30}	0.006×10^{-30}	
0.607	100.0	0.0801	0.565×10^{-30}	0.006×10^{-30}	
0.647	110.0	0.0801	0.326×10^{-30}	0.002×10^{-30}	
0.682	120.0	0.0801	0.187×10^{-30}	0.001×10^{-30}	
0.711	130.0	0.0801	0.1072×10^{-30}	0.0005×10^{-30}	
0.724	135.0	0.0801	0.0802×10^{-30}	0.0004×10^{-30}	
0.513	40.0	0.1494	10.330×10^{-30}	0.064×10^{-30}	
0.573	45.0	0.1494	5.796×10^{-30}	0.040×10^{-30}	
0.631	50.0	0.1494	3.447×10^{-30}	0.023×10^{-30}	
0.688	55.0	0.1494	2.110×10^{-30}	0.015×10^{-30}	
0.743	60.0	0.1494	1.331×10^{-30}	0.011×10^{-30}	
0.796	65.0	0.1494	0.8609×10^{-30}	0.0057×10^{-30}	
0.847	70.0	0.1494	0.5675×10^{-30}	0.0044×10^{-30}	
0.515	40.0	0.1498	10.220×10^{-30}	0.186×10^{-30}	
0.575	45.0	0.1498	5.760×10^{-30}	0.045×10^{-30}	
0.633	50.0	0.1498	3.458×10^{-30}	0.027×10^{-30}	
0.690	55.0	0.1498	2.0770×10^{-30}	0.020×10^{-30}	
0.745	60.0	0.1498	1.345×10^{-30}	0.023×10^{-30}	

Continued on next page

[4] The authors did not clearly list all the systematic errors and how the total systematic errors should be determined. They stated that "The over-all normalization error, linearly added, was 0.48% and the maximum of the systematic errors 0.46%." They also stated that "The error in the ratio determination is less 0.07%" for gas target and "of the order of 1%" with the liquid target system. An over-all 0.46% systematic error is added to the statistical uncertainties listed in the publication. For the data points that are not consistent with the rest of the world data, a 1% systematic error is added.

Table A.1 –continued from previous page

$Q(\mathrm{fm}^{-1})$	$\theta_e(^\circ)$	E_0(GeV)	$d\sigma/d\Omega(\mathrm{cm}^2/\mathrm{sr})$	error	Ref.
1.033	90.0	0.1498	0.1235×10^{-30}	0.0012×10^{-30}	
*1.245	120.0	0.1498	0.0191×10^{-30}	0.0003×10^{-30}	
0.712	53.0	0.1602	2.064×10^{-30}	0.018×10^{-30}	
1.476	157.0	0.1602	0.00142×10^{-30}	0.00002×10^{-30}	
0.486	28.0	0.1995	25.360×10^{-30}	0.142×10^{-30}	
0.520	30.0	0.1995	18.450×10^{-30}	0.117×10^{-30}	
0.603	35.0	0.1995	8.890×10^{-30}	0.073×10^{-30}	
0.683	40.0	0.1995	4.484×10^{-30}	0.037×10^{-30}	
0.762	45.0	0.1995	2.388×10^{-30}	0.020×10^{-30}	
0.839	50.0	0.1995	1.362×10^{-30}	0.007×10^{-30}	
0.985	60.0	0.1995	0.4780×10^{-30}	0.0028×10^{-30}	
1.245	70.0	0.2225	0.1157×10^{-30}	0.0015×10^{-30}	
1.446	85.0	0.2225	0.0311×10^{-30}	0.0005×10^{-30}	
*1.836	125.0	0.2225	0.0180×10^{-30}	0.0003×10^{-30}	
*1.995	157.0	0.2225	0.00296×10^{-30}	0.00006×10^{-30}	
1.225	53.0	0.2784	0.257×10^{-30}	0.0032×10^{-30}	
1.456	65.0	0.2784	0.0646×10^{-30}	0.0011×10^{-30}	
*1.863	90.0	0.2784	0.0485×10^{-30}	0.0010×10^{-30}	
*1.995	100.0	0.2784	0.0251×10^{-30}	0.0006×10^{-30}	
0.776	30.0	0.2989	5.570×10^{-30}	0.084×10^{-30}	
1.017	40.0	0.2989	1.057×10^{-30}	0.015×10^{-30}	
1.245	50.0	0.2989	0.270×10^{-30}	0.008×10^{-30}	
1.353	55.0	0.2989	0.1363×10^{-30}	0.015×10^{-30}	
*1.456	60.0	0.2989	0.0803×10^{-30}	0.001×10^{-30}	
*1.833	80.0	0.2989	0.00940×10^{-30}	0.00019×10^{-30}	
*1.990	90.0	0.2989	0.00384×10^{-30}	0.00006×10^{-30}	

Continued on next page

Table A.1 –continued from previous page

$Q(\text{fm}^{-1})$	$\theta_e(^\circ)$	$E_0(\text{GeV})$	$d\sigma/d\Omega(\text{cm}^2/\text{sr})$	error	Ref.
2.592	155.0	0.300	5.610×10^{-35}	0.522×10^{-35}	[23]
2.818	155.0	0.330	2.880×10^{-35}	0.245×10^{-35}	
3.041	155.0	0.360	1.650×10^{-35}	0.134×10^{-35}	
3.296	155.0	0.395	8.020×10^{-36}	0.722×10^{-36}	
3.543	155.0	0.430	4.380×10^{-36}	0.416×10^{-36}	
3.820	155.0	0.470	1.980×10^{-36}	0.192×10^{-36}	
4.022	155.0	0.500	1.180×10^{-36}	0.106×10^{-36}	
4.254	155.0	0.535	5.490×10^{-37}	0.598×10^{-37}	
4.482	155.0	0.570	3.290×10^{-37}	0.349×10^{-37}	
4.673	155.0	0.600	1.940×10^{-37}	0.254×10^{-37}	
4.893	155.0	0.635	9.810×10^{-38}	1.589×10^{-38}	
5.108	155.0	0.670	6.760×10^{-38}	1.528×10^{-38}	
5.289	155.0	0.700	3.770×10^{-38}	0.916×10^{-38}	
3.583	90.0	0.571	2.200×10^{-35}	0.12×10^{-35}	[24]
3.583	99.0	0.534	1.670×10^{-35}	0.11×10^{-35}	
3.925	139.0	0.501	2.320×10^{-36}	0.25×10^{-36}	
4.476	115.0	0.639	1.030×10^{-36}	0.15×10^{-36}	
5.068	116.0	0.738	3.100×10^{-37}	0.12×10^{-37}	
*5.778	139.0	0.806	2.080×10^{-37}	0.26×10^{-37}	
*5.778	77.5	1.100	2.180×10^{-38}	0.43×10^{-38}	

Continued on next page

Table A.1 –continued from previous page

$Q(\mathrm{fm}^{-1})$	$\theta_e(^\circ)$	E_0(GeV)	$d\sigma/d\Omega(\mathrm{cm}^2/\mathrm{sr})$	error	Ref.
5.551	180.		60.40×10^{-40}	11.90×10^{-40}	[25]
6.186	180.		13.40×10^{-40}	2.70×10^{-40}	
6.430	180.		4.74×10^{-40}	1.29×10^{-40}	
6.685	180.		0.62×10^{-40}	0.34×10^{-40}	
7.131	180.		0.18×10^{-40}	0.17×10^{-40}	
7.568	180.		0.24×10^{-40}	0.12×10^{-40}	
7.981	180.		0.28×10^{-40}	0.11×10^{-40}	
8.061	180.		0.314×10^{-40}	0.170×10^{-40}	
8.434	180.		0.050×10^{-40}	0.075×10^{-40}	

Continued on next page

Table A.1 –continued from previous page

$Q(\mathrm{fm}^{-1})$	$\theta_e(^\circ)$	$E_0(\mathrm{GeV})$	$d\sigma/d\Omega(\mathrm{cm}^2/\mathrm{sr})$	error	Ref.
0.678	40.0	0.200	4.497×10^{-30}	0.076×10^{-30}	[26]
0.837	50.0	0.200	1.349×10^{-30}	0.024×10^{-30}	
0.985	60.0	0.200	4.649×10^{-31}	0.084×10^{-31}	
1.118	70.0	0.200	1.822×10^{-31}	0.035×10^{-31}	
1.245	80.0	0.200	7.450×10^{-32}	0.134×10^{-32}	
1.357	90.0	0.200	3.387×10^{-32}	0.058×10^{-32}	
1.459	100.0	0.200	1.633×10^{-32}	0.031×10^{-32}	
1.546	110.0	0.200	8.141×10^{-33}	0.163×10^{-33}	
1.622	120.0	0.200	4.344×10^{-33}	0.096×10^{-33}	
1.688	130.0	0.200	2.303×10^{-33}	0.046×10^{-33}	
0.775	30.0	0.300	5.546×10^{-30}	0.083×10^{-30}	
0.900	35.0	0.300	2.348×10^{-30}	0.040×10^{-30}	
1.020	40.0	0.300	1.067×10^{-30}	0.016×10^{-30}	
1.245	50.0	0.300	2.634×10^{-31}	0.040×10^{-31}	
1.460	60.0	0.300	7.408×10^{-32}	0.111×10^{-32}	
1.655	70.0	0.300	2.400×10^{-32}	0.041×10^{-32}	
1.833	80.0	0.300	8.802×10^{-33}	0.150×10^{-33}	
1.990	90.0	0.300	3.417×10^{-33}	0.058×10^{-33}	
2.131	100.0	0.300	1.466×10^{-33}	0.264×10^{-33}	
1.487	35.0	0.500	2.457×10^{-31}	0.037×10^{-31}	
1.679	40.0	0.500	8.914×10^{-32}	0.134×10^{-32}	
1.866	45.0	0.500	3.470×10^{-32}	0.063×10^{-32}	
2.042	50.0	0.500	1.425×10^{-32}	0.021×10^{-32}	
2.214	55.0	0.500	6.129×10^{-33}	0.092×10^{-33}	
2.377	60.0	0.500	2.830×10^{-33}	0.043×10^{-33}	
2.530	65.0	0.500	1.353×10^{-33}	0.024×10^{-33}	
2.676	70.0	0.500	6.695×10^{-34}	0.100×10^{-34}	

Continued on next page

Table A.1 –continued from previous page

$Q(\mathrm{fm}^{-1})$	$\theta_e(^\circ)$	E_0(GeV)	$d\sigma/d\Omega(\mathrm{cm}^2/\mathrm{sr})$	error	Ref.
2.814	75.0	0.500	3.594×10^{-34}	0.054×10^{-34}	
2.945	80.0	0.500	2.041×10^{-34}	0.043×10^{-34}	
3.066	85.0	0.500	1.164×10^{-34}	0.027×10^{-34}	
1.918	35.0	0.650	5.088×10^{-32}	0.087×10^{-32}	
2.163	40.0	0.650	1.537×10^{-32}	0.023×10^{-32}	
2.400	45.0	0.650	5.261×10^{-33}	0.079×10^{-33}	
2.512	47.5	0.650	3.200×10^{-33}	0.058×10^{-33}	
2.623	50.0	0.650	1.946×10^{-33}	0.029×10^{-33}	
2.731	52.5	0.650	1.182×10^{-33}	0.018×10^{-33}	
2.836	55.0	0.650	7.627×10^{-34}	0.114×10^{-34}	
3.036	60.0	0.650	3.206×10^{-34}	0.064×10^{-34}	
3.226	65.0	0.650	1.469×10^{-34}	0.029×10^{-34}	
3.406	70.0	0.650	7.085×10^{-35}	0.163×10^{-35}	
3.730	80.0	0.650	2.039×10^{-35}	0.055×10^{-35}	
4.010	90.0	0.650	7.574×10^{-36}	0.258×10^{-36}	
4.250	100.0	0.650	3.029×10^{-36}	0.117×10^{-36}	

Continued on next page

Table A.1 –continued from previous page

$Q(\mathrm{fm}^{-1})$	$\theta_e(^\circ)$	$E_0(\mathrm{GeV})$	$d\sigma/d\Omega(\mathrm{cm}^2/\mathrm{sr})$	error	Ref.
4.219	15.22		3.81×10^{-34}	0.23×10^{-34}	[27]
4.592	16.67		1.56×10^{-34}	0.09×10^{-34}	
4.934	18.03		7.16×10^{-35}	0.43×10^{-35}	
5.257	19.32		3.60×10^{-35}	0.22×10^{-35}	
5.558	20.56		1.94×10^{-35}	0.12×10^{-35}	
5.847	21.77		9.89×10^{-36}	0.59×10^{-36}	
6.309	23.77		3.58×10^{-36}	0.22×10^{-36}	
6.761	25.79		1.39×10^{-36}	0.08×10^{-36}	
7.813	30.82		1.32×10^{-37}	0.08×10^{-37}	
8.836	27.98		2.33×10^{-38}	0.18×10^{-38}	
9.407	33.25		5.18×10^{-39}	0.45×10^{-39}	
10.080	36.59		1.29×10^{-39}	0.14×10^{-39}	
10.684	36.24		4.43×10^{-40}	0.68×10^{-40}	
11.276	39.30		1.17×10^{-40}	0.21×10^{-40}	
11.723	37.18		4.69×10^{-41}	1.44×10^{-41}	
11.729	41.83		4.46×10^{-41}	1.31×10^{-41}	
12.366	40.46		3.48×10^{-41}	1.03×10^{-41}	
12.369	45.74		8.08×10^{-42}	8.08×10^{-42}	
4.1077	35.67		7.710×10^{-35}	2.89×10^{-36}	[28]
4.4929	33.53		4.330×10^{-35}	1.68×10^{-36}	
5.1106	29.83		1.940×10^{-35}	7.76×10^{-37}	
5.5000	27.52		1.160×10^{-35}	4.73×10^{-37}	
6.2273	23.29		0.520×10^{-35}	2.54×10^{-37}	
6.7802	20.27		0.275×10^{-35}	1.54×10^{-37}	

A.2 Polarized Observables

$Q(\mathrm{fm}^{-1})$	$\theta_e(^\circ)$	$E_0(\mathrm{GeV})$	T_{20}	δT_{20}	ΔT_{20}	T_{21}	δT_{21}	ΔT_{21}	T_{21}	δT_{21}	ΔT_{21}	Ref.
1.74	71.5	0.310 ± 0.0020	-0.41	0.072								[30]
2.03	70	0.371 ± 0.0018	-0.58	0.14								
0.86	34.5	0.29	-0.30	0.16								[31]
1.15	33.56	0.4	-0.18	0.073								[32]
2.49	14.11	2.02	-0.77	0.16	0.07							[33]
2.93	16.62	2.02	-1.32	0.32	0.11							
3.566	21.		-2.01	1.13								[34]
3.78 [a]	80.9	0.653	-1.24	0.17		0.11	0.21		0.48	0.15		[35, 104]
4.22	78.7	0.755	-0.82	0.15		0.42	0.14		-0.05	0.10		
4.62	76.7	0.853	-0.41	0.18		0.57	0.17		-0.04	0.13		
1.58	32.81	0.565	-0.401	0.024	0.028				0.022	0.019	0.003	[36, 72]
2.026	34.07	0.704	-0.713	0.082	0.036							[37, 59] [b]
2.352	40.24	0.704	-0.897	0.081	0.045							
2.788	49.07	0.704	-1.334	0.223	0.066							
4.090	35.584		-.546	0.174		.463	0.124		.087	0.056		[38]
4.460	33.349		-.322	0.093		.315	0.093		-.027	0.048		
5.090	29.751		.191	0.054		.201	0.088		-.018	0.041		
5.470	27.327		.301	0.074		.220	0.109		.022	0.051		
6.150	22.968		.625	0.169		.166	0.111		-.023	0.073		
6.640	19.789		.477	0.189		.001	0.162		-.133	0.088		
2.900	16.8	2.0025	-1.294	0.084	0.088	0.234	0.094	0.015				[39]
3.143	18.3	2.0025	-1.398	0.100	0.093	0.318	0.165	0.020				
3.432	20.1	2.0025	-1.384	0.102	0.092	0.521	0.168	0.033				
3.808	22.5	2.0025	-0.982	0.169	0.066	0.435	0.177	0.027				
4.204	25.1	2.0025	-0.818	0.269	0.058	0.808	0.289	0.051				
4.643	28.1	2.0025	0.557	0.342	0.044	0.299	0.414	0.019				

[a] This T_{22} measurement is not consistent with the rest of G_M data and is a 3-σ outlier in the gloabal fit. It is nevertheless included in the fit which includes all polarized measurements.

[b] The listed values are for $T_{20}(70^\circ)$.

Table A.2: World data for polarized deuteron observables used in the global parameterizations. The sign of T_{21} is negated following the convention set by the recoil polarimeter experiments.

Bibliography

[1] A. Chodos *et al.*, Phys. Rev. **D9**, 3471 (1974).

[2] S. Théberge, A. Thomas, and G. Miller, Phys. Rev. **D22**, 2838 (1980).

[3] H. Yukawa, Proc. Phys. Math. Soc. Jpn **17**, 48 (1935).

[4] M. Lacombe *et al.*, Phys. Rev. **C21**, 1980 (861).

[5] R. Reid Jr., Ann. Phys. **50**, 411 (1968).

[6] V. Stocks, R. Klomp, C. Terheggen, and J. de Swart, Phys. Rev. **C49**, 2950 (1994).

[7] R. Wiringa, V. Stock, and R. Schiavilla, Phys. Rev. **C51**, 38 (1995).

[8] R. Machleidt, Phys. Rev. **C63**, 024001 (2001).

[9] S. Beane *et al.*, *From hadrons to nuclei: Crossing the border* (2000), nucl-th/0008064.

[10] T. W. Donnelly and A. S. Raskin, Annals Phys. **169**, 247 (1986).

[11] J. Friedman, H. Kendal, and P. Gram, Phys. Rev. **120**, 992 (1960).

[12] D. Drickey and L. Hand, Phys. Rev. Lett. **9**, 521 (1962).

[13] C. Buchnanan and M. Yearian, Phys. Rev. Lett. **15**, 303 (1965).

[14] B. Grossetête, D. Drikey, and P. Lehmann, Phys. Rev. **141**, 1425 (1966).

[15] D. Benaksas, D. Drickey, and D. Feérejacque, Phys. Rev. **148**, 1327 (1966).

[16] R. Rand, R. Frosch, C. Littig, and M. Yearian, Phys. Rev. Lett. **18**, 469 (1967).

[17] J. Elias *et al.*, Phys. Rev. **177**, 2075 (1969).

[18] S. Galster *et al.*, Nucl. Phys. **B 32**, 221 (1971).

[19] D. Ganichot, B. Grossetête, and D. Isabelle, Nucl. Phys. **A 178**, 545 (1972).

[20] R. Arnold *et al.*, Phys. Rev. Lett. **35**, 776 (1975).

[21] Y. Akimov *et al.*, Sov. J. Phys. **29**, 335 (1979).

[22] G. Simon, C. Schmitt, and V. Walther, Nucl. Phys. **A364**, 285 (1981).

[23] S. Auffret *et al.*, Phys. Rev. Lett. **54**, 649 (1985).

[24] R. Cramer *et al.*, Z. Phys. **C 29**, 513 (1985).

[25] P. Bosted *et al.*, Phys. Rev. **C 42**, 38 (1990).

[26] S. Plachkov *et al.*, Nucl. Phys. **A510**, 740 (1990).

[27] L. Alex *et al.* (JLab Hall A Collaboration), Phys. Rev. Lett. **82**, 1374 (1999).

[28] D. Abbott *et al.* (JLab t_{20} Collaboration), Phys. Rev. Lett. **82**, 1379 (1999).

[29] M. N. Rosenbluth, Phys. Rev. **79**, 615 (1950).

[30] M. Schulze *et al.*, Phys. Rev. Lett. **52**, 20 (1984).

[31] V. Dmitriev *et al.*, Phys. Lett. **157B**, 143 (1985).

[32] B. Voitsekhovskii *et al.*, JEPT Lett. **43**, 733 (1986).

[33] R. Gilman *et al.*, Phys. Rev. Lett. **65**, 1733 (1990).

[34] B. Boden *et al.*, Z. Phys. **C 49**, 175 (1991).

[35] I. The *et al.*, Phys. Rev. Lett. **67**, 173 (1994).

[36] M. Ferro-Luzzi *et al.*, Phys. Rev. Lett. **77**, 2630 (1996).

[37] M. Bouwhuis *et al.*, Phys. Rev. Lett. **82**, 3755 (1999).

[38] D. Abbott *et al.* (JLab t_{20} Collaboration), Phys. Rev. Lett. **84**, 5053 (2000).

[39] D. Nikolenko *et al.*, Phys. Rev. Lett. **90**, 072501 (2003).

[40] R. Gilman and F. Gross, J. Phys. **G 28**, R37 (2002).

[41] H. Henning, J. Adam, P. Sauer, and A. Stadler, Phys. Rev. **C 52**, 471 (1995).

[42] J. Adam and H. Arenhövel, Nucl. Phys. **A 614**, 289 (1997).

[43] H. Arenhövel, F. Ritz, and T. Wilbois, Phys. Rev. **C 61**, 034002 (2000).

[44] J. Forest *et al.*, Phys. Rev. **C 54**, 646 (1996).

[45] R. Wiringa, V. Stoks, and R. Schiavilla, Phys. Rev. **C 51**, 38 (1995).

[46] J. Forest, Phys. Rev. **C 61**, 034007 (2000).

[47] E.Hummel and J. Tjon, Phys. Rev. Lett. **63**, 1788 (1989).

[48] D. Phillips, S. Wallace, and N. Devine, Phys. Rev. **C 58**, 2261 (1998).

[49] J. van Orden, N. Devine, and F. Gross, Phys. Rev. Lett. **75**, 4369 (1995).

[50] D. Phillips, Phys. Lett. **B 567**, 13 (2003).

[51] M. Garçon and J. Van Orden, Adv. Nucl. Phys. **26**, 293 (2001), nucl-th/0102049.

[52] P. Karpius, *Vector Polarization Observables of the Deuteron*, Ph.D. thesis, University of New Hampshire (2005).

[53] A. Maschinot, *Analysis of Scattered Protons in Deuteron Electrodisintegration with a Polarized Electron Beam and an Internal Vector/Tensor Polarized Target at BLAST*, Ph.D. thesis, Massachusetts Institute of Technology (2005).

[54] V. Ziskin, *Measurement of the Electric Form Factor of the Neutron at low Q^2 from a Vector Polarized Deuterium Target at BLAST*, Ph.D. thesis, Massachusetts Institute of Technology (2005).

[55] N. Meitanis, *A Measurement of the Neutron Magnetic Form Factor G_M^n from Quasi-elastic $^2H(e,e')$ at low Q^2*, Ph.D. thesis, Massachusetts Institute of Technology (2006).

[56] J. Carlson and R. Schiavilla, Rev. Mod. Phys. **70**, 743 (1998).

[57] I. Sick, *Elastic electron scattering from light nuclei* (2002), nucl-ex/0208009.

[58] N. Rodning and L. Knutson, Phys.Rev. **C41**, 898 (1990).

[59] M. Bouwhuis, *Tensor-Polarization Observables in Electron-Deuteron Scattering*, Ph.D. thesis, Universiteit Utrecht (1998).

[60] R. Gilman, D. Higinbotham, X. Jiang, *et al.*, *A(q) at low q in ed elastic scattering*, update jeopardy proposal for experiment E02-004, Hall A Collaboration.

[61] D. Abbott *et al.* (JLab t_{20} Collaboration), Eur. Phys. J. **A7**, 421 (2000).

[62] W. Bertozzi, S. Gilad, W. Turchinetz, and Z.-L. Zhou, *A study of the deuteron structure using tensor polarized deuterium and the blast detector*, a new proposal submitted to the Bates P.A.C Meeting, March,2000.

[63] M. Farkhondeh *et al.*, in *Proceedings of the SPIN-2004 Symposium* (2004), pESP-2004 Workshop.

[64] G. T. Zwart, *Polarized electrons at the Bates Accelerator Center South Hall Ring: Extracted beams and internal targets*, Ph.D. thesis, Boston University (1986).

[65] K. A. Dow, M. Farkhondeh, and J. D. Zumbro, *South Hall Ring: Magnetic Measurements of the Lattice Dipoles*, Tech. rep., Bates Linear Accelerator Center (1993).

[66] K. B. Unser, AIP Conf. Proc. **252**, 266 (1991).

[67] M. H. Hurwitz, *The Compton Polarimeter at Bates*, Tech. rep., Bates Linear Accelerator Center (2003).

[68] W. Franklin *et al.*, in *Proceedings of the SPIN-2004 Conference* (2004).

[69] T. Akdogan, *akdogan@mit.edu*, private communication.

[70] V. S. Morozov *et al.*, Phys. Rev. ST Accel. Beams **4**, 104002 (2001).

[71] Z.-L. Zhou *et al.*, Nucl. Instrum. Methods **A 378**, 40 (1996).

[72] Z. Zhou, *A Study of the Spin Dependence of Electron Scattering from a Tensor Polarized Deuterium Internal Target*, Ph.D. thesis, University of Wisconsin - Madison (1996).

[73] P. de Witt Huberts, Nucl. Phys. **A553**, 845c (1993).

[74] L. Anderson and D. Swenson, Nucl. Inst. Meth. **B12**, 157 (1985).

[75] L. Holland, *Vacuum Manual* (Spon, 1974).

[76] A. Shinozaki, *shino@lns.mit.edu*, private communication.

[77] Z.-L. Zhou, *zzhou@ridgefield.oilfield.slb.com*, private communication.

[78] R. Gilman *et al.*, Nucl. Inst. Meth. **A327**, 277 (1993).

[79] M. Bouchiat and J. Brossel, Phys. Rev. **147**, 41 (1966).

[80] Z.-L. Zhou *et al.*, Nucl. Instrum. Methods A **405**, 165 (1997).

[81] A. Goodhue, *Analysis of Measurements of the BLAST Magnetic Field*, Tech. rep., Bates Linear Accelerator Center (2002).

[82] K. Dow *et al.*, *Magnetic field measurements of the blast spectrometer*.

[83] C. Crawford, *Precision Measurement of the Proton Electric to Magnetic Form Factor Ratio with BLAST*, Ph.D. thesis, Massachusetts Institute of Technology (2005).

[84] B. Tonguc, in *RICH2004 Proceedings; Nucl. Instr. and Methods A* (2005).

[85] B. Zhang, *Searching for short range correlations using* $(e, e'NN)$ *reactions*, Ph.D. thesis, Massachusetts Institute of Technology (2003).

[86] D. Hassel, *hasell@mit.edu*, private communication.

[87] A. Afanasev, I. Akushevich, and N. Merenkov (2005), hep-ph/0102086.

[88] W. Press, S. Teukolsky, W. Vetterling, and B. Flannery, *Numerical Recipes in C* (Cambridge University Press, 1992).

[89] H. Niederreiter, *Random Number Generation and Quasi-Monte Carlo Methods* (Soc for Industrial & Applied Math, 1992).

[90] P. D. Group, *Statistics (review)* (2004).

[91] D. Nikolenko, *nikolenk@jlab.org*, private communication.

[92] H. Arenhövel, F. Ritz, and T. Wilbois, Phys. Rev. **C 55**, 2214 (1999), nucl-th/9910009.

[93] D. Phillips, S. Wallace, and N. Devine (1999), nucl-th/9906086.

[94] A. Krutov and V. Troitsky, Eur.Phys.J. **A16**, 285 (2003).

[95] M. Zuilhof and J. Tjon, Phys. Rev. **C 24**, 736 (1981).

[96] S. Dubovichenko, *Deep potentials of the nn interactions with forbidden states* (1998), nucl-th/9805030.

[97] A. Buchmann, Y. Yamauchi, and A. Faessler, Nucl. Phys. **A496**, 621 (1989).

[98] D. Phillips, *phillips@phy.ohiou.edu*, private communication.

[99] H. Arenhövel, W. Leidemann, and E. Tomusiak, Phys. Rev. **C 46**, 455 (1992).

[100] H. Arenhövel, private communication.

[101] R. Machleidt, K. Holinde, and C. Elster, Phys. Rept. **149**, 1 (1987).

[102] R. Fatemi, *Presentation at blast analysis meeting, 08/19/2005.*

[103] P. Mergell, U.-G. Meissner, and D. Drechsel, Nucl. Phys. A **596**, 367 (1996).

[104] M. Garçon *et al.*, Phys. Rev. **C 49**, 2516 (1994).

[105] M. Kohlm *et al.*, *Blast @ elsa: An opportunity fo rprecision measurements of fundamental nucleon and few-body properties at low q^2* (2005).